Carboxymethyl cellulose as artificial solid/electrolyte interphases and separator for Zn-based battery

Miss Phonnapha Tangthuam

จุฬาลงกรณ์มหาวิทยาลัย
CHULALONGKORN UNIVERSITY

A Dissertation Submitted in Partial Fulfillment of the Requirements
for the Degree of Doctor of Engineering in Chemical Engineering
Department of Chemical Engineering
Faculty Of Engineering
Chulalongkorn University
Academic Year 2023

คาร์บอกซีเมทิลเซลลูโลสเป็นชั้นผิวประดิษฐ์เชื่อมต่อวัฏภาคของแข็ง-อิเล็กโทรไลต์ และแผ่นกั้น

สำหรับแบตเตอรี่ฐานสังกะสี

น.ส.พรนภา ต่างท้วม

วิทยานิพนธ์นี้เป็นส่วนหนึ่งของการศึกษาตามหลักสูตรปริญญาวิศวกรรมศาสตรดุษฎีบัณฑิต

สาขาวิชาวิศวกรรมเคมี ภาควิชาวิศวกรรมเคมี

คณะวิศวกรรมศาสตร์ จุฬาลงกรณ์มหาวิทยาลัย

ปีการศึกษา 2566

Thesis Title   Carboxymethyl cellulose as artificial solid/electrolyte interphases
                      and separator for Zn-based battery
By   Miss Phonnapha Tangthuam
Field of Study   Chemical Engineering
Thesis Advisor   Associate Professor Dr. SOORATHEP KHEAWHOM
Thesis Co Advisor   Assistant Professor Dr. JITTI KASEMCHAINAN

Accepted by the FACULTY OF ENGINEERING, Chulalongkorn University in Partial Fulfillment of the Requirement for the Doctor of Engineering

.... Dean of the FACULTY OF
ENGINEERING
(Professor Dr. SUPOT TEACHAVORASINSKUN)

DISSERTATION COMMITTEE

.... Chairman
(Assistant Professor Dr. Pornchai Bumroongsri)

.... Thesis Advisor
(Associate Professor Dr. SOORATHEP KHEAWHOM)

.... Thesis Co-Advisor
(Assistant Professor Dr. JITTI KASEMCHAINAN)

.... Examiner
(Associate Professor Dr. SUPAREAK PRASERTHDAM)

.... Examiner
(Assistant Professor Dr. PHUET PRASERTCHAROENSUK)

.... Examiner
(Assistant Professor Dr. NATTAPORN TONANON)

.... Examiner
(Associate Professor Dr. ROJANA PORNPRASERTSUK)

พรนภา ต่างท้วม : คาร์บอกซีเมทิลเซลลูโลสเป็นชั้นผิวประดิษฐ์เชื่อมต่อวัฏภาคของแข็ง-อิเล็กโทรไลต์ และแผ่นกั้น สำหรับแบตเตอรี่ฐานสังกะสี. (Carboxymethyl cellulose as artificial solid/electrolyte interphases and separator for Zn-based battery) อ.ที่ปรึกษาหลัก : รศ. ดร.สุรเทพ เขียวหอม, อ.ที่ปรึกษาร่วม : ผศ.ดร. ดร.จิตติ เกษมชัยนันท์

การแสวงหาระบบกักเก็บพลังงานที่มีขนาดใหญ่และทนทานต่อการใช้งานกำลังได้รับความสนใจมากขึ้น ขณะเดียวกันแบตเตอรี่ฐานสังกะสีแบบชาร์จไฟในอิเล็กโทรไลต์แบบฐานน้ำนี้ก็ได้รับการผลักดันเพื่อใช้สำหรับการทำงานในการกักเก็บระดับโครงข่ายไฟฟ้าเนื่องด้วยมีค่าความจุทางทฤษฎีที่มากและมีความปลอดภัยสูง อย่างไรก็ตาม แบตเตอรี่ชนิดนี้เผชิญกับปัญหาบางอย่างบนขั้วแอโนดสังกะสี ซึ่งเป็นอุปสรรคต่อการประยุกต์ใช้งานจริง ปัญหาเหล่านั้นประกอบด้วย การเกิดก๊าซไฮโดรเจน การกร่อนตัว และก่อตัวของโครงสร้างเดนไดรต์ และเกิดชั้นเคลือบผิวที่ลดการเกิดปฏิกิริยาบนผิวขั้ว ดังนั้นการสร้างชั้นผิวประดิษฐ์เชื่อมต่อวัฏภาคของแข็ง-อิเล็กโทรไลต์ด้วยสารพอลิอิเล็กโทรไลต์ เช่น สารคาร์บอกซีเมทิลเซลลูโลส จึงเป็นทางออกของปัญหาที่กล่าวมาข้างต้น ด้วยข้อได้เปรียบในเรื่องของ เศรษฐกิจและสิ่งแวดล้อม สารคาร์บอกซีเมทิลเซลลูโลสประกอบด้วยหมู่คาร์บอกซิล โดยหมู่ฟังก์ชันกลุ่มนี้สามารถส่งเสริมการกระจายตัวของไอออนสังกะสีบนพื้นผิวของอิเล็กโทรดได้อย่างสม่ำเสมอกัน เพิ่มความเสถียรให้กับพื้นผิวขั้วได้มากขึ้น การศึกษานี้จึงมุ่งเน้นดูบทบาทของสารคาร์บอกซีเมทิลเซลลูโลส ในฐานะชั้นผิวประดิษฐ์เชื่อมต่อวัฏภาคของแข็ง-อิเล็กโทรไลต์ในแบตเตอรี่สังกะสี-ไอโอดีน ในการตรวจสอบผลกระทบของชั้นผิวประดิษฐ์ดังกล่าว จะได้รับการศึกษาบนทั้งขั้วแผ่นโลหะสังกะสีเปล่า และแผ่นขั้วสารประกอบผสมโลหะสังกะสี และประยุกต์เข้ากับระบบแบตเตอรี่ที่ใช้ขั้วแคโทดที่เป็นสารประกอบคาร์บอนผสมไอโอดีน นอกจากนี้ยังมีการนำเสนอแผ่นพอลิอิเล็กโทรไลต์ ที่ประกอบด้วยสารคาร์บอกซีเมทิลเซลลูโลสและพอลิไวนิลแอลกอฮอล์ แผ่นกั้นนี้จะได้รับการสาธิตในเซลล์ไฟฟ้าเคมีแบบรูปตัวแอช และนอกจากนี้ สารคาร์บอกซีเมทิลเซลลูโลสยังถูกเคลือบบนแผ่นคาร์บอนสักหลาดเพื่อใช้เป็นขั้วแบตเตอรี่ ในระบบแบตเตอรี่สังกะสี-ไอโอดีนแบบอิเล็กโทรไลต์ไหล ซึ่งได้รับการนำเสนอถึงศักยภาพในการเพิ่มประสิทธิภาพในการทำงานให้กับแบตเตอรี่ได้ จากผลการศึกษาชี้ให้เห็นว่า ชั้นผิวประดิษฐ์สารคาร์บอกซีเมทิลเซลลูโลสที่เกิดอย่างสม่ำเสมอ ช่วยลดผลกระทบของปฏิกิริยาข้างเคียงและเสริมการกระจายประจุสังกะสีได้ดี ส่งผลให้เซลล์แบตเตอรี่สังกะสี-ไอโอดีนที่ใช้ขั้วแผ่นสังกะสีที่มีชั้นผิวประดิษฐ์ฯ แสดงความสามารถในการคายประจุที่มากกว่า 98 เปอร์เซ็นต์ สามารถอัด/คายประจุได้ถึง 2,000 รอบ ที่ความหนาแน่นของกระแส 5 มิลลิแอมป์ต่อตารางเซนติเมตร นอกจากนี้ แผ่นกั้นที่ได้รับการพัฒนาจากสารคาร์บอกซีเมทิลเซลลูโลสและพอลิไวนิลแอลกอฮอล์ สามารถป้องกันการข้ามผ่านของโมเลกุลอย่าง ไอโอดีนและพอลิไอโอไดด์ได้สำเร็จ ดูได้จากการทำงานบนเซลล์ไฟฟ้าเคมีแบบรูปตัวแอช ที่สามารถทำงานได้ถึง 300 รอบ ความหนาแน่นของกระแส 10 มิลลิแอมป์ต่อตารางเซนติเมตร นอกจากนี้การใช้แผ่นขั้วคาร์บอนสักหลาดที่มีชั้นผิวประดิษฐ์คาร์บอกซีเมทิลเซลลูโลสเป็นอิเล็กโทรดในแบตเตอรี่แบบอิเล็กโทรไลต์ไหล ยังช่วยเพิ่มการสะสมของสังกะสีบนเส้นใย ทำส่งเสริมให้แบตเตอรี่ทำงานได้อย่างมีประสิทธิภาพกว่าถึง 90 เปอร์เซ็นต์หลังผ่านการทำงาน 100 รอบ ที่ความหนาแน่นของกระแส 80 มิลลิแอมป์ต่อตารางเซนติเมตร ที่ความจุ 120 มิลลิแอมป์ชั่วโมง (25 มิลลิแอมป์ชั่วโมงต่อตารางเซนติเมตร) การค้นพบนี้เองได้ยืนยันถึงบทบาทที่สำคัญของสารคาร์บอกซีเมทิลเซลลูโลส ในการพัฒนาเทคโนโลยีของแบตเตอรี่ฐานสังกะสี นับว่าเป็นสารที่น่าสนใจสำหรับระบบกักเก็บพลังงานต่อไป

สาขาวิชา	วิศวกรรมเคมี	ลายมือชื่อนิสิต ....
ปีการศึกษา	2566	ลายมือชื่อ อ.ที่ปรึกษาหลัก ....
		ลายมือชื่อ อ.ที่ปรึกษาร่วม ....

\# \# 6273034821 : MAJOR CHEMICAL ENGINEERING

Phonnapha Tangthuam : Carboxymethyl cellulose as artificial solid/electrolyte interphases and separator for Zn-based battery. Advisor: Assoc. Prof. Dr. SOORATHEP KHEAWHOM Co-advisor: Asst. Prof. Dr. JITTI KASEMCHAINAN

As the quest for robust large-scale energy storage systems (EESs) intensifies, aqueous rechargeable zinc-based batteries are gaining traction for grid-scale applications due to their high theoretical capacity and safety. Despite this, their practical application is compromised by several zinc anode issues, including hydrogen evolution, corrosion, dendritic growth, and passivation. An artificial solid electrolyte interphase (ASEI) using polyelectrolytes, such as carboxymethyl cellulose (CMC), is emerging as a solution, offering economic and environmental advantages. CMC's structure, enriched with carboxyl groups, allows for the refined management of zinc ion distribution at the electrode surface, promising enhanced surface stability. This study delves into CMC's role as ASEI in zinc-iodine batteries (ZIBs), examining its effect on both the zinc anode, fabricated from a zinc sheet, and a composite anode with integrated CMC in systems with a composite carbon-iodine cathode. A novel CMC and polyvinyl alcohol (PVA) polyelectrolyte membrane, trialed in an electrochemical H-cell configuration, and CMC-coated carbon felt (CF) in a Zn-iodine flow battery, are also presented, highlighting their potential in enhancing battery operation. Our results show that a uniform CMC-ASEI layer mitigates side reactions and improves zinc ion distribution, with a Zn-CMC//I_2 cell maintaining over 98% capacity after 2000 cycles at 5 mA/cm². The CMC/PVA membrane successfully prevents iodine and polyiodide migration, evidenced by over 300 stable cycles at 10 mA/cm² in an H-cell setup. Moreover, CMC-coated CF in a flow battery enhances zinc deposition, yielding more than 90% efficiency after 100 cycles at 80 mA/cm² and a capacity of 120 mAh/cm². These findings affirm CMC's vital role in advancing zinc-based battery technology, marking it as a key player for the next generation of EESs.

Field of Study:	Chemical Engineering	Student's Signature ....
Academic Year:	2023	Advisor's Signature ....
		Co-advisor's Signature ....

ACKNOWLEDGEMENTS

Phonnapha Tangthuam

TABLE OF CONTENTS

Page

LIST OF FIGURES

LIST OF TABLES

Chapter 1
INTRODUCTION

1.1 Background

Energy generation is experiencing an intense transformation, reducing traditional fossil fuels in favor of sustainable, eco-friendly alternatives like renewable energy sources. This pivotal shift is catalyzed by a combination of escalating electricity demand and the critical need to address environmental degradation, as depicted in Figure 1.1(1).
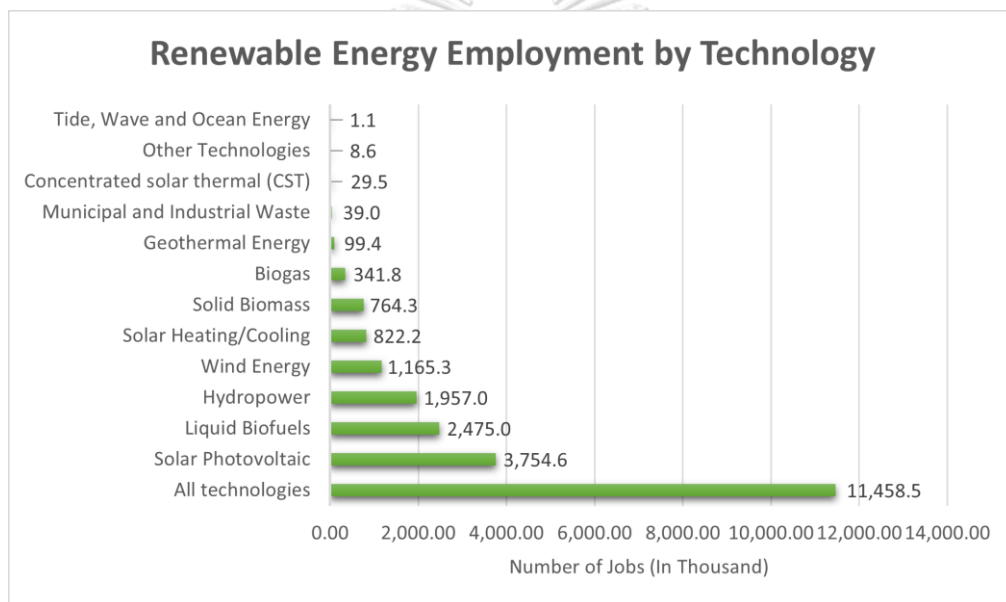
Figure 1. 1 Renewable energy employment by technology, excluding Number of jobs (In thousand) of all worlds in 2020 (Source: International Renewable Energy Agency (IRENA))

Renewable energy technologies, including photovoltaic systems, wind turbines, thermochemical conversions, and hydropower, are becoming the cornerstone of this new energy era. Nevertheless, the weather-dependent and variability of renewable energy sources pose considerable challenges for their integration into power grids, particularly smaller ones, where maintaining stable power, frequency, and voltage is intricate (2).

Electrical Energy Storage (EES) systems have been identified as vital for mitigating the fluctuating outputs of renewable sources. These systems are pivotal for stabilizing power, minimizing emissions, and enhancing power quality (3). Within the EES landscape, electrochemical storage technologies have taken center stage, represented by a spectrum of rechargeable batteries including, but not limited to, lead-acid, Ni-Cd, Ni-metal hydride, Na-S, lithium-ion, and flow batteries (4-8). Despite their ubiquity and potential contributions to sustainability, these technologies are encumbered by significant limitations such as finite lifespans, low energy densities, hazardous materials, elevated costs, safety issues, and the requirement for complex management systems.

In the vanguard of energy storage research, novel rechargeable battery technologies such as Na-ion, Zn-ion and Al-ion are drawing significant attention. Particularly, aqueous Zinc-based batteries (ZBBs) have emerged as a promising solution for large-scale storage, courtesy of zinc's high theoretical capacity (820 mAh g^{-1}), favorable electrode potential (-0.76 V versus SHE in near-neutral aqueous electrolyte), low toxicity, abundance, economic feasibility, and processing advantages, all of which are critical for sustainable energy technologies (9-11).

ZBBs utilize intercalation host materials at the cathode, with a rich variety of cathode materials such as vanadium and manganese-based compounds driving research efforts to optimize ZBB technology (12) Despite their potential, Zinc-based batteries face challenges like side reactions, including hydrogen evolution, corrosion, passivation, and anode zinc dendrite formation as shown in Figure 1.2. As for zinc dendrite, this problem can result in battery life reduction due to short circuits (13, 14). Moreover, irreversible parasitic reactions at both the anode and cathode are problematic, with anode corrosion leading to zinc and electrolyte depletion, hydrogen gas production, and adverse effects on Coulombic efficiency and pH levels (15, 16).
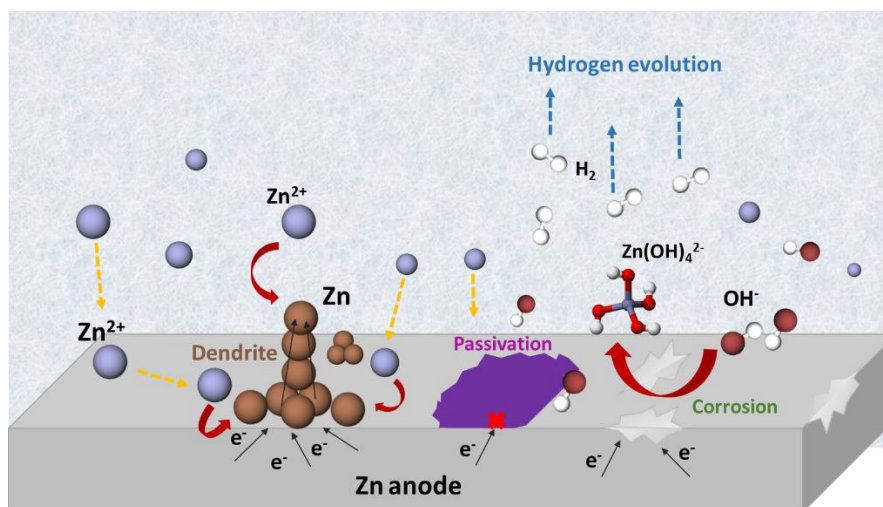
Figure 1. 2 Schematic illustration of the issues of zinc anode.

To improve ZBBs, strategic advancements in electrode and electrolyte design and their interfacial engineering are crucial. Strategies involve electrode innovation, such as additive incorporation and novel configurations like composite zinc (Zn) anodes with activated carbon to prevent direct contact between the Zn anode and the electrolyte, enhancing discharge capacity and cycling performance (17, 18). Additionally, layered double hydroxides have shown potential in increasing voltage stability and efficiency, despite some persistent dendritic growth (19, 20). Research has also delved into manipulating electrolyte additives to influence the crystallographic orientation and surface texture of the zinc metal, aiming for more uniform deposition (21).

Furthermore, ex-situ and in-situ solid-electrolyte interphase (SEI) approaches have been developed to regulate ion distribution and suppress side reactions at the electrode-electrolyte interface. This includes the fabrication of an artificial SEI as a protective barrier on the zinc electrode's surface, with various materials like polyamides and viscoelastic films demonstrating their ability to inhibit dendrite formation and reduce side reactions (22-24), Metal oxides like zinc oxide have been explored to improve deposition kinetics and facilitate Zn ion de-solvation, with metals such as indium, copper, and oxides like scandium oxide, titanium dioxide, aluminum oxide, and barium titanate being investigated to enhance interfacial stability and zinc metal plating uniformity (25-32).

Polyelectrolytes serve as promising materials for solid-electrolyte interphase (SEI) formation. These materials consist of repeating units that contain electrolyte groups. In an aqueous solution, the polymer becomes charged and capable of carrying ions. One prominent example in this category is carboxymethyl cellulose (CMC), which is a biodegradable cellulose ether. CMC possesses a variety of hydroxyl and carboxylic functional groups, making it highly advantageous due to its ability to retain water, its biodegradability, its cost-effectiveness, and its potential for electrochemical applications in battery technology.

The iodide/iodine (I^-/I_2) redox couple has garnered attention in zinc-based batteries (ZBBs) due to its superlative electrochemical attributes and its abundance in oceanic reserves, estimated at 50-60 mg/l, which resonates with the pursuit of sustainable energy. Nonetheless, the rechargeable zinc-iodine battery (ZIB) grapples with challenges such as self-discharge, sluggish reaction kinetics, and the formation of undesired by-products and structures on zinc anodes, which is a commonality with ZBBs. For comparison between ZIBs and other Zn-based batteries such as Zn-ion batteries, ZIBs utilize the redox reaction to charge/discharge while Zn-ion batteries use the intercalation instead.

To surmount these hurdles, innovative approaches in electrode, electrolyte, and membrane design are imperative to bolster the ZIB's performance and longevity. Proposals include the utilization of three-dimensional carbon cathodes and the development of cost-effective cation exchange membranes (CEMs) to hinder the crossover of iodine species. Additionally, complexing agents in electrolytes have been suggested to stabilize iodine and augment battery capacity.

CMC, laden with negative charges due to its functional groups, has been employed to coat a dense and homogeneous CMC-ASEI film on Zn composite anodes. This artificial SEI layer, imbued with CMC, demonstrates commendable ionic conductivity. The carboxyl groups in CMC-Na facilitate a uniform Zn^{2+} ion dispersion on the electrode surface, thereby attenuating dendrite growth and curtailing side reactions through their coordinating action.

The integration of CMC into polyelectrolyte membranes, in tandem with polyvinyl alcohol (PVA), has been scrutinized for its potential as a cost-effective CEM in ZIBs. CMC enhances the cationic exchange capacity, while PVA contributes

hydrogen-binding robustness and superior ion conductivity. Consequently, the CMC/PVA amalgamation in membranes yields heightened ion conductivity and diminishes polyiodide crossover in ZIBs.

Furthermore, CMC's application as an ASEI on a 3D structured carbon felt (CF) electrode within a Zn-iodine flow battery has been explored. The findings reveal a markedly uniform and compact Zn deposition on the CMC-CF electrode, underscoring CMC's beneficial impact on battery operation. The quest for optimized and sustainable energy storage systems continues unabated, with zinc-based batteries poised to play a transformative role in the integration and utilization of renewable energy sources.

1.2 Objective

The primary goal of this research endeavor is to conceptualize and synthesize a highly reversible zinc (Zn) electrode, operational in neutral or slightly acidic electrolyte mediums, for utilization in rechargeable battery systems. The approach harnesses an artificial solid-electrolyte interphase (ASEI), composed of strategic polyelectrolyte materials, to address and mitigate prevalent challenges such as dendritic zinc growth, electrode corrosion, and undesirable side reactions that have historically impeded the efficacy and longevity of zinc-based batteries. Furthermore, the fabricated zinc electrodes, bolstered by this ASEI, will be incorporated into zinc-iodine and zinc-ion battery architectures to critically assess their performance metrics and potential scalability for practical applications.

The research also aims to innovate a cost-effective cation exchange membrane (CEM), optimized for the unique demands of rechargeable zinc-iodine batteries. This membrane will harness the ion-selective properties of polyelectrolytes to impede the migration of iodine species, effectively minimizing self-discharge phenomena and promoting ion exchange processes essential for high-efficiency energy storage solutions.

1.3 Scope of research

The research outlined herein spans several critical development areas, each pivotal to advancing the domain of negative electrodes and saparator:

1. A multifaceted approach guides the development process, encompassing the synthesis of electrodes with diversely tuned molecular weights and concentrations of polyelectrolytes, aiming to discern the optimal configuration for enhanced electrochemical performance.

2. Carboxymethyl cellulose (CMC) is selected as the polyelectrolyte of choice. Its molecular weight and concentration are documented in Table 1.1. Utilizing these parameters, the solid electrolyte interphase (SEI) layer is engineered through a meticulously controlled solution-coating process.

3. The construction of a zinc-ion battery system is undertaken, featuring a composite zinc anode coupled with the aforementioned SEI layer, all within a coin-cell architecture. This system is subject to comprehensive performance evaluations to quantify its operational capabilities.

4. The coin-cell configuration is designed, with careful selection of cathode and electrolyte materials. Detailed specifications of these components are systematically shown in Table 1.1.

5. In parallel, an innovative separator is synthesized, employing CMC as the main polyelectrolyte. This separator is composed of various polyelectrolyte ratios, crafted to enhance ionic selectivity and mechanical stability.

6. Additionally, a zinc-iodine battery is finely assembled within an H-cell framework. After assembly, its performance are analyzed to assess its practicality and efficiency.

7. Comprehensive details of the specific choices of electrode and electrolyte materials within the H-cell construct are collated and presented in Table 1.2, offering a transparent view of the material composition and design considerations.

Table 1. 1 The details of cathode and electrolyte in coil-cell

Polyelectrolyte	
Chemical	Carboxy methyl cellulose (CMC)
Molecular weight	90,000 and 250,000
Concentration (%wt.)	1.5%wt ,2.5%wt and 3.5%wt
Electrolyte	
Chemical	$ZnSO_4$
Concentration (Molar)	1.5 molar
Battery component	
Type	Coil cell
Negative site	
Current collector	Stainless-steel mesh
Electrode	Zn composite with SEI layer
Positive site	
Current collector	Carbon clothes
Electrode	Manganese oxide
Separator	PPE membrane

จุฬาลงกรณ์มหาวิทยาลัย

CHULALONGKORN UNIVERSITY

Table 1. 2 The details of electrode and electrolyte in H-cell

Polyelectrolyte membrane	
Chemical	Carboxy methyl cellulose (CMC) And Poly vinyl alcohol (PVA)
Molecular weight	CMC: Mw.250,000 and PVA: Mw.117
Ratio of Concentration (CMC: PVA %wt.)	75:25, 50:50 and 25:75
Battery component	
Type	H-cell
Negative site	
Current collector	Stainless-steel mesh
Electrode	Carbon felt with Zn-electroplate
Electrolyte	$ZnSO_4$ 1 Molar
Positive site	
Current collector	Stainless-steel mesh
Electrode	Carbon felt
Electrolyte	N iodine solution

จุฬาลงกรณ์มหาวิทยาลัย

CHULALONGKORN UNIVERSITY

1.4 Structure of the dissertation

This dissertation unfolds across six meticulously structured chapters, beginning with an introductory foray and culminating in a conclusive synthesis of the research findings.

Chapter 1: Introduction - This opening chapter lays the groundwork for the dissertation, delineating the research background, objectives, and scope. It provides a foundational understanding of zinc-based batteries (ZBBs), the inherent challenges they present, the specific tribulations faced by zinc-iodine batteries (ZIBs), and the pivotal role of the polyelectrolyte carboxymethyl cellulose (CMC), setting the stage for the detailed exploration that follows.

Chapter 2: Theory and Literature Review - This chapter presents a comprehensive review of the literature, highlighting the merits of aqueous ZBBs and dissecting the challenges associated with the Zn anode. It surveys various strategies to ameliorate these challenges, with a focus on electrode additives and the application of artificial solid electrolyte interphases (ASEIs). The chapter also introduces the unique properties and advantages of polyelectrolytes, particularly CMC, and delves into the zinc-iodide ($Zn-I_2$) redox chemistry. It concludes with an exposition of the analytical techniques employed in this research, encompassing both physical and electrochemical characterization.

Chapter 3: Carboxymethyl Cellulose as an ASEI for Zinc-Based Anodes - This chapter details the innovative application of CMC as an ASEI for zinc-based anodes in aqueous electrolytes. It discusses the initial design and development of Zn anodes, from simple Zn sheets to composite anodes integrating graphite and CMC-ASEI. The chapter highlights the role of the Zn-CMC electrode in promoting uniform Zn^{2+} ion distribution, forestalling dendrite formation, and curtailing undesirable side reactions. It also outlines the experimental methodologies and assesses the anode's performance within a fully assembled Zn-CMC//I_2 cell. This work has been published in Materials Science for Energy Technologies (2023) Volume 6, pages 417-428.

Chapter 4: CMC-Based Polyelectrolyte as a Cationic Exchange Membrane - Here, the exploration continues with CMC's application as a polyelectrolyte membrane, in concert with polyvinyl alcohol (PVA), to mitigate iodine-species crossover in $Zn-I_2$ batteries and address the cost concerns of membrane production.

The chapter showcases CMC's efficacy in enhancing cationic exchange capabilities and PVA's contribution to ionic conductivity. It presents the empirical results and experimental conditions within an H-cell setup, acknowledging the system's limitations. The findings of this chapter have been published in Heliyon (2020) Volume 6, Number e05391.

Chapter 5: pH-Buffered Electrolyte for Zinc-iodine Flow Batteries - This chapter is devoted to the employment of CMC as an ASEI on a 3D carbon felt (CF) electrode within a Zn-I_2 flow battery. It begins by detailing the formulation of ZnI_2 electrolytes with NH_4OAc as a pH-buffering agent, a critical advancement for pH stabilization and the minimization of side reactions and passivation. The chapter further illustrates the enhanced Zn ion distribution achieved with CMC-modified CF electrodes. Experimental procedures and performance evaluations of the CMC-CF anode in a Zn-I_2 flow battery are discussed, noting that this chapter is pending publication.

Chapter 6: Conclusion - The final chapter synthesizes the key discoveries from the research, encapsulating the significant strides made and proposing avenues for further investigation to advance the field.

Chapter 2
THEORY AND LITERATURE REVIEW

This chapter is meticulously crafted to serve as an exhaustive repository of foundational information pivotal to the study of zinc anodes within mildly acidic, aqueous ZBBs. It encompasses a thorough overview, delves into the essential principles, elucidates the underlying reaction mechanisms, addresses the prevailing challenges, and critically assesses the selection of materials. Furthermore, it offers a detailed examination of the analytical techniques employed in this field of research, establishing a well-rounded discourse essential for both novices and experts alike.

2.1 Aqueous Zn-based batteries: overview

An electrochemical, or Galvanic, cell is ingeniously designed to convert chemical energy directly into electrical energy through spontaneous redox reactions. This cell is constituted by two electrodes, the anode and cathode, each immersed in an electrolyte that facilitates ionic exchange. At the anode, oxidation reactions release electrons, whereas the cathode becomes the site for reduction reactions. The electrolyte plays a critical role, acting as a medium for ion transport and completing the internal circuit of the cell. As the liberated electrons journey from the anode to the cathode through an external pathway, they harness the potential to generate electrical power.

In the quest for safer energy storage alternatives, aqueous rechargeable batteries emerge as a promising avenue, circumventing the safety pitfalls associated with their organic electrolyte-based counterparts. These aqueous variants bring to the table several compelling advantages: they are inherently safer, more cost-efficient, exhibit superior ionic conductivity, and are simpler to manufacture. Such characteristics make them highly attractive for large-scale energy storage systems (33). Within this class, zinc (Zn) emerges as an exceptional anode material due to its relatively low reduction potential (-0.76 V vs. Standard Hydrogen Electrode, SHE) coupled with a significant overpotential for the hydrogen evolution reaction, which mitigates gas generation and enhances safety. Zinc's theoretical capacity (820 mAh/g) is notably superior to that of the traditional intercalation anode materials found in

aqueous systems, positioning it as a frontrunner for use in Aqueous Zinc-based Batteries. For visual clarity on the operational principles of Aqueous Zinc-based Batteries, readers are referred to the schematic delineation provided in Figure 2.1.
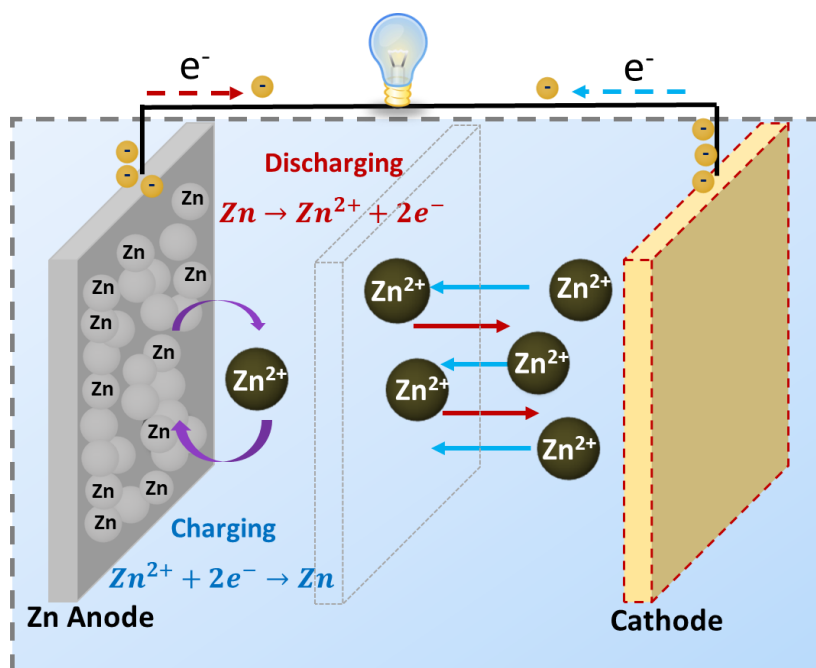
Figure 2. 1 Schematic illustration of the principle of aqueous Zn-ion battery

2.2 Zn anode issues

The utilization of zinc anodes has been diversifying across a spectrum of battery chemistries, encompassing Zn-air (34), Zn-Manganese (Mn) (35), and Zn-Vanadium (V) (36) configurations. Aqueous Zn-ion batteries (AZIBs) are commonly operated within either mildly acidic or alkaline electrolytes. In the mildly acidic context, the electrochemistry is rather straightforward—during the charge cycle, Zn deposits onto the electrode, whereas it is removed, or stripped, during discharge, proceeding without the formation of ZnO or any other insoluble by-products.

The situation is notably different within alkaline media, where the oxidation of Zn leads to the formation of soluble zincate ions that can subsequently precipitate to form ZnO, a process that is reversed upon charging. Alkaline electrolytes typically include hydroxides such as LiOH, NaOH, or KOH. The pertinent electrochemical reactions at the Zn anode in alkaline solutions are as follows:

Discharge process

$$Zn \ + \ 4OH^- \rightarrow Zn(OH)_4^{2-} + 2e^- \tag{2.1}$$

$$Zn(OH)_4^{2-} \rightarrow ZnO \ + \ 2OH^- + H_2O \tag{2.2}$$

Charge process

$$ZnO + 2OH^- + H_2O \ \rightarrow Zn(OH)_4^{2-} \tag{2.3}$$

$$Zn(OH)_4^{2-} + 2e^- \rightarrow Zn + 2OH^- \tag{2.4}$$

Alkaline systems often grapple with the dissolution-precipitation mechanism's predisposition to zinc dendrite formation and the production of insulating ZnO layers. These outcomes lead to challenges including dendritic growth, anode passivation by ZnO, hydrogen evolution, and diminished Coulombic efficiency, which in turn precipitate capacity fade and restrain the technology's practical application prospects.

In stark contrast, mild aqueous systems, with a Zn anode in proximity to a nearly neutral electrolyte, operate using Zn^{2+} ions as the primary charge carriers. Such electrolytes are typically composed of soluble Zn salts such as $ZnCl_2$, $Zn(NO_3)_2$, $Zn(CH_3COO)_2$, and $ZnSO_4$. Notably, electrolytes having $ZnSO_4$ demonstrate a broad electrochemical window and excellent reversibility for the Zn anode. Unlike their alkaline counterparts, these systems facilitate the reversible stripping and plating of Zn ions on the Zn anode during operation. The electrochemical reactions involving the Zn electrode in mild aqueous systems can be summarized as follows:

Discharge process

$$Zn \rightarrow Zn^{2+} + 2e^- \tag{2.5}$$

Charge process

$$Zn^{2+} + 2e^- \rightarrow Zn \tag{2.6}$$

Mild electrolytes potentially alleviate the complications associated with Zn passivation and morphological alterations, attributed to the distinct electrochemical

interactions at the Zn anode. Although anode reversibility may be enhanced, the Coulombic efficiency for the redox processes is not ideal, given the persistent formation of Zn dendrites and various side reactions.

The hydrogen evolution reaction (HER) is somewhat subdued in mild environments due to the low redox potential of the Zn/Zn^{2+} couple (-0.76 V vs SHE) and the elevated HER overpotential at the Zn anode surface. Nevertheless, HER may still occur during both the rest period and active cell operation. Furthermore, Zn anode corrosion in aqueous conditions can result in continuous water consumption, irreversible hydrogen gas production, and the formation of insoluble by-products, all of which curtail reversible capacity and cycle life.

Commercial zinc foils or sheets, often adopted as the Zn anode, provide a flat surface but are not devoid of limitations. Post-operation, Zn ion distribution may become irregular, and the slow ion diffusion rate can further intensify dendrite development.

Ultimately, the reusability of Zn-based aqueous batteries is significantly limited by the Zn anode, primarily due to its inadequate reversibility. This stems from the thermodynamic instability of Zn within the aqueous electrolyte, engendering several pressing challenges for Zn anodes, including dendrite formation, self-discharge or corrosion, hydrogen evolution, and surface passivation.

2.2.1 Zn dendrite formation

The development of high-performance zinc anodes in mildly acidic electrolytes is significantly impeded by the formation of zinc dendrites, a phenomenon at the forefront of contemporary research aimed at its mitigation. The anodic surface often exhibits an irregular morphology, which induces a non-uniform zinc ion distribution. As zinc ions undergo reduction to their elemental state near the anode surface, this leads to localized concentration polarization within the electrolyte. Moreover, the uneven surface features, or protrusions, produce amplified electric fields at their tips, which act as preferential sites for zinc ion attraction and subsequent dendritic nucleation and growth.

The multifaceted nature of dendrite formation is influenced by several variables: the overpotential, the concentration of ions, ambient temperature, the

surface roughness of the anode, and the electrolyte's pH. Pavlovic et al. provided an analytical expression to determine the minimum overpotential required for dendrite formation, asserting that a higher bulk concentration of zinc ions in the electrolyte exacerbates the dendritic issue. Addressing dendrite formation is thus crucial for enhancing the Coulombic efficiency (CE) of the zinc anode.

Elevated temperatures also play a role, facilitating faster diffusion of ions within the electrolyte and potentially altering the morphology of zinc deposition. On a rough anode surface, ions are more likely to aggregate at the protrusions during plating, leading to non-uniform zinc deposition. In contrast, a smoother anode surface promotes uniform zinc deposition, which is often characterized by a regular hexagonal pattern. Furthermore, dendrite growth is found to be more pronounced at higher pH levels, where the crystals tend to grow with a defined inclination, compounding the challenges associated with the zinc anode structure and performance.

2.2.2 Hydrogen evolution reaction

The investigation of HER in zinc-based electrochemical systems remains relatively embryonic, especially when juxtaposed with the abundant literature concerning zinc dendrite formation. A handful of exploratory studies into HER have begun to unravel the complexities of its interactions with zinc anodes in mildly acidic electrolytes. HER presents a threefold dilemma: it precipitates the depletion of both the zinc anode and electrolyte, and it instigates the evolution of hydrogen gas. These phenomena in tandem exert detrimental effects on battery longevity, leading to diminished CE and causing internal pressure build-up that could compromise the integrity of the cell.

According to the Pourbaix diagram for the stability of water, the potential at which hydrogen evolution becomes thermodynamically feasible in a neutral medium stands at approximately -0.41 V versus the Standard Hydrogen Electrode (SHE). This potential is substantially more positive than the Zn/Zn^{2+} couple potential of -0.76 V versus SHE, denoting a thermodynamic proclivity towards hydrogen gas evolution in mild electrolytes. The HER progresses via the following electrochemical steps:

$$H^+ + e^- \rightarrow H_{ads} \tag{2.7}$$

$$2H_{ads} \rightarrow H_2 \qquad\qquad (2.8)$$
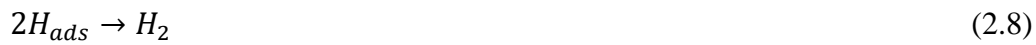
The occurrence of HER in ZIBs is an intricate event shaped by numerous interdependent variables. Critical factors such as the surface texture of the zinc anode, which often exhibits considerable irregularities, the molarity and specific makeup of the electrolyte solution, and the temperature at which the battery operates, each play pivotal roles in influencing the kinetics and extent of HER. These variables do not operate in isolation but rather interact synergistically, affecting the overall propensity for hydrogen gas generation and, by extension, the efficiency and safety of the ZIB system.

2.2.3 Zn corrosion

Corrosion of the zinc anode in ZIBs is a detrimental process that leads to the gradual degradation of the electrode's integrity and the depletion of active material. This corrosion is an inherent electrochemical response that occurs when the metallic zinc is exposed to a mild aqueous electrolyte, persisting even during the quiescent states when the battery is not in use. The result of such continuous corrosion is an increase in the interphase resistance, which subsequently impairs the battery's cycle life (15). Hydrogen evolution, a reaction that occurs simultaneously with the electrochemical degradation of the zinc anode, further compounds the issue. The underlying mechanisms of zinc corrosion in ZIBs, akin to those of HER, are relatively under-explored in the literature. The corrosion reaction, integral to understanding and mitigating this process, is typically illustrated in electrochemical terms as follows:

Cathode process
$$2H_2O + 2e^- \leftrightarrow H_2 + 2OH^- \qquad\qquad (2.9)$$

Anode process
$$Zn \leftrightarrow Zn^{2+} + 2e^- \qquad\qquad (2.10)$$

The degradation of zinc metal within ZIBs is predominantly precipitated by electrochemical reactions associated with HER. This phenomenon causes localized shifts in pH levels as a result of the augmented presence of hydroxide ions (OH⁻), creating a more alkaline environment at the anode. Such conditions foster the corrosion process, posing a formidable challenge to the operational stability and longevity of ZIBs. Crucially, the corrosion of the zinc anode commences during the periods of shelf-life and transportation, phases that precede the battery's active service, thereby impacting the battery's performance potential from the outset, as highlighted in the citation (37). This early-onset reaction between the anode and electrolyte necessitates strategies for corrosion mitigation to ensure the practical applicability and durability of ZIB technology.

2.2.4 Passivation of the Zn anode

In the context of mildly acidic systems, the occurrence of insoluble by-products, notably zinc hydroxide ($Zn(OH)_2$) and zinc oxide (ZnO), has been observed to manifest on the surface of the zinc electrode. This typically transpires as the concentration of hydroxide ions increases within the system, a phenomenon well-documented in the literature (13, 14). In more recent discourse, it has been posited that certain zinc salts can precipitate on the zinc metal interface. Notably, a hexagonal crystalline structure, $Zn_4SO_4(OH)_6 \cdot H_2O$, has been identified as one of the by-product layers forming upon the zinc electrode (38, 39). The chemical reaction culminating in the formation of this by-product layer is delineated in equation 11:

$$4Zn^{2+} + 6OH^- + SO_4^{2-} + xH_2O \leftrightarrow Zn_4SO_4(OH)_6 \cdot xH_2O \qquad (2.11)$$
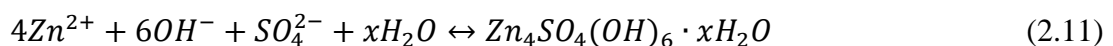
This nascent interphase layer is characterized by its porosity and the consequent inability to effectively shield the underlying zinc metal from ongoing electrochemical interactions with the electrolyte. As such, the formation of this layer, primarily arising from zinc corrosion, does not provide a robust barrier. It fails to arrest further corrosive activity, leaving the freshly deposited zinc layers vulnerable and unable to segregate the electrolyte fully, thereby allowing corrosion processes to continue unabated.

2.3 Approaches to address Zn anode issues

From the foregoing discussion, it becomes evident that various problem-solving approaches for Zn-ion batteries have emerged. Current developments are primarily centered on the design and engineering of the electrode, the electrode-electrolyte interface, and electrolyte modification. This work specifically concentrates on electrode augmentation and the application of ASEI layers in mildly acidic aqueous electrolytes. The literature review herein places particular emphasis on recent advancements.

2.3.1 Zn electrode additive

Functional additives in the electrode manufacturing process have been proposed as a means to enhance battery performance (16). Powdered Zn is often employed in Zn-ion batteries due to its large surface area and porous structure, which facilitate electrolyte infiltration. However, this increased surface area can also contribute to Zn passivation and exacerbate undesirable side reactions, such as HER. To mitigate these challenges, various additives are integrated into the porous Zn electrode structure. These additives serve multiple purposes: they improve the electrode network at low concentrations, enhance inter-particle contacts, incorporate inert materials, and optimize electrolyte accessibility.

Previous studies have explored the use of oxide additives to suppress Zn passivation and HER. For instance, Shivkumar et al. (40). demonstrated that the inclusion of HgO and Pb_3O_4 in the Zn anode effectively reduced corrosion, extended lifespan, and minimized shape changes. Bindiya et al. posited that a $Zn-V_2O_5$ composite could enhance corrosion resistance. Other oxide materials, such as SiO_2 (41), Al_2O_3 (42), ZrO_2 (43), and TiO_2 (44), have also been investigated. However, from both environmental and commercial standpoints, these additives may not be ideal.

Carbon-based materials, widely used in lithium-ion batteries, fuel cells, and chemical sensors, offer an alternative due to their affordability, safety, high conductivity, and chemical stability. In commercial Zn anodes, a slurry mixture comprising Zn powder, conductive carbon, and a binder is often coated onto the

current collector. This approach has proven effective in suppressing dendritic growth. For example, Masri et al. enhanced the performance of Zn-air batteries by incorporating carbon black into the Zn anode (45). Kang et al. fabricated a composite anode by blending Zn particles with activated carbon (AC), finding that this led to preferential Zn ion deposition within the AC pores, thereby improving electrochemical kinetics and reversibility (18). Tao et al. also reported enhanced discharge capacity and cycling performance in Zn anodes prepared with various carbon additives, such as AC, acetylene black, and carbon nanotubes, in mildly aqueous electrolytes (17). Consequently, carbon materials, with their high specific surface areas providing ample reaction channels, emerge as a promising choice for Zn anode modification.

2.3.2 Artificial SEI Coating

To meet the escalating demands for Zn-ion batteries, it is imperative to augment both the electrochemical and thermodynamic compatibility between the Zn anode and the aqueous electrolyte. This necessitates sophisticated interfacial engineering, specifically the formulation of functional interfacial layers designed to bolster compatibility and shield the Zn anode from deleterious side reactions. A myriad of materials, ranging from metal oxides and metals to organic polymers and other specialized substances, have been scrutinized for their potential as coatings. These coatings can be applied either ex-situ or in-situ to create artificial interphases, akin to SEI, on the Zn electrode surface.

As a result, the notion of artificial coatings has crystallized into a compelling and pragmatic strategy for the interfacial engineering of Zn anodes. Subsequent research endeavors are geared towards devising techniques that regulate compatibility while mitigating side reactions. These methodologies encompass a diverse array of protective materials, each giving rise to unique artificial SEI coating strategies on the Zn anode. These strategies include but are not limited to, carbon-based coatings, metal oxides serving as passivation layers, organic polymer coatings, and other innovative coating materials.
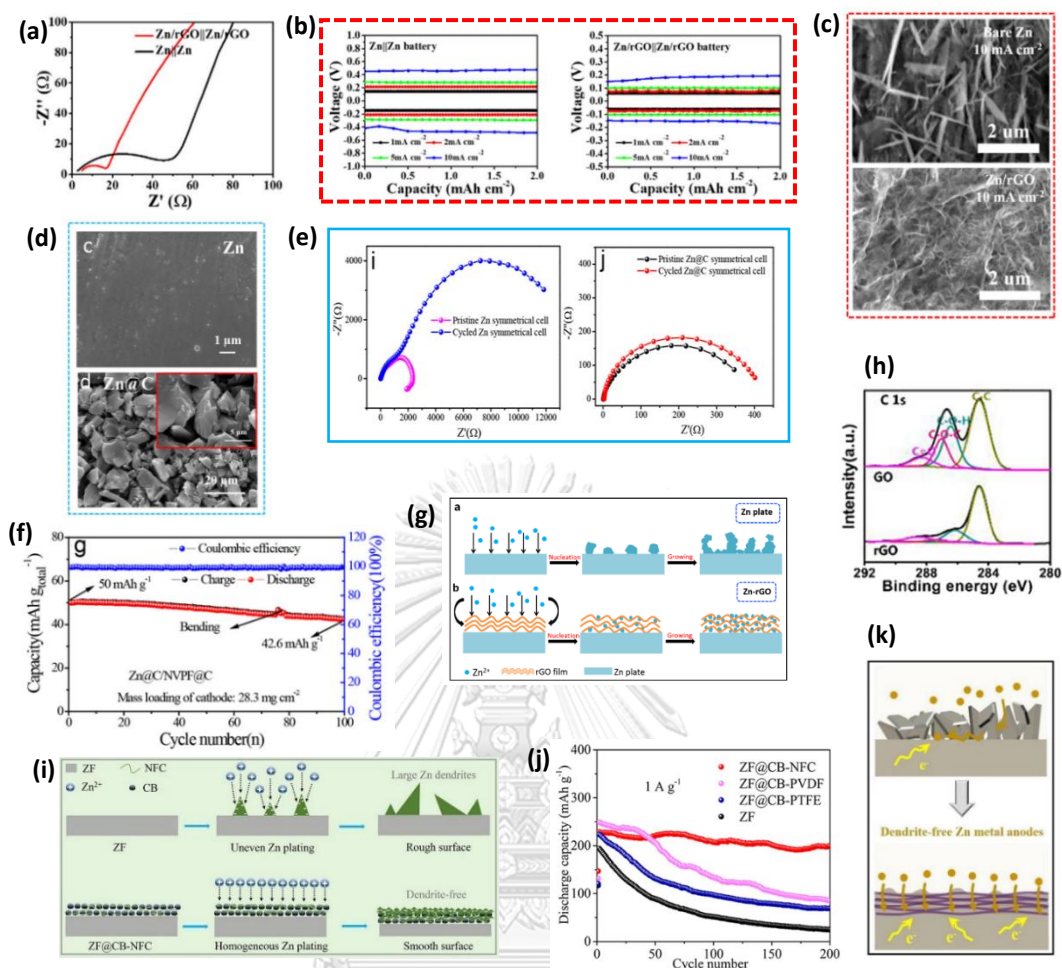
Figure 2. 2 Artificial SEI coating strategies on the Zn anode include carbon-base coating,

(Nyquist plot pf the impedance spectra of the Zn/rGO and bare Zn symmetric cells after cycles at 1mA cm^{-2} (a). Voltage profile of bare Zn and Zn/rGO symmetric cells at different current densities (b). SEM images of bare Zn and Zn/rGO anode after cycles at current density of 10 mA cm^{-2} (c). (Reprinted with permission from ref. 49. Copyright 2018, Chemical Engineering Journal). SEM images of bare Zn and Zn@C (d). Nyquid plots of bare Zn and Zn@c symmetric cells before and after 100 cycles (e). Cycling performance of Zn@C in full cell (pouch battery) at 0.117 A g^{-1}. (Reprinted with permission from ref. 50. Copyright 2018, Chemical Engineering Journal). Schematic illustrating the Zn plating behavior for the bare Zn and Zn/rGO electrode (g). XPS spectra of C 1s of the pristine GO and rGO coated on the Zn surface (h). (Reprinted with permission from ref. 51. Copyright 2019, Applications of Surface Science). Schematic illustration of the surface morphology evolution of Zn foil and Zn foil with CB-NFC coating anode during the Zn plating process (i). cycling performance of full cell without and with carbon black coating anode using different binder at 1 Ag^{-1} (j). (Reprinted with permission from ref. 52. Copyright 2020, Journal of Colloid and Interface Science). Schematic illustration of interface kinetics for Zn deposition of without and with CNF interlayer modification(k).). (Reprinted with permission from ref. 53. Copyright 2021, Chemical Engineering Journal).)
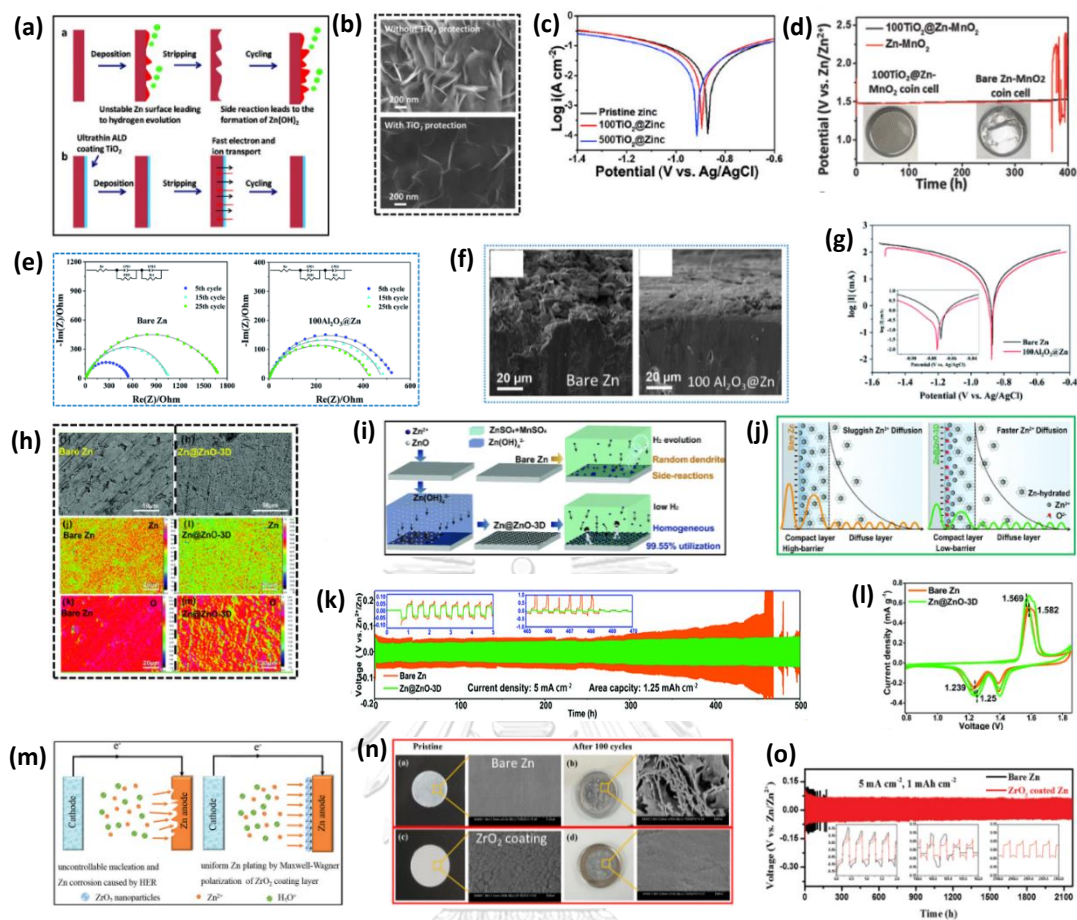
Figure 2. 3 Artificial SEI coating strategies on the Zn anode include metal oxide as passivation payers I

(Schematic illustration of bare Zn anode and TiO$_2$ coating Zn anode (a). SEM images of 100TiO$_2$@Zn and bare Zn anode after cycling at1mA cm^{-2} for over 140 h in symmetric cells (b). Corrosion curves of bare Zn and TiO$_2$@Zn (100 cycles ALD and 500 cycles ALD) in 3M Zn(SO$_3$CF$_3$)$_2$ (c). Self-discharge test TiO$_2$@Zn-MnO$_2$ cell for more 400 h (d). (Reprinted with permission from ref. 29. Copyright 2018, Advance Materials Interfaces). The EIS of symmetric cell with bare Zn and 100Al2O3@Zn anode at 5th, 15th, and 25th cycle charging (e). Cross-section SEM morphology of cycled bare Zn and 100Al$_2$O$_3$@Zn for over 200 h at 1mA cm^{-2} with capacity of 1mA h cm^{-2} in symmetric cells (f). Linear polarization curve of bare Zn and 100Al$_2$O$_3$ (g). (Reprinted with permission from ref. 30. Copyright 2020, Journal of Material Chemistry A). Morphology and corresponding EPMA mapping of bare Zn and Zn@ZnO-3D (h). Schematic images depicting the preparation Zn@ZnO-3D anode and deposition process in an aqueous electrolyte compared with bare Zn (i). Electric double layer structure (EDLs) in the vicinity of Zn@ZnO-3D (green line) and the corresponding energy barrier compared with bare Zn (orange line) (j). Long-term galvanostatic cycling performance of symmetrical Zn@ZnO-3D and bare Zn cells at 0.5 mA cm^{-2}(k). cycling voltammetry testing of Zn@ZnO-3D/MnO$_2$ cells (l). (Reprinted with permission from ref. 25. Copyright 2020, Energy & Environmental Science). Schematic the plating/stripping process of bare Zn and ZrO$_2$-coated Zn anode (m). Digital images and corresponding SEM images of bare Zn and ZrO$_2$ coating Zn anode before and after 100 cycles at 5 mA cm^{-2} with a capacity of 2.5 mA h cm^{-2} (n). Voltage profiles the bare Zn and ZrO$_2$-coated Zn

plating/stripping in symmetric cells at 5 mA cm^{-2} for 1mA h cm^{-2} (o). (Reprinted with permission from ref. 54. Copyright 2020, Advanced Functional Materials).)

2.3.2.1 Carbon-based material

The incorporation of reduced graphene oxide (rGO) onto zinc foil (Zn/rGO) has been shown to effectively mitigate the formation of zinc dendrites and diminish the overpotential during the stripping and plating processes. Shen et al. (46) demonstrated that Zn electrodes coated with rGO exhibited lower impedance compared to their uncoated counterparts, as evidenced by Figure 2.2a. This reduction in impedance subsequently led to a decrease in interface resistance within symmetric cells.

As illustrated in Figure 2.2b, the rGO coating on the Zn anode significantly curtails overpotential, even under conditions of elevated current densities. This beneficial effect can be attributed to rGO's expansive specific surface area, which not only promotes uniform zinc deposition but also likely inhibits dendritic growth and the emergence of poorly conductive zinc structures, as shown in Figure 2.2c. Consequently, both symmetric and vanadium full cells manifest admirable cycling reversibility.

Moreover, the application of porous carbon as a coating on the Zn anode (Zn@C), depicted in Figure 2.2d, also enhances zinc reversibility and optimizes reaction kinetics, effectively eliminating dendrite formation. The carbon layer serves to distribute current uniformly and facilitates the zinc plating process. Even after 100 cycles in a symmetric cell, the Zn@C anode exhibits only a marginal increase in charge transfer resistance, as indicated in Figure 2.2e. When employed in a pouch battery configuration, as shown in Figure 2.2f, this carbon-based coating strategy yields high capacity retention and a stable charge/discharge profile (47).

Xia et al. advanced the field by introducing a meticulously engineered layer-by-layer reduced graphene oxide (rGO) coating onto zinc foil. This rGO layer serves as a formidable barrier against the formation of zinc dendrites, as illustrated in Figure 2.2g, which schematically depicts Zn plating on a Zn/rGO anode. The successful deposition of the rGO layer on the zinc surface was corroborated through X-ray photoelectron spectroscopy (XPS), as shown in Figure 2.1h. This rGO layer conferred

multiple benefits, including augmented cycling stability in symmetric cells and superior electrochemical performance in full cells, relative to uncoated Zn anodes (48).

In a parallel development, Wang et al. innovatively modified the Zn anode by applying a carbon black (CB) coating, denoted as Zn@CB, in conjunction with a nano-fibrillated cellulose (NFC) binder. As depicted in Figure 2.2i, the spherical morphology of the carbon black particles furnishes an ample electroactive surface area, effectively thwarting both Zn dendrite proliferation and undesirable side reactions. Intriguingly, the NFC binder possesses the capability to retain the electrolyte, thereby expediting the transport of Zn ions. This unique property allows carbon black to act as a formidable deterrent against Zn dendrite formation. In a Zn-MnO_2 full cell, the Zn@CB-NFC anode outperformed its unmodified counterpart, especially at a current density of 1 A g^{-1}, as evidenced by Figure 2.2j (49).

Beyond carbon-based materials, the incorporation of carbon nanofiber (CNF) interlayers onto the Zn metal electrode has been shown to be highly effective in capturing Zn^{2+} ions and promoting uniform Zn electrodeposition. As illustrated in Figure 2.2k, this modification not only amplifies Zn reversibility but also diminishes nucleation overpotential. The result is a remarkably stable cycling lifespan, extending up to 1200 hours at a current density of 5 mA cm^{-2} (equivalent to 1 mAh cm^{-2}) in both symmetric cells and Zn-MnO_2 batteries (50).
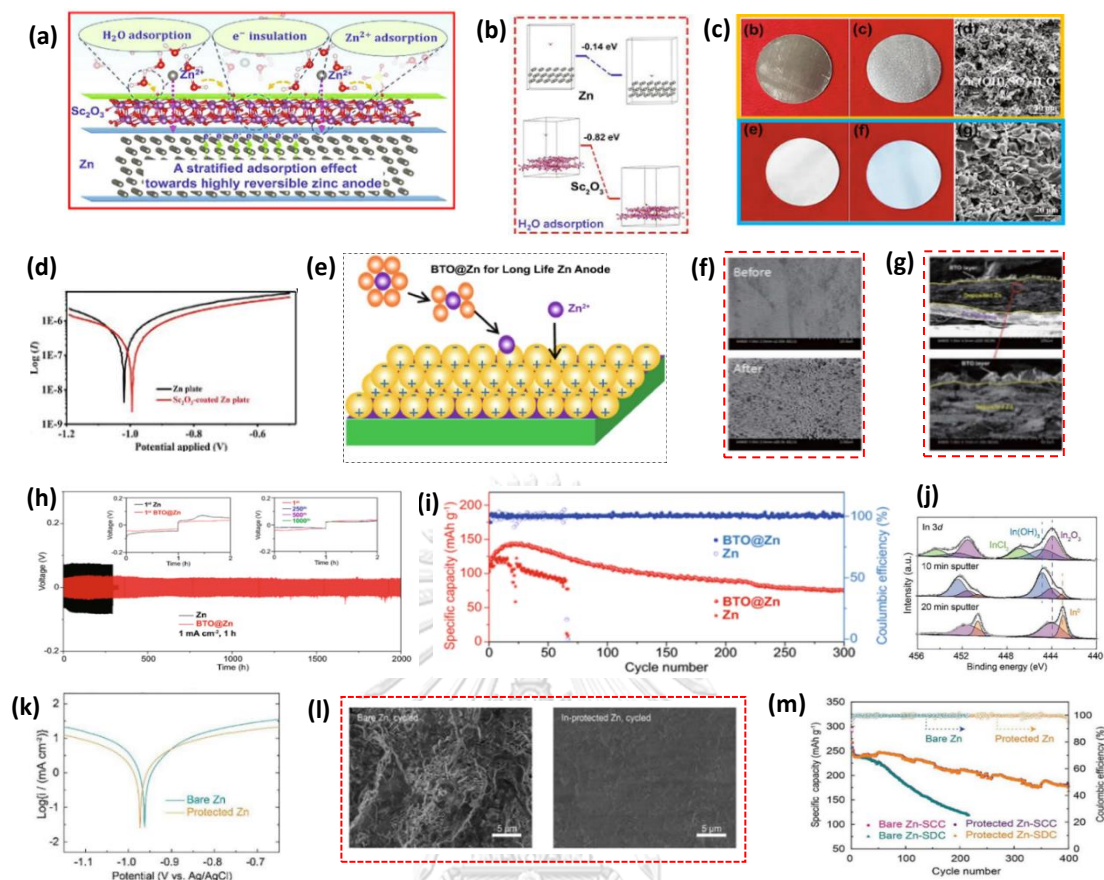
Figure 2. 4 Artificial SEI coating strategies on the Zn anode include metal oxide as passivation payers II

(Schematic diagram of reaction process the surface of Sc$_2$O$_3$-coated Zn anode (a). The calculation of H$_2$O adsorption energy on the surface of the bare Zn and Sc$_2$O$_3$ coating Zn anode (b). Digital images of the bare and Sc$_2$O$_3$-coated Zn plates before and after soaking in electrolyte for 15 days, and the corresponding SEM images (c). Linear polarization curves of the bare and Sc$_2$O$_3$-coated Zn anode (d). (Reprinted with permission from ref. 28. Copyright 2021, Journal of Energy Chemistry). Schematic diagrams od Zn ions transport at between Zn anode and electrolyte during Zn plating process (e). SEM images of the Zn anode morphology: BTO@Zn before and after 100 cycles at 1 mA cm^{-2} and 1 mAh cm^{-2} of the symmetric cells (f). Highlight typical cross section SEM images in BTO layer, deposited Zn and Zn foils are separated by yellow lines (g). Cycling performance of the symmetric cell with Zn and BTO@Zn at 1 mA cm^{-2} with capacity of 1 mA h cm^{-2} (h). Cycling performance of the Zn- MnO$_2$ full cell with Zn and BTO@Zn at 2 A g^{-1} (i) . (Reprinted with permission from ref. 31. Copyright 2021, Nano-Micro Letters.). In 3d XPS spectrums of In-coated Zn (j). Corrosion curves of bare Zn and In-coated Zn anode (k). Morphology of bare Zn and In-coated Zn anode in symmetric cell after cycling for 100 cycles at 0.25 mA cm^{-2} for 0.05 mA h cm^{-2} (l). Cycling performance of Zn-MnO$_2$/CNT cells at 1.5 A g^{-1} (m). (Reprinted with permission from ref. 26. Copyright 2020, Chemical Engineering Journal).)

2.3.2.2 Metal and metal oxide

Inert metals and metal oxides have emerged as promising candidates for surface modification coatings. Mai et al. (28) employed atomic layer deposition (ALD) to deposit an ultrathin TiO_2 layer onto the Zn anode, serving as a robust passivation layer that precludes direct contact between the Zn anode and the electrolyte (Figure 2.3a). This strategic intervention effectively curtailed the proliferation of Zn dendrites (Figure 2.3b) and mitigated Zn corrosion. As evidenced by Figure 2.3c, the corrosion currents for both bare Zn and TiO_2-coated Zn were comparable, but the overpotential for the latter was markedly reduced. This led to enhanced electrochemical performance, including reduced overpotential in symmetrical batteries and improved self-discharge rates during idle periods (Figure 2.3d). The TiO_2-coated Zn anode achieved a Coulombic efficiency (CE) of 85% at 3 mA cm^{-2} and an extended cycle life of up to 1000 cycles in Zn-MnO_2 full cells.

He et al.(29) showcased a Zn anode coated with a 100-cycle ALD Al_2O_3 layer, denoted as $100Al_2O_3$@Zn, which attenuated the reactivity between the Zn anode and the electrolyte. This led to reduced impedance and enhanced Zn plating/stripping kinetics (Figure 2.3e). Figure 2.3f reveals that this Al_2O_3 layer effectively suppressed Zn dendrite growth and Zn plating beneath the layer. The ALD Al_2O_3 layer acted as a corrosion inhibitor, similar to its TiO_2 counterpart, as indicated by the linear polarization curves (Figure 2.2g). Consequently, the $100Al_2O_3$@Zn configuration achieved a CE of 89.4% at a current density of 1 mA cm^{-2} in Zn-MnO_2 full cells.

Xie et al. (25) introduced a Zn anode modified with a three-dimensional nanoporous ZnO architecture, termed Zn@ZnO-3D (Figure 2.3h). This ion-conductive ZnO-3D interphase was synthesized through in-situ solution-phase deposition of $Zn(OH)_4^{2-}$ on a Zn plate, subsequently converted into ZnO (Figure 2.3i). This Zn@ZnO-3D configuration facilitated Zn^{2+} ion desolvation and improved deposition kinetics. The ZnO-3D layer effectively suppressed the side reaction of H_2 generation, thanks to the solvated sheath structure of Zn^{2+} regulation in the electric double layer (Figure 2.3j). In full cells, the CV curves exhibited a higher current density compared to bare Zn (Figure 2.3l), indicating the enhanced capacity and

electrochemical reactivity of the ZnO-3D layer. As a result, the ZnO-3D-modified Zn anode achieved a reversibility CE of 99.55% compared to pristine Zn plates.

Exploring other metal oxides, Liang et al.*(51)* scrutinized the ZrO_2-coated Zn anode, which exhibited Maxwell-Wagner polarization, also known as space charge polarization (Figure 2.3m). ZrO_2 is distinguished by its remarkable chemical stability and resistance to corrosion, making it an ideal candidate for facilitating uniform Zn stripping and plating on the Zn anode. This led to accelerated Zn ion transport kinetics and the effective suppression of undesirable side reactions. When it comes to plating and stripping behavior, the ZrO_2 coating layer yielded smooth Zn plating even after 100 cycles at elevated current densities (Figure 2.3n). This can be attributed to the Maxwell-Wagner polarization mechanism, which orchestrates controllable nucleation sites, thereby ensuring uniform Zn ion diffusion across the interphase. Moreover, the compact ZrO_2 layer on the Zn surface minimized the interphase contact area, effectively quelling HER. As a result, the symmetric cells demonstrated remarkable longevity, enduring over 3800 hours at a low current density of 0.25 mA cm^{-2} and 0.125 mAh cm^{-2}, and 2100 hours under more demanding conditions of 5 mA cm^{-2} and 1 mAh cm^{-2} (Figure 2.3o).

Expanding the scope to other elements, Zhou et al.*(27)* showcased the efficacy of a Sc_2O_3 coating on the Zn electrode in mitigating interfacial side reactions, a feat attributed to the adsorptive properties of the Sc_2O_3 layer on the Zn surface (Figure 2.4a). This Sc_2O_3 coating serves a dual purpose: it minimizes the Zn anode's contact with the electrolyte and forms hydrogen bonds with water molecules. Density Functional Theory (DFT) energy calculations substantiated the adsorption of water molecules from $[Zn(OH_2)_6]^{2+}$ onto this layer (Figure 2.4b), revealing its proclivity for capturing and immobilizing water molecules.

Addressing the layer's low electronic conductivity emerged as a pivotal step in curtailing the hydrogen evolution reaction (HER) and suppressing the formation of by-products such as $Zn_4(OH)_6SO_4 \cdot H_2O$ (Figure 2.4c). Comparative HER measurements for both the uncoated and Sc_2O_3-coated Zn anodes in mildly acidic aqueous electrolytes were conducted (Figure 2.4d). The results indicated a higher corrosion potential and a diminished corrosion current density, thereby affirming the Sc_2O_3 layer's role in stymieing corrosion and averting self-discharge *(52)*.

The unique dielectric constant interplay between Zn and Sc_2O_3, known as Maxwell-Wagner polarization *(51)*, facilitated a reduced barrier for Zn deposition, thereby accelerating Zn ion adsorption kinetics. This led to the hydrophilic Sc_2O_3 protective film on the Zn anode achieving an extraordinary Coulombic efficiency (CE) of 99.85% at a current density of 1.13 mA cm^{-2}. In both symmetric and full-cell configurations, this artificial layer conferred upon the Zn anode lower polarization and enhanced lifespan relative to its uncoated counterpart.

Additionally, in pursuit of precise control over Zn deposition, SEI featuring perovskite-type material, specifically $BaTiO_3$ *(30)*, has been ingeniously engineered. This $BaTiO_3$ layer, often abbreviated as BTO, exhibits a unique sensitivity to external electric fields, thereby facilitating the controlled migration of Zn ions during electrochemical processes (Figure 2.4e). Remarkably, the BTO coating on the Zn anode demonstrates robust integrity, maintaining its structural coherence even after multiple electrochemical cycles (Figures 2.4f and 2.4g).

These technological strides have culminated in a significantly extended lifespan for reversible electrochemical processes, reaching up to 2000 hours at a current density of 1 mA cm^{-2} and a capacity of 1 mAh cm^{-2} (Figure 2.4h). In the context of $Zn-MnO_2$ full cells, the incorporation of electric dipoles into the Zn anode has yielded substantial improvements in cycling stability. Specifically, a near-perfect Coulombic efficiency (CE) of approximately 100% was achieved at a current density of 2 A g^{-1}, even after 300 cycles (Figure 2.4i).

Another intriguing approach involves the application of an indium-based protective layer on the Zn anode, specifically designed to mitigate both Zn corrosion and dendrite formation. Hu et al.*(26)* embarked on a comprehensive study of a Zn anode coated with indium, which incorporates $In(OH)_3$ and In_2O_3 as its insulating constituents (Figure 2.4j). This indium-based layer functions as a critical buffer, establishing the requisite potential gradient that facilitates the controlled diffusion of Zn ions through the interphase. This, in turn, orchestrates the Zn deposition occurring beneath the protective layer.

Significantly, this indium-based interfacial layer has been shown to attenuate the current density linked to corrosion, as substantiated by Figure 2.4k. This effectively quells the undesirable corrosion phenomena at the anode. Symmetric cell

evaluations have further corroborated that the indium-coated anode maintains a surface morphology devoid of dendritic structures (Figure 2.4l). As a result, full cells equipped with this indium-coated Zn anode demonstrate enhanced cycling performance. This is characterized by both elevated capacity and diminished polarization, particularly at a current density of 1.5 A g^{-1}, when juxtaposed with cells featuring an uncoated Zn anode (Figure 2.4m).
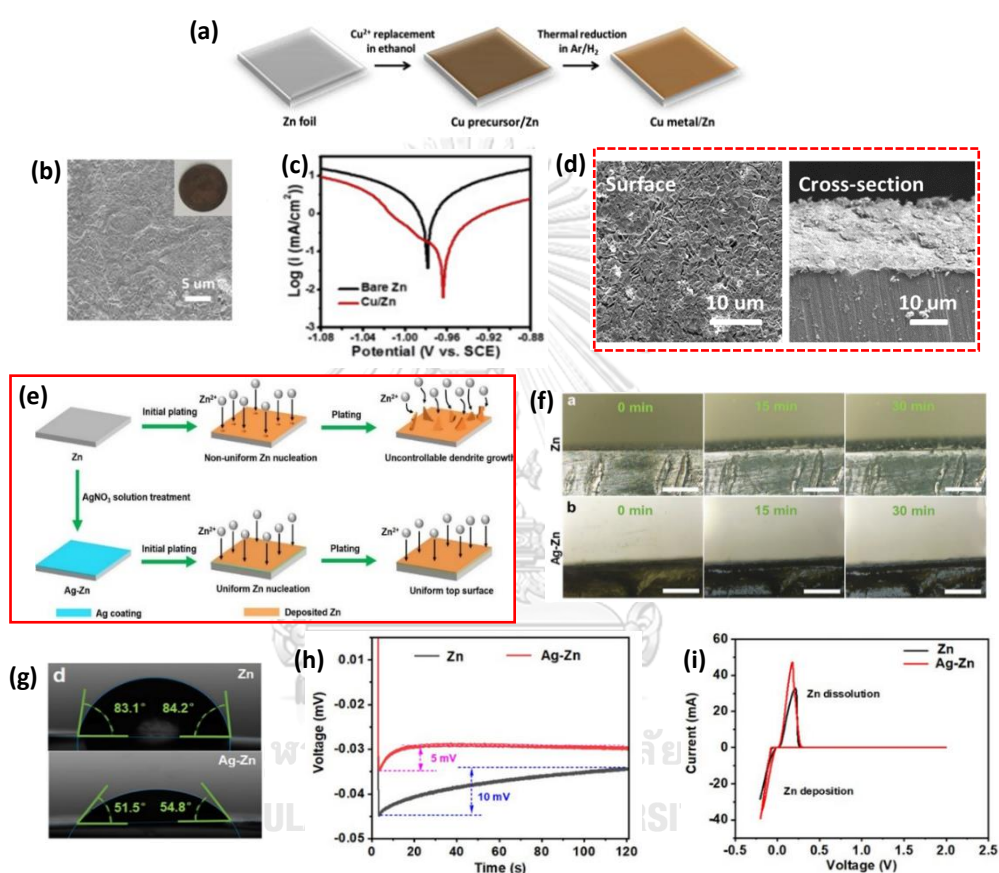
Figure 2. 5 Artificial SEI coating strategies on the Zn anode include metal.
(Schematic illustration of the fabrication process of the Cu/Zn electrode (a). SEM image of the Cu/Zn anode (b). Linea polarization curve of the Cu/Zn and bare Zn electrode (c). The Top-view and cross-section SEM images of Cu/Zn after soaking 3 M ZnSO4 electrolyte for 30 days (d). (Reprinted with permission from ref. 27. Copyright 2020, Energy Storage Materials). Schematic illustration of a Zn plating process on the untreated Zn and Ag-Zn anode (e). In situ digital microscopy images of the cross-section surface of bare Zn and Ag-Zn at different deposition time (f). Contact angles of the electrolyte on bare Zn and Ag-Zn foil (g). In symmetric cells: voltage-time profile during Zn nucleation and deposition on bare Zn and Ag-Zn at 0.2 mA cm^{-2} (h). CV curve of bare Zn amd Ag-Zn anode at scan rate 0.1 mV s^{-1} (i). (Reprinted with permission from ref. 57. Copyright 2021, American Chemical Society).)

In addition to oxide coatings, the exploration of metallic layers on the Zn anode has emerged as a compelling avenue for mitigating interfacial reactivity, curtailing by-product formation, and fostering uniform Zn metal deposition. Capitalizing on the favorable electrode potential of copper (Cu) metal, which stands at +0.34 V vs. SHE, a protective Cu layer was ingeniously introduced. The inherent high electrical conductivity of Cu serves as a conduit for orchestrating the precise deposition of Zn metal onto the Zn foil substrate (53).

Zhao et al. conducted an in-depth study on a Cu/Zn composite surface integrated into the Zn anode. This surface was meticulously engineered through a galvanic reaction, as illustrated in Figure 2.5a and Figure 2.5b. Remarkably, this Cu/Zn surface modification acted as a bulwark against the corrosive tendencies of the Zn anode. It manifested in a more positive corrosion potential and a diminished corrosion current for the Cu/Zn-modified electrode, as evidenced by Figure 2.5c. Linear polarization tests further corroborated the enhanced chemical stability and reduced corrosion rates of this novel electrode. Notably, the electrode maintained its structural integrity, showing negligible morphological alterations even after a 30-day quiescent period in a 3M $ZnSO_4$ electrolyte (Figure 2.5d). Consequently, a symmetric cell equipped with this Cu/Zn-modified electrode demonstrated robust plating/stripping cycling performance, sustaining over 1500 cycles at a current density of 1 mA cm^{-2} and a capacity of 0.5 mA h cm^{-2}.

An innovative Ag metal coating was applied to the Zn anode via an in-situ chemical coating technique, serving as a roadmap for uniform Zn deposition (Figure 2.5e). The Ag coating, acting as a nucleation agent, exerted a profound influence on the interphase, thereby fostering uniform Zn nucleation and deposition. Additionally, the Ag-coated anode surface exhibited enhanced electrolyte wettability, which in turn facilitated the transport of Zn ions and effectively curtailed dendritic growth. This was largely due to the heightened accessibility of electrolyte ions (54). Consequently, this led to the formation of a dense, dendrite-free Zn plating on the Ag-Zn anode, even under the challenging conditions of a high current density of 10 mA cm^{-2} (Figures 2.5f and 2.5g).

To delve deeper into the Zn nucleation process, the Ag-Zn anode displayed a low nucleation overpotential, signifying a reduced energy barrier for Zn nucleation on

the anode surface (Figure 2.5h). Remarkably, the Ag-Zn anode outperformed its bare Zn counterpart in terms of current intensity, thereby catalyzing enhanced kinetic reactions and Zn reversibility (Figure 2.5i). As a corollary, both symmetric cells and Zn-vanadium cells exhibited extended cycle life and augmented performance when equipped with the Ag-Zn anode (55).
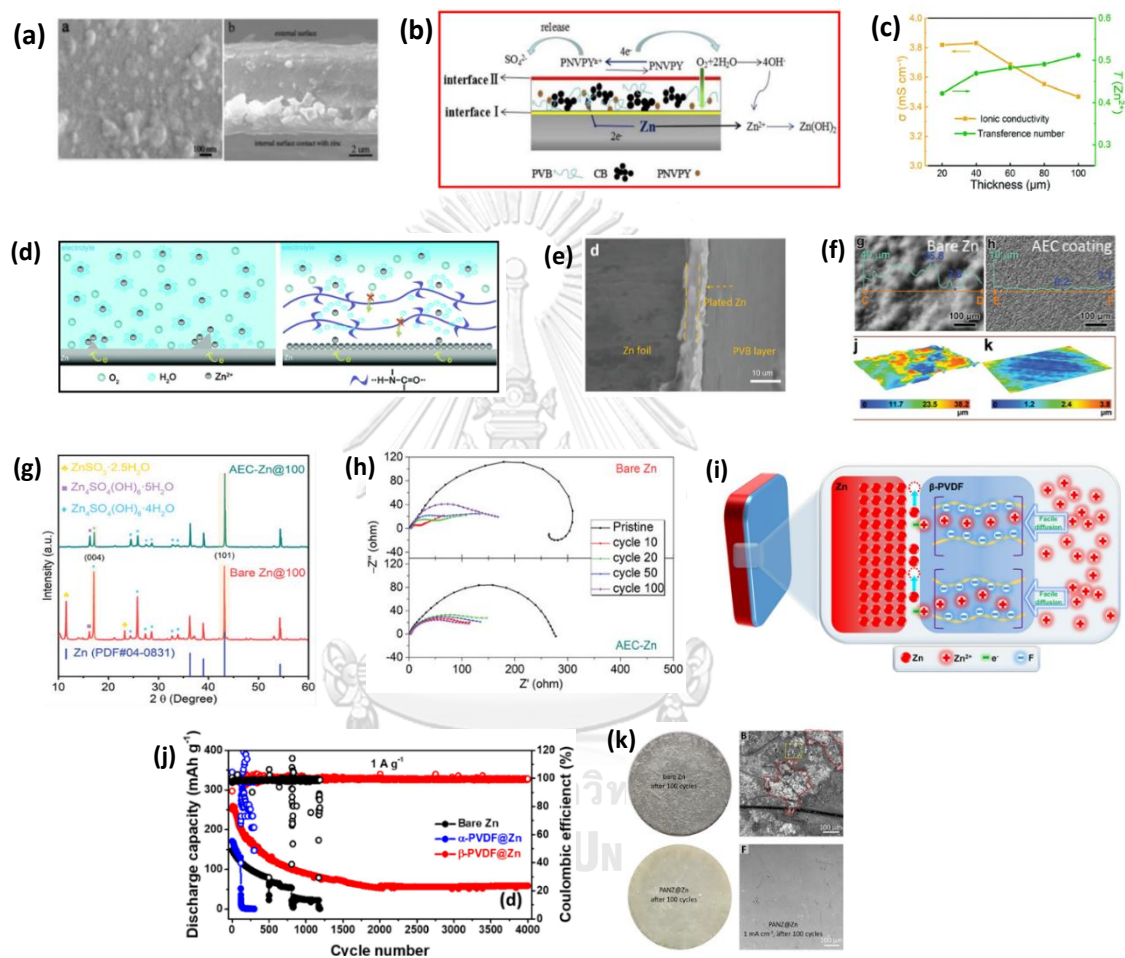
Figure 2. 6 Artificial SEI coating strategies on the Zn anode include organic polymer coating.

(The top-view and cross-section SEM images of the PNVPY/CB/PVP coating exfoliated form Zn plate (a). schematic illustration of the corrosion mechanism of the PVNPY/CNB/PVB composite coating on Zn electrode (b). (Reprinted with permission from ref. 24. Copyright 2018, Material). Ionic conductivity and Zn ions transference number (c). Schematic illustration for Zn plating on the bare Zn and the PA-coated Zn anode (d). (Reprinted with permission from ref. 23. Copyright 2019, Energy & Environmental Science). Cross-section SEM image of PVB@Zn anode after Zn plating at 0.5 mA h cm^{-2}(e). (Reprinted with permission from ref. 24. Copyright 2020, Advanced Functional Materials). The high-magnification optical and corresponding 3D height images for the surface of electrolyte-soaked Zn plates and AEC-Zn plates (f). The XRD patterns of the cycled Zn and AEC-Zn plates (g). The Nyquist of the symmetric cell of bare Zn and AEC-Zn anode after different cycles (h).

(Reprinted with permission from ref. 33. Copyright 2020, Advanced Functional Materials). Illustration of the ion distribution and uniform deposition through the β-PVDF film (i). Long-term cycling performance at a current density of 1 A g^{-1} (j). (Reprinted with permission from ref. 34. Copyright 2021, Chemical Engineering Journal). Digital picture and Morphologies of bare Zn and PANZ@Zn anode in symmetric cell after 100 cycles at 1 mA cm^{-1} with capacity 1 mA h cm^{-2} (k). (Reprinted with permission from ref. 71. Copyright 2021, Advanced Science).)

2.3.2.3 Conducting polymer and organic polymer

Polymeric coatings offer a compelling avenue for surface modification, owing to their inherent resistance to water and oxygen, as well as their mechanical flexibility and viscoelastic attributes. Achieving a homogenous, defect-free coating is particularly feasible with polymers that amalgamate both conductive and insulative properties (56). Conducting polymers (CPs), such as polypyrrole (PPy), polyaniline (PANI), and polythiophene (PTh), stand out as particularly efficacious anti-corrosive coatings. They serve a dual purpose: acting as physical barriers while also providing electronic insulation (57).

However, the application of CPs is not without its challenges. Their rigid molecular frameworks often result in poor solubility in standard solvents, leading to a cascade of issues. Firstly, this solubility constraint can trigger the irreversible depletion of stored charge within the CP, culminating in metal oxidation and the subsequent formation of a passive oxide layer. Secondly, the adhesion between CPs and the metal substrate may be compromised, thereby undermining the coating's efficacy (58, 59).

To circumvent these limitations, composite systems incorporating CPs have been developed, exhibiting augmented mechanical resilience and physicochemical stability. These enhancements manifest as superior barrier properties, improved adhesion, and heightened protection against metal corrosion. Notably, these composite fillers often integrate a diverse range of components, including metal oxides, inorganic substances, and organic polymers.

Hao et al. (24) introduced a multifaceted composite coating for the Zn anode, ingeniously integrating poly N-(vinyl)pyrrole (PNVPY), a derivative of polypyrrole (PPy), with carbon black, all encapsulated within a polyvinyl butyral (PVB) binder. This composite denoted as PNVPY/CB/PVB, is illustrated in Figure 2.6a. The coating

serves a dual purpose: it acts as a physical barricade, inhibiting cations from making direct contact with the Zn metal, and it also offers anodic protection via electronic barrier effects, a feature pivotal for mitigating corrosion.

As substantiated in Figure 2.6b, the conductive polymer (CP) layer manifests a robust oxidation potential on the Zn surface. This phenomenon triggers the liberation of doped anions and the acceptance of electrons during the corrosion process, thereby enhancing electron transport between the Zn anode and the electrolyte (60). Moreover, the unique properties of conductive polymers enable the translocation of side reactions from the metal-polymer interface to the polymer-electrolyte interface, effectively diminishing the corrosion rate of the Zn surface encapsulated by this coating.

However, it is worth noting that an overabundance of conductive polymers in the composite could be counterproductive. Excessive amounts can escalate the corrosion current, thereby undermining the coating's ability to inhibit corrosion effectively.

Conversely, organic polymers have garnered attention for their prospective utility in dendrite suppression, side reaction mitigation, and corrosion resistance enhancement in zinc anodes. Historically, these polymers, originally engineered as brighteners for zinc coatings, were incorporated into the electrolyte to tackle dendrite proliferation and corrosion. However, empirical evidence substantiating their efficacy in the suppression of side reactions remains elusive (61-63).

A solid-state polymeric interphase has emerged as a compelling alternative. Specifically, polyamide (PA) coatings, which exhibit ionic conductivity but lack electronic conduction, have been identified as optimal candidates for crafting artificial protective layers for zinc electrodes (22). As delineated in Figure 2.6c, the PA layer not only reduces ionic conductivity but also elevates the transference number, thereby retarding the migration of Zn ions (64). This layer has proven to be remarkably effective in water resistance and exhibits low permeability to oxygen gas in the electrolyte.

In terms of its corrosion-mitigating prowess, the PA layer significantly diminishes the corrosion current and nudges the corrosion potential toward more positive values compared to uncoated zinc. Additionally, it effectively curtails gas

bubbling and sustains a pristine morphology throughout the electrochemical cycling. The PA-coated layer offers a twofold advantage over bare zinc anodes. First, it serves as a buffer, impeding the infiltration of bulk aqueous electrolytes due to its hydrophobic and oxygen-resistant characteristics. Second, it employs an extensive hydrogen bonding network to sequester hydride ions, thereby quelling H_2 evolution and other undesirable reactions (Figure 2.6d). The net result is an extended operational lifespan for zinc plating and stripping, both in dormant and active states.

A poly(vinyl butyral) (PVB) polymer film has been scrutinized as a synthetic solid electrolyte interphase (SEI) for zinc electrodes. Research by Hao et al. (23) elucidates the multifaceted advantages conferred by this PVB layer. It not only efficaciously eradicates solvated water molecules surrounding the zinc during electrochemical operations but also suppresses undesirable side reactions. Additionally, the PVB layer boasts strong adhesion to the zinc substrate, coupled with mechanical flexibility and hydrophilic properties.

Under the aegis of this ASEI, zinc electrodes maintain a pristine, corrosion-free surface even after a week-long immersion in a 1 M $ZnSO_4$ solution (Figure 2.6e). Electrochemical assays further corroborate the protective efficacy of the PVB film on the zinc foil. Intriguingly, the corrosion potential of the PVB-coated zinc shifts toward a more positive value, attributable to the passivating influence of the layer. As a corollary, symmetrical cells equipped with a PVB@Zn anode exhibit a markedly extended cycle life. Worthy of special note is the diminution of the contact angle on the PVB@Zn foil after a mere 20 minutes of exposure, implying an enhancement in hydrophilicity. This is likely ascribable to the PVB film's rich content of polar functional groups (65). Consequently, the PVB@Zn anode distinguishes itself by delivering both high Coulombic efficiency (CE) and an elongated operational lifespan, outperforming its uncoated zinc counterpart.

Moreover, an innovative Anti-Corrosion Elastic Constraint (AEC) has been formulated, featuring a TiO_2 nanoparticle dispersion within a polyvinylidene fluoride (PVDF) matrix. The PVDF serves a dual-purpose role: it acts as a formidable barrier against water and oxygen ingress while synergistically aiding TiO_2 in ensuring uniform Zn deposition. This orchestrated interaction effectively stymies dendritic

growth, mitigates undesirable side reactions, and orchestrates controlled Zn deposition in aqueous electrolytic environments.

Analogous to the PVB-based coating, the AEC layer adeptly precludes any direct interaction between the Zn metal and aqueous or gaseous species, thereby attenuating detrimental interfacial reactions (Figure 2.6f). X-ray diffraction (XRD) analyses divulge the existence of hydrated Zn compounds on uncoated Zn substrates after 100 plating/stripping cycles (Figure 2.6g). Intriguingly, both the intrinsic resistance and charge transfer resistance of a symmetric cell equipped with an AEC-Zn anode remain remarkably stable throughout the cycling process, as evidenced in Figure 2.6h. This stability is indicative of a marked reduction in the formation of surface side-products. Employing this advanced AEC layer, the system achieves long-term Zn reversibility, extending up to 2000 hours. This performance is further characterized by an ultra-low overpotential (less than 50 mV) and a commendably high Coulombic efficiency (31).

Additionally, the efficacy of a highly polar β-PVDF layer has been substantiated (32). Owing to the intrinsically polar nature of β-PVDF, it serves as a facilitator for the transport of Zn ions, while concurrently inhibiting the dendritic growth of Zn. The mechanistic underpinnings of the β-PVDF layer's action are illustrated in Figure 2.6i. Specifically, the layer orchestrates a preferential diffusion pathway, constituted by the alignment of fluorine (F) atoms within the compound. This orchestrated pathway enables Zn ions to traverse the coating layer with relative ease, thereby manifesting a reduced charge transfer resistance in comparison to an uncoated substrate.

As Zn ions circulate through this layer, it functions as a regulatory conduit, modulating Zn ion migration and sustaining a long-chain molecular conformation characterized by a zigzag configuration in β-PVDF. This unique configuration fosters a uniform distribution of Zn ions, facilitated by interactions between the Zn ions and the electronegative carbon-fluorine (C-F) functional groups. Under the auspices of this coating, akin to previous studies (31), the overpotential of the β-PVDF@Zn system diminishes to approximately 40 mV, irrespective of high current rates or extended cycling durations. Moreover, an enhanced long-term lifespan is realized in

full cells, operating at 1 A g^{-1} and delivering a capacity of 60 mA h g^{-1}, as delineated in Figure 2.6j.

Chen et al. (66) introduced a composite coating for the Zn anode, ingeniously amalgamating polyacrylonitrile (PAN) with Zn(TfO)$_2$, henceforth referred to as PANZ. These composites manifested remarkable hydrophilic properties, thereby substantially diminishing the Zn anode's interfacial resistance. Intriguingly, the architecture of the PANZ layer incorporates microchannels within its polymer matrix. These microchannels, in concert with the synergistic interactions between Zn ions and the cyano functional groups (-CN) inherent in PANZ, orchestrate the uniform electrodeposition of Zn metal.

As a consequence of these attributes, the PANZ layer outperforms a bare Zn anode by significantly reducing interfacial impedance. Performance-wise, the PANZ@Zn anode showcases a dendrite-free, smooth surface morphology even after 15 cycles, as illustrated in Figure 2.6k. Moreover, this anode configuration exhibits extraordinary cycling stability, enduring beyond 1000 hours at a current density of 1 mA cm^{-2} in a symmetric cell setup. These empirical findings corroborate the efficacy of the PANZ layer in not only mitigating Zn metal corrosion but also in forestalling the genesis of Zn dendrites. Additionally, this innovative layer augments the nucleation sites on the anode surface, thereby amplifying both the rate performance and the cycling longevity when deployed in a full-cell configuration.
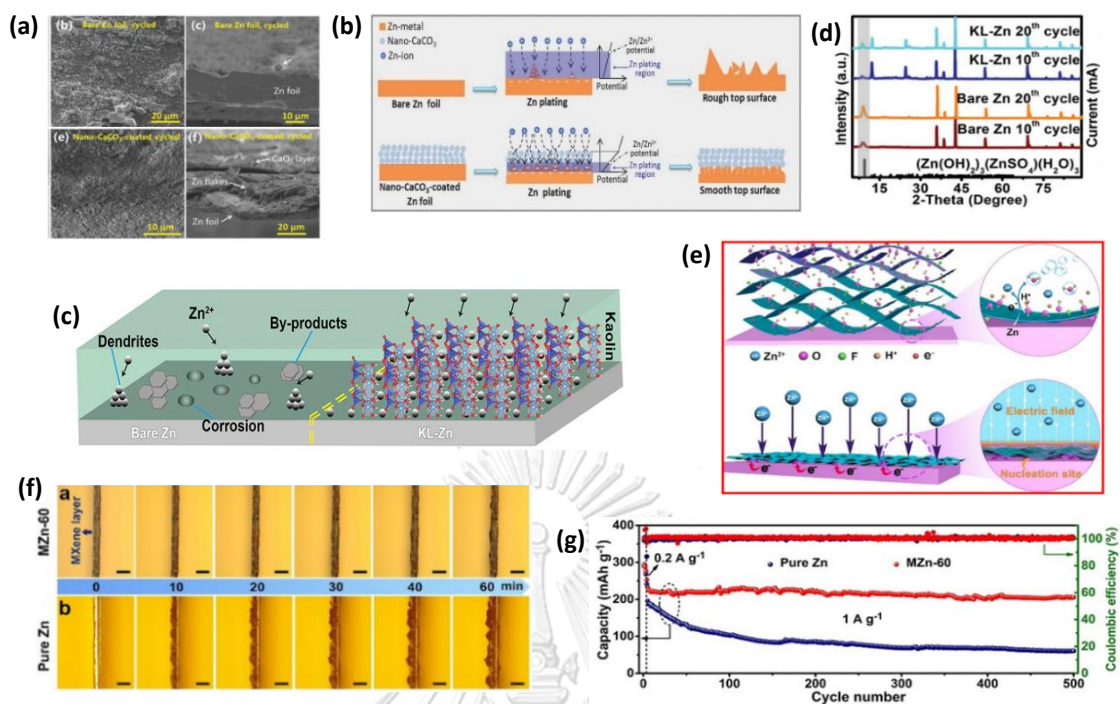
Figure 2. 7 Artificial SEI coating strategies on the Zn anode include other coating materials.

(SEM images of bare Zn and nano-CaCO3-coated Zn foil before and after 100 plating/stripping cycles at 0.25 mA cm^{-2} with 0.05 mA h cm^{-2} (a). Schematic illustration of morphology evolution for bare and nano-CaCO3-coated Zn foils during Zn cycling (b).(Reprinted with permission from ref. 72. Copyright 2018, Advanced Energy Materials). Schematic illustration of morphology of bare Zn and KL-Zn anode during deposition process (c). XRD patterns of the Zn and KL-Zn anode of Zn/MnO$_2$ cells cycled at 0.5 A g^{-1} for different times (d). (Reprinted with permission from ref. 74. Copyright 2020, Advanced Energy Materials). Illustration of synchronously reducing and assembling MXene layer on the of Zn foil and Zn plating behavior of MXene-coated (e). In situ optical microscopy visualization of Zn plating on MXene-coated Zn and bare Zn anode at 5mA cm^{-2} (f). Long-term cycling performance at 1 Ag^{-2} for 500 cycles (g). (Reprinted with permission from ref. 79. Copyright 2021, A Journal of the German Chemical Society).)

2.3.2.4 Other material coating

In a quest to mitigate uneven growth and curb undesirable side reactions in Zn metal anodes for mildly aqueous Zn-ion batteries, a porous CaCO$_3$ coating has been put forth as a viable solution. Research indicates that the judicious application of a porous CaCO$_3$ layer onto a Zn electrode serves as a catalyst for the uniform deposition of Zn, thereby amplifying the stability of both Zn plating and stripping processes (67). The

merits of employing $CaCO_3$ as a coating material are manifold: it is environmentally benign, ubiquitously available, facile to apply, and possesses a low density.

Notably, this $CaCO_3$ layer manifests minimal polarization escalation and exhibits augmented cycling stability, particularly at elevated current densities ranging from 1 to 3 mA cm^{-2} and a capacity of 0.5 mAh cm^{-2}. In alignment with prior research, the observed low polarization in Zn anodes coated with $CaCO_3$ intimates a diminished energy barrier for Zn nucleation, thereby fostering a more homogenous metal plating process (68). Moreover, the $CaCO_3$-coated Zn surface reveals a smoothly porous morphology, as illustrated in Figure 2.7a, accompanied by a decline in charge transfer resistance. It is crucial, however, to underscore that this performance was realized at a relatively low current density of 0.25 mA cm^{-2} and a modest capacity of 0.05 mA h cm^{-2}.

Given that $CaCO_3$ is an electrical insulator, its combination with polyvinylidene fluoride (PVDF) engenders a significant potential differential across this composite layer, as schematically delineated in Figure 2.7b. This unique configuration culminates in enhanced cycling stability and a heightened discharge capacity in Zn-MnSO$_4$ full cells, outperforming their counterparts with bare Zn foil.

Deng et al. (69) delved into the utilization of porous kaolin (KL) coating on zinc metal surfaces, aiming to address the inherent challenges tied to zinc anodes in mild aqueous electrolytes. This innovative approach engendered the uniform migration of Zn ions, culminating in a dendrite-free surface. The kaolin coating, characterized by selective ion channels and narrow pores of approximately 3 nm, acted as a protective layer on the zinc surface, as depicted in Figure 2.7c. This layer orchestrated the Zn ion transfer while effectively isolating the bulk electrolyte.

Upon evaluating the kaolin coating's influence on the electrical resistance within the battery, it was discerned that the KL-coated Zn anode manifested a reduced resistance. Intriguingly, impedance spectroscopy of the 21-micron-thick anode layer revealed dual semicircles, indicative of ion adsorption/desorption processes in the high-frequency domain and charge transfer resistance in the medium-frequency spectrum (70). However, caution is warranted, as an overabundance of kaolin coating can adversely affect ionic conductivity and escalate the interfacial resistance between kaolin particles.

Remarkably, the KL-Zn anode maintained its structural integrity, showing no signs of by-product formation even after 20 cycles at a current density of 0.5 A g^{-1} in a full cell, as illustrated in Figure 2.7d (71). Characterization results further unveiled that the primary transference of Zn ions predominantly occurred within the kaolin layer. Consequently, when deployed in MnO$_2$ cells, the KL-Zn anode showcased commendable cycling stability, high-rate performance, and well-preserved morphology post-cycling.

Metal-organic frameworks (MOFs), specifically ZIF-8, a zeolitic imidazole framework, have been scrutinized for their potential to ameliorate the challenges inherent to zinc anodes. Yuksel and colleagues (54) elucidated that the integration of ZIF-8 with zinc anodes could markedly enhance the reversibility of zinc plating and stripping cycles. This integration also serves as a formidable countermeasure against dendritic growth and undesirable side reactions.

In the realm of symmetric cells, the ZIF-8-integrated anode exhibited a marginal uptick in polarization, yet maintained stable reversibility, even when subjected to elevated current densities of 10 mA cm^{-2}. This compelling evidence underscores the MOF-based anode's capacity to substantially bolster the stability of zinc anodes.

When it comes to electrochemical performance, the ZIF-8-modified anodes outperformed their bare zinc counterparts, delivering superior capacity. The MOF-based anode ingeniously leverages coordinated zinc ions as a predefined ion gate, while its narrow pore structure acts as a safeguard against uneven charge distribution.

In an intriguing development, Zhang et al. (72) have introduced a Zn anode integrated with MXene, a two-dimensional material. The redox potential for the removal of oxygen-containing functional groups from MXene is higher than the Zn/Zn^{2+} redox potential. This thermodynamic favorability allows the MXene layer to undergo reduction via electron transfer from the oxidized Zn foil.

This electron transfer engenders a charge interaction between the Zn metal and the negatively charged oxygen-containing moieties on the MXene layer, culminating in the reduction of MXene. As a consequence, the MXene layer self-assembles onto the Zn surface, as depicted in Figure 2.7e. Once this MXene layer is in situ, it serves as a catalyst for uniform Zn deposition by lowering the nucleation energy barrier and

facilitating an evenly distributed electric field, as illustrated in Figure 2.7f. The net result is a Zn anode that exhibits enduring cycling stability, reduced voltage polarization, and an absence of dendritic growth. In the specific context of MnO_2 batteries, cells incorporating these MXene-coated Zn anodes demonstrate remarkable capacity retention at a current density of 1 A cm^{-2} over extended cycling periods, as evidenced in Figure 2.7g.

2.4 Polyelectrolyte: carboxy methyl cellulose

Polyelectrolytes, polymers embedded with electrolyte groups within their repeating units, span a versatile class of compounds encompassing polycations and polyanions. In aqueous solutions, these groups dissociate, endowing the polymer with a charge that enables ionic conduction. This dual characteristic confers upon polyelectrolytes the distinctive ability to exhibit behaviors reminiscent of both salts and polymers. Analogous to salts, they facilitate electrical conductivity in their solutions, while akin to polymers, they imbue their solutions with a notable viscosity or thickness due to their substantial molecular weight. These charged macromolecules are pivotal in the domain of soft matter systems, influencing the structure, stability, and interactions within various molecular constructs.

Among the polymers, cellulose, a preeminent natural polymer, and its derivatives have captivated research interests due to their unique properties. The chemical modification of cellulose typically involves the substitution of hydrogen atoms in hydroxyl groups with alkyl or substituted-alkyl groups. Remarkably, these soluble polymers can engage in crosslinking upon dissolution, imbibing substantial quantities of solvent and displaying impressive mechanical robustness, all the while preserving their morphological integrity.

Carboxymethyl cellulose (CMC), a biodegradable cellulose ether, stands out within this category. Characterized by a high degree of substitution (DS), CMC is capable of forming hydrogels in aqueous solutions at certain concentrations (73). Despite its relatively limited electrical conductivity, CMC's semi-crystalline nature coupled with its superior film-forming properties render it an invaluable material for a broad spectrum of applications.

The exploration into CMC's utility has been extensive, spanning from its role as an independent polymer to its incorporation into composite polymer electrolytes and hydrogel formulations. The polymer's diverse hydroxyl and carboxylic functional groups confer several desirable properties, such as an elevated water retention capability, biodegradability, and cost-efficiency (74).

Particularly of note is CMC's contribution to enhancing ionic conductivity in polymer electrolytes, a quality that underscores its potential in advancing electrochemical applications, including its integration into the burgeoning field of battery technology.

2.5 Zn-iodine batteries

The zinc-iodine (Zn-I$_2$) redox chemistry, particularly the iodide/iodine (I$^-$/I$_2$) redox pair, is emerging as a particularly promising avenue in the realm of energy storage, showcasing superior electrochemical attributes. The abundant presence of iodine in oceanic waters, with concentrations ranging from 50 to 60 mg/l, aligns with the global pursuit of sustainable energy resources. Zinc-iodine batteries distinguish themselves by offering a volumetric energy density that outstrips that of other flow battery systems.
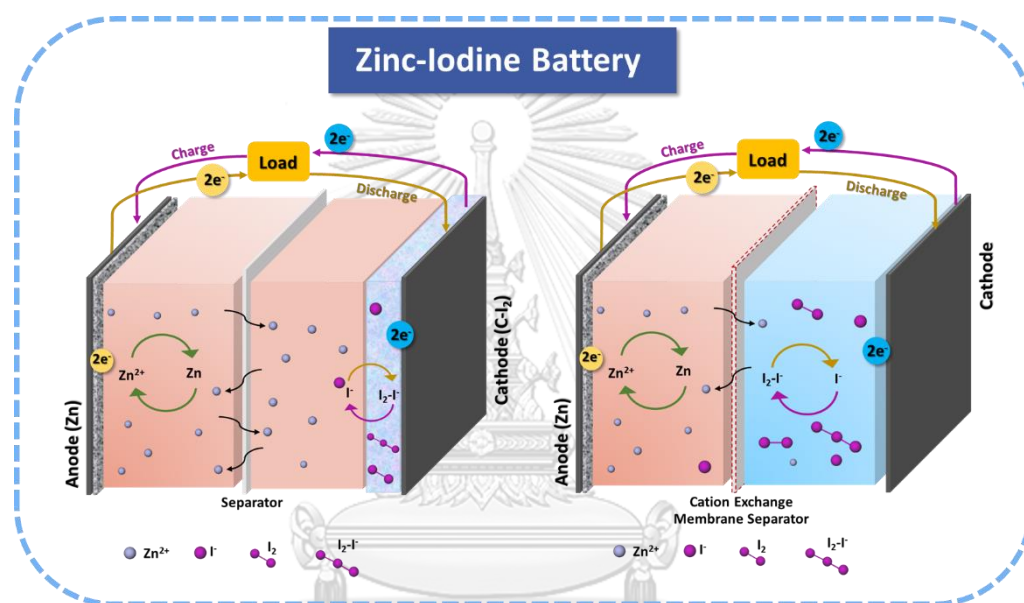
Figure 2. 8 Schematic illustrations of the principle of aqueous Zn-iodine battery use (left) a solid composite cathode made of carbon and iodine (C-I$_2$) and (right) a Zn metal anode in a ZnI$_2$ redox electrolyte.

Currently, typical Zn-I$_2$ batteries use a solid composite cathode made of carbon and iodine (C-I$_2$), where a cathode's porous structure captures iodine ions (75-78), and a Zn metal anode in a ZnI$_2$ redox electrolyte (79-81) as shown in Figure 2.8. The chemical reaction in a Zn-I$_2$ battery involves the use of Zn as the anode and iodine (I$_2$) as the cathode. During the discharge process, the following reactions occur:

At the anode (Zn side):

$$Zn^{2+} + 2e^- \leftrightarrow Zn \; : \; E^0 = -0.762 \, V \; (vs \, SHE) \tag{2.12}$$

At the cathode (iodine side):

$$2I^- \leftrightarrow I_2 + 2e^- \tag{2.13}$$

$$I^- + I_2 \leftrightarrow I_3^- \tag{2.14}$$

$$3I^- \leftrightarrow I_3^- + 2e-: \ E° = 0.536\,V\,(vs\,SHE) \tag{2.15}$$

Overall reaction

$$3I^- + Zn^{2+} \leftrightarrow I_3^- + Zn : \ E° = 1.3\,V\,(vs\,SHE) \tag{2.16}$$

During the charging phase of a zinc-iodine battery, Zn ions are reduced to metallic zinc, forming a solid electrode, a process that can be represented by the reversible reaction (Eq. 2.12). Concurrently, iodide ions (I^-) undergo oxidation to form iodine (I_2), as depicted in the reaction (Eq. 2.13). The predominant redox activity within the catholyte is the interconversion between iodide (I^-) and triiodide (I_3^-), which is favored due to the rapid charge transfer kinetics associated with the polyiodide reduction reaction. Iodine then reacts with free iodide ions to form soluble polyiodide species (I_3^-), as indicated in Eq. 2.14. The overarching electrochemical process is summarized in Eq. 2.15.

Upon discharging, the aforementioned reactions are reversed at their respective electrodes. According to the stoichiometry of the reaction equations, a minimum of one-third of the iodide ions are consumed in the formation of triiodide complexes with I_2, which serves to avert the precipitation of iodine. This stoichiometric requirement, however, limits the full exploitation of the active materials within the battery, leading to a reduced energy density. This presents a significant limitation in the battery's design, necessitating further research to enhance the utilization of active materials and thereby increase the energy density.

Zinc-iodine (Zn-I_2) batteries and their flow battery counterparts share a common chemistry but diverge significantly in design, application, and operational dynamics (82), as illustrated in Figure 2.9:

1. Design: Traditional Zn-I_2 batteries are self-contained units, akin to conventional batteries, comprising a zinc anode, an iodine-based cathode, and an electrolyte, all housed within a single casing. Zn-I_2 flow batteries, however, adopt a markedly different architecture, utilizing dual electrolyte reservoirs, one for the zinc-rich anolyte and another for the iodine-rich catholyte, with the electrochemical reactions occurring in a separate reaction chamber as the reactants are circulated through it. This design is typically larger, catering to grid-scale storage solutions.

2. Application: The compact Zn-I_2 batteries are well-suited for smaller, portable applications, whereas Zn-I_2 flow batteries, with their higher energy throughput, are tailored for large-scale storage, such as in grid energy storage systems, where they can aid in renewable energy integration and grid stabilization.

3. Operating Principle: In Zn-I_2 batteries, the electrochemical interaction between zinc ions and iodine leads to electricity generation, but these batteries often face rechargeability constraints. Conversely, Zn-I_2 flow batteries operate by circulating zinc and iodine ions between two tanks, with the cell stack facilitating the charge and discharge cycles. This system allows for electrolyte replacement or reconditioning, thus extending the battery's operational lifespan and cycle count.

4. Scalability: The scalability of Zn-I_2 batteries is limited by their compact, sealed design, making them less versatile for large-scale applications. Zn-I_2 flow batteries, on the other hand, can be scaled up by increasing the volume of the electrolyte tanks, making them ideal for scenarios that demand high-capacity energy storage.

Despite their promise, both Zn-I_2 and Zn-I_2 flow batteries confront significant hurdles in commercial deployment. They are prone to high self-discharge rates, primarily due to polyiodide ions (e.g., I_3^- and I_5^-) migrating through the anolyte, which typically necessitates the integration of a cation-exchange membrane (CEM) (79) to mitigate this issue. Additionally, the zinc electrodes are susceptible to dendrite growth, side reactions, and passivation over multiple charging cycles (78, 83), which can severely impair the batteries' performance and longevity. These challenges are critical considerations that must be addressed to enhance the viability and practicality of Zn-I_2 battery technologies for commercial applications.
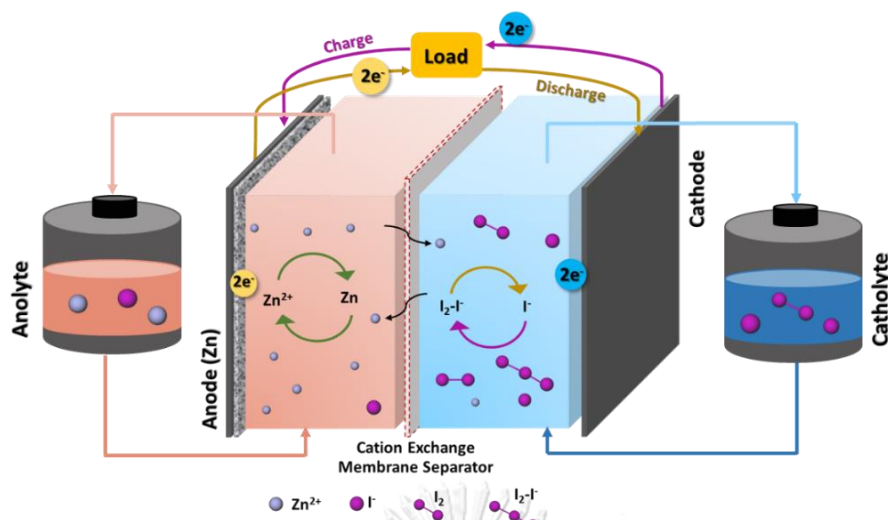
Figure 2. 9 Schematic diagram and working principle of proposed Zn-iodine flow cell.

2.5.1 Electrolytes

In Zinc-iodine (Zn-I$_2$) batteries, the electrolyte configuration is bifurcated into an anolyte containing a zinc salt solution and a catholyte composed of an iodine species solution, as referenced in the literature (76, 84, 85). Iodine, with its low dielectric constant, is naturally soluble in organic solvents at the molecular level, yet it demonstrates limited solubility in aqueous solutions due to the propensity to form halogen bonds. This solubility can be enhanced through the formation of compounds with potassium iodide (KI) and bromide ions (Br$^-$). The stable electric potentials generated by the redox reactions among I$_2$, I$_3^-$, and I$^-$ are extensively harnessed in flow batteries, as delineated in the reaction equations previously discussed (86). However, the inherent solubility limitations of iodine curtail the full exploitation of active materials, consequently diminishing the energy density of the battery.

To mitigate these constraints, a variety of strategies have been explored to maximize the capacity of Zn-I$_2$ batteries. Notably, the addition of choline ions (Cl$^-$) and bromide ions (Br$^-$) has been investigated as a means to stabilize I$_2$. These ions act as complexing agents, forming I$_2$-Cl$^-$ or I$_2$-Br$^-$ complexes, which serve to bolster the capacity and performance of Zn-I$_2$ batteries by enhancing iodine solubility and stability within the electrolyte (78, 87-89).

2.5.2 Cathode

In the domain of rechargeable zinc-iodine batteries, the quest for optimal cathode materials has led to the exploration of various substances. One notable advancement is the use of nanoporous structures within composite electrodes, which effectively immobilize polyiodides, thereby mitigating the shuttling effect that can degrade battery performance.

Graphene oxide hydrogel has emerged as a promising cathode material for Zn-I_2 batteries, forming a three-dimensional porous network that not only provides a substantial surface area but also promotes facile ion transport (85). Despite its advantages, the production of this hydrogel cathode necessitates a relatively high annealing temperature, which is a consideration for the manufacturing process.

Chong Bai et al. (75) investigated the use of conductive nanoporous activated carbon (ACC/I_2) that had been treated with dilute HCl and subsequently impregnated with iodine within the catholyte. This treatment significantly enhances the electrical conductivity of the composite electrode, offering a more efficient electron transfer during battery operation.

Yixin Li et al. (76) explored the potential of carbon cloth/I_2 as a cathode material, noting its exceptional flexibility and mechanical strength. However, this material's electron conductivity was identified as a limitation, suggesting that further modifications might be necessary to optimize its performance in practical applications.

Additionally, graphite felt has attracted attention as a cathode contender due to its high porosity and expansive specific surface area, which are conducive to the rapid discharge and charge kinetics of active ions in the electrolyte (78, 84). The intrinsic properties of graphite also contribute to the improved electrochemical behavior of the cathode, making it a material of significant interest for future development in zinc-iodine battery technology.

2.5.3 Cation Exchange Membrane

The alternative CEM is designed to permit the use of a cost-effective separator instead of the more expensive ion-exchange membranes, which also have relatively higher

electrical resistance. Research into hydrogel membranes for selective Zn ion transport in high-performance batteries has garnered considerable attention.

Xie et al.(78) examined a polyolefin separator combined with a Nafion layer, serving as a Zn ion selective membrane. While this configuration exhibited high performance, the cost of the Nafion layer remains prohibitively expensive, even when amalgamated with polyolefin. Commercial options like PAN membrane (77) and Durapore (84) also exist but are similarly costly.

2.6 Analytical techniques in ZBBs

2.4.1 Physical characterization

2.4.1.1 Scanning electron microscope (SEM)

Scanning Electron Microscopy (SEM) is a powerful characterization technique that employs a focused beam of electrons to scan the surface of a sample, such as a Zn anode or other solid materials. This method generates highly magnified images that facilitate detailed analysis. The resultant two-dimensional images produced by SEM provide insightful information regarding the sample's external morphology, including texture, structure, and the spatial arrangement of the constituent materials. This technique is instrumental in understanding the surface characteristics and composition of samples at the microscale.

2.4.1.2 The energy dispersive X-ray spectroscopy (EDS)

The Energy-Dispersive X-ray Spectroscopy (EDS) module, when integrated with Scanning Electron Microscopy (SEM), serves as a critical tool for the elemental analysis of a sample. This combination allows for the identification and characterization of elements present on or within the sample's surface, providing qualitative insights. EDS measures the elemental composition, offering semi-quantitative results that can discern the presence of inorganic foreign substances and detect coatings on metals. This analytical technique is essential for a comprehensive understanding of the material composition and for investigating the elemental constituents of a sample with precision.

2.4.1.3 X-ray diffraction (XRD)

X-ray Diffraction (XRD) is a swift and non-destructive analytical technique predominantly utilized for the phase identification of crystalline materials, offering insights into their crystal structure and unit cell dimensions. Through XRD analysis, one can obtain intricate details about the crystallographic structure, which is pivotal for understanding the morphology of Zn in the context of battery electrodes. Additionally, XRD can elucidate the chemical composition of substances deposited on electrodes and reveal the physical properties of materials, such as particle size,

strain, and crystallinity. This information is crucial for the assessment and optimization of materials, particularly in applications where the microstructural characteristics significantly influence the material's performance.

2.4.1.4 Raman spectroscopy

Raman spectroscopy is a sophisticated analytical technique employed to discern the vibrational modes of molecules. It is particularly adept at probing the molecular structure and local chemical environments within electrolyte solutions. This technique is invaluable not only for the characterization of novel electrolyte materials but also for detecting more nuanced changes within materials over time or under different conditions.

A Raman spectrum is characterized by its distinctive peaks, each representing the intensity and wavelength position of the Raman scattered light. These peaks are indicative of specific molecular bond vibrations, encompassing a wide array of bonds such as C-C (single bond), C=C (double bond), N-O, C-H, and others. Additionally, the spectrum can reflect the collective vibrations of groups of bonds, including polymer chain vibrations and lattice modes. The detailed information provided by Raman spectroscopy makes it an essential tool in the study and development of materials, especially in the context of chemical engineering and materials science.

2.4.1.6 X-ray tomographic microscopy (XTM)

X-ray Tomography (XTM) is a sophisticated characterization technique that provides a variety of three-dimensional insights. It enables the analysis of microstructures, defects, and crystallography in a wide range of materials with sub-micron resolution. The technique is typically conducted using Synchrotron radiation X-ray tomographic microscopy at beamlines such as BL1.2W, renowned for its non-destructive approach to visualizing and analyzing the internal features of solid opaque objects.

At BL1.2W (SLRI), the system is equipped to achieve X-ray imaging with a resolving power of up to 1 micron as its maximum resolution. The process involves capturing a dataset of X-ray images which are then compiled into a sinogram. This sinogram is integral to the reconstruction of computed tomography (CT) slices. By stacking these CT slices, a three-dimensional representation of the object is produced,

allowing for the detailed investigation and visualization of internal structures and features. This technique is invaluable for in-depth material analysis, providing a window into the internal composition of materials without altering or damaging them.

2.4.1.7 Fourier-transform infrared spectroscopy (FTIR)

Fourier-Transform Infrared Spectroscopy (FTIR) is an analytical technique that captures high-resolution spectral data across a broad spectral range in a simultaneous manner. This method operates by measuring the absorbance of infrared light by molecular bonds during their vibrational states, thereby providing a distinctive molecular fingerprint of the material under study.

When examining the artificial solid-electrolyte interphase (ASEI) layer using FTIR, the technique identifies different functional groups by their unique absorption frequencies, which are intrinsically linked to the molecular structure of the ASEI sample. The resulting vibrational spectrum is a powerful tool for determining the types of functional groups present within the sample.

Interpreting the data from FTIR involves comparing the absorption peaks in the spectrum to known frequency values for various functional groups. This comparison allows for the identification of the specific functional groups present in the ASEI layer, offering insights into the material's molecular composition and potential interactions within the battery system.

2.4.1.7 X-ray photoelectron spectroscopy (XPS)

X-ray Photoelectron Spectroscopy (XPS) is a quantitative spectroscopic technique that leverages the photoelectric effect to glean information about the elemental composition, chemical state, and electronic structure of the material being analyzed. It is particularly adept at probing the surface layers of a material, revealing both the elements present and their specific chemical environments.

The XPS procedure typically commences with a survey scan, which covers the full energy range with the highest sensitivity to identify and quantify the elements present on the surface of the sample. Following the survey, high-resolution XPS analysis is conducted with narrow scans at a higher energy resolution to discern the chemical states of the elements. This detailed examination allows for the precise

determination of chemical bonding states, inferred from the position and shape of the spectral peaks.

XPS analysis is invaluable for characterizing the surface composition of materials, such as identifying impurities and chemical functionalities on Zn depositions. Furthermore, it can provide chemical mapping, which is essential for evaluating surface structures and detecting irregularities. This level of detail is crucial for understanding the interfacial phenomena in various applications, including battery technology, where surface interactions play a pivotal role in device performance.

2.4.1.8 X-ray absorption spectroscopy (XAS)

X-ray Absorption Near Edge Structure (XANES) and Extended X-ray Absorption Fine Structure (EXAFS) are specialized techniques within the broader field of X-ray Absorption Spectroscopy (XAS). These techniques are predicated on measuring the X-ray absorption coefficient of a material as a function of photon energy. During the measurement process, a beam of X-rays with a finely tuned energy range is directed at a sample, and the intensity of the incident and transmitted X-rays is recorded as the energy of the incident X-ray beam is incrementally increased.
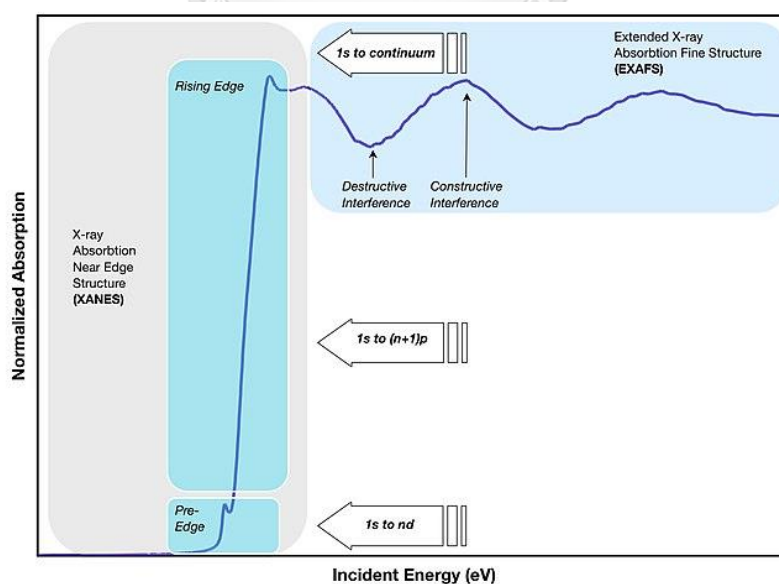
Figure 2. 10 Three regions of XAS data

The characteristic feature of XAS is the absorption edge, which occurs when the energy of the incident X-rays matches the binding energy of core electrons in the atoms of the sample. At this point, the absorption of X-rays by the sample surges, resulting in a notable decrease in transmitted intensity. This phenomenon is depicted as an absorption edge in the XAS data, XANES spectra include three parts: pre-edge, edge, and near-edge as illustrated in Figure 2.10. EXAFS spectra are displayed as graphs of the absorption coefficient of a given material versus energy, typically in the 150–1000 eV range, beginning before an absorption edge of an element in the sample. Each element has distinct absorption edges that correspond to the binding energies of its electrons, which imparts element-specific selectivity to XAS.

XAS spectra are typically collected using synchrotron radiation sources due to their high intensity, which enables the detection of elements in the sample at concentrations as low as a few parts per million.

XANES provides insights into the oxidation state of the absorbing atoms, the symmetry of the local electronic structure, and the electronic band structure, including energy bandwidth and bond angles. On the other hand, EXAFS can reveal detailed structural information about the material, such as interatomic distances, coordination numbers (indicating the number of nearest neighbors to a given atom), and information about the disorder and dynamics within the lattice structure.

These techniques are invaluable for probing the electronic and structural properties of materials at the atomic level, and they are widely used in material science, chemistry, and physics to study a variety of materials, including catalysts, semiconductors, and complex biological systems.

2.4.2 Electrochemical characterization

Electrochemical analysis is a collection of techniques that use electrical stimulation to analyze the chemical reactivity of a sample surface or a solution.

2.4.2.1 Galvanostatic charge-discharge (GCD)

The Galvanostatic Charge-Discharge (GCD) test is a pivotal method for evaluating the performance and cyclability of electrochemical cells. It involves the application of

a constant current to the cell over a series of charge and discharge cycles within predetermined voltage limits, as well as upper and lower cut-off currents. The resulting voltage profile as a function of time yields critical data from which key performance metrics can be derived (90).

The specific capacity of the cell, which represents the amount of charge transferred during the charge and discharge processes, is calculated using the integral of the current over the time of the cycle:

$$Capacity = \left(\int_{t_0}^{t_f} I dt \right) \qquad (2.16)$$

Here, I denotes the current, t is the time, t_0 is the starting time, and t_f is the ending time of the charge or discharge period.

Furthermore, the energy involved in the charging or discharging process can be quantified by incorporating the voltage (V) into the calculation, as expressed by the following equation:

$$Energy = \left(\int_{t_0}^{t_f} V I dt \right) \qquad (2.17)$$

CE, a critical parameter for assessing the reversibility of the battery, is the percentage of the discharge capacity relative to the charge capacity. It is calculated as follows:

$$Coulombic\ Efficiency = \frac{Discharging\ Capacity}{Charging\ Capacity} \times 100\ \% \quad (2.18)$$

2.4.2.2 Cyclic voltammetry (CV)

Cyclic Voltammetry (CV) is an analytical technique widely employed to study the redox behavior of electrochemical systems. It is particularly useful for examining the electrochemical properties of an electrode material within a cell (90).

In CV, the potential of a working electrode is swept linearly between two or more set values at a fixed rate, while the current is measured. The process begins at an initial potential, progresses to a vertex potential where the direction of the sweep is reversed, and then returns to the initial potential. This cycle can be repeated multiple times to observe the stability and reversibility of the redox reactions.

The resulting current-potential plot, typically displayed as a graph (as depicted in Figure 2.11), provides a current response that is directly related to the rate of the redox reactions occurring at the electrode surface. Peaks in the CV curve correspond to the oxidation and reduction processes, and their positions and shapes can provide insights into the kinetics of the electrode reactions, the reversibility of the electrochemical processes, and the diffusion characteristics of the active species.

By analyzing the CV data, researchers can deduce valuable information about the electrochemical pathways, the activity of the electroactive species, and the potential windows within which the electrode operates efficiently. This makes CV an indispensable tool in the characterization and development of new electrode materials and battery systems.
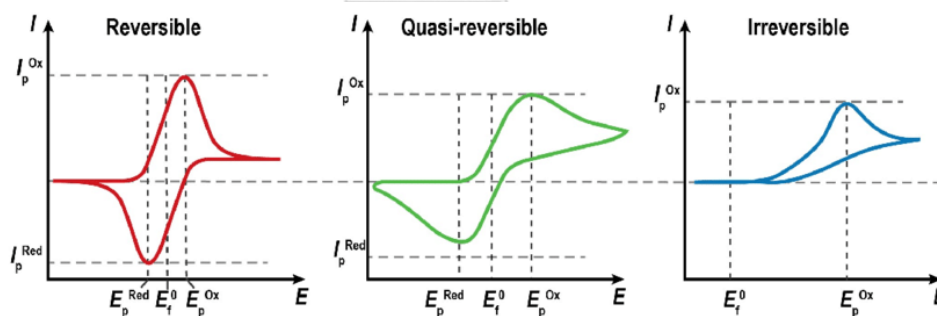
Figure 2. 11 The typical cyclic voltammogram of (red) the reversible reaction, (green) the quasi-reversible reaction, and (blue) the irreversible reaction.

In the context of cyclic voltammetry (CV), the key parameters that influence the outcome of the characterization are the potential range and the scan rate, which is the rate at which the potential is ramped during the experiment.

The potential range determines the window within which the redox reactions are probed. It is selected based on the expected electrochemical activity of the system and ensures that all relevant oxidation and reduction processes are captured within the sweep.

The scan rate, on the other hand, affects the shape and size of the peaks observed in the CV profile. A faster scan rate typically results in broader peaks and higher peak currents, as the system has less time to reach equilibrium at each potential. Conversely, a slower scan rate allows for more equilibrium-like conditions, resulting in sharper peaks that can provide more accurate information about the redox processes.

In the CV trace, as indicated in Figure 2.11, the terms E_p^{ox} and E_p^{red} refer to the peak potentials for the anodic (oxidation) and cathodic (reduction) reactions, respectively. These values indicate the potential at which the current reaches a maximum during the respective oxidation and reduction processes.

I_p^{ox} and I_p^{red} denote the peak currents for the anodic and cathodic reactions. These values are indicative of the number of electroactive species participating in the redox reactions and can provide insights into the kinetics of the electrode processes. By analyzing these parameters, researchers can gain a deeper understanding of the electrochemical behavior of the system, including the reversibility of the electrode reactions and the kinetics of electron transfer. This information is crucial for the optimization of electrochemical devices such as batteries and fuel cells.

2.4.2.3 *Electrochemical impedance spectroscopy (EIS)*

Electrochemical Impedance Spectroscopy (EIS) is an advanced technique used to characterize the properties of electroactive compounds or electrochemical cells. It involves the application of a small amplitude, frequency-varying sinusoidal potential (typically 2-10 mV) superimposed on a static potential to the cell under test. The resulting data is an impedance spectrum that reflects the magnitude of impedance and

the phase shift (or phase lag) between the applied voltage and the resultant current at each frequency point (91).

In the context of battery research, EIS is an invaluable diagnostic tool that allows for the examination of changes in the charge transfer characteristics during battery cycling. The impedance spectrum obtained can be modeled using equivalent electrical circuits to extract parameters such as internal resistance, double-layer capacitance, charge transfer resistance, and other parameters related to charge transport within the battery.

The models used for impedance analysis typically resemble networks composed of basic electrical components such as resistors, capacitors, and inductors. These components represent different physical phenomena within the cell:

- Resistors often represent ohmic resistances, such as the resistance of the electrolyte, separators, and electrode materials.

- Capacitors are used to model the capacitive behavior of the electrochemical interfaces, often represented as a constant phase element (CPE) to account for non-ideal capacitive behavior.

- Inductors may represent magnetic field effects, although, in battery systems, an inductive response can also be due to electrode kinetics or mass transport phenomena.

By fitting the experimental impedance data to these models, researchers can deduce valuable information about the electrochemical processes occurring within the cell, such as the kinetics of electrochemical reactions, the diffusion of ions in the electrolyte, and the state of health of the battery. This information is critical for optimizing battery design and for the development of better battery management systems.

2.4.2.4 Linear polarization

The linear polarization method is a widely accepted electrochemical technique for estimating the corrosion rate of electrodes. It is based on the measurement of the polarization behavior of an electrode when a small potential is applied. The resulting polarization curves can be analyzed to obtain the anodic and cathodic Tafel slopes, which are indicative of the kinetics of the corrosion processes (90).

The Tafel slopes, derived from the linear portions of the anodic and cathodic branches of the polarization curve as shown in Figure 2.12, are essential for calculating the corrosion current density (i_{corr}), which is directly proportional to the corrosion rate. The Tafel equation, which relates the overpotential to the logarithm of the current density, is used to extrapolate the Tafel slopes to the corrosion potential, allowing for the determination of i_{corr}.

Modern techniques involve the use of software that can fit the curvature of the Tafel slopes to the Tafel equation, providing a more accurate and automated means of determining both the corrosion potential and the corrosion current. This method is particularly useful because it is non-destructive and can be performed relatively quickly, making it suitable for routine monitoring of corrosion in various systems.
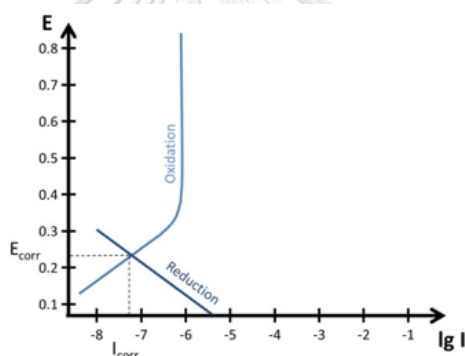
Figure 2. 12 The typical linear polarization curve

In electrochemical systems where reactions are segregated into distinct anodic and cathodic half-reactions, the Tafel equation provides a quantitative description of the relationship between the overpotential (ΔE) and the current density (i). This relationship is particularly useful for analyzing the kinetics of electrode processes. The Tafel equation is expressed as:

$$\Delta E = a + b\ log[\,i\,] \tag{2.19}$$

Here, ΔE represents the overpotential, i is the current density, and a and b are constants, with b being the Tafel slope. The Tafel slope can be derived from the fundamental principles of electrochemical kinetics and is given by the equation:

$$b = \frac{2.303RT}{\alpha F} \qquad (2.20)$$

In this equation, b is the Tafel slope, R is the universal gas constant, T is the absolute temperature in Kelvin, α is the charge transfer coefficient (a dimensionless number typically between 0 and 1), n is the number of electrons transferred in the half-reaction, and F is the Faraday constant, which represents the charge of one mole of electrons.

The Tafel slope provides insight into the mechanism of the electrochemical reaction, with its value being indicative of the rate-determining step. A smaller Tafel slope suggests a more facile electron transfer process. This equation is fundamental in electrochemistry and corrosion science, as it allows for the determination of kinetic parameters that are crucial for the design and optimization of electrochemical cells and the assessment of corrosion rates.
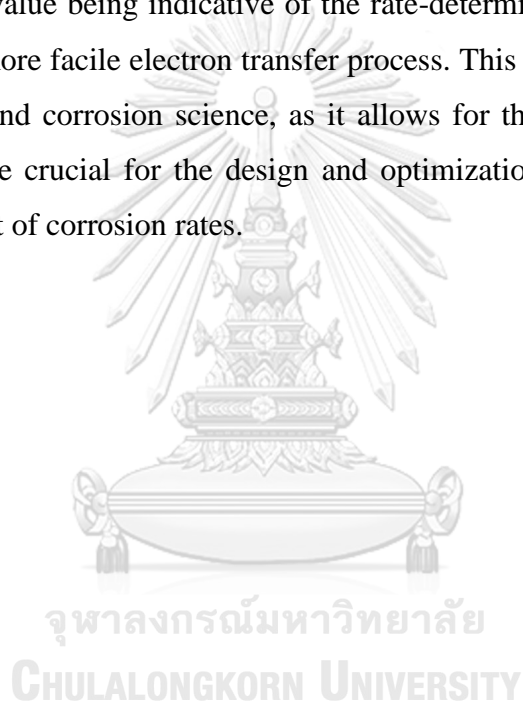
จุฬาลงกรณ์มหาวิทยาลัย

CHULALONGKORN UNIVERSITY

Chapter 3
Carboxymethyl cellulose as an artificial solid electrolyte interphase for zinc-based anode in aqueous electrolyte

Author Name: Phonapha Tangthuam[a], Wathanyu Kao-ian[a], Jinnawat Sangsawang[a], Catleya Rojviriya[b], Prae Chirawatkul[b], Jitti Kasemchainan[c,d], Falko Mahlendorf[e], Mai Thanh Nguyen[f], Tetsu Yonezawa[f], Soorathep Kheawhom[a,d,g,*]

Affiliation(s):

[a]Department of Chemical Engineering, Faculty of Engineering, Chulalongkorn University, Bangkok 10330, Thailand.

[b]Synchrotron Light Research Institute, 111 University Avenue, Muang District, Nakhon Ratchasima 30000, Thailand

[c]Department of Chemical Technology, Faculty of Science, Chulalongkorn University, Bangkok 10330, Thailand

[d]Center of Excellence on Advanced Materials for Energy Storage, Chulalongkorn University, Bangkok 10330, Thailand.

[e]Department of Energy Technology, University Duisburg-Essen, Duisburg 47057, Germany

[f]Division of Materials Science and Engineering, Faculty of Engineering, Hokkaido University, Hokkaido 060-8628, Japan

[g]Bio-Circular-Green-economy Technology & Engineering Center (BCGeTEC), Faculty of Engineering, Chulalongkorn University, Bangkok 10330, Thailand.

*Corresponding author: soorathep.k@chula.ac.th

stable zinc-based anodes in aqueous electrolytes - ScienceDirect and is also provided in Appendix A of this thesis.

Abstract

Zinc (Zn) is viewed as a promising anode material for large-scale secondary batteries. However, due to parasitic reactions and uneven Zn distribution during repeated stripping/plating cycles, Zn anodes show inferior performance and stability. To overcome such drawbacks, carboxymethyl cellulose (CMC) as an artificial solid electrolyte interphase (ASEI) is fabricated on a Zn sheet and Zn-graphite composite anode. The roles of CMC-ASEI are examined using X-ray tomography, X-ray absorption near edge structure (XANES) and extended X-ray absorption fine structure (EXAFS). Results show that the carboxyl group in CMC can regulate the flux and local concentration of Zn ions at the surface, allowing uniform Zn dissolution/deposition, and can suppress corrosion by reducing water activities on the anode's surface. At 5 mA cm^{-2} , the Zn-iodine battery having CMC-ASEI can cycle up to 2,000 cycles. This work provides a simple and scalable solution for advanced Zn anodes for Zn-based batteries.

Keywords: Anionic polyelectrolyte, Zn-polyiodide, Protective layer, Cyclability, X-ray tomography, Zinc battery

3.1 Introduction

Due to growing energy demands, more energy storage is required. Energy storage can enhance dependability and resilience and can have a positive effect on the environment (92, 93). Of late, there has been a lot of focus on the advancement of electrochemical energy storage systems (ESSs) (94). Researchers have developed rechargeable aqueous batteries and are interested in naturally abundant and cost-effective materials. Among the many alternatives for aqueous batteries, Zn-based batteries (ZBBs) have emerged as viable systems that can satisfy the present energy demands. Because of their inherent host-free property, Zn anodes stand out, allowing them to increase capacity and voltage via direct stripping/plating processes (95, 96).

Practical applications of ZBBs using neutral or mildly acidic aqueous electrolytes still face several challenging issues. The uneven dissolution/deposition of Zn causes short circuits and quick battery failure (13, 97, 98). The diffusion of Zn ions (Zn^{2+}) can be interrupted by the dense passivation layer that forms on the surface of the anode. Irreversible undesired reactions degrade the performance of the batteries. Extensive research has been devoted to addressing these issues, such as the introduction of additives into electrodes or electrolytes and the construction of nanoscale interfaces (99, 100). However, these strategies continue to have poor coulombic efficiency (CE). Recently, highly concentrated electrolytes have been applied to regulate the solvation sheath of divalent cations as well as stabilize Zn anodes. Such a strategy helps to minimize water-induced parasitic reactions and enhance CE of Zn plating/stripping. As yet, the mechanisms of Zn dendrite inhibition have not been fully understood. The instability of the Zn-electrolyte interface continues to be an issue today. The interfacial protection strategy is highly sought but mostly unexplored.

To suppress water activity and Zn dendritic growth, considerable efforts have been devoted to constructing an ASEI on a Zn surface using inorganic polymers or organic polymers. ASEI allows the transport of Zn^{2+} but restricts water molecules from penetrating the surface of the anode (101, 102). Controlling the distribution of Zn^{2+} concentration on the anode surface is essential. Numerous ASEI strategies have been suggested to promote Zn diffusion (103-107). Although many strategies for uniform Zn deposition have been carried out, the fundamental kinetics of Zn reduction have not been fully explored.

Another effective strategy for enhancing the properties of the Zn anode is via modification of the Zn surface using polymers. Conductive polymers such as polypyrrole (PPy) have been applied to restrain the dendritic growth of Zn by regulating nucleation and manipulating the distribution of Zn^{2+} over the anode surface (108). However, inadequate protection layers result in lower electrons and poor Zn^{2+} transport, thus increasing battery polarization (38). Polyaniline (PANI) was studied as a porous interphase layer on Zn electrode for regulating the transport and deposition of Zn^{2+}, providing improved stability and reversibility of Zn anode (109). Polar groups of PANI molecules (110) have a strong attraction to water molecules, allowing

immobilization of water molecules around Zn^{2+}. Further, PANI-complex nanocomposites were investigated for their anti-corrosion performance (111). Moreover, effective Zn anodes via fabricating ASEI with non-conductive polymers have been studied in aqueous ZBBs. Chen et al. (112) used Zn foil coated with polyamide (PA) to suppress the growth of Zn dendrites. Amide groups can effectively distribute and restrict Zn^{2+} flux. Shin et al. (113) investigated ASEI made of cross-linked gelatin on a Zn metal electrode; the hydrogel allowed for an electrolyte interphase to be formed and protect the Zn surface from undesirable reactions. Ding et al. (114) fabricated a quasi-gel interphase on a Zn plate using covalent organic polymer (COFs) to improve the transport of Zn^{2+} and provide uniform nucleation of Zn. It is seen that polymeric protective layers can improve reversible Zn electrodeposition beneath the layer, leading to intensified electrochemical activity and prolonged cycling. A coating layer prevents a Zn surface from hydrogen evolution reaction (HER) and undesirable by-products. Among the many types of polymers, CMC shows the greatest promise because of its affordability and biocompatibility. CMC molecules consist of mobile positive charge carriers and stationary negative charge carriers, thus controlling the local concentration of Zn^{2+} at the anode surface (115). However, the behavior of Zn deposition/dissolution under the effect of CMC has not been adequately investigated. The cation regulated property of CMC for use as ASEI in ZIBs and other batteries shows promise.

To overcome critical problems of the Zn anodes, the design of Zn anodes based on a Zn sheet and a composite-type Zn anode having graphite and CMC-ASEI are demonstrated. The roles of CMC-ASEI were examined via X-ray tomography, X-ray absorption near edge structure (XANES) and extended X-ray absorption fine structure (EXAFS). The influence of CMC is examined via electrochemical characterization. Subsequently, it is seen that the CMC-ASEI can safeguard the Zn anode, both ensuring low polarization and enhancing the plating/stripping cycle life. Carboxyl groups in CMC-Na tend to coordinate with Zn^{2+}, providing fast ion transport channels, thus reducing the desolvation penalty. Such an effect can facilitate the even distribution of Zn^{2+} flux near the surface of the Zn electrode, exhibiting rapid kinetics of Zn^{2+} transfer. Consequently, the CMC-Zn anode possesses high CE and has a long lifespan by decreasing the water within the Zn^{2+} solvation sheath, thus

suppressing the decomposition of the electrolyte. It is noted that a Zn anode having CMC-ASEI displays a low nucleation energy barrier, enabling faster transport of Zn^{2+}, and can suppress both Zn corrosion and HER. Accordingly, the coated Zn composite anode provided stable cycling: >1,000 cycles at current density of 1 mA cm^{-2} and areal capacity of 0.1 mA h cm^{-2} in the symmetrical cell and displayed low voltage hysteresis. To further investigate the practical implementation of CMC-ASEI, a polyiodide-carbon as a cathode has been employed. Consequently, a Zn anode having CMC-ASEI exhibited superior stability, revealing excellent capacity retention (>98% of CE) compared with the pristine Zn metal anode and an ultralong life of over 2000 cycles (5 mA cm^{-2}).

3.2 Materials and methods

3.2.1 Materials

To prepare the composite negative electrode, PTFE, graphite and alloyed Zn powder (EverZn, Loncin, Belgium) were purchased. For binder solution (5 wt.%), PVDE and NMP were used. Two molecular weights of analytical grade i.e. 90,000 and 250,000 Mw of CMC (Sigma-Aldrich, St. Louis, MO, USA) were used as a polyelectrolyte layer on the negative electrode. Electrodes made of 90,000 and 250,000 CMC are denoted as A90x and A25x, respectively. Zn sulfate ($ZnSO_4 \cdot 7H_2O$) was used for the electrolyte (Kemaus, New South Wales, WA, Australia). Stainless steel mesh (304) was used as the current collector (Alikafeii Trading Co., Ltd. China).

3.2.2 Negative electrode preparation

A Zn composite anode was prepared by mixing Zn powder, polytetrafluoroethylene (PTFE) and graphite powder in a ratio: 8:1:1. The components were mixed via ball mill (400 rad/min) for 24 h. Subsequently, 5 wt.% PVDE in NMP, in the ratio of 500 µl: 1 g, was added to the mixture and then stirred together for 20 min. Next, the mixture was coated and pressed onto the stainless-steel mesh. The thickness of the anode was controlled by rolling. The average thickness of

the anode was 0.1 mm. After that, the electrode was processed via annealing at 330 °C for 15 min. Further, the anode was cut into pieces: 1.5 cm in diameter. The concentration of CMC in the polyelectrolyte layer on the electrode was as follows: 1.5 wt.%, 2.5 wt.% and 3.5 wt.%. Subsequently, the CMC (90,000 MW) solutions were denoted as A901, A902, and A903. As for the CMC (250,000 MW) solutions, they were denoted as A251, A252 and A253, respectively. The solution was prepared by dissolving CMC in deionized water. The solution was stirred for 1 h at 60 °C. Finally, the electrodes were dip-coated with the prepared polyelectrolyte and then dried at 90 °C for 1 min.

3.2.3 Battery fabrication

To examine the electrochemical performance, coin-type cells (CR2025) were assembled. As for the separator and electrolyte, a glass microfiber filter membrane and 1.5 M $ZnSO_4$ solution were used. For the cathode, both iodine and activated carbon powder were mixed in a ratio of 1:2 and stirred for 1 h. The mixture was then dried in a vacuum oven at 60 °C for 4 h. After cooling down, the as-prepared mixed polyiodide-activated carbon, super-P, and CMC solution (250,000 MW; 2 wt.%) were mixed in a ratio: 8:1:1 and stirred for 30 min to form a homogeneous slurry. Next, the slurry was coated on graphite foil and dried at 30 °C for 1 h; the thickness of the cathode was 150 μm. In the three-electrode cell, the modified Zn electrode was applied as working electrode (WE), platinum as counter electrode (CE), and Ag/AgCl electrode as reference electrode (RE), respectively.

3.2.4. Characterization

Both scanning electron microscopy (SEM; JEOL, USA (JSM-6480LV)) as well as field-emission (FE-SEM; FEI, USA (Quanta-250 FEG)) were used to investigate the morphology of the samples. Energy-dispersive spectroscopy (EDS) was carried out to confirm that Zn, fluorine, and carbon elements were distributed over the electrode surface. The CMC structure on the electrode, before and after cycling, was examined via Fourier-transform infrared spectroscopy (FTIR;

PerkinElmer Inc., USA (PerkinElmer Spectrum One)), in the range of wave numbers: 4000-400 cm^{-1}. X-ray diffraction (XRD) was used to examine the by-products on the electrode surface. Contact angles (CA; Kruss, Germany (DSA 10 MK2)) of the anodes were measured. X-ray absorption near edge structure (XANES), extended X-ray absorption fine structure (EXAFS) and X-ray tomographic microscopy (XTM) were carried out at the Synchrotron Light Research Institute (SLRI), Thailand.

3.2.5 Electrochemical tests

Galvanostatic charge/discharge cycling was carried out using Battery Tester CT-4008-5V 20mA (Neware Technology Ltd., Shenzhen, China). Cyclic voltammetry (CV), electrochemical impedance spectroscopy (EIS) and linear scan voltammetry (LSV, corrosion testing of the electrodes) were all carried out using Squidstat Plus with EIS (Admiral Instruments, USA). CV was performed in the voltage range: -1.5 – 0 V (vs. Ag/AgCl) using Pt counter electrode at different scan rates for the symmetrical cells. EIS measurements were obtained in the range: 1 MHz to 0.01 Hz in symmetrical cells and the three-electrode cell. LSV experiments were set up the same as for CV testing i.e. 5 mV s^{-1} of scan rate in 1.5 M ZnSO$_4$ solution. For the battery testing, both charge and discharge specific capacities were calculated based on the active surface area. CV of the full cell was investigated in the voltage range: 0.7-1.7 V (vs Zn/Zn^{2+}) at scan rates 1 mV s^{-1}). EIS of the batteries was carried out in the frequency range: 1 MHz to 0.01 Hz, before and after CV cycling. All electrochemical testing was conducted at room temperature (27 °C).
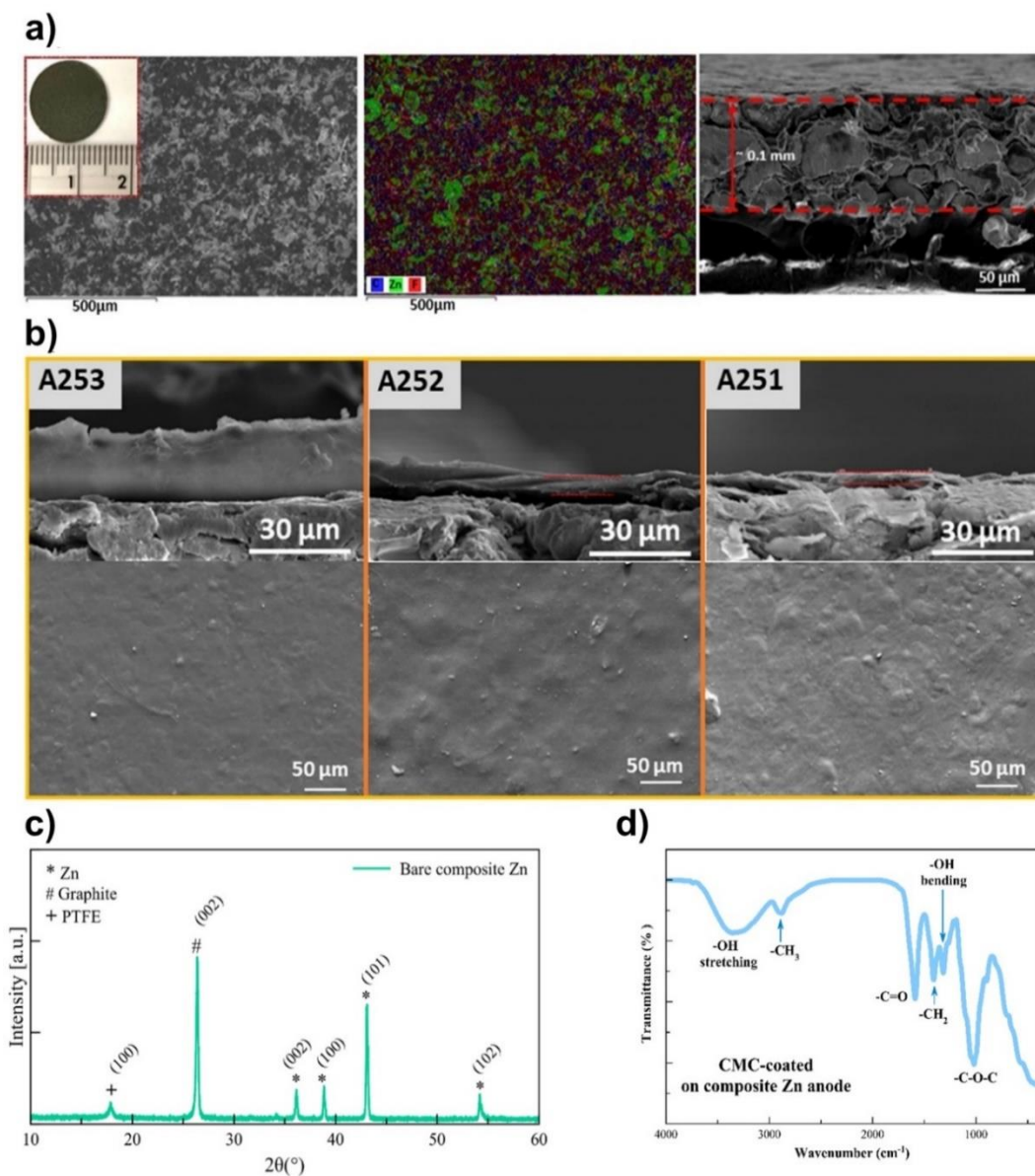
Figure 3. 1 (a) FE-SEM images and EDS mapping of the Zn composite anode without coating (scale bar: 500 μm); inset: digital photo of the bare Zn composite anode , (b) FE-SEM images of the Zn anode with coating 3.5 wt.% of CMC (left), 2.5 wt.% of CMC (middle), 1.5 wt.% of CMC (right) (Mw.250,000) : CMC-ASEI samples are in the order A253, A252, and A251, respectively, (c) XRD pattern of the bare Zn composite anode, and (d) FTIR spectrum of CMC coated on the Zn composite anode.

3.3. Results and discussion

In Fig. 3.1 a, the Zn composite anode without CMC-ASEI is seen to have a textured surface and is well-distributed. In Fig. A1, EDS confirms the existence of Zn, fluorine (F), and carbon (C) on the surface of the Zn composite anode. In Figs. 3.1b

and A2, the FE-SEM images of the Zn composite anodes having CMC are shown. The thickness of the high molecular weight samples: Mw.250,000: A253, A252 and A251 of the CMC-coated layer was determined at ~17.1, 7.0, and 2.3 μm, respectively. The thickness of the low molecular weight samples (Mw.90,000: A903, A902 and A901) was determined at ~ 2.8, 1.6, and 0.86 μm, respectively. The thickness of A253 proved to be larger than the other CMC-coated layers and the layer completely covered the electrode. In contrast, the A901 is not very thin, and the layer is uneven. In Fig. 3.1c, a strong XRD peak of graphite(116) at $2\theta = 26.4°$ (002) and a slight peak of PTFE(117) at $2\theta = 17.8°$ (100) were observed in the bare Zn composite anode spectrum. Peaks of metallic Zn with a hexagonal crystal structure were noted at $2\theta = 36.2°, 38.9°, 43.1°$ and $54.2°$, corresponding to (002), (100), (101) and (102) lattice planes, respectively(118). No ZnO was detected in the XRD pattern.

FTIR spectra confirmed the presence of CMC on the electrode surface. In Fig. 3.1d and Table A1, absorption bands of CMC can be seen at 1019 cm^{-1}, 1316 cm^{-1}, 1409.6 cm^{-1}, 1589 cm^{-1}, 2881 cm^{-1} and 3356 cm^{-1}, corresponding to C-O-C stretching, O-H bending, -CH$_2$ scissoring, -C=O region, -CH$_3$ stretching and -OH stretching, respectively (119-121).

The contact angles of the anodes were measured using water. As depicted in Fig A3, the contact angles decreased from 90.4° on the bare Zn sheet to 67.8° on the CMC-Zn sheet: the change in surface property is assigned to the CMC coating. Similarly, the contact angle of water on the pristine composite Zn anode was found to be 117.7°. The contact angles of the CMC-coated on the electrodes were smaller being 73.6°. When CMC content increased from 1.5 to 3.5 wt.%, the electrode became more hydrophilic, and the contact angle decreased. The contact angles of the low molecular weight samples (Mw.90,000: A901, A902 and A903) were determined, corresponding to 51.5°, 49.7° and 41.2°, respectively. Likewise, the contact angles of the samples having a high molecular weight (Mw.250,000: A251, A252 and A253) corresponded to 73.6°, 63.5° and 45.9°, respectively. Results of the contact angle measurements show that CMC changed the surface chemistry of the anode, affecting the electrolyte wetting property. The hydrophilic property, therefore, is seen to improve the affinity of the Zn anodes for the electrolyte. Thereby, the electrolyte can wet the anode and is distributed widely over the anode.
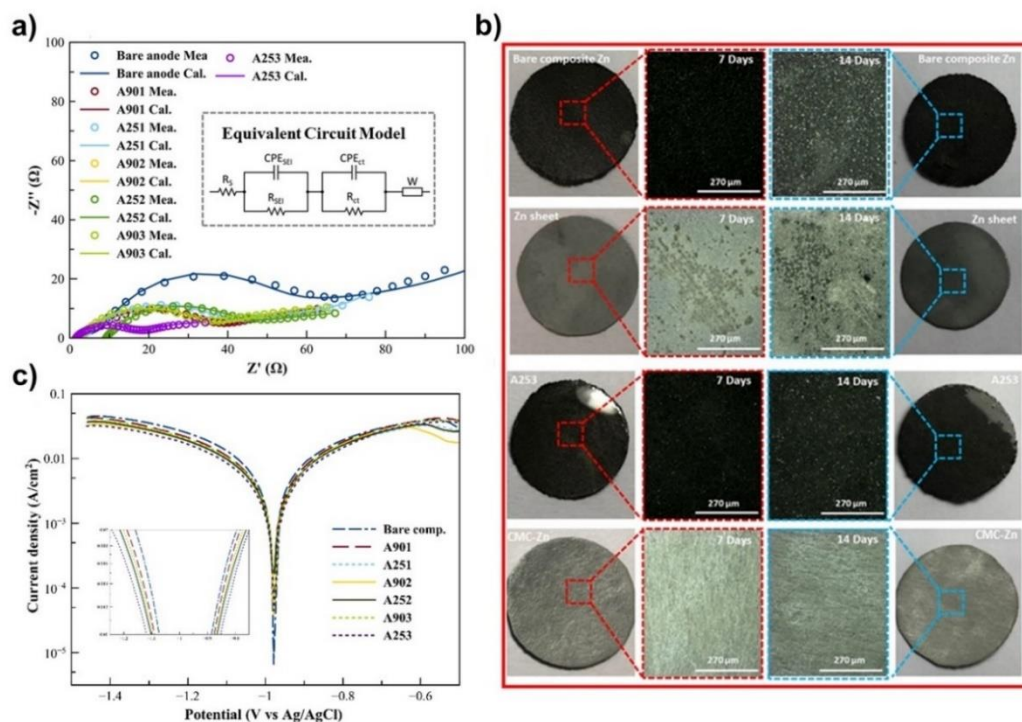
Figure 3. 2 (a) Electrochemical impedance spectra of the symmetrical cells, (b) Images of the Zn sheet and fabricated Zn without/with CMC layer (A253) anode soaked in 1.5 M ZnSO$_4$ for 7 and 14 days, and (c) LSV spectra of all samples.

To evaluate the ionic conductivity of the CMC layer, EIS measurements were carried out. EIS data were fitted in accordance with the equivalent circuit model using Zsimpwin software, which is used in any application field of electrochemistry but also in conductive material (122). In Fig. 3.2a, the semicircle in the high frequency region corresponds to the resistant SEI formation (123-125). This semicircle was depressed due to the overlap of the multi-resonances in the frequency space between the anode and SEI layer. It is significant that the radius of the semicircle reduced when both CMC molecular weight and content increased. In subsequent data fitting of without CMC-ASEI coating, a large capacitive loop is seen. At low frequency, a small oblique line indicating Warburg impedance (W) is revealed and corresponds to the governed salt diffusion. Subsequently, limited diffusion and plating/stripping process of Zn^{2+} in the bulk material was simulated. In Table A2, EIS impedances of the symmetrical cells are listed. Owing to the decrease in charge transfer resistance, improved Zn stripping/plating kinetics of Zn deposition was achieved. Although the A253 sample

had the largest thickness of CMC layer, it also had the lowest charge transfer resistance, providing an even Zn^{2+} deposition underneath the ASEI layer. The negative charge of the CMC molecule was able to repel a certain amount of SO_4^{2-} anions, restricting interaction between anions and cations, and inhibiting side reactions, thereby improving the de-solvation of the hydrated Zn^{2+} (30).

In Fig. A4, the Nyquist plots of the fabricated CMC-ASEI electrode in the three-electrode cell reveal that both a capacitance of CMC layer and a charge transfer resistance are present at high and middle frequency capacitive loops, respectively. An inductive loop obscured in the low frequency region infers the inductance (L) equivalent, which likely indicates the absorption/desorption of Zn^{2+} on the SEI layer (126). In Fig. A5, the electrode without CMC-ASEI came under the influence of inductance, owing to the graphite and highly polar nature of the PTFE polymer in the electrode matrix. Previously, both carbon material and polar polymers were recommended as ASEI coating layers (48, 127-129). In Fig. A6, the CV curves of the Zn plating/stripping of CMC-ASEI (A253), at varying scan rates, demonstrate typical cathodic loops and anodic peaks, indicating identical redox processes with Zn oxidation. When scan rate increases, anodic peaks shift to positive potential, revealing that the kinetics of the electrode is limited by the surface-reaction (130).

To study the anti-corrosion properties of the CMC coating on the modified Zn anode and Zn sheet, both the Zn sheet and fabricated anodes with/without CMC layer were soaked in an aqueous electrolyte: 1.5 M $ZnSO_4$ solution. In Fig. 3.2b, the plain Zn sheet turned gray and had an uneven surface with pits of corrosion after 7 days, indicating the formation of corrosion-reaction products. After 14 days, both the bare Zn composite anode and plain Zn sheet displayed an uneven surface, indicating a severe side reaction. In comparison, the CMC-ASEI samples remained the same having a fresh surface after 14 days and a flatter surface, revealing much improved stability of SEI and Zn against the aqueous electrolyte (128). Thus, CMC-ASEI has the potential to protect Zn metal from corrosion caused by aqueous electrolytes.

In aqueous electrolytes, it is acknowledged that a Zn anode encounters both interface corrosion and HER. Under protection of the CMC interphase, LSV experiments were carried out at scan rate 5 mVs^{-1} (Fig. 3.2c). In Table A3, corrosion potential shows a positive shift from -980.71 mV to -967.583 mV. Both the higher corrosion potential and the lower corrosion current density denote a reduction in corrosion tendency and lower rate corrosion in the aqueous electrolyte (124, 131, 132). In Fig. 3.2c, the CMC-A253 layer having the highest hydrogen evolution overpotential and lowest rate corrosion is seen to inhibit the side reactions between the electrode/electrolyte.
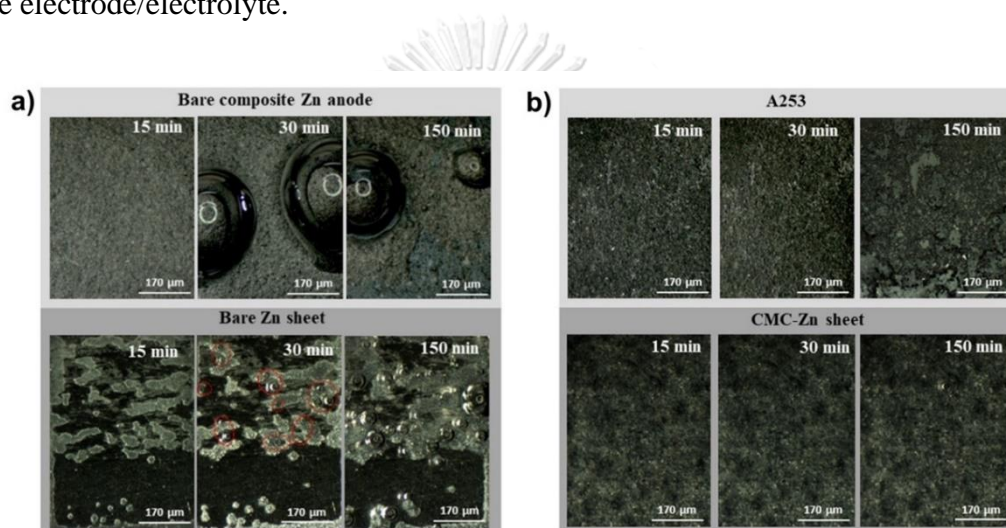
Figure 3. 3 In situ observation of the Zn deposition by optical microscopy in Zn/Zn cells: (a) Bare Zn electrode without CMC layer, and (b) Zn electrode with CMC protective layer. The deposition current density is 20 mA cm^{-2} with an areal capacity of 10 mAh cm^{-2}.

Observation showing enhancement in Zn plating/stripping enabled by CMC-ASEI was obtained via in-situ optical visualization technique of Zn deposition (in a home-made cell, Fig. A7). In Fig. 3.3a, after 15min soaking, rather uneven Zn electrodeposition, and copious air bubbles were seen on the pristine Zn sheet. Although the bare cell Zn composite electrode showed an even and compact Zn deposition, generation of gas occurred and hindered the surface area of Zn. In Fig. 3.3b, the cells having the CMC protective layer provided uniform and compact Zn

deposits at a capacity of 10 mAh cm^{-2} with 20 mA cm^{-2}. Gas generation is suppressed when the CMC-coated Zn sheet and fabricated Zn anodes are contained in the cell. However, after 150 min, the composite materials (PTFE and carbon) under the CMC layer lifted up during the charging process.
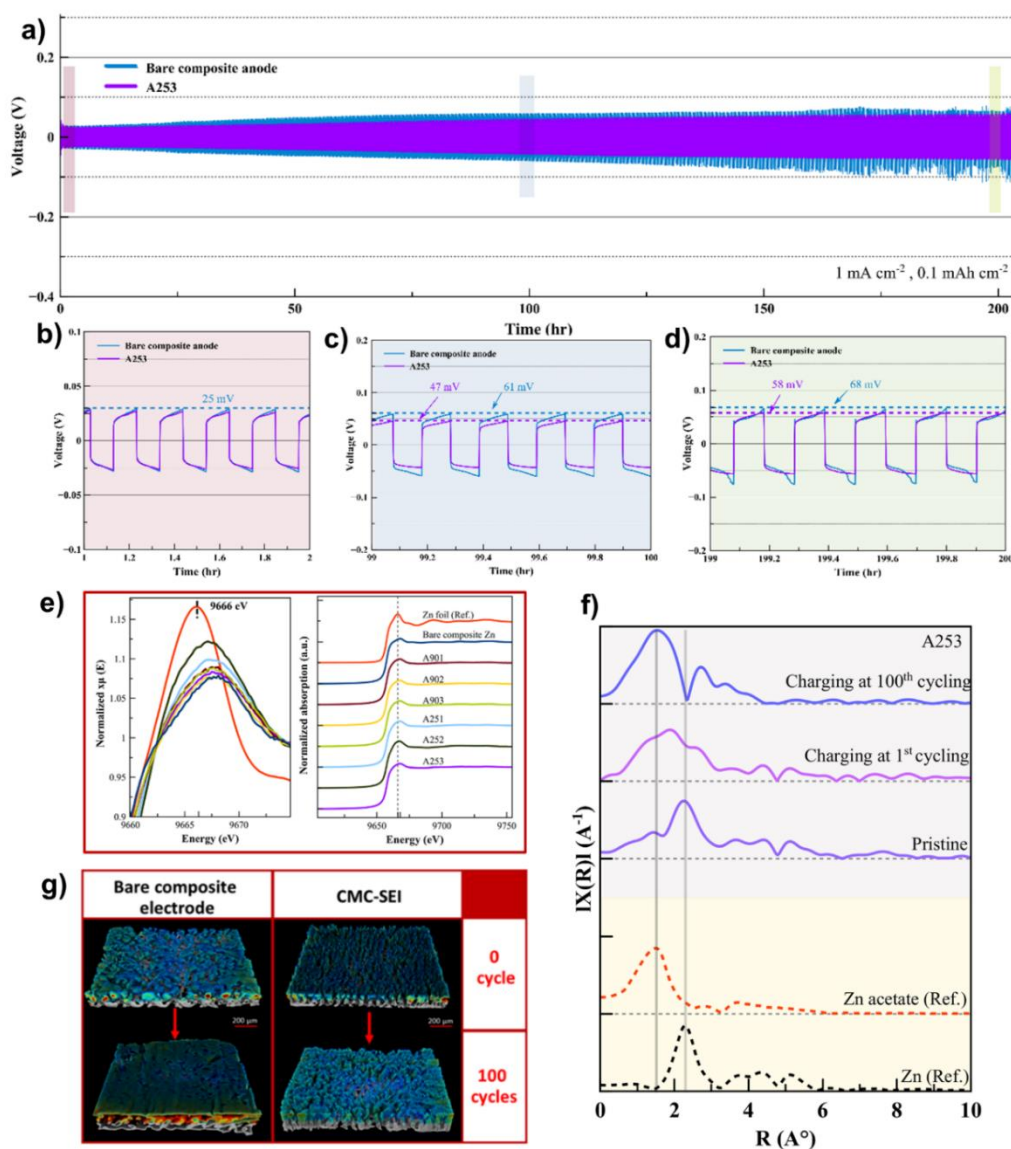
Figure 3. 4 (a) Cycling performance of the bare Zn, bare composite, and A253 at 1 mA cm^{-2} with capacity of 0.1 mA h cm^{-2} for 2000 cycles, (b-d) the comparison of different cycling times. (e) Zn K-edge XANES spectra of bare composite and difference CMC-ASEI electrode at initial charging process; Zn foil is used as reference, (f) Fourier transform of Zn K-edge EXAFS spectra of A253, (g) XTM 3D images: Zn deposition of bare Zn composite anode and modified CMC-coating Zn composite anode at 1 mA cm^{-2} with capacity of 0.1 mA h cm^{-2} anode for 100 cycles; only the deposited Zn metal appears under the CMC layer.

Next, the effect of the CMC layer on the behavior of Zn plating/stripping was evaluated via long-term galvanostatic cycling of the Zn composites. In Fig.3.4a, under a gentle current density and areal capacity (1 mA cm^{-2} and 0.1 mAh cm^{-2}, 2000 cycling), the A253//A253 symmetrical cells showed outstanding cycling stability, displaying a stable voltage trend up to 2000 cycles (more than 200 h). In Fig.3.4b-d, it is seen that a small voltage hysteresis of 25 mV was attained and increased slightly, indicating a highly stable CMC layer at 3.5% of Mw.250,000 on the bare Zn composite anode. In Fig.A8, in contrast, the bare Zn composite//Zn symmetrical cells having other CMC formulas showed a severe increase in overpotential upon long cycling.

To investigate the chemical environment of the Zn^{2+}, X-ray absorption spectroscopy (XAS) was adopted. Two sub-techniques: XANES and EXAFS were implemented (133, 134). In Fig. 3.4e, Zn K-edge XANES results of the symmetrical cells (charged) are shown. The data were analyzed via ATHENA software. It is seen that the shape of the spectrum corresponding to the pristine Zn is slightly different from that corresponding to the Zn anodes associated with carboxyl groups in the CMC and the bare Zn composite anode. The first peaks in the XANES spectra of the pristine Zn and Zn anodes associated with carboxyl groups are listed in Table A4. The change in the XANES spectra indicates the change in the local coordination environment, which was investigated further using EXAFS.

In Fig. 3.4f, the real-space EXAFS spectra of the pristine A253, and the A253 after the 1st and the 100th cycling are plotted together with the Zn foil and Zn acetate standards. The two standards were selected as a representation of the Zn-Zn and the Zn-carboxyl group nearest neighbor. As seen from the figure, the EXAFS spectrum of the pristine A253 showed the first peak at around 2.27 A°, similar to that of the Zn-Zn nearest neighbor of the standard Zn foil whereas the position of the first peak of the A253 after the 100th cycling at around 1.53 A° is similar to that of the Zn-carboxyl group of the Zn acetate. The first peak of the A253 after the 1st cycling showed a combination of the Zn-Zn and the Zn- carboxyl group environments. Such an outcome suggests the increased presence of the bonding between Zn and the carboxyl groups in CMC with the cycling .In Fig. A9, FTIR results show that the peak at 1316 cm^{-1} (-OH bending) has disappeared, Yet, the two peaks at 446 cm^{-1} and 608 cm^{-1} (Z-

O Bonding and -OH bending, respectively) are clearly seen, probably due to the coordination of Zn-carboxyl group in Zinc acetate (105). This observation further confirms that Zn is associated with carboxyl groups in the CMC-molecular in this ASEI-coated Zn electrode.

The morphology of the bare Zn composite anode and A253, after cycling in symmetrical cells (1 mA cm^{-2}, 0.1 mAh cm^{-2}) were studied via SRXTM. In Fig. 3.4e, Zn metal was detected via XTM, demonstrating considerable Zn metal deposition behavior on the electrode matrix. After several cycles, the bare composite electrode had a flat and dense Zn surface. However, Zn deposition covering the electrode surface revealed that further problems could arise during long-term cycling, causing severe shape-change and increasing corrosion of the Zn.
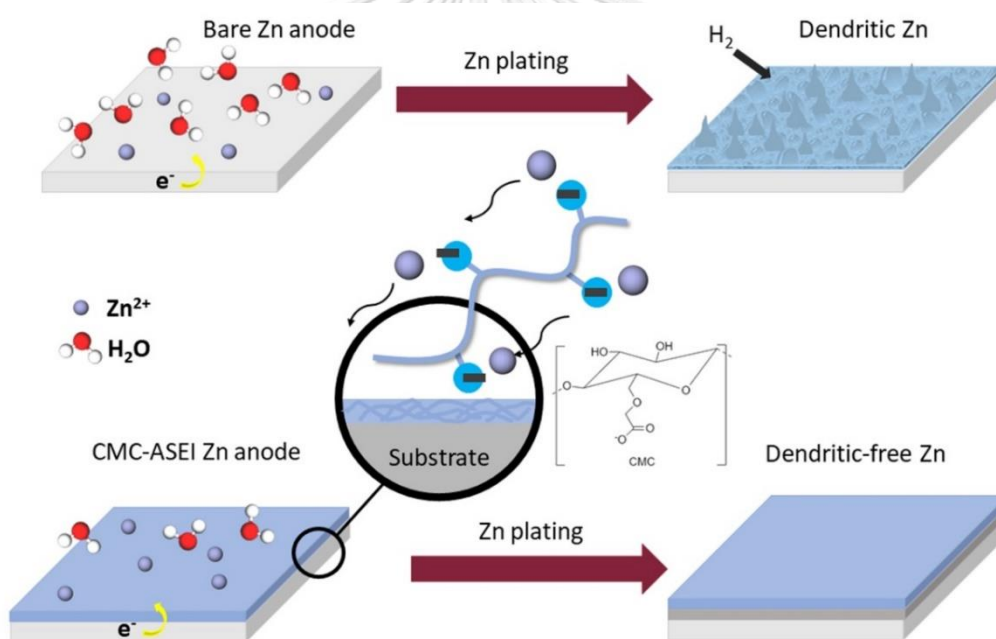
Figure 3. 5 Schema of in-situ Zn plating/stripping behavior for the bare Zn sheet and CMC-SEI Zn composite plate in an aqueous electrolyte.

In Fig. 3.5, it is seen that an electrode without a CMC protective layer led to poor Zn plating/stripping performance. CMC-ASEI serves as a blocking layer to prevent direct contact between the anode/electrolyte and can provide favorable nucleation sites, resulting in uniform local current density and uniform Zn electrodeposition (135). The polymer interphase serves as a buffer layer to retard the

chaotic bulk aqueous electrolyte. Due to its electronic insulator and good ionic condition, the high potential gradient in the CMC layer can facilitate Zn^{2+} diffusion through the CMC interphase. Moreover, the carboxylic-containing group in CMC ensures active sites for the transfer of Zn^{2+}. It is noted that the solvated water and anions from diffusion via CMC can be prevented by having a dense CMC layer. It is evident that the CMC layer can significantly regulate uniform Zn nucleation and alleviate unfavorable side reactions in aqueous electrolytes.
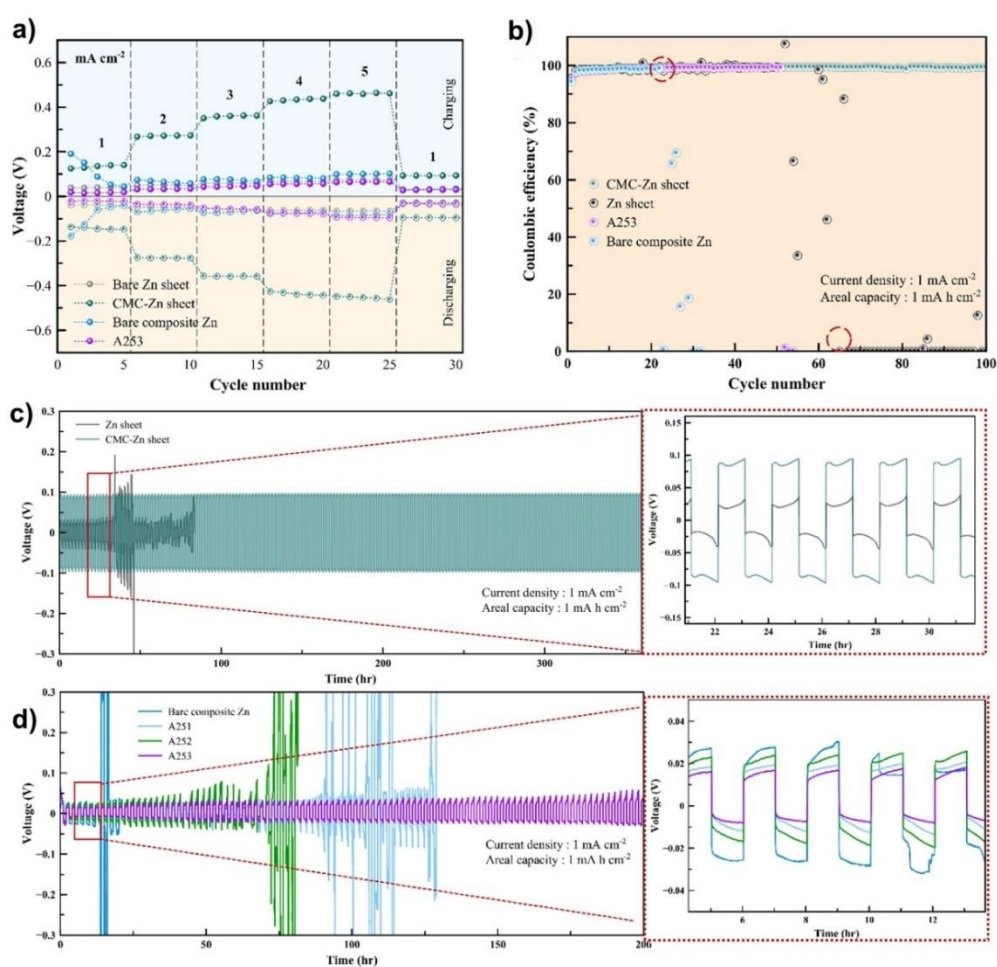
Figure 3. 6 (a) Rate performance of symmetrical cells: 1 to 5 mA cm^{-2} with 1 mA h cm^{-2} of the bare Zn sheet, Zn sheet with CMC layer, bare Zn composite, and A253 anode, (b) Coulombic efficiency of the Zn composite with and without CMC-ASEI and bare Cu foil at 1 mA cm^{-2} of current density with 1 mA h cm^{-2} of capacity, (c) Galvanostatic cycling of the bare Zn sheet and CMC-Zn sheet, at 1 mA cm^{-2} with capacity of 1 mA h cm^{-2}, and (d) Galvanostatic cycling of the bare Zn composite, A251, A252 and A253, at 1 mA cm^{-2} with capacity of 1 mA h cm^{-2}.

To explore the electrode reaction kinetics of the symmetrical cells, at various current densities, rate performance was carried out from 1 to 5 mA cm^{-2} with 1 mAh cm^{-2} (Fig.3.6a and Fig.A10). As observed, the A253 anode presented the smallest voltage hysteresis at different current densities. Similarly, as for A253, the bare Zn sheet, and the bare Zn composite anode exhibited low voltage hysteresis. In contrast, the Zn sheet having CMC layer revealed a high voltage hysteresis. Besides, the reversibility of Zn plating/stripping was studied using asymmetrical Zn//Cu cells. Here, the coating layer was introduced onto the Zn sheet and Zn composite anode assembled with bare Cu foil into Zn//Cu cells. In Fig.3.6b, the Zn sheet with CMC layer delivered ~99% CE for over 100 cycles. The CE of Zn//Cu cells, however, with the bare Zn sheet, A253 and bare Zn composite anode rapidly declined after the 50th and 25th cycle. To understand the feasibility of the CMC-ASEI layer on the Zn electrode, electrochemical measurements were carried out in the symmetrical cells at 1 mA cm^{-2} with capacity 1 mAh cm^{-2} in 1.5 M ZnSO$_4$ solution (Fig. 3.6c-d and Fig.A11).

In Fig. 3.6c, the Zn sheet having 3.5%wt with 250,000 of CMC layer displayed a stable trend of Zn plating/stripping. Although the symmetrical cells based on the Zn/CMC anode revealed a large voltage hysteresis, the protective CMC layer significantly stabilized the Zn anode surface by improving the reversibility of the Zn plating/stripping. After ~34 h, an increased voltage hysteresis and sudden voltage drop took place in the bare Zn sheet-based cell, resulting in the cell exploding due to gas-induced internal pressure. Similarly, in the case of the bare Zn composite anode without a protective layer after ~14 h, a large voltage fluctuation appeared (Fig. 3.6d). Of the CMC layer coatings on the Zn composite anode, the A253 anode (250,000 Mw. of CMC, 3.5 wt.% solution) revealed a more stable voltage profile having a lower voltage hysteresis in comparison with the others (Fig. 3.6d). When the molecular weight and concentration of CMC increased, polarization voltage decreased. Such a reaction occurred since the relatively thin CMC layers suffered from mechanical instability owing to the change in volume during the Zn plating/stripping process. It is noted that the voltage profiles of the symmetrical cells with the CMC layer are substantially much smoother in comparison with the

fabricated electrode without a protective layer and the bare Zn sheet, indicating a more reversible Zn deposition/dissolution process due to the existence of the CMC layer.

Zn deposition involves volume changes between the electrode and the layer interphase. At the same time, the flexibility of CMC molecules can maintain a moderate amount of mechanical robustness. During cycling, the CMC layer remains intact with the supportive architecture of the Zn composite material, having a positive effect on the result. The protective interphase of the polymer-based SEI on the Zn foil/plate is seen to improve the cycling of ZBBs. However, both the weak adhesion and the limited contact area between polymer and Zn current collectors cause gaps associated with the volume changes at the polymer/Zn electrode interface. This issue leads to poor performance or capacity loss specifically at high rates.

Table 3. 1 Electrochemical performance of symmetrical cells: polymer-based SEI on the Zn anodes.

Polymer	Electrode	Current density	Areal capacity	Overpotential	CE	Ref.
Polypyrrole (PPy)	PPy-coated Zn foil	2.0 mA cm^{-2}	1.0 mAh cm^{-2}	~45mV	-	(108)
Polyamide (PA 6)	Polymeric layer using Zn(TfO)$_2$ and PA on Zn foil	0.5 mA cm^{-2}	0.25 mAh cm^{-2}	~100mV	~95 %/~300 cycles @ 0.4 mA cm^{-2} /0.4 mAh cm^{-2}	(22)
Poly (vinyl butyral) (PVB)	PVB-coated Zn foil	0.5 mA cm^{-2}	0.5 mAh cm^{-2}	~108.5-~ 84.5 mV	~ 99 % / 100 cycles @ 4.0 mA cm^{-2}/2.0 mAh cm^{-2}	(23)
Gelatin	Gel-methacrylic anhydride (MA)-Zn (CF$_3$SO$_3$)$_2$ coated on Zn foil	1.0 mA cm^{-2}	1.0 mAh cm^{-2}	> ~200 mV	-	(113)
CMC	CMC-COP on Zn foil	0.25 mA cm^{-2}	0.05 mAh cm^{-2}	~28 mV	~99 % / 490 cycles @ 1.0 mA cm^{-2} / 0.5 mAh cm^{-2}	(114)
CMC	CMC-coated on Zn composite anode (A253)	1.0 mA cm^{-2}	1.0 mAh cm^{-2}	~20.0 mV	~99 % / 1,000 cycles @ 1.0 mA cm^{-2} / 0.1 mAh cm^{-2}	This work
	CMC-coted Zin foil	1.0 mA cm^{-2}	1.0 mAh cm^{-2}	~100 mV	~99%/100 cycles @1.0 mA cm^{-2} /1.0 mAh cm^{-2}	

In Table 3.1, the performance of polymer-based SEI, as previously reported in the literature, is outlined. It is seen that CMC shows high potential for SEI material. Herein, the voltage hysteresis of the anode using CMC-ASEI was lower than other polymers investigated and cyclability was maintained. Over long-term cycling, CMC-ASEI exhibits slightly increased overpotential. In contrast, the overpotential of other systems, as seen when PA6-Zn(TfO)$_2$, PVB, and gelatin were used, proved to be higher. At higher current density, PPy revealed lower overpotential value, followed by increased overpotential. It is known that PPy, as a typical conductive polymer, possesses many mobile electrons in the molecules, which can lead to unrequired reactions and by-products on the electrode upon long cycling.

It is well known that CMC processes numerous hydrophilic hydroxyl and carboxyl groups, providing active sites for the transfer of Zn^{2+} via the high potential gradient in the molecules. The synergic effect of the CMC-covalent organic polymer (COP) is able to protect the electrode surface. Although CMC-COP displays lower voltage polarization than the CMC Zn composite, testing conditions in such works were much gentler compared to others. In terms of Zn deposition, the CE of CMC-ASEI was maintained at 99.0% for over 1,000 cycles while other systems showed more than 95% CE, revealing limited short-term cycling. Consequently, CMC-ASEI coated on a Zn composite anode is a promising electrode, with the ability to form an ASEI layer ex-situ for aqueous Zn-ion battery application. Apart from enhancing the kinetics of Zn deposition/dissolution, the CMC layer also plays a role in modifying Zn nucleation and homogeneous Zn deposition.
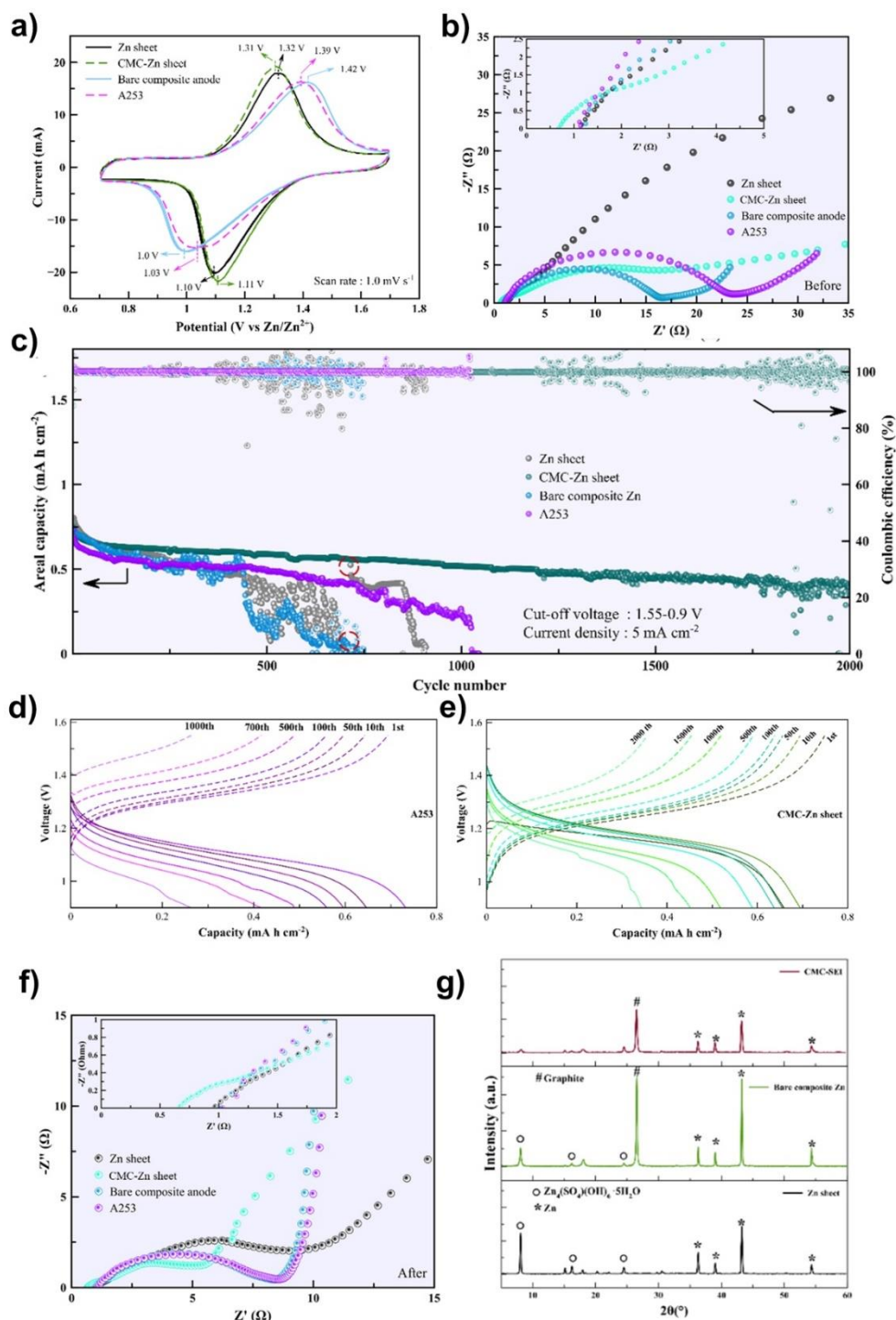
Figure 3. 7 Comparison of electrochemical performance of Zn-polyiodide full cells with bare Zn sheet and Zn composite without/with CMC-ASEI: (a) CV curves at scan rate of 1 mV s^{-1} at 4th cycling, (b) EIS Nyquist plots before CV cycling, (c) Long-term cycling performance at 0.8 mA cm^{-2} after 500 cycles. Galvanostatic charge-discharge profiles of (d) A253 and (e) Zn sheet with CMC layer full cell at 5 mA cm^{-2}. (f) EIS

Nyquist plots after CV cycling, (g) X-ray diffraction of the Zn sheet and fabricated Zn anode after long-term cycling.

Both the efficiency and practical application of the fabricated Zn anode were further evaluated. To evaluate the practical application of the CMC layer on Zn anode, Zn-I_2 full batteries were assembled using a Zn sheet or Zn composite with CMC layer as an electrode, fabricated carbon-iodine cathode, and 1.5 M $ZnSO_4$ electrolyte. Designing of the cathode based on 2D or 3D carbon structure evidently shows excellent reversibility, cycling stability (136, 137). It provides enormous catalytic sites for adsorption of iodine-polyiodide. In Fig. 3.7a, the CV curves of the bare Zn//I_2 cell and CMC-Zn//I_2 cell within the voltage range: 1.7-0.7 V at a scan rate of 1 mV s^{-1} presented distinct redox peaks. Similar CV profiles with a slight peak shift were observed. One pair of cathodic and anodic peaks at ~1.1 and ~1.3 V can be seen in the CV curve of the Zn sheet with/without CMC layer, corresponding to the reversible conversion reaction between ZnI_2 and I_2 (76). Similarly, the bare Zn composite with/without CMC layer displayed a pair of redox peaks at ~1.0 and ~1.4 V. The reduction peak of CMC-Zn and A253 showed a positive shift and higher peak current density for the CMC-Zn//I_2 cell. The improved currents and the positive potential shifts imply faster kinetics for the coated CMC layer anodes.

In Figs. A12-15, the 5 cycle CV curves (1 mV s^{-1}) of the ZIBs for the bare Zn sheet and fabricated anodes are illustrated. In Fig 3.7b, the EIS spectra of full cells were also investigated. The Nyquist plots of the pristine Zn plate reveal low ionic conductivity with larger interface impedances more than that of the others. The cell with the Zn sheet is seen to demonstrate higher charge-transfer resistance after cycling. In contrast, the cell with the CMC layer reveals lower charge-transfer resistance (Fig. 3.7f). The cell with the ASEI layer exhibited a depressed semicircle, indicating the development of a polymer or film layer on the surface of the electrode (138, 139).

Cyclability of the batteries was evaluated at 5 mA cm^{-2} with cut-off voltage 0.9-1.55 V. In Fig. 7e, the Zn//I_2 cell with the bare Zn anode showed continuous capacity decay and stopped running after 700 cycles due to the short-circuit issue. Similarly, the bare Zn composite anode without CMC showed sharp capacity decay.

In contrast, the A253 cycled over 1000 cycles. 2000 cycles were reached via CMC-Zn sheet sample, displaying a steadier cycling trend than others (Fig. 3.7d-e and A16). By-products on the surface of the cycled fabricated Zn anodes were investigated via XRD. In Fig. 7g, strong XRD reflections of $Zn_4(SO_4)(OH)_6 \cdot 5H_2O$ were observed in the bare Zn sheet after 500 plating/stripping cycles. On the other hand, the fabricated Zn anode with CMC as protective layer was rarely detected. The large amount of Zn-containing by-products in the passivation layer reveals the loss of Zn metal during the electrochemical process (128). This attempt to apply CMC as ASEI layer on the modified anode into ZBBs demonstrates its potential to improve the performance, cycling stability and CE of Zn electrode at the same time.

3.4. Conclusion

In this study, it is noted that Zn metal shows poor reversibility of Zn^{2+} deposition in symmetrical cells. To effectively suppress side reactions and uneven Zn^{2+} distribution, a dense and homogeneous CMC-ASEI film was coated on the surface of a Zn composite anode. Benefitting from the abundant negative charge of the CMC-containing functional group, this ASEI polymer exhibited good ionic conductivity. The carboxyl groups in CMC-Na afford a spatially homogenous distribution of Zn^{2+} against the formation of dendrites and reduced side reactions owing to the coordination effect. Subsequently, side reactions were inhibited and the smooth CMC layer on the Zn anode facilitated repeated plating/stripping over 1000 cycles along with low polarization in the symmetrical cells (1 mA cm^{-2} with 0.1 mAh cm^{-2}) much longer than for the bare Zn composite cell. Furthermore, the Zn-CMC anode delivered a lifespan of 300 h and high CE: ~ 99% (1 mA cm^{-2} with 1 mAh cm^{-2}). The assembled Zn-CMC//I$_2$ full cell presented a long lifespan having high-capacity retention more than 98% for 2000 cycles under current density of 5 mA cm^{-2}. It is hoped that this study can be of value to construct a polymer protective layer, breaking ground for the development of a high-performance coating layer for Zn anodes.

Chapter 4
Carboxymethyl cellulose-based polyelectrolyte as cationic exchange membrane for zinc-iodine batteries

Author Name: Phonnapha Tangthuam [1], Jirapha Pimoei [1], Ahmad Azmin Mohamad [2], Falko Mahlendorf [3], Anongnat Somwangthanaroj[1] and Soorathep Kheawhom [1,4,*]

Affiliation(s):

[1]Department of Chemical Engineering, Faculty of Engineering, Chulalongkorn University, Bangkok 10330, Thailand; 6273034821@student.chula.ac.th (P.T.); 6170127321@student.chula.ac.th (J.P.); anongnat.s@chula.ac.th (A.S.)

[2]School of Materials and Mineral Resources Engineering, Universiti of Sains Malaysia, Nibong Tebal 14300, Malaysia; aam@usm.my (A.A.M)

[3]Department of Energy Technology, University Duisburg-Essen, Duisburg 47057, Germany; falko.mahlendorf@uni-due.de (F.M.)

[4]Research Unit of Advanced Materials for Energy Storage, Chulalongkorn University, Bangkok 10330, Thailand

*Correspondence: soorathep.k@chula.ac.th (S.K.)

This research paper is a part of dissertation publication for graduation and is already published in the journal 'Heliyon (2020)', Volume 6, Article e05391. The publication also includes supplementary material which can be found at : Carboxymethyl cellulose-based polyelectrolyte as cationic exchange membrane for zinc-iodine batteries - ScienceDirect and is also provided in Appendix B of this thesis.

Abstract

The aim of this research is an evaluation of polyelectrolytes. In the application of zinc-iodine batteries (ZIBs), polyelectrolytes have high stability, good cationic exchange properties and high ionic conductivity. Polyelectrolytes are also cost-effective. Important component of ZIBs are cation exchange membranes (CEMs). CEMs prevent the crossover of iodine and polyiodide from zinc (Zn) electrodes. However, available CEMs are costly and have limited ionic conductivity at room temperature. CEMs are low-cost, have high stability and good cationic exchange properties. Herein, polyelectrolyte membranes prepared from carboxymethyl cellulose (CMC) and polyvinyl alcohol (PVA) are examined. It is seen that an increase in the ratio of PVA leads to enhanced ionic conductivity as well as increased iodine and polyiodide crossover. ZIBs using polyelectrolytes having 75:25 wt.% CMC/PVA and 50:50 wt.% CMC/PVA show decent performance and cycling stability. Due to their low-cost and other salient features, CMC/PVA polyelectrolytes prove they have the capacity for use as cation exchange separators in ZIBs.

Keywords: Chemical engineering, Energy, Materials science, Chemical energy storage, Electrochemical energy engineering, Energy storage technology, Polymers, Electrochemistry, Zinc-iodine battery, Polyiodide crossover, Ionic conductivity, Cationic exchange, Anionic polyelectrolyte

4.1 Introduction

Owing to an excess of carbon dioxide (CO_2) in the atmosphere, global environmental issues are becoming progressively stringent (140-142). The use of renewable energy sources, therefore, such as solar and wind, are rapidly developing. Renewable energy sources are very intermittent and highly erratic; stabilizing electricity production is becoming demanding (143-145). Effective stabilization in electricity production and utilization can be fulfilled using rechargeable batteries. The demand for large-scale battery systems has increased dramatically. Rechargeable batteries having a large capacity, reliable safety and cost effectiveness are preferred (146-148).

As their capacity depends on their power, traditional enclosed batteries are seen to have limited potential. Flow batteries, however, can store active material on the outside and can independently scale up the power and capacity of the system (149). For this reason, flow batteries demonstrate significant advantages over other types of batteries. Existing flow batteries, however, are based on vanadium (V), which is toxic and costly. Therefore, the development of flow batteries that are cheap and eco-friendly is of vital importance (150, 151).

Nowadays, due to their low-cost, high stability and eco-friendliness, Zn-based aqueous flow batteries are much in demand (152-155). Among various Zn-based redox chemistries, the iodide/iodine (I^-/I_2) redox couple show the most promise and excellent electrochemical performance. The abundance of iodine in ocean water (50-60 mg/l) meets the need for sustainable energy (156). ZIBs exhibit much higher volumetric energy density than other flow battery systems (157). In Fig. 4.1a, a schematic diagram of a ZIB is shown. ZIBs use iodine solution as an active catholyte and a porous carbon electrode as the cathode. Previous studies suggest that a CEM separator is pivotal in determining the performance of ZIBs (87, 158). As shown in Fig. 4.1b., a CEM separator facilitates the transfer of Zn ions across cells while preventing the crossover of iodine and polyiodide.
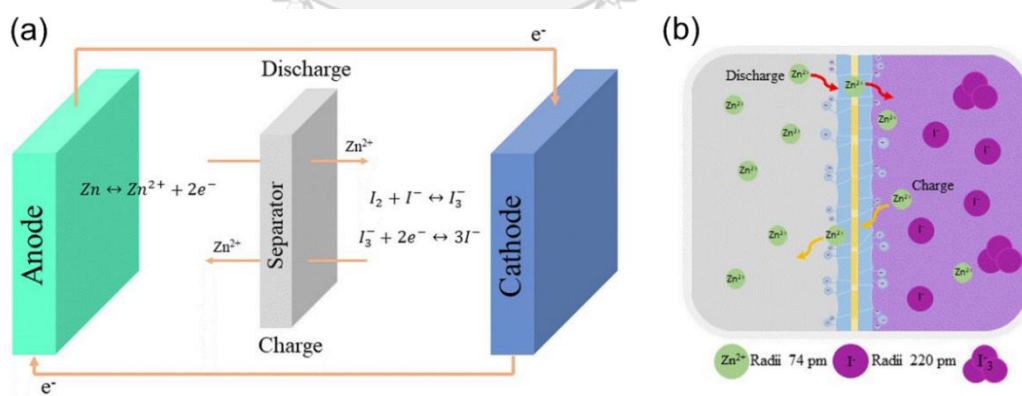
Figure 4. 1 Schematic diagram and functions of CEM separator in ZIBs: (a) Schematic diagram of ZIBs and (b) Functions of CEM separator in ZIBs

One of the most significant obstacles limiting ZIBs from achieving their expected performance is the very high cost of commercial CEMs (78, 87). Subsequently, developments are duly being carried out to produce alternative low-

cost CEMs, having excellent chemical resistance, good mechanical stability, and decent ionic conductivity (159). Anionic polyelectrolytes, which are capable of cation exchange, are favorable alternatives to costly CEMs.

Of the various types of anionic polyelectrolytes, CMCs exhibit great promise due to their biocompatibility, low-cost, and good film-forming ability (119). A CMC molecule contains fixed negative charge carriers and mobile positive charge carriers (160, 161). A CMC molecule can also form a complex with some salts, resulting in the enhancement of ionic conductivity (162). CMCs have been applied in various applications such as superabsorbent hydrogel skin-protection and biopolymer electrolytes (163, 164). Mechanical properties of CMCs can be improved by blending with other polymers. PVA is an interesting polymer for blending with CMCs due to its prominent advantage of a physical crosslinking between hydroxyl groups (163, 165). However, studies on the application of CMCs and PVA polyelectrolytes in ZIBs have not been properly addressed. The cation exchange property of CMC for use as a low-cost separator in ZIBs and other batteries shows promise.

A Zn-iodine flow battery (ZIFB) was first demonstrated by the PNNL National Laboratory at Northwestern University (166). The ZIFB exhibited excellent performance delivering a volumetric energy density of 167 Wh/l, which is close to the energy density of common lithium-ion batteries (LIBs). Weng et al. (87) reported another ZIFB system using bromide ions as a complexing agent to stabilize free iodine in the electrolyte, improving energy density even more. ZIFBs, however, are still limited on account of their short cycle life ($<$ 50 cycles), low current density ($<$ 10 mA cm^{-2}), and relatively high cost, resulting from the costly Nafion membrane (500-700 \$ m^{-2}). Both the low conductivity of electrolytes and the low ionic conductivity of the Nafion membrane, in a neutral electrolyte, can lead to low discharge current densities of ZIFBs (167).

In this work, rechargeable ZIBs using polyelectrolyte membrane separators, having different ratios of CMC/PVA, are investigated. Graphite felt, having a highly porous architecture, is used as the positive electrode. As for the negative electrode, Zn electrodeposited on graphite felt is employed. Results highlight the capability of CMC/PVA polyelectrolytes for use as CEM separators in ZIBs. The effects of the ratios of CMC/PVA on performance of ZIB are studied.

4.2 Material

Analytical grade PVA (Mw 117, Chem-Supply Pty Ltd, Gillman, SA, Australia) and CMC (Mw 250,000, Sigma-Aldrich, St. Louis, MO, USA) were used to prepare the polyelectrolyte membranes. Iodine (I_2) and potassium iodide (KI, 99.0%) used for the catholyte were purchased from Univar (Shanghai, China). Graphite felt (AvCarb G200, AvCarb Material Solutions, Lowell, MA, USA.) was employed for both negative and positive electrodes. Zinc sheet (99.9% purity, Shandong AME Energy Co., Ltd., Shenzhen, China) and zinc sulfate ($ZnSO_4 \cdot 7H_2O$, Kemaus, New South Wales, WA, Australia) were used for the electroplating process to prepare the negative electrode. Nylon membrane filter (0.1 µm) was purchased from Sterlitech Corporation (Kent, WA, USA). 100 mesh of woven wire 304 stainless steel, purchased from Alikafeii Trading Co., Ltd. (China), was used as the current collector.

4.3 Battery fabrication

To fabricate the negative electrode, graphite felt was cut into pieces 1×1 cm^2 in dimension. Zn was electroplated on graphite felt using a Zn sheet (counter electrode) and a Zn sulfate solution (2 M) under a current density of 50 mA/cm^2, for a duration of 1 h. As for the positive electrode, the graphite felt was cut into pieces 1×1 cm^2 in dimension and used, as is, without any treatment.

Polyelectrolyte membranes were synthesized by a casting process using solutions of CMC and PVA having different ratios. The weight ratios of CMC:PVA in the polymer electrolyte membrane used in this study were as follows: 25:75, 50:50 and 75:25 and were denoted as C25, C50 and C75. First, the solution having different ratios was prepared by dissolving CMC (1.25, 2.5 and 3.75 g) in 95 ml distilled water. Then, PVA (3.75, 2.5 and 1.25 g) was added to the solution. The solution was further stirred for 1 h at 60 °C. After that, 1 M Zn sulfate (100 ml) was gradually dripped into the solution while the solution was continuously stirred, using a homogenizer (10,000 rpm). After that, the mixture was de-gassed using an ultrasonic sonicator for 2 min. The mixture (10 ml) was cast into a glass Petri dish where nylon membrane was used as a supportive structure. The sample was dried naturally at 27 °C for 36 h. A

schematic diagram of the polymer electrolyte membrane is shown, as in Fig. B1a. The thickness of the membrane was controlled by the volume of polymer solution in the Petri dish. The average thickness of the polyelectrolytes was 1 mm.

Fig. B1b shows a schematic diagram of the testing cell. The cell consists of an anode, a polymer electrolyte membrane, and a cathode. The anode and cathode are attached to both sides of the electrolyte membrane. Strips of stainless-steel mesh (1×10 cm^2) were used as current collectors for both the anode and cathode. The anolyte contained 15 ml of 1 M Zn sulfate. A mild acidic aqueous electrolyte based on Zn sulfate supports highly reversible Zn deposition/dissolution behavior on the negative electrode anode. The catholyte contained 15 ml of 0.5 N iodine solution (1:1 molar ratio between I_2 and KI). In an aqueous solution, the increase in solubility of iodine is due to the formation of triiodide ions.

4.4 Characterization

Both, the CMC/PVA interaction and the stability of the polyelectrolyte membranes were investigated via FTIR, PerkinElmer Spectrum One (PerkinElmer Inc., Waltham, MA, USA.), in transmission mode in the range of wave numbers: 400-4000 cm^{-1}. Surface morphological analysis of the membrane was studied using scanning electron microscope (SEM), JEOL (Peabody, MA, USA) JSM-6480LV, 15 kV. Iodine and polyiodide crossover were investigated via titration using thiosulfate solution and starch indicator (1 g starch in 100 ml of water).

Electrochemical performance was studied via Versa STATE 3A (Ametek Inc., Berwyn, PA, USA) in the frequency range: 0.1 - 200,000 Hz at ambient temperature for conductivity measurement. Galvanostatic charge-discharge cycling tests were carried out using Battery Tester CT-4008-5V20mA, Neware Technology Ltd. (Shenzhen, China). The discharge voltage-current polarization characteristics of the batteries were investigated in the range of current density: 5 - 50 mA/cm^2. Cycling capability was examined at a constant current density of 10 mA/cm^2 and charge-discharge capacity of 0.1 mAh.

4.5 Results and discussion

The structures of CMC and PVA were investigated via Fourier Transform Infrared Spectroscopy (FTIR). In Figs. 4.2a and 4.2b, the FTIR spectra of CMC and PVA are presented. At 1065 cm^{-1}, 1326 cm^{-1}, 1417 cm^{-1}, 1603 cm^{-1} and 3442 cm^{-1}, corresponding to C-O-C bonding, O-H bonding, -CH_2 scissoring, COO- asymmetric and -OH stretching, the absorption bands of CMC can be seen. These results were found to be in good agreement with those reported by Saadiah et al., confirming the presence of cellulose and carboxymethyl groups which are the backbone of CMC (119). At 849 cm^{-1}, 1093 cm^{-1}, 1376 cm^{-1} and 3326 cm^{-1}, corresponding to C-C bonding, C-O stretching, C-H wagging, and -OH stretching, the absorption bands of PVA can be observed. In addition, the absorption bands in the range: 1065 - 1376 cm^{-1} represent the vibration of the carbon skeletal of the cellulose backbone structure (168).

According to Riaz and Ashraf (169), the mechanical properties of a polymer blend are directly related to the molecular chain between the constituent polymers and their miscibility, in which interaction between the functional groups in the polymer blend could be observed via FTIR. The properties of a homogeneous blend are often an arithmetical average of the properties of each component whilst the miscibility of the components is usually caused by the formation of hydrogen bonds. The common complexation between CMC and PVA is through hydrogen bonding. Hydrogen bonding is an important factor which affects the crystalline nature of the polymer (170).

As shown in Fig. 4.2b, the absorption bands in the region of 3400 cm^{-1} represent all types of hydrogen bonds (-OH groups). Meanwhile, the peaks shifted their position due to the process of complexation. In the CMC-PVA blend, the peaks of the pure CMC: 1065 cm^{-1}, 1326 cm^{-1}, 1417 cm^{-1} and 1603 cm^{-1} shifted position slightly as follows: 1059 cm^{-1}, 1314 cm^{-1}, 1413 cm^{-1} and 1619 cm^{-1}. In addition, the peaks of the pure PVA: 849 cm^{-1}, 1093 cm^{-1} and 1376 cm^{-1} also shifted position slightly: 849 cm^{-1}, 1106 cm^{-1} and 1382 cm^{-1}.
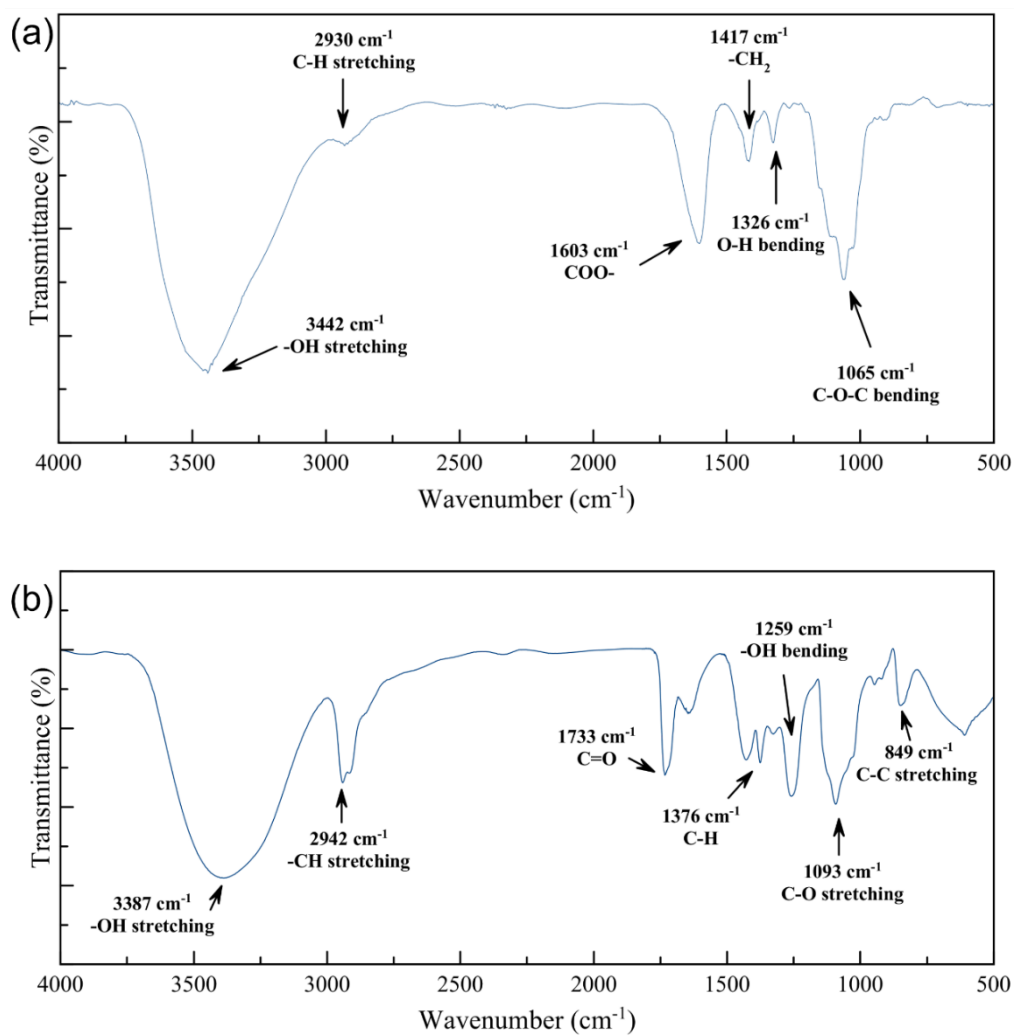
Figure 4. 2 FTIR spectra of (a) Pure CMC and (b) Pure PVA

As illustrated in Figs. 4.3a and 4.3b, the new shoulder of absorption regions appear at 849 cm^{-1} and 1714 cm^{-1} in C25. These regions represent C-C of PVA. When CMC was added, the intensities of the absorption peaks of PVA i.e. 849 cm^{-1}, 1382 cm^{-1}, 1714 cm^{-1} and 2942 cm^{-1} decreased. Some peaks, however, disappeared such as the pure CMC peak at 2930 cm^{-1} (C-H) and the pure PVA peak at 1259 cm^{-1} (-OH). Shin et al. (164) reported that the FTIR spectra of PVA/CS (chitosan) polymer blend at 1255 cm^{-1} disappeared (-OH of pure PVA) and that hydrogen bonds formed between PVA and CS.
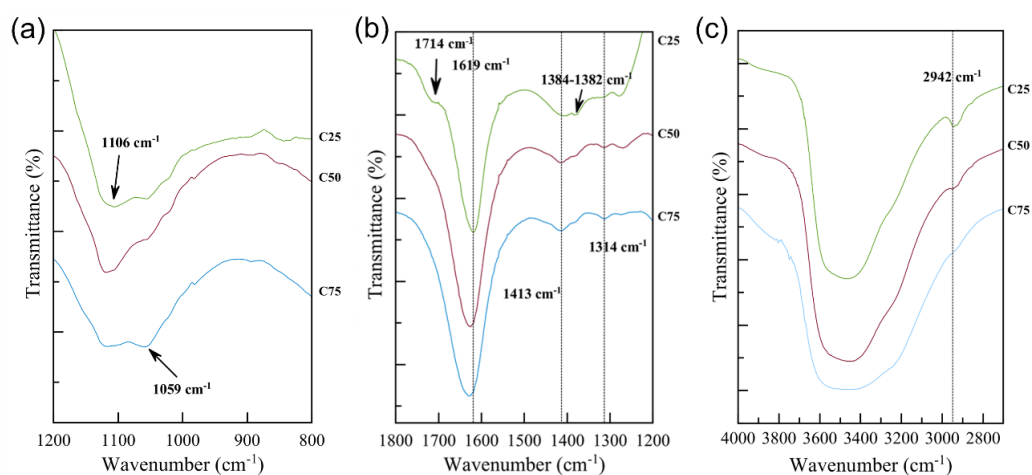
Figure 4. 3 FTIR spectra for CMC/PVA polyelectrolytes in wavenumbers of: (a) 800-1200 cm^{-1} (b) 1200-1800 cm^{-1} and (c) 2800-4000 cm^{-1}

In Fig. 4.3a, the interaction between CMC and PVA molecules is presented. At wavenumbers 1059 cm^{-1} to 1106 cm^{-1}, a band appeared which is attributed to ether linkage (C-O-C), consisting of an oxygen site that could form intermolecular hydrogen bonding with other molecules. In Fig. 4.3b, the peaks in the region between 1314-1619 cm^{-1} can be seen to correspond to the carboxylate and hydroxyl groups where the intensity of both peaks increased, as the ratio of CMC increased. Intermolecular hydrogen bonding for the CMC/PVA system occurs at the region assigned to the bonding of -OH and -COO functional groups for the complexation (119). In Fig. 4.3c, it was noted that the addition of CMC led to the formation of hydrogen bonds of the hydroxyl groups, as crosslinking increased; thus, the absorption bands in the region 3200-3500 cm^{-1} were seen to get wider (164). Besides, at 2942 cm^{-1}, a small peak is seen which represents -CH stretching. Consequently,

C75 showed significant changes because the highest interaction occurred between CMC and PVA.

As shown in Fig. 4.4, SEM images of the surface morphology of the polyelectrolyte membranes are shown. It can be observed that the surfaces of the images C25, C50 and C75 are not smooth, and each structure is very flaky. Apparently, the polyelectrolyte membranes, having a higher ratio of CMC, exhibit a flaky structure and smaller sized pores. The more compact morphology and lesser pore structure act as a barrier to water diffusion (171). In comparison, C25 had larger pores and a less compact structure.
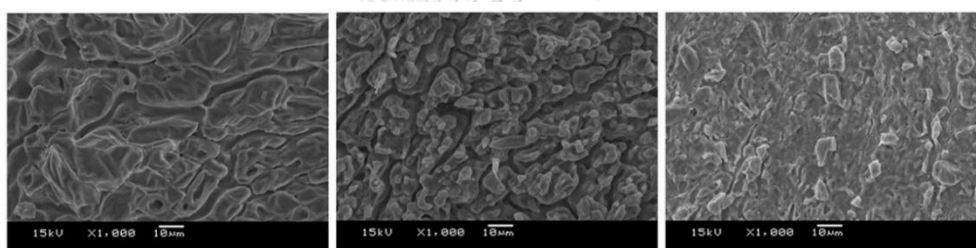
Figure 4. 4 SEM images of C25, C50 and C75 (from left to right)

The ionic conductivity of each polyelectrolyte membrane was determined via EIS (172). In Fig. 4.5a, the ionic conductivity of the membrane as a function of CMC ratio is shown. It is noted that the ionic conductivity of C25 was higher than the others. In contrast, C75 exhibited the lowest ionic conductivity. The ionic conductivities of C25, C50, and C75 are as follows: 119.8 mS/cm^2, 93.5 mS/cm^2, and 48.7 mS/cm^2, respectively. In Fig. 4.5b, the trend of iodine and polyiodide crossover of each membrane is presented. It was found that the iodine and polyiodide crossover exhibited a similar trend to the ionic conductivity. C75 demonstrated the lowest iodine and polyiodide crossover, indicating the highest iodine blocking effect.
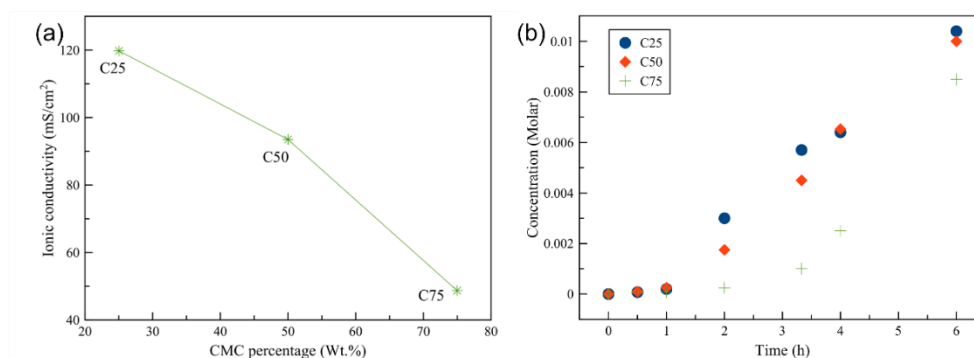
Figure 4. 5 Ionic conductivity and iodine and polyiodide crossover of different polyelectrolyte membranes: (a) Ionic conductivities of C25, C50 and C75 and (b) Iodine and polyiodide crossover of C25, C50 and C75

It is acknowledged that PVA consists of hydroxyl groups that provide hydrogen bonding with CMC and water. These hydroxyl groups of PVA can absorb a large amount of water and hence encourage ionic conductivity (173). In the case of C75, the movement of ions through the membrane was beset by obstacles because the cation-exchange property of CMC only allowed cations to penetrate through the membrane, preventing other species. However, the membrane in all cases could not totally prevent the iodine and polyiodide crossover because iodine molecules could pass through the membrane via different mechanisms (174). During the long-term experiment, the leaking of a small amount of iodine to the anolyte could be observed.

In Fig. 4.6a, the discharge polarization of ZIBs using C25, C50 and C75 is shown. In all cases, the batteries indicated ohmic polarization characteristic, which was dominated by the internal resistance, as contributed by the separator, electrode, and current collector. In determining battery performance, ionic conductivity plays an important role. A battery using a membrane having high ionic conductivity could discharge at a higher voltage. The ionic conductivity of polyelectrolytes strongly affects internal resistance and can determine the performance of the batteries. Although C25 exhibited the highest ionic conductivity as well as the highest battery performance, its poor iodine and polyiodide crossover raised concern about its long-term stability. C25 was excluded, therefore, from the galvanostatic charge-discharge cycling test.
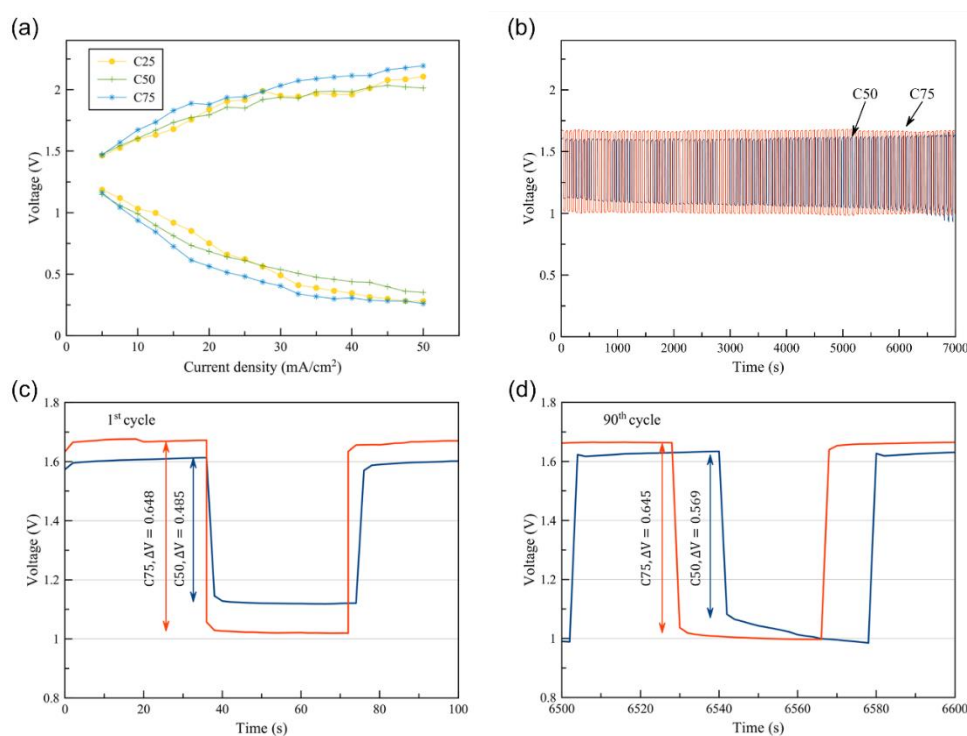
Figure 4. 6 Electrochemical performances of ZIBs using different polyelectrolyte membranes: (a) Polarization of the voltage with respect to the current density 5-50 mA/cm² (b) Galvanostatic cycling test of C50 and C75 battery at current density 10 mA/cm² (c) Galvanostatic cycling test from 0-100 sec and (d) Galvanostatic cycling test from 4900-5000 sec

In Fig. 4.6b, the galvanostatic charge-discharge cycling of ZIBs using C50 and C75 is presented. As shown in Fig. 4.6b, both charge and discharge voltages follow the trend of ionic conductivity. Due to their galvanostatic cycling performance, the C50 and C75 cells provided excellent reversibility; cycle life reached more than 300 cycles. During the long-term cycling, discharge voltage dropped slightly, and charge voltage increased just a little. In Fig. 4.6c, at the 1st cycle, the voltage gap between charge and discharge of the C50 and C75 cells was found to be 0.485 V and 0.648 V, respectively. This voltage gap occurred as a result of the iodine and polyiodide crossover, which increased through time. In Fig. 4.6d, at the 90th cycle, the voltage gap of the C50 cell increased to 0.569 V, exhibiting a 17.32% increase in voltage gap. In contrast, the voltage gap of the C75 cell decreased slightly to 0.645 V, a decrease of 0.46%. Consequently, C75 demonstrated higher stability. The high stability of the C75 cell was due to the smaller iodine and polyiodide crossover during the long-term cycling.

The stability of the C75 membrane was further studied via FTIR. In Fig. 4.7, the spectra for the membrane sample immersed in 0.5 N iodine solution (10 ml), at different periods of time (0-24 h), can be observed. Previous studies on the spectrum band of alkyl halide reported that alkyl halide vibration frequencies appeared in the region 550-850 cm^{-1} (175, 176). Alkyl halides are compounds in which one or more hydrogen atoms have been substituted by halogen atoms. The absorption band at 490-620 cm^{-1} is attributed to halogen compounds viz. C-I stretching (176). Owing to the different electronegativity between the halogen and carbon atoms, the C-halogen bonds were found to be polar. However, in the case of the C-I bond, the electronegativity between carbon and iodine were found to be similar, forming temporary dipoles between carbon and iodine. This outcome led to a weak bond between carbon and iodine atoms. In the polymeric chain, iodine atoms were see to migrate and bond together with different carbon atoms.
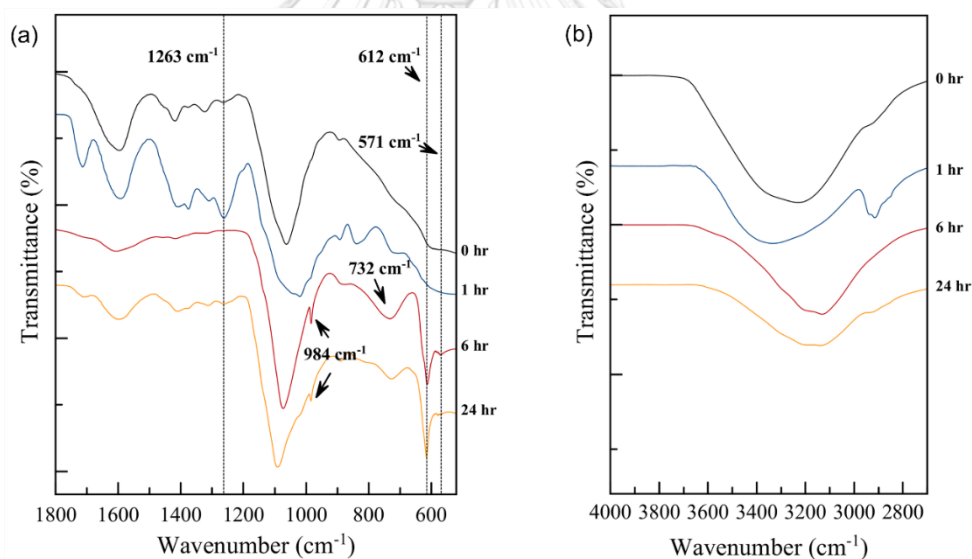
Figure 4. 7 FTIR spectra for the hydrogel membrane immersed in iodine electrolyte in wavenumbers: a) 500-1800 cm^{-1} and b) 2800-4000 cm^{-1}

In Fig. 4.7a, a peak appeared at around 612 cm^{-1} together with another small peak at 571 cm^{-1}, corresponding to the alkyl halide which suddenly developed after the membrane was immersed in iodine longer than 6 h. Results demonstrated that iodo compounds occurred in the system. As for the band region viz. 1150-1300 cm^{-1}, this region corresponded to C-H wagging, in the presence of alkyl halides. Meanwhile, the

spectrum peak at 984 cm^{-1} is attributed to the C-H stretching vibration. The phenomenon of the alkyl halogen relates to the crossover of iodine and polyiodide in the system after the C75 membrane had been immersed in iodine for a long time. Results revealed that the crossover of the iodine and polyiodide was due to the appearance of the alkyl halide in the CMC/PVA polyelectrolyte membrane system.

Zhang et al.(177) reported that a ZIB exhibited a significantly high discharge voltage i.e.1.47V at 10 mA/cm^2, as the anolyte contained alkaline solution. This outcome occurred due to the dissolution of Zn in an alkaline solution, resulting in a more negative potential than in an acidic solution. Nafion 117 was used as separator. However, the use of polyelectrolyte membranes in the system having alkaline anolytes must be examined further. Li et al. (166) reported that the discharge voltage exhibited 1.10V at 10 mA/cm^2 in the ZnI$_2$ electrolyte system and used Nafion 115 as the separator. As observed, the above results differed due to the various parameters used: electrolyte, negative electrode, current collector, separator, and cell configuration. As for the positive electrode, all works used graphite felt. The ZIBs which used CMC/PVA polyelectrolyte membranes exhibited comparable performances: namely, 1.12 discharge voltage (C50) and 1.02 discharge voltage (C75). Hence, the CMC/PVA membranes proved to have a competitive cost advantage. When employed on a large-scale, this cost-benefit can be in their favor. Based on their excellent ionic conductivity and decent stability, CMC/PVA polyelectrolytes can be considered as promising CEM separators for ZIBs.

4.6 Conclusion

This paper investigated the effect of polyelectrolyte membranes, having different ratios of CMC/PVA, for use as CEM separators in ZIBs. It is evident that the polyelectrolyte membranes were found to prevent the crossover of both iodine and polyiodide. Besides, the increase in ratio of CMC in the separator provided greater cationic exchange property. The ionic conductivity of the polyelectrolyte membranes is proportionally related to the ratio of PVA. Nevertheless, the membranes having higher ionic conductivity exhibited higher iodine and polyiodide crossover. Though C25 demonstrated the highest ionic conductivity having 1.12V discharge at 10

mA/cm^2, its high iodine and polyiodide crossover raised concern regarding its long-term stability. The ZIBs using C50 and C75 membranes displayed acceptable charge-discharge performance and good cycling stability. CMC/PVA polyelectrolytes show high potential as low-cost CEM separators for ZIBs. This concept can be extended to other types of battery that require cation exchange properties.

Chapter 5
Unveiling the synergy of pH-buffered electrolytes and CMC in zinc deposition and dissolution for zinc-iodine flow batteries

Preface

This chapter, which is in the final stages of preparation for publication and as yet unpublished, constitutes the concluding portion of an extensive dissertation. It delves into an in-depth examination of Carboxymethyl Cellulose-Coated Carbon Felt (CMC-CF) utilized as an anode material in Zinc-Iodine flow batteries. These batteries have been uniquely modified by the addition of a pH-buffer, a novel approach aimed at augmenting their efficiency and operational stability. This investigation is pivotal in understanding the electrochemical behavior and performance enhancements brought about by this integration in the realm of advanced energy storage systems.

Abstract

This study focuses on improving the performance of Zinc-iodine flow batteries (ZIFBs) through the strategic use of pH-buffering additives to support the anolyte and the implementation of carboxymethyl cellulose (CMC) as an artificial solid-electrolyte interphase (ASEI) on carbon fiber electrodes to facilitate satisfactory zinc (Zn) deposition. Firstly, we introduce ammonium acetate (NH_4OAc) as a self-regulating electrode interface to address two critical challenges: severe Zn dendrite formation and undesirable side reactions. NH_4^+ ions form a dynamic electrostatic shielding layer around Zn protuberances, while OAc^- ions serve as pH buffers, preventing the precipitation of isolable by-products. Consequently, ZIBs with OAc^- ion media exhibit extended cycling stability, achieving approximately 500 cycles at a current density of 40 mA cm^{-2}, with an areal capacity of 20 mAh cm^{-2} and a high Coulombic efficiency of approximately 95%. Secondly, we employ carboxymethyl cellulose (CMC) as an ASEI, applied to a carbon felt substrate. The presence of carboxyl groups in CMC enables precise regulation of Zn ion flux and local concentration on the carbon fiber, ensuring uniform Zn deposition and dissolution. At a current density of 80 mA cm^{-2}, ZIBs with CMC-coated carbon felt electrodes

demonstrate exceptional cycling performance, sustaining up to 600 cycles. This research presents a promising pathway for the practical development of Zn-polyiodide flow batteries with enhanced performance and stability, addressing key challenges in the field.

Keyword: Zn-polyiodide battery, Zn-I_2 flow battery, CMC, solid-electrolyte interface

5.1 Introduction

Zinc hybrid flow batteries (ZHFBs) are increasingly recognized as a formidable choice for large-scale electrochemical energy storage, especially in the context of renewable energy applications. The burgeoning interest in ZHFBs can be attributed to the distinctive attributes of zinc electrodes, notable for their low electrochemical potential, substantial specific capacity, widespread availability in the earth's crust, and cost-efficiency (88, 178). Distinctively, ZHFBs deviate from traditional flow batteries in terms of anode composition. Unlike conventional systems that employ a dissolved active material within the electrolyte, ZHFBs utilize a solid-form active material, with the discharged product being solubilized in the electrolyte. This unique characteristic is pivotal: hybrid-flow batteries are defined by the presence of at least one redox state of an active species in an insoluble form, distinctly setting them apart from standard flow battery architectures. Such a configuration not only impacts the operational mechanisms of these batteries but also bears considerable significance for their design considerations, operational efficiency, and the broad spectrum of potential applications in the domain of energy storage solutions.

Zinc anodes paired with halogen cathodes, such as in bromine and iodine, have emerged as notable contenders in the realm of energy storage (88, 179-183). Among these, iodide stands out as a particularly promising redox-active species for ZHFBs. Its advantages include rapid kinetics, high reversibility, and excellent solubility in both aqueous and nonaqueous media (166, 184, 185). Take, for example, the Zinc-iodine flow battery (ZIFB) system. This system seeks to combine desirable ambipolar and bifunctional characteristics with the benefits of high solubility and environmental sustainability, thereby achieving high energy density. Leveraging the redox chemistry of I^-/I_x^-, ZIFB could theoretically reach an energy density as high as 322 Wh/l, which is the solubility limit of zinc iodide in water (7 M) (166). In a recent

study by Li et al. (166) the focus was on a ZIFB utilizing an ambipolar ZnI_2 electrolyte with a high concentration of 5 M ZnI_2, resulting in an energy density of 167 Wh/l. Within the ZIFB, ZnI_2 is a key player in the battery's operation, which is based on the following electrochemical redox reaction:

Anode: $Zn^{2+} + 2e^- \leftrightarrow Zn$ $\qquad E^0 = -0.762$ V (vs. SHE) (5.1)

Cathode: $2I^- \leftrightarrow I_2 + 2e^-$ (5.2)

$I^- + I_2 \leftrightarrow I_3^-$ (5.3)

$3I^- \leftrightarrow I_3^- + 2e^-$ $\qquad E^0 = +0.536$ V (vs. SHE) (5.4)
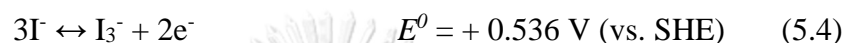
During the charging phase of ZIFB, Zn^{2+} ions are typically reduced to solid zinc metal, a process that can be represented as reversible in Eq. 5.1. Concurrently, iodide ions (I^-) undergo oxidation to form iodine (I_2), as described in Eq. 5.2 during the charge/discharge cycling. A key reaction in the catholyte predominantly involves the conversion between I^- and I_3^-, as depicted in Eq. 5.4. This reaction is favored due to the rapid charge transfer rate of the polyiodide reduction reaction (186, 187). Iodine then forms a soluble polyiodide (I_3^-) complex with free-iodide ions, as illustrated in Eq. 5.3. During discharge, these processes are reversed at their respective electrodes. Importantly, at least a third of the I^- ions are used to form complexes with I_2, preventing iodine precipitation. However, this limits the full utilization of active materials, resulting in a reduced energy density of the battery.

Innovative strategies to maximize the potential of ZIFBs include the addition of bromide ions (Br^-) as a complexing agent. This approach stabilizes I_2 by forming I_2-Br^- complexes, which in turn enhances the battery's capacity (78, 87, 88). Despite these advancements, ZIFBs face challenges in maintaining capacity over prolonged cycles. Key technical hurdles include (i) managing interfacial reactions, (ii) preventing dendritic zinc growth during recharging, (iii) curbing gas evolution from water splitting, and (iv) minimizing parasitic reactions and the formation of undesired products (188, 189).

The primary challenges encountered the ZIFBs are rooted at the electrode/electrolyte interface, particularly concerning the interaction between the Zn

surface and the aqueous electrolyte. A promising strategy to mitigate these issues involves integrating inert cations into the electrolyte. This addition fosters the formation of a positively charged, self-healing electrostatic barrier at the initial stages of Zn dendrite growth, thereby enhancing the integrity of the Zn anode formation. Pioneering research by Jian et al (88), Mousavi et al. (157) and Ge et al. (190) has demonstrated that inorganic NH_4^+ ions can complex with Zn^{2+} ions in a neutral electrolyte, thereby improving the reversibility of the Zn anode while maintaining high ion conductivity.

In a typical aqueous electrolyte, Zn^{2+} ions are surrounded by six water molecules. However, the introduction of ammonia (NH_3) molecules leads to the displacement of these water molecules around the Zn^{2+} ion. This process results in the solvation of Zn^{2+} with the coordinating nitrogen atoms in ammonia, forming $[Zn(NH_3)_4]^{2+}$ (Tetraamminezinc (II) ion) (191). This method not only promotes efficient Zn electrodeposition but also diminishes the kinetics of water splitting at the interface between water and the electrode. Nevertheless, while this approach does make strides in addressing certain issues, it falls short in fully suppressing side reactions and the formation of a passivation layer.

Decreasing the pH of the electrolyte in ZIFBs can inadvertently increase the concentration of protons at the interface, leading to heightened side reactions such as corrosion and hydrogen evolution. Conversely, increasing the electrolyte's pH may escalate the risk of inert by-product precipitation or passivation (192). Consequently, it becomes crucial to maintain the interfacial pH within an optimal range. Developing interfaces that are dynamically stable and possess self-regulating features to concurrently address these issues is an intricate task. Such advancements are relatively nascent in the field of ZIFBs. These complex challenges not only hinder the performance and longevity of these batteries but also affect their potential for commercial viability and widespread application.

In this study, we explore the use of ammonium acetate (NH_4OAc) as a complexing agent to create a self-regulated interface between zinc and the electrolyte in ZIFBs. This novel approach utilizes NH_4OAc for its dual functionality. It acts as a competing cation and serves as a pH buffer, thereby enhancing the stability of the

interface. This dual action significantly reduces side reactions. A key observation is that NH_3 tends to preferentially bind with Zn^{2+} ions rather than water molecules, forming an electrostatic shield at the Zn/electrolyte interface. This shield effectively prevents excessive zinc deposition and reduces water splitting. The addition of the OAc^- buffer elevates the electrolyte's pH to an optimal value of approximately 5.14, which remains stable during battery operation. This stabilization mitigates side reactions and curtails the formation of the passivation layer, as illustrated in Fig. 5.1. Consequently, the Zn anode exhibits enhanced durability, sustaining over 200 cycles at 80 mA cm^{-2}, and maintains a high zinc plating/stripping CE of around 95% in an aqueous zinc iodide (ZnI_2) electrolyte. This improvement is attributed to the synergistic effect of NH_4^+ and OAc^- ions. Furthermore, this modified electrolyte also reduces the formation of by-products on the Zn electrode's surface, suggesting its potential as an effective electrolyte solution for practical ZIFBs.

To further optimize zinc deposition, we incorporated carbon felt as the anode, treated with CMC-ASEI, in the ZIFBs using the ZnI_2 electrolyte enhanced with NH_4OAc. As discussed in Chapter 3, CMC-ASEI plays a crucial role in protecting the Zn anode by reducing polarization and extending the plating/stripping cycle life. The carboxyl groups in CMC-Na are found to coordinate effectively with Zn^{2+}, facilitating rapid ion transport and thus lowering the energy penalty associated with desolvation. This interaction results in a more uniform zinc distribution across the entire carbon fiber surface of the carbon felt facing the membrane, particularly when compared to configurations lacking the CMC layer. Ultimately, employing a CMC-CF anode in a full cell configuration achieves a high-capacity retention of approximately 7.5 mAh cm^{-2} with CE of 77% over 300 cycles.

5.2 Material and chemical

Commercial carbon felt (CF, thickness of 2.5 mm) was used as an electrode (AvCarb Material Solutions). A Nafion 115 membrane (Fuel Cell Earth) was pretreated via a standard acid boiling procedure. Zinc iodide (ZnI_2, purity 98.0 %) was purchased from the Sigma-Aldrich. Potassium bromide (KBr, purity 99.0%) was purchased from the Junsei Chemical. Ammonium bromide (NH_4Br, purity 99.0%) and

Lithium bromide monohydrate (LiBr·H$_2$O, purity 95.0%) were purchased from the Tokyo chemical. Ammonium acetate (NH$_4$OAc, purity 98.0%) was purchased from the Kemaus. All chemicals used in the experiments were of reagent grade and used without further purification.

5.3 Electrode preparation

To obtain the CF electrode, Commercial CF was uniformly cut into a rectangle of 3.5 cm × 3.4 cm, and washed with deionized water. The washed commercial CF was placed in a container containing 20% (w/V) nitric acid in a beaker and soaked for 24 h, and then washed with deionized water to make the pH of the washing solution more than 6.0. Then, the material was put in a drying oven at 70 °C for 24 h and put into dry contain until it was used. For the CMC-CF electrode, the CF electrodes were immersed in 2 %wt of CMC solution (250,000 MW) and then dried at 90 °C for 15 min. The CMC solution was prepared by dissolving CMC in deionized water for 1h at 60 °C.

5.4 Characterization

The morphologies of CF electrodes were carried out via a field emission scanning electron microscope (FE-SEM; Quanta-250 FEG, USA) at an acceleration voltage of 15.0 kV. Energy-dispersive spectroscopy (EDS) was used to confirm the elements over the carbon fiber and electrode surface. The CMC structure on the carbon felt, before and after cycling on the electrode was examined by Fourier-transform infrared spectroscopy (FTIR; PerkinElmer Inc., USA), in the range of wave number: 4000-400 cm^{-1}. X-ray diffraction (XRD) was used to examine the by-product (Malvern PANalytical, AERIS, UK) using Cu Kα radiation. Contract angles (CA; Kruss, DSA 1 MK2, Germany) of the carbon felts were observed. X-ray photoelectron spectroscopy (XPS) was carried out. pH value of the electrolyte was measured via a pH meter (OAKTON pH550, USA). Raman spectroscopy (Thermo Scientific DXR, USA) was used to identify molecules, chemical bonding, and intermolecular bonds in electrolytes.

5.5 Electrochemical measurements

To measure the electrochemical characteristics of electrolytes, a cycling voltammetry (CV) test was conducted using a potentiostat/galvanostat device (Hokuto Denko, Japan) with a conventional three-electrode system. Platinum (Pt) wire electrode and Pt coil auxiliary electrode were used as working electrode and counter electrode, respectively, with Ag/AgCl electrode (0.23 V vs. the standard hydrogen electrode) as reference electrode using a pure 0.1 M ZnI_2 and 0.1M ZnI_2 with 0.05 M of different salt solution as the electrolyte. The electrochemical performances of full cells were fabricated by stacking the end plat, copper current collector, flow field channel (Parallel pattern), silicone gasket, CF electrode, and membrane. The active area of the CE electrode for the battery test was 12 cm^2, and Nafion 115 was applied as the separator. 30 ml of different electrolytes were prepared as both the anolyte and catholyte and stable pumped at 20 rpm (~32 ml min^{-1}) through a peristaltic pump. The battery test was performed by NEWARE BTS-5V6A with a voltage window: of 0.4-1.5 V at a current density of 20 mA cm^{-2}. The long-term performance of the full cell was carried out using a potentiostat/galvanostat-specific capacity under various current densities ranging from 40 and 80 mA cm^{-2}. The coulombic efficiency (CE), voltage efficiency (VE), and energy efficiency (EE) were calculated.
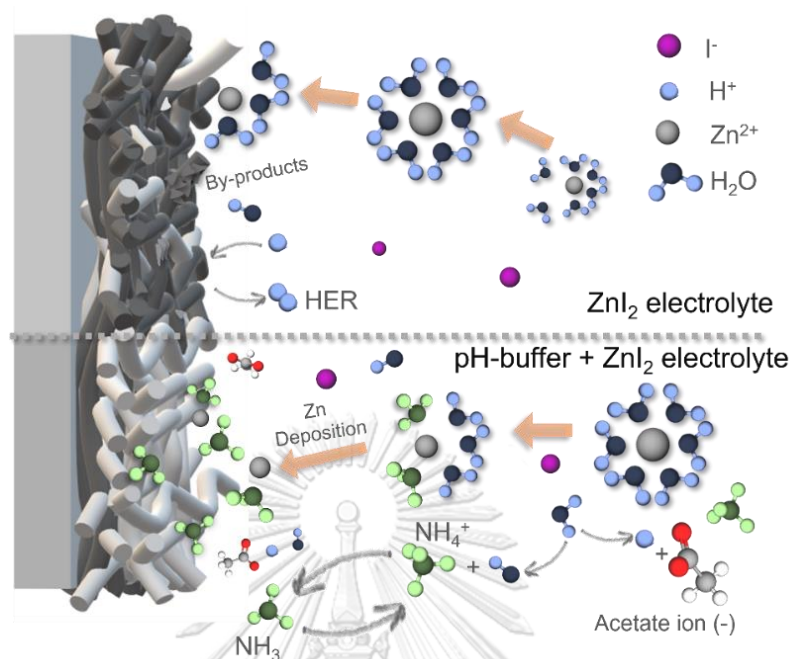
Figure 5. 1 Schematic illustration of in-situ Zn deposition/dissolution behavior for carbon felts in ZnI₂ electrolyte with/without pH-buffer.

5.6 Results and discussions

In our study, to avert iodine precipitation in the aqueous electrolyte, bromide ions (Br⁻) were employed as the complexing agent to form soluble polyiodide species. To evaluate the impact of different cation complexes on electrochemical characteristics, cycling voltammetry tests were performed. These tests probed the effects of various bromide ions in supporting electrolytes on the electrochemical behavior of both Zn/Zn^{2+} and I_3^-/I^- redox reactions, as illustrated in Fig. 5.2 and 5.3.

The findings revealed a significant shift in the Zn^{2+} oxidation onset potential to -0.78 V, -0.62 V, and -0.5 V in the presence of Li^+, NH_4^+, and K^+ ions, respectively, compared to around -0.46 V for the pristine ZnI_2 solution. This shift is indicative of an enhanced reversibility of Zn in the modified electrolytes. Notably, in the ammonium salt additive electrolyte, the Zn stripping peak current was observed to be substantially higher than that in other salt additive electrolytes, suggesting superior reaction kinetics with NH_4^+ ions. In contrast, the Zn stripping peak current in the lithium salt additive electrolyte was lower than in the pristine electrolyte.
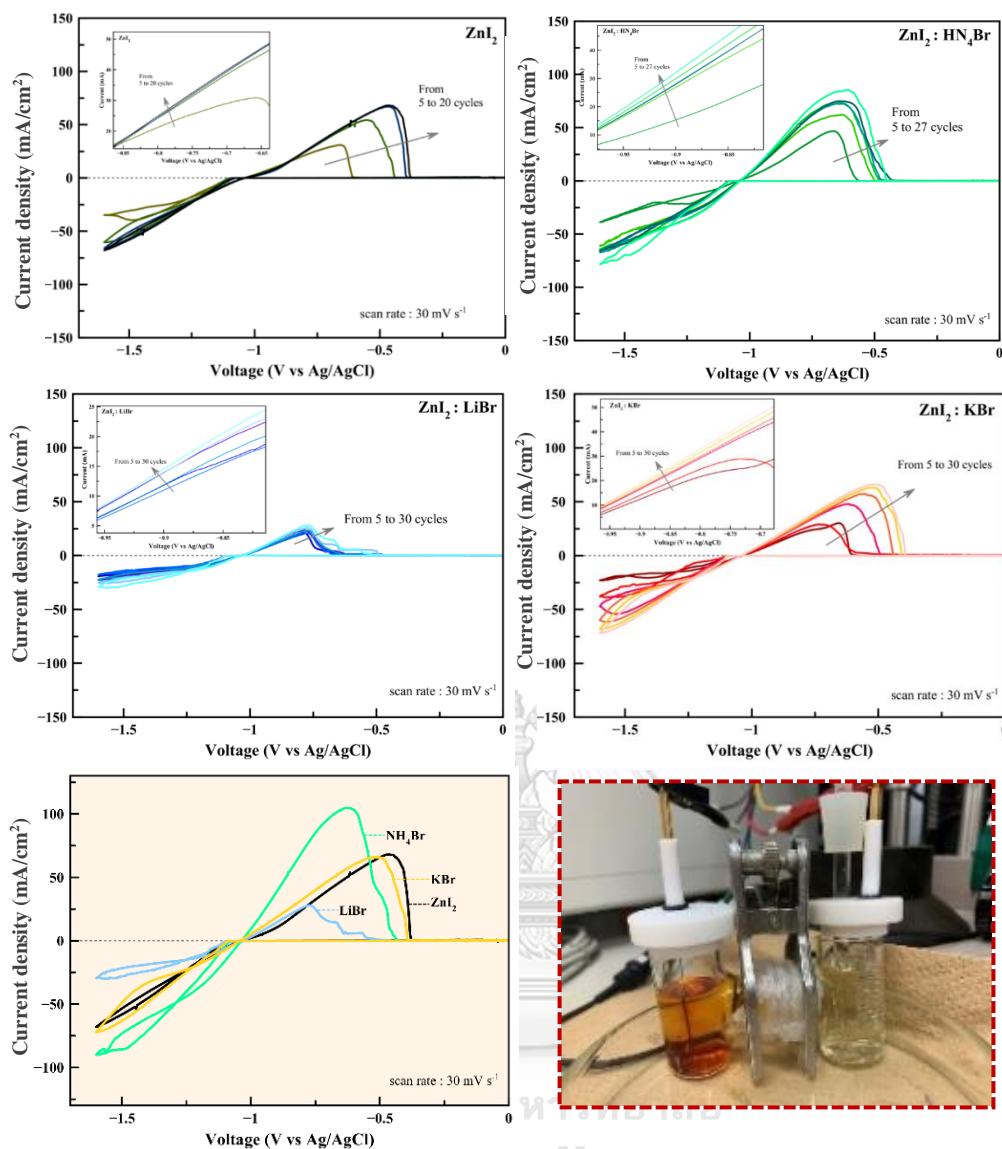
Figure 5. 2 Zn/Zn^{2+} redox reaction on 0.1 M ZnI$_2$, 0.1 M ZnI$_2$: 0.05 M NH$_4$Br, 0.1 M ZnI$_2$: 0.05 M LiBr and 0.1 M ZnI$_2$: 0.05 M KBr electrolyte at scan rates of 30 mV s^{-1}. (Right-Bottom) The inset shows a photo of the three-electrode cell, where a dark brown phase of solid I$_2$ emerges from the Pt electrode.
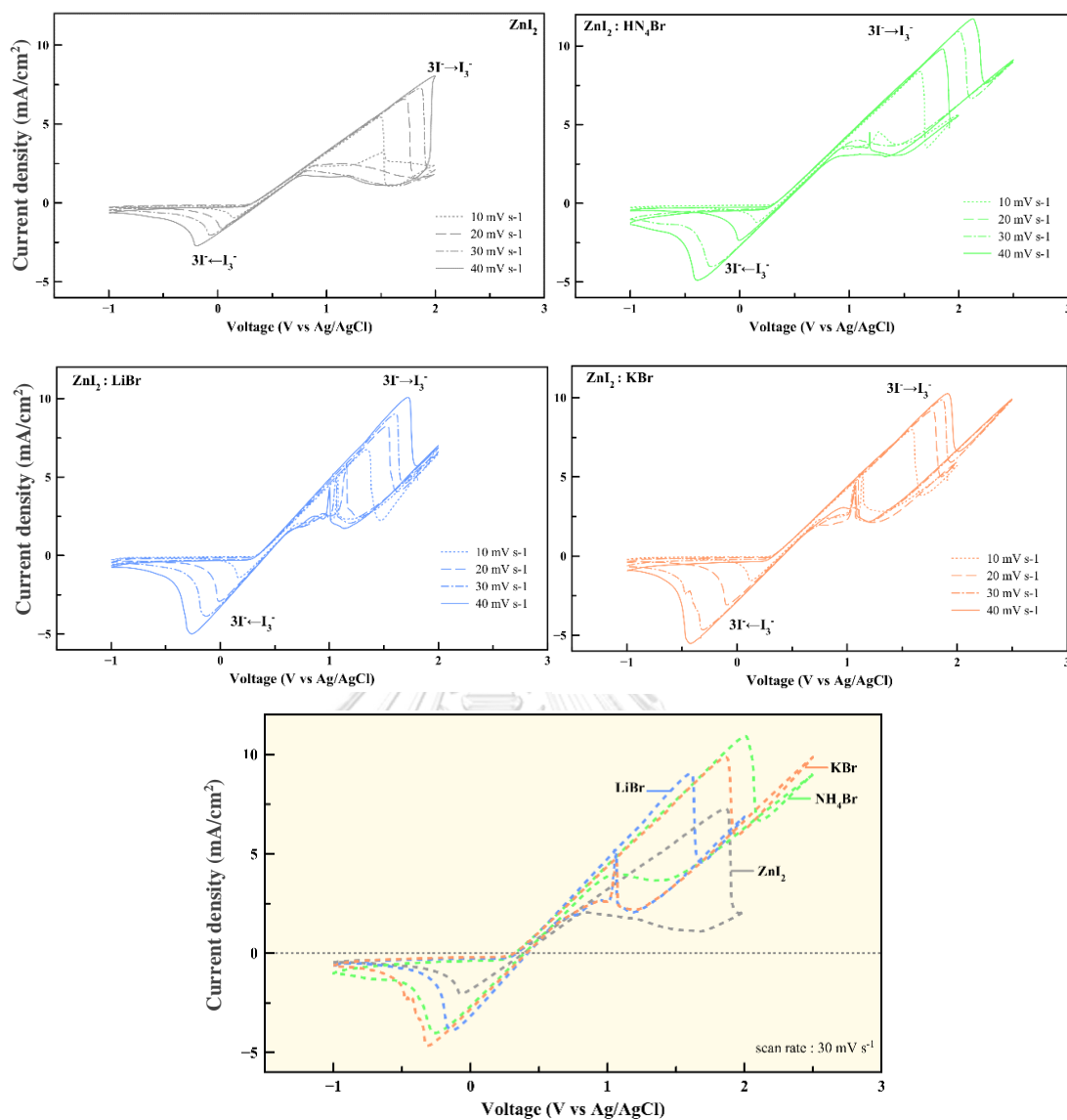
Figure 5. 3 I_3^-/I^- redox reaction on 0.1 M ZnI_2, 0.1 M ZnI_2 : 0.05 M NH_4Br, 0.1 M ZnI_2 : 0.05 M LiBr and 0.1 M ZnI_2 : 0.05 M KBr electrolyte at scan rates of 10-40 mV s^{-1}.

Further insights are provided in Fig. 5.3, which depicts the Cyclic Voltammetry (CV) results of the I_3^-/I^- redox reaction in different bromide ion salt electrolytes. The oxidation peaks in the presence of Br- salt electrolytes shifted positively to 1.6 V and 2.0 V with Li^+ and NH_4^+, respectively. Similarly, the reduction peaks shifted negatively to -0.13 V, -0.28 V, and -0.31 V in the presence of Li^+, NH_4^+, and K^+ ions, correspondingly. Additionally, the presence of Br- ions in the aqueous electrolyte resulted in a higher current peak compared to the pristine electrolyte, denoting an enhancement in the reaction kinetics of the I_3^-/I^- redox reaction.

In Fig. 5.4a, we present the charge-discharge voltage curves for ZIFBs using different supporting electrolytes at a current density of 20 mA cm^{-2}. Remarkably, a battery with a 1 M ZnI_2 electrolyte demonstrates a high charge voltage plateau, surpassing 1.45 V. This value decreases to approximately 1.35 V upon the introduction of 0.5 M NH_4Br. During discharge, the battery containing NH_4Br displays a voltage plateau around 1.22 V, indicating a reduced voltage gap. This reduction is ascribed to the improved conductivity of the electrolyte and the enhanced electrochemical kinetics for both the anodic and cathodic redox reactions.

Furthermore, the discharge capacity of the battery using the unmodified ZnI_2 electrolyte registers at only 8.2 Ah l^{-1}, was calculated based on the catholyte volume (30 ml). However, this capacity experiences a significant boost to 30 Ah l^{-1} with the addition of Br$^-$ ions. This enhancement is due to the complexation between Br$^-$ ions and I_2, which facilitates the release of I$^-$ ions back into the electrolyte. As depicted in Fig. 5.4b-c, the discharge polarization curve and power density curves reveal that the battery with NH_4Br as the electrolyte achieves an impressive high-power density of 72 mW cm^{-2} at a current density of 100 mA cm^{-2}. These observations highlight the profound impact of NH_4Br as a supportive electrolyte in the ZIFBs, primarily through its role in enhancing ionic conductivity and promoting kinetic and reversibility improvements for both the negative and positive redox couples.
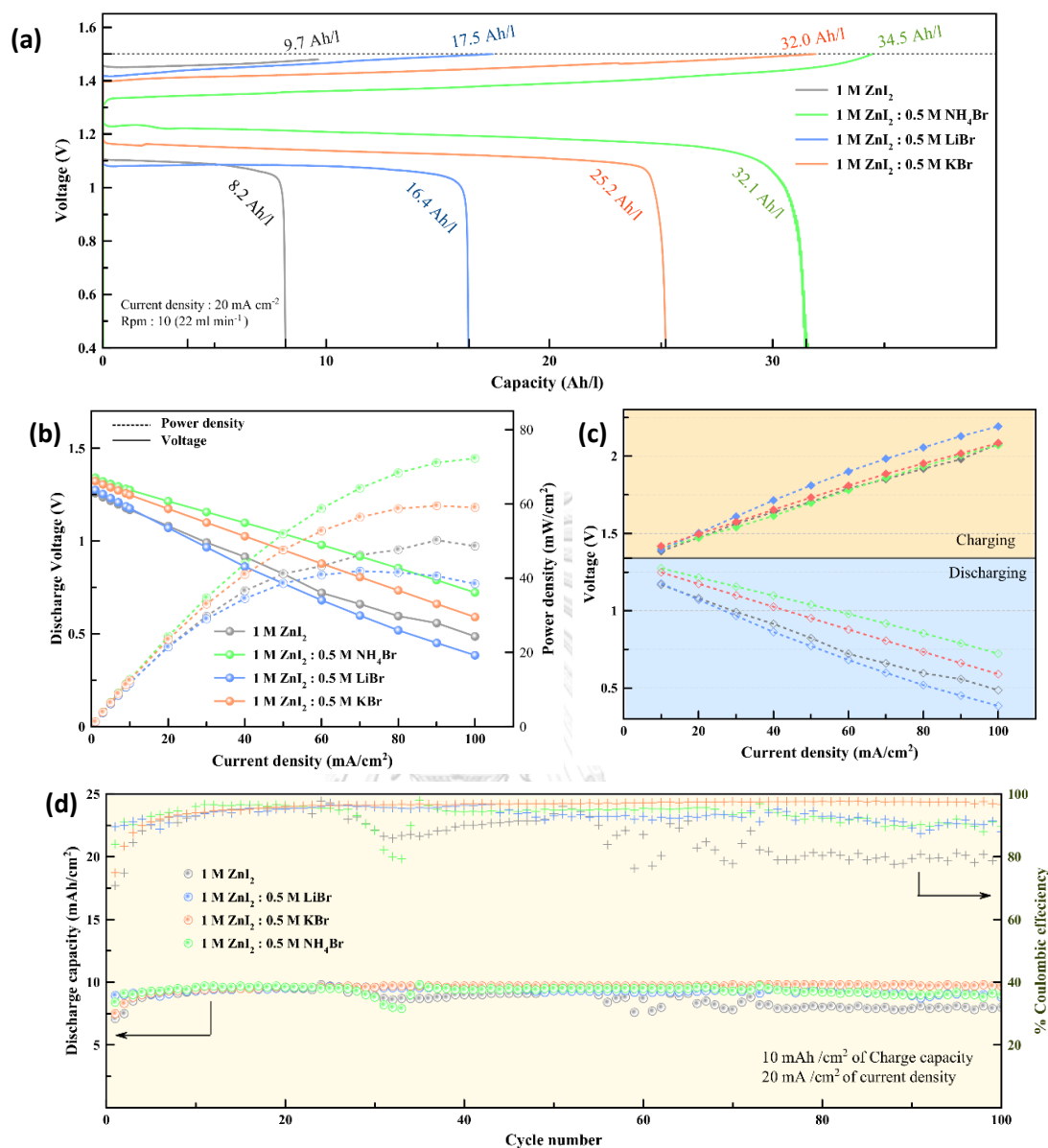
Figure 5. 4 Galvanostatic voltage profiles (a) of the ZIBs with 1 M ZnI₂, 1 M ZnI₂: 0.5 M NH₄Br, 1 M ZnI₂: 0.5 M LiBr and 1 M ZnI₂: 0.5 M KBr electrolyte at current density of 20 mA cm⁻². (b) Discharge polarization curves and calculated power density curves of 1 M ZnI₂, 1 M ZnI₂: 0.5 M NH₄Br, 1 M ZnI₂: 0.5 M LiBr and 1 M ZnI₂: 0.5 M KBr electrolyte at charge voltage 1.5 V. (c) Charging/discharging voltages versus operating current densities of 20-100 mA cm⁻². (d) Discharge capacity and coulombic efficiency (CE) at 10 mA h cm⁻² with 20 mA cm⁻².

Han et al. (193) explored methods to prevent irregular Zn deposition on the electrode surface and found that selecting NH_4^+ as a coordinating cation induces an electrostatic shielding effect on the Zn metal plate. This choice is based on the high binding energy between NH_4^+ ions and the initially deposited Zn metal, measured at -2.10 eV. The cation preferentially adsorbs onto the Zn surface, functioning as an ion distributor. To further mitigate side reactions in the electrolyte, $CH3COO^-$ (OAc^-) anions are introduced into the anolyte. The resulting hydrolysis reaction ($OAc^- + H^+ \leftrightarrow HOAc$) leads to an increase in the bulk electrolyte's pH, reaching values of 4.39 and 4.52 for 0.5 M NH_4OAC and 1 M NH_4OAC, respectively, as shown in Fig. 5.5a. This pH elevation effectively diminishes Zn anode corrosion.

To comprehensively analyze the roles of OAc- and NH_3 ions in the electrolyte, Raman spectroscopy was utilized. As depicted in Fig. 5.5b, both solutions, with and without supportive electrolytes, display three distinct bands at approximately 122, 138, and 164 cm^{-1}. These bands represent the symmetric stretching vibrations of the $[ZnI_4]^{2-}$, $[ZnI_3]^-$, and $[ZnI_2]$ complexes, respectively (194). The introduction of NH_4OAc introduces notable changes in the Raman spectra, including a new band around 940 cm^{-1}, indicative of $Zn(OAc)_2$ formation, likely due to Zn^{2+} coordination with acetate anions. Additionally, peaks at 1350 and 1420 cm-1 appear, corresponding to the antisymmetric C-O stretching mode and the ethyl group in the acetate anion. This observation correlates with a marked decrease in the intensity of the $[ZnI_4]^{2-}$ complex peak, suggesting iodide substitution with acetate in this complex (195). In NH4Br media, the peak associated with the $[Zn(NH_3)_4]^{2+}$ complex shifts to lower energies at 149 cm^{-1}, aligning with the stretching vibrations of four NH_3 groups (Zn-N stretching) (196, 197), while the coordination of Zn^{2+} with acetate anions is absent. In summary, the comparison of Raman spectra between supporting agent-based electrolytes and the pristine electrolyte confirms the coordination interactions between Zn^{2+} ions and the tetrahedrally arranged four ammonia ligands and acetate ions.
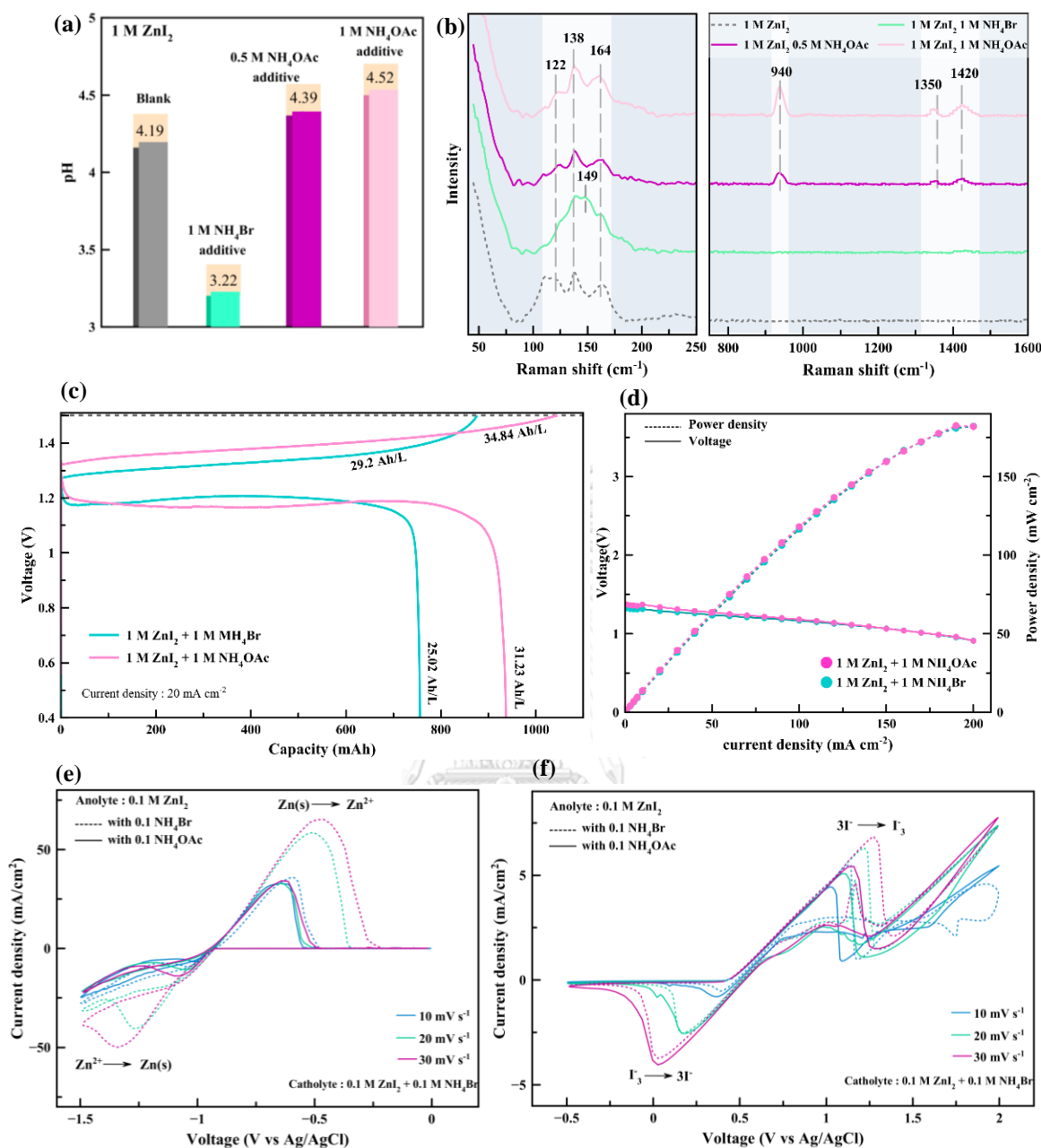
Figure 5. 5 (a) pH of different electrolyte with/without NH₄⁺ additive, (b) Raman spectra of the 1 M ZnI₂ electrolyte with/without NH₄Br additive and NH₄OAc additive. (c) Galvanostatic voltage profiles of the ZIBs with 1 M ZnI₂ + 1 M NH₄Br and 1 M ZnI₂ + 1 M NH₄OAc electrolyte at current density of 20 mA cm⁻². (d) Discharge polarization curves and calculated power density curves of 1 M ZnI₂ + 1 M NH₄Br and1 M ZnI₂ + 1 M NH₄OAc and at charge voltage 1.5 V. Cyclic voltammetry (CV) curve of (e) Zn/Zn²⁺ redox reaction and (f) I₃⁻/I⁻ redox reaction in 0.1 M ZnI₂ + 0.1 M NH₄Br and 0.1 M ZnI₂ + 0.1 M NH₄OAc at a scan rate of 10-30 mV s⁻¹.

In order to evaluate the influence of NH$_4$OAc as a supporting electrolyte on the performance of ZIFs, Fig. 5.5c presents the charge-discharge profiles using different anolytes at a current density of 20 mA cm^{-2}. A notable observation is that the battery utilizing a 1 M NH$_4$OAc electrolyte displays a higher charge voltage plateau, reaching around 1.33 V, compared to the inclusion of 1 M NH$_4$Br, which stabilizes at approximately 1.20 V during discharge, regardless of the supporting electrolyte type.

In terms of discharge capacity, the battery with an NH$_4$Br-enhanced anolyte achieves 25.02 Ah l^{-1}, based on 30 ml of electrolyte. In contrast, the cells incorporating OAc$^-$ ions exhibit a notably higher discharge capacity of 31.23 Ah l^{-1}. The comparative power density and polarization curves for ZIFs with either OAc$^-$ ions or Br$^-$ as supportive ions in the anolyte are showcased in Fig. 5.5d. Interestingly, the battery with NH$_4$OAc electrolyte reaches a high-power density of 182.5 mW cm^{-2} at 190 mA cm^{-2}, paralleling the performance of the NH$_4$Br enhanced battery (182.0 mW cm^{-2}) under similar conditions. Furthermore, as depicted in Fig. 5.6, the introduction of NH$_4$OAc into the anolyte notably narrows the voltage window at current densities ranging from 20-100 mA cm^{-2}.

These findings underscore the significant role of the OAc$^-$ supportive electrolyte in enhancing the Zn/Zn^{2+} redox reaction. This enhancement is achieved by improving ionic conductivity and facilitating the kinetics and reversibility of both the anodic and cathodic redox couples in ZIFBs.

In an effort to understand the influence of NH$_4$OAc as a supporting anolyte on the electrochemical behavior of both Zn/Zn^{2+} and I$_3^-$/I$^-$ redox reactions, we conducted cyclic voltammetry (CV) tests. These tests were performed with OAc$^-$ ions across a scan rate spectrum from 10 to 30 mV s^{-1}. Fig. 5.5e displays the CV curve for the Zn/Zn^{2+} redox reaction in anolytes containing either Br$^-$ or OAc$^-$ ions. The data reveal that Zn metal deposition initially takes place on the surface of the working electrode (a Pt wire electrode) at potentials between -0.92 and -0.94 V (vs Ag/AgCl) at all tested scan rates for both Br$^-$ and OAc$^-$ based anolytes.

During the reverse scan in the anodic peak position, which reflects Zn oxidation at the anode, a marked difference in peak shifting is noted between the

anolytes containing NH₄Br and NH₄OAc, when NH₄Br is employed as the catholyte. The peak corresponding to Zn oxidation is situated around -0.64 V (vs Ag/AgCl) with minimal shifting at a concentration of 0.1 M OAc⁻ ions across various scan rates. Conversely, a more pronounced positive shift is observed in the solution with a mix of 0.1 M Br⁻ and 0.05 M OAc⁻ ions. Furthermore, the gap between the anodic and cathodic peaks significantly narrows with the addition of 0.1 M OAc⁻ ions, indicating an enhancement in the reversibility of Zn plating and stripping processes.

In Fig. 5.5f, the CV curves for the I_3^-/I^- redox reaction in various electrolytes are demonstrated. With the incorporation of NH₄OAc, the oxidation peaks shift to more negative potentials, thereby reducing overpotentials. This shift is beneficial for both the anodic and cathodic redox reactions, signaling a decrease in redox polarization and an improvement in the kinetics of the I_3^-/I^- reaction. These CV results compellingly suggest that incorporating NH₄OAc as a supporting anolyte significantly benefits the electrochemical performance of ZIFBs.
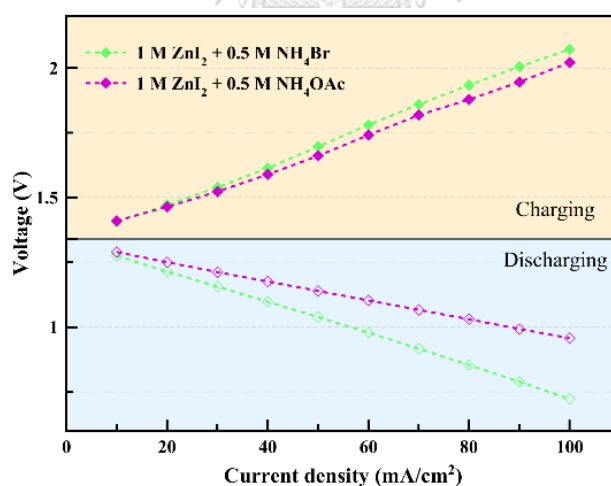
Figure 5. 6 Charging/discharging voltages versus operating current densities of 20-100 mA cm⁻².
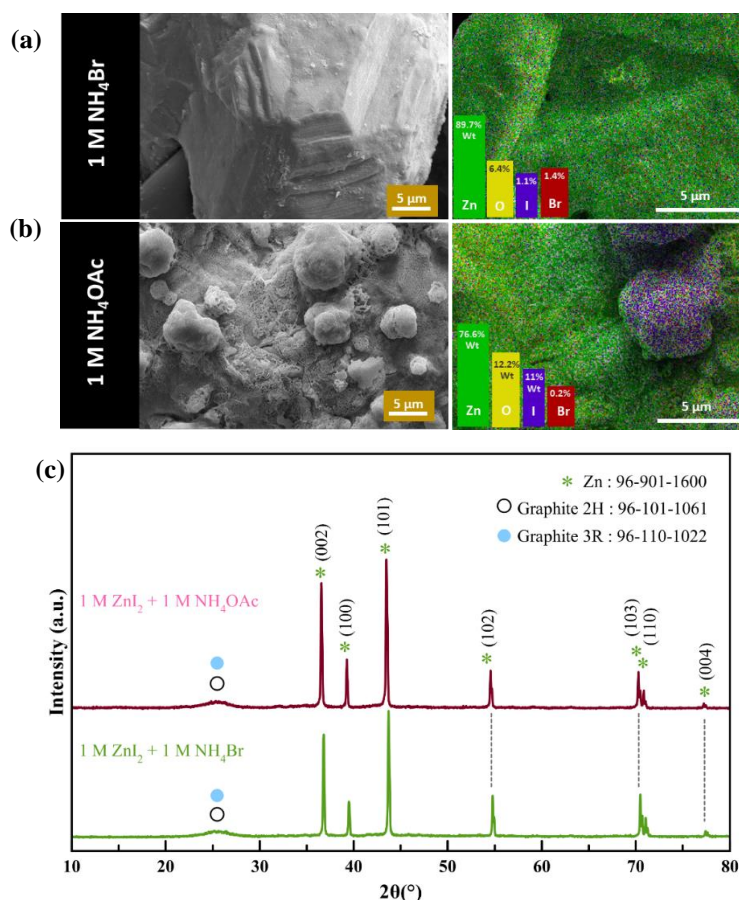
Figure 5. 7 SEM Morphologies and EDX composition for electrodeposited layer on carbon fibers at 20 mA cm⁻² with an aerial capacity of 10 mA h cm⁻² in (a) 1 M ZnI₂ + 1 M NH₄Br and (b) 1 M ZnI₂ + 1 M NH₄OAc. (c) XRD patterns of the Zn deposited in electrolytes with NH₄Br and NH₄OAc.

The notorious issue of zinc dendrite formation presents a significant challenge in the development of ZIFBs, as these dendrites can damage the membrane and cause internal short circuits. This problem is exacerbated at higher current densities, facilitating more rapid dendrite formation within the circulating electrolyte (198). To evaluate the effectiveness of NH₄Br and NH₄OAc in mitigating Zn dendrite formation, we examined FE-SEM images of zinc electrodeposition on carbon felts. These felts were exposed to a current density of 20 mA cm^{-2} and a specific capacity of 10 mA cm^{-2}, in electrolytes containing either NH₄Br or NH₄OAc.

Our observations indicate that in both types of electrolytes, zinc tends to deposit on the side of the carbon felt facing the membrane rather than the side facing the flow field, likely due to the disparity in ionic and electronic conductivity (199).

The FE-SEM images in Fig. 5.7a illustrate that in the Br$^-$ electrolyte, Zn deposits on the carbon felt in a more dispersed manner. In contrast, the introduction of NH$_4$OAc results in a compact and smooth zinc deposition on the carbon fibers, as shown in Fig. 5.7b, effectively inhibiting the formation of severe Zn dendrites.

Additionally, X-ray Diffraction (XRD) analysis of the deposited zinc, displayed in Fig. 5.7c, reveals prominent diffraction peaks. These peaks are characteristic of the hexagonal close-packed structure of zinc metal. Specifically, the distinct peaks at diffraction angles of 36.56°, 39.27°, 43.47°, 54.56°, 70.29°, 70.86°, and 77.29° correspond to the (002), (100), (101), (102), (103), (110), and (004) planes, respectively. These findings suggest that the compact layer of Zn deposition enhances ion transport and maintains a uniform electric field distribution. It is important to note that while NH$_4^+$ ions contribute to forming a dynamic electrostatic shielding layer around Zn protrusions, the presence of OAc$^-$ ions in the electrolyte plays a vital role in stabilizing the electrochemical performance of Zn.

จุฬาลงกรณ์มหาวิทยาลัย

CHULALONGKORN UNIVERSITY

(a) Survey XPS spectra of 1 M ZnI₂ + 1 M NH₄Br and 1 M ZnI₂ + 1 M NH₄OAc. (b–i) High-resolution XPS spectra of Zn 2p, O 1s, I 3d, and C 1s.
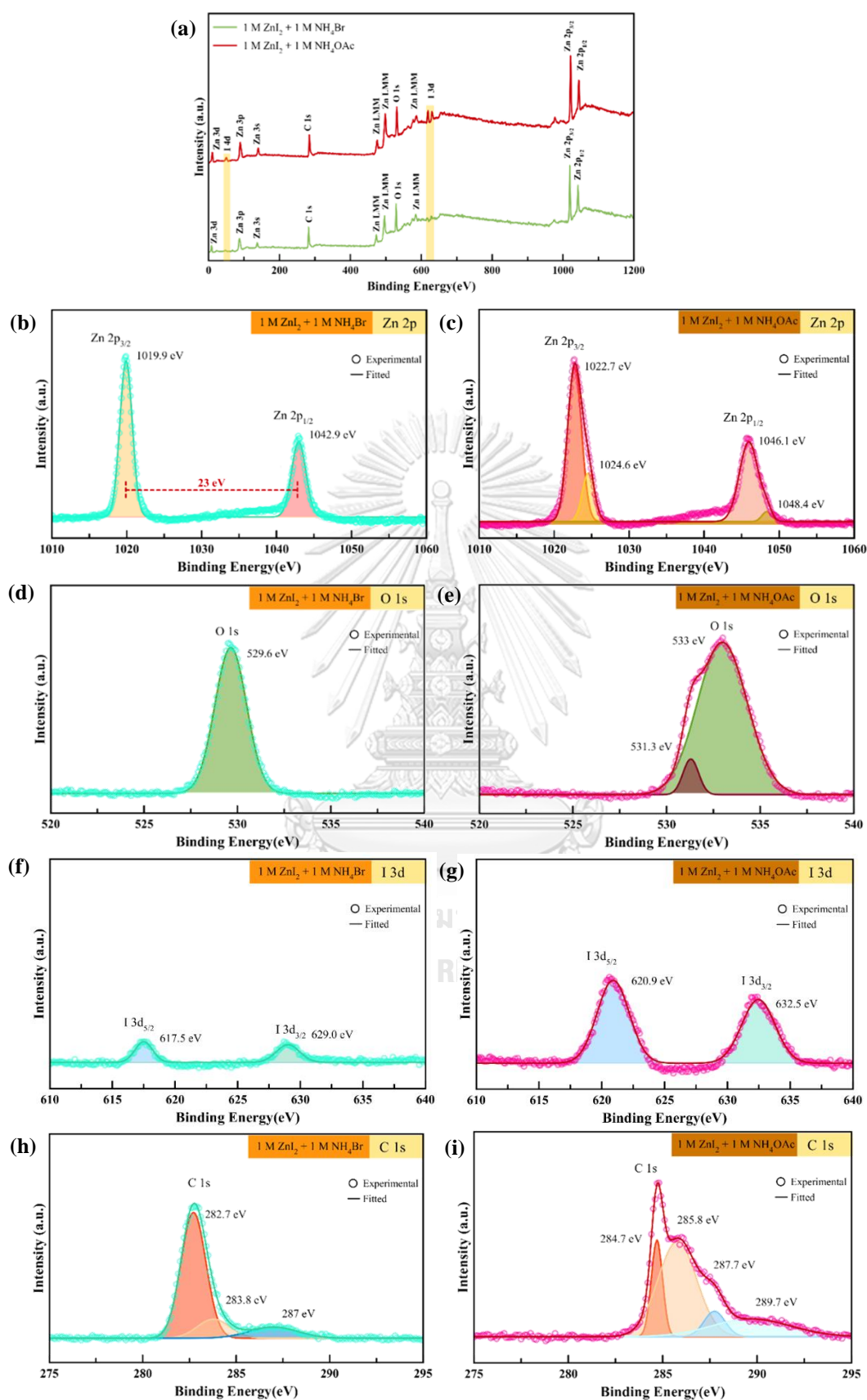
Figure 5. 8 (a) XPS survey spectra of Zn deposition in different electrolyte; high-resolution XPS spectra of (b,c) Zn 2p, (d,e) O 1s, (f,g) I 3d and (h,i) C 1s of different electrolyte.

Further examination of the zinc-deposited structures using X-ray Photoelectron Spectroscopy (XPS) analysis is depicted in Fig. 5.8a. The wide XPS spectra for the different electrolytes confirm the presence of C, Zn, O, and I components (200, 201). Figs. 5.8b and 5.8c showcase the deconvoluted Zn 2p spectra of zinc deposition on carbon felt. A notable single doublet peak is observed in the Zn 2p3/2) spectrum, indicative of the small energy separation between Zn^{2+} and Zn^0 contributions.

In Fig. 5.8b, the Zn 2p peak centers in Br- ion media align with those of the pristine sample, located at 1019.9 eV and 1042.9 eV for Zn 2p3/2 and Zn 2p1/2, respectively. In the presence of NH_4Br, Zn^{2+} ions, solvated by ammonia molecules, diffuse into the bulk electrolyte, allowing metallic zinc to form on the carbon felt fibers, akin to pristine conditions. Conversely, with the addition of OAc⁻ ions, a shift in peak towards higher binding energy is seen in Fig. 5.8c, suggesting the presence of Zn^{2+} on the zinc surface, potentially forming complex molecules with anion species and residing on the surface as a surface electrode (202).

The O 1s binding energy peaks are presented in Figs. 5.4d and 5.4e. The symmetric peak for O 1s in Br- ion electrolyte is observed, with the peak at 529.6 eV linked to O^{2-} bonding with Zinc metal (203-205). In contrast, the O 1s XPS spectrum with OAc⁻ ions, shown in Fig. 5.8e, exhibits an asymmetric peak, indicative of various oxygen species. The peak at 531.3 eV is attributed to O^{2-} from defects or vacancies, while the peak at 533 eV corresponds to weaker oxygen bonds on the surface, such as O-H, O=C-O groups, and possibly Zn-O-I (206, 207).

Figs. 5.8f and 5.8g display the XPS spectra of I 3d in 1 M ZnI_2 with 1 M NH_4Br and 1 M NH_4OAc electrolytes, respectively. Fig. 5.8f shows two intense peaks in the I 3d region with NH_4Br, corresponding to doublets I 3d5/2 and I 3d3/2 at lower binding energies of 617.5 eV and 629 eV, respectively, which are indicative of triiodide (I_3^-) (208). A positive shift in the I 3d region is observed with NH_4OAc

addition in Fig. 5.8g, suggesting electronic interactions between the electrode surface and iodine species (201, 209). The peak at 620.9 eV is associated with IO^{2-} at the electrode surface (207).

Finally, high-resolution C 1s XPS of zinc deposition in 1 M ZnI_2 with 1 M NH_4OAc electrolyte is presented in Fig. 5.8i. The deconvoluted peaks are centered at 284.7, 285.8, 287.7, and 289.7 eV, corresponding to C-C, C-OH, C=O, and O=C-O groups, respectively (210, 211). This data suggests that the XPS spectra of zinc deposited in OAc^- ion media are likely indicative of the presence of iodide acetate ($C_2H_3IO_2$) on the zinc deposition surface.

In order to evaluate the effectiveness of NH4OAc in reducing zinc dendrite formation and side reactions, we conducted cycling tests on ZIFBs. These tests were performed at a constant current density, maintaining an areal capacity of 20 mAh cm^{-2} (240 mAh). As shown in Fig. 5.9a, the battery employing NH_4Br as the anolyte, tested at a current density of 40 mA cm^{-2}, displayed a pronounced decline in discharge capacity, energy, and coulombic efficiency after 200 cycles. On the contrary, the ZIFB using NH_4OAc as the anolyte initially recorded a discharge capacity of around ~19 mAh cm^{-2} (230 mAh). Remarkably, it sustained superior cycling performance over 400 cycles with a coulombic efficiency hovering around 90%, as depicted in Fig. 5.9b.

To further investigate the stability of the supporting electrolyte under more rigorous conditions, the current density was escalated to 80 mA cm^{-2}. Consistent with the performance of the battery utilizing NH4Br in the electrolyte under high current densities, this setup endured only 65 cycles. It exhibited a lower discharge capacity of just over ~18 mAh cm^{-2} (220 mAh), alongside a notable decrease in capacity retention, with CE falling below 92%, as illustrated in Fig. 5.10a.
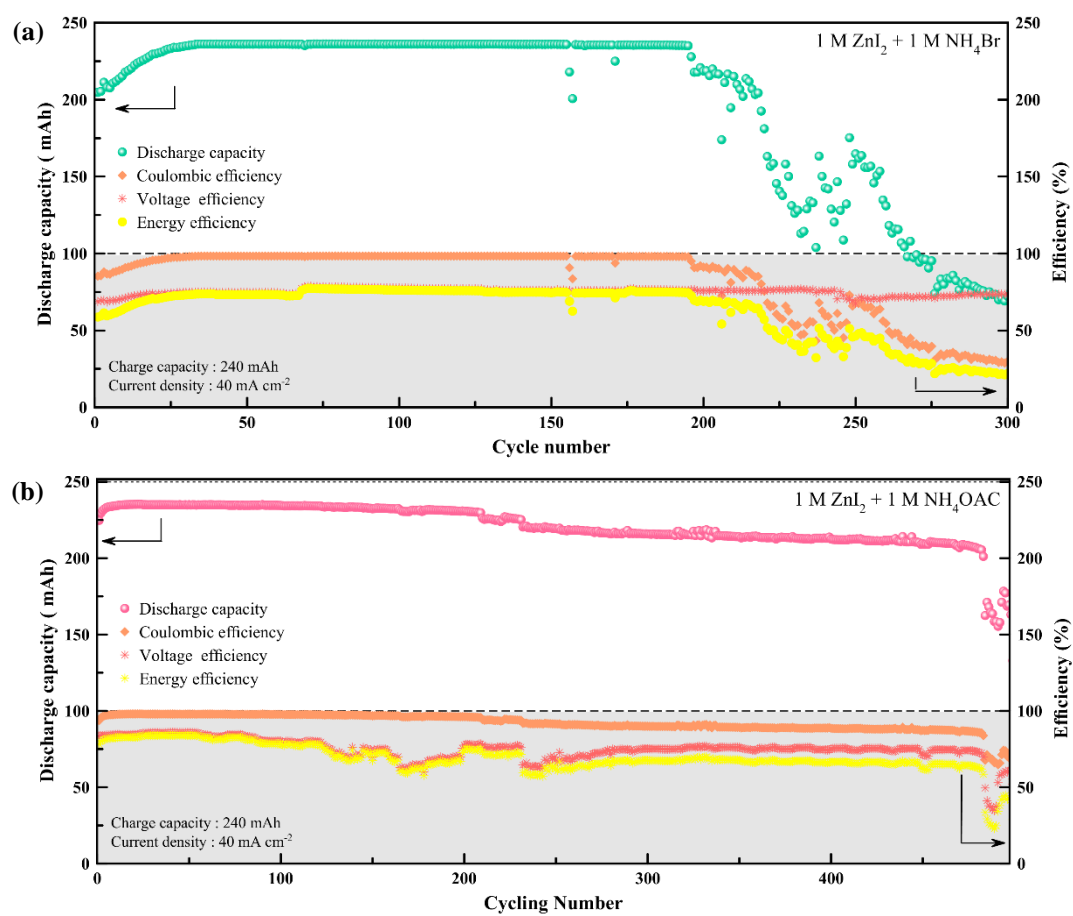
Figure 5. 9 Discharge capacity and efficiencies of the ZIFBs with (a) NH₄Br and NH₄OAc at current density of 40 mA cm⁻².

Figure 5. 10 Discharge capacity and efficiencies of the ZIFBs with (a) NH₄Br80 mA cm⁻² with charge capacity of 240 mAh. (b) Optical images of post-cycled anode and cathode with 1 M ZnI₂ + 1 M NH₄Br under current density of 80 mA cm⁻² with charge capacity of 240 mAh after 127 cycles. (c) FE-SEM images and (b) EDS mapping of Zn deposition on anode after 127 cycles. XRD pattern (e) and FTIR spectrum (f) of deposited products on anode after finish at 127 cycles.

In order to understand the underlying mechanisms, we analyzed cycled carbon felts. Optical images of the post-cycled anode and cathode in a 1 M ZnI₂ + 1 M NH₄Br electrolyte are presented in Fig. 5.10b. According to FE-SEM and EDS measurements, numerous flake-like particles were observed on the anode's surface in

the NH$_4$Br-enhanced anolyte (Figs. 5.6c and 5.6d). These were identified as Zn(OH) and ZnIO$_3$(OH) via XRD analysis (Fig. 5.10e). Correspondingly, FTIR results revealed sharp peaks between 3420-3290 cm^{-1}, attributable to O–H vibrations, and peaks at 652, 604, 507, and 429 cm^{-1}, which correspond to vibrations from I–O groups (Fig. 5.10f) (212, 213). This suggests that the Zn anode surface was covered with undesired products, leading to diminished ZIFB performance. Additionally, a significant accumulation of iodine was detected on the cathode surface by FE-SEM and EDS measurements, as seen in Fig. 5.11.
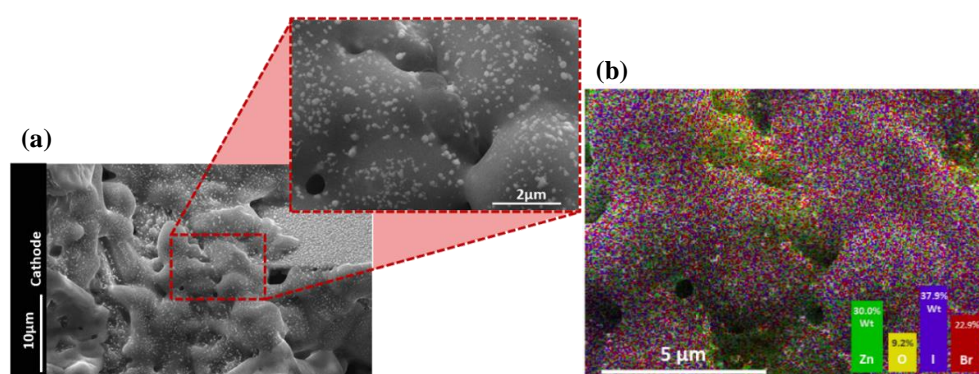
Figure 5. 11 FE-SEM images (a) and EDS mapping (b) of Zn deposition on cathode after 127 cycles.

In contrast, the ZIFB with NH$_4$OAc demonstrated stable cycling over 200 cycles, with a notably lower capacity decay rate and a final capacity retention rate of approximately 95%, as shown in Fig. 5.12a. Optical images of the post-cycled anode and cathode in this electrolyte are displayed in Fig. 5.12b. The pH regulation and buffering effect of OAc$^-$ ions prevented the precipitation of undesired products on the electrode surface, as confirmed by XRD results (Fig. 5.12c). Sharp and strong diffraction peaks at 2θ angles of 24.99°, 42.35°, and 52.11° were observed, corresponding to the crystal planes of hexagonal and rhombohedral graphite structures. Additionally, optical and FE-SEM images (Fig. 5.12d) revealed no insulating by-products on electrodes cycled with the NH$_4$OAc additive. The acetate ions acted as an interfacial pH buffer, suppressing potential side reactions and the formation of insoluble by-products. These findings indicate that OAc$^-$ ions play a

crucial role in reducing by-product formation and enhancing the cycling stability of ZIFBs. However, at a higher charge capacity of 40 mAh cm^{-2} (480 mAh) and a current density of 80 mA cm^{-2}, both Br$^-$ and OAc$^-$ based media exhibited a gradual decline in delivered capacity and stability during the initial cycling phase, as illustrated in Fig. 5.13.

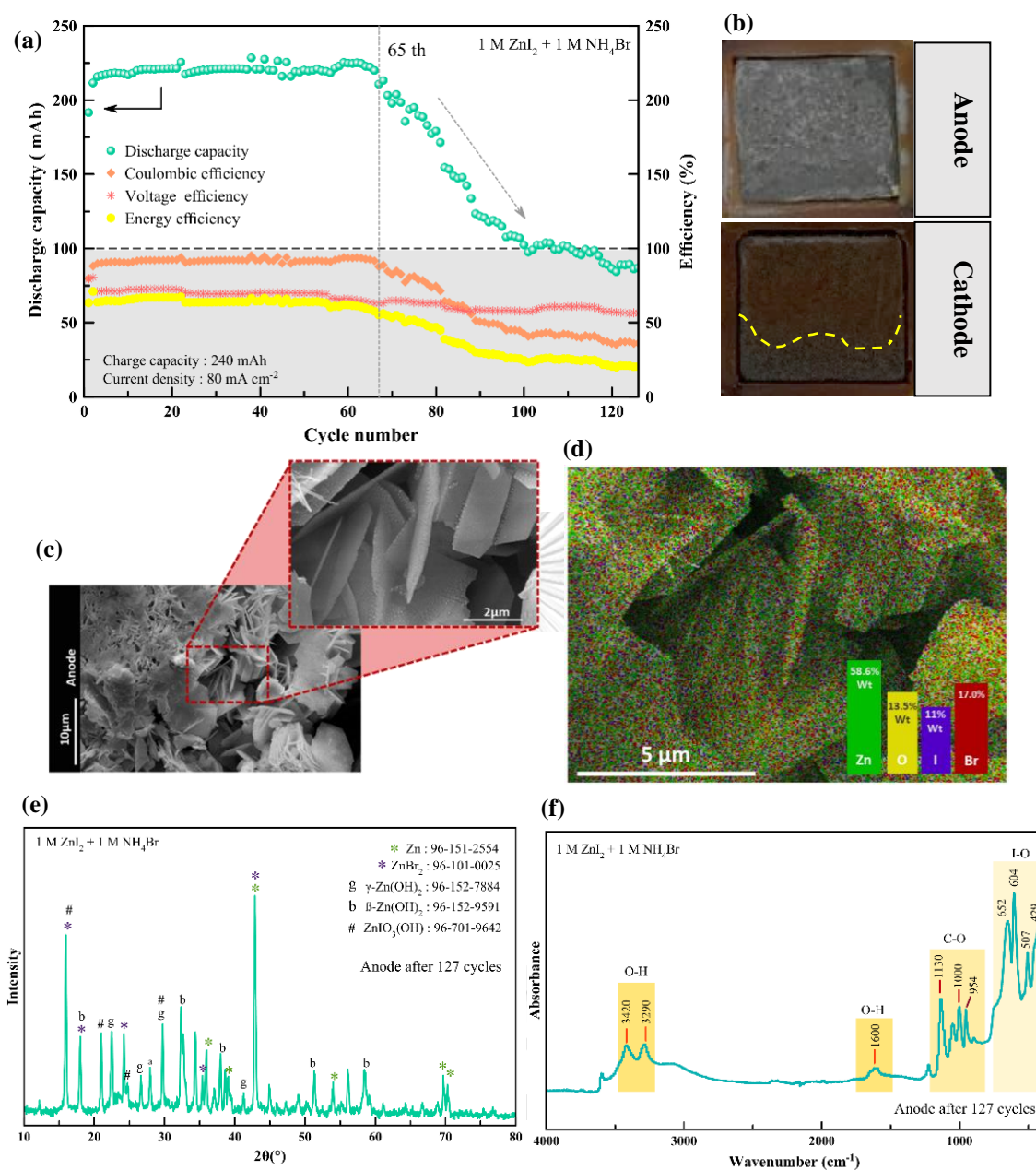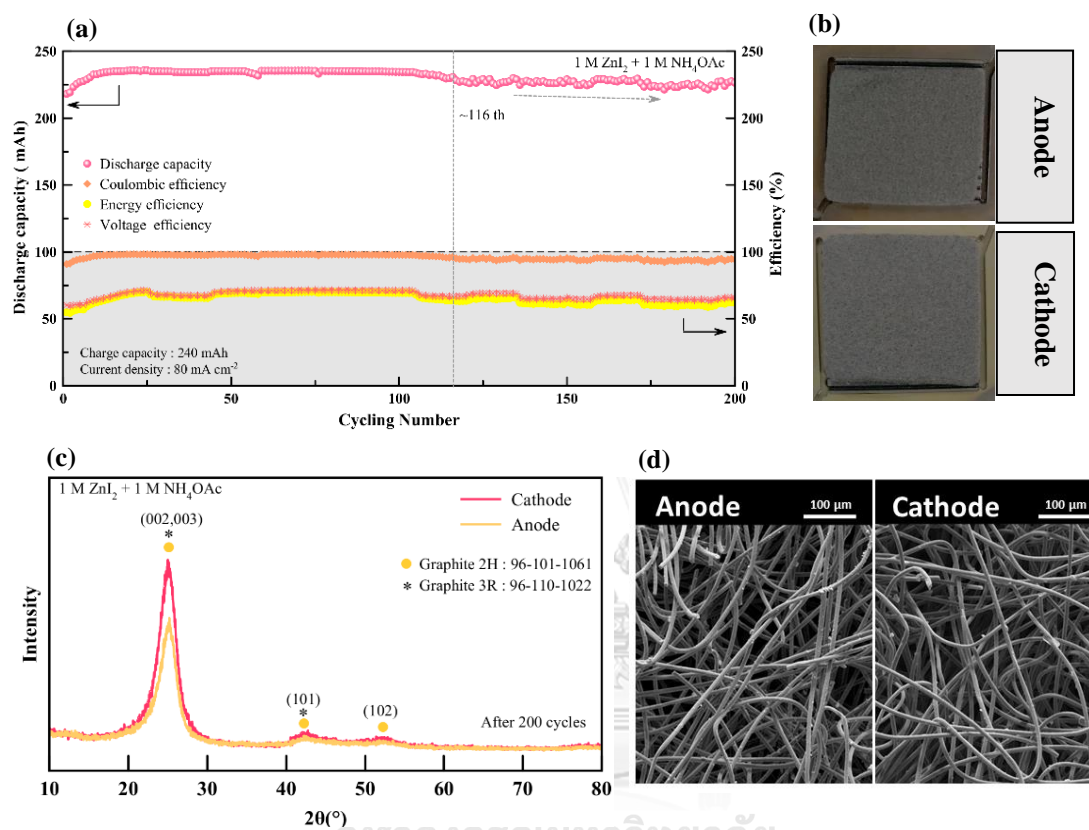*Figure 5. 12 Discharge capacity and efficiencies of the ZIFBs with NH$_4$OAc at current density of (a) 80 mA cm^{-2} with charge capacity of 240 mAh. (b) Optical images of post-cycled anode and cathode with 1 M ZnI$_2$ + 1 M NH$_4$OAc under current density of 80 mA cm^{-2} with charge capacity of 240 mAh after 200 cycles. (c) XRD patterns and (d) FE-SEM and EDS measurements of both anode and cathode in 1 M ZnI$_2$ + 1 M NH4OAc electrolyte after 200 cycles under current density of 80 mA cm^{-2} with charge capacity of 240 mAh.*
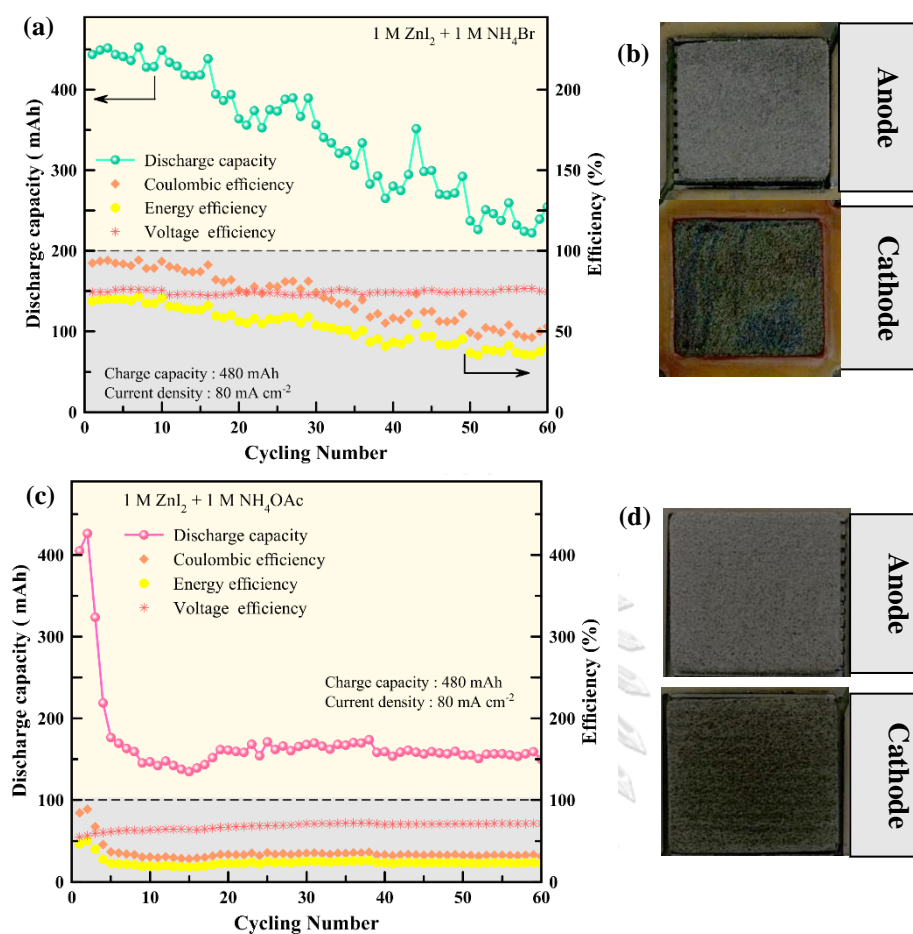
Figure 5. 13 Discharge capacity and efficiencies of the ZIFBs with (a) NH₄Br and (c) NH₄OAc at current density of 80 mA cm⁻² with charge capacity of 480 mAh. (b) Optical images of post-cycled anode and cathode with (b) 1 M ZnI₂ + 1 M NH₄Br and (d) 1 M ZnI₂ + 1 M NH₄OAc under current density of 80 mA cm⁻² with charge capacity

The pH value of the electrolyte significantly influences the interfacial reactions on the electrode. To address side-product formation in aqueous electrolytes, OAc⁻ anions are introduced to the anolyte. Even when proton-induced side reactions occur, any locally increased OH⁻ ions can be rapidly neutralized by HOAc, dynamically maintaining the interfacial pH at a steady level. This prevents the formation of inert by-products. Additionally, the intrinsic hydrolysis reaction leads to an increase in the pH of the bulk electrolyte, effectively mitigating the corrosion of the Zn anode. In Fig. 5.14a, it is observed that ZIFB with OAc⁻ ions in the anolyte maintains a pH value of approximately 4.45 at the initial charging and discharging

stages, and this value remains stable at around 5.14 after 300 cycles. In contrast, the interfacial pH in the OAc⁻ free electrolyte increases from 3.20 initially to approximately 5.30 after 300 cycles, with a tendency to increase further after 300 cycles, as shown in Fig. 5.14b. In the absence of proper pH control, ZIFB without buffer additives results in the severe accumulation of by-products after extended cycling.

Notably, the performance of ZIFB with NH₄OAc as an anolyte additive is satisfactory when compared to NH₄Br addition. Therefore, the following section will primarily focus on investigating the use of a 1 M ZnI₂ + 1 M NH₄OAc anolyte.
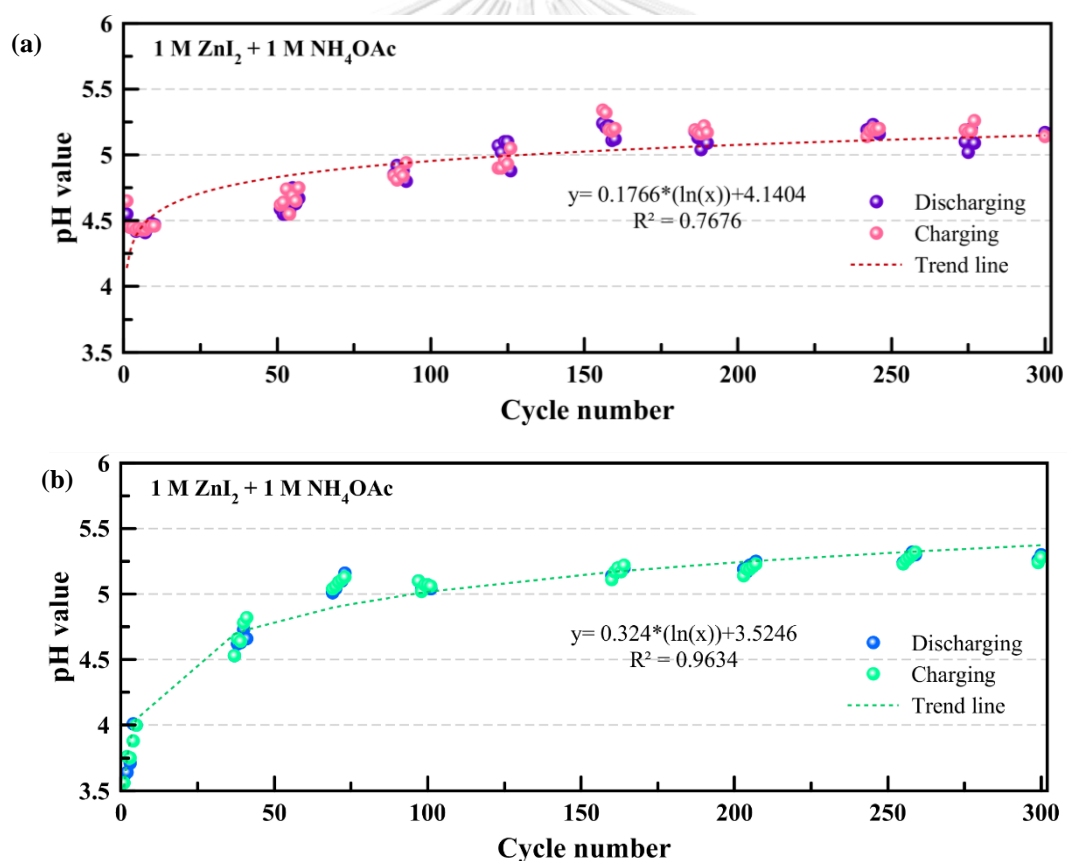
Figure 5. 14 pH value of anolyte in ZIFB using 1 M ZnI₂ with (a) 1 M NH₄OAc and (b) 1 M NH₄Br electrolyte under the current density of 80 mA cm⁻² with 120 mAh for 300 cycles.
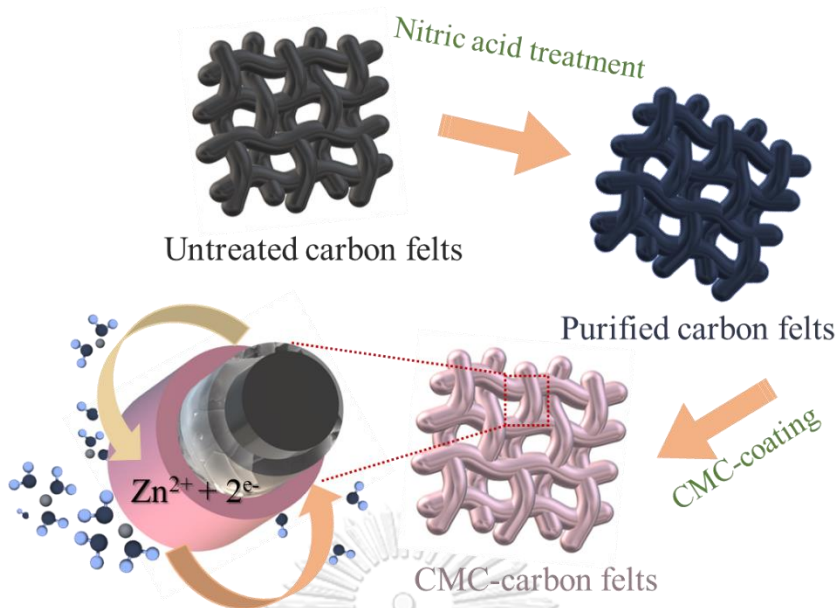
Figure 5. 15 Schematic illustration of CMC-AT electrode fabrication process.

As mentioned earlier, achieving high cycling stability and long-term performance in a ZIFB is still challenged by complex issues, such as the formation of inhomogeneous Zn plating during charging. This non-uniform Zn plating accelerates corrosion and reduces the usability of Zn^{2+} ions. Furthermore, the excessive accumulation of Zn deposits can result in inactive Zn areas, leading to a decline in coulombic efficiency (214). Therefore, achieving uniform and dense Zn deposition is of paramount importance for the long-term performance of a ZIFB. While the proposal addresses the issue from the electrolyte perspective, the challenge of achieving satisfactory Zn plating remains. On the other hand, anode modification is likely to work more effectively in combination with efficiency-enhancing additives, such as the introduction of an artificial solid-electrolyte interface (ASEI). This ASEI, when applied to the Zn surface, serves to reduce water activity and inhibit Zn dendritic growth, allowing the transport of Zn^{2+} ions while preventing the infiltration of water molecules into the anode's surface (102). from previous work (215), We conducted an investigation into the potential of carboxymethyl cellulose (CMC) for effectively controlling the local concentration of Zn^{2+} ions and reducing side reactions at the anode surface. This is made possible by the bulky negative charge associated with the functional groups within CMC. In the subsequent part of our study, we proposed and fabricated a modified carbon felt by coating it with carboxymethyl

cellulose (CMC-CF) using a straightforward and scalable solution-coating approach. The process involved first purifying the carbon felt with nitric acid, followed by immersing it in a CMC solution (250,000 MW with 2%wt) and drying it at 70°C for 30 minutes, resulting in what we denote as CMC-CF. The schematic representation of the CMC-CF electrode fabrication process is illustrated in Fig. 5.15. We conducted a comprehensive investigation into the physical, electrochemical, and battery performance of CMC-CF electrodes in a ZIFB setup using 1 M ZnI_2 + 1 M NH_4OAc as the anolyte and 1 M ZnI_2 + 1 M NH_4Br as the catholyte.
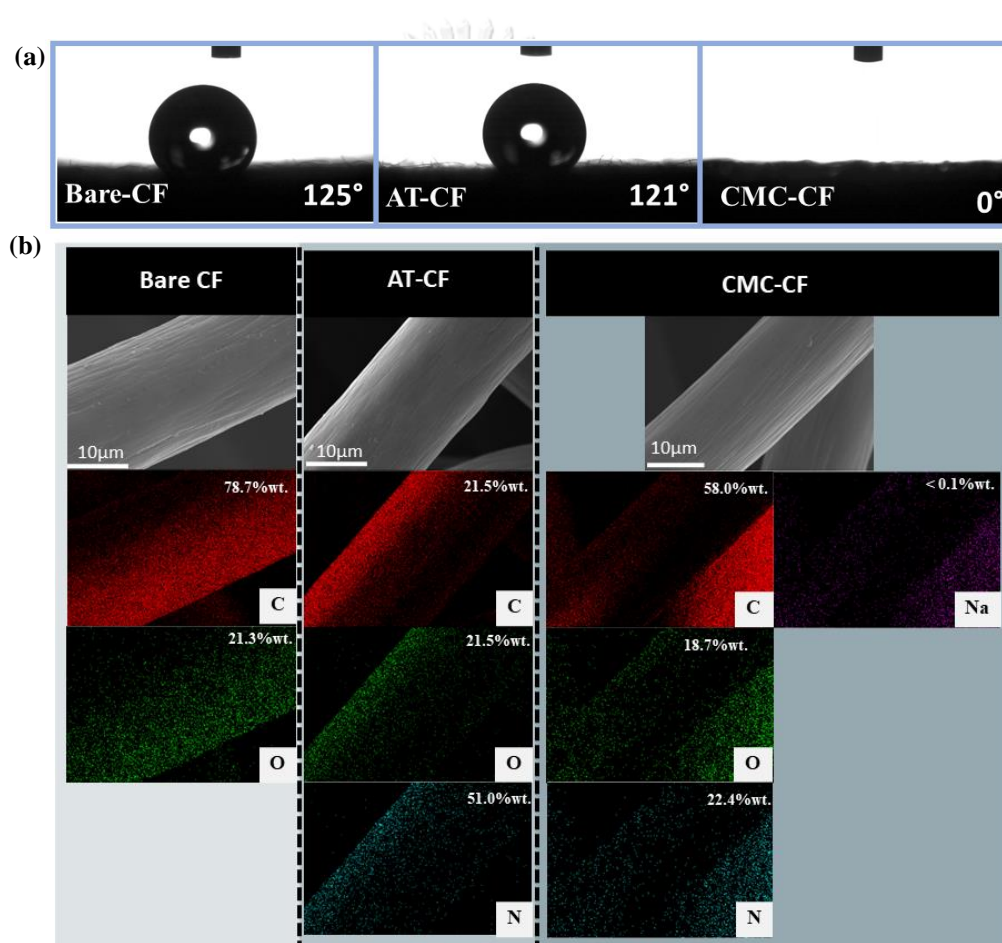
Figure 5. 16 Contact angle measurement (a) for DI water on different surface of carbon felts. (b) SEM-EDS mapping of different carbon felts for C (red), O (green), N (blue) and Na (purple).
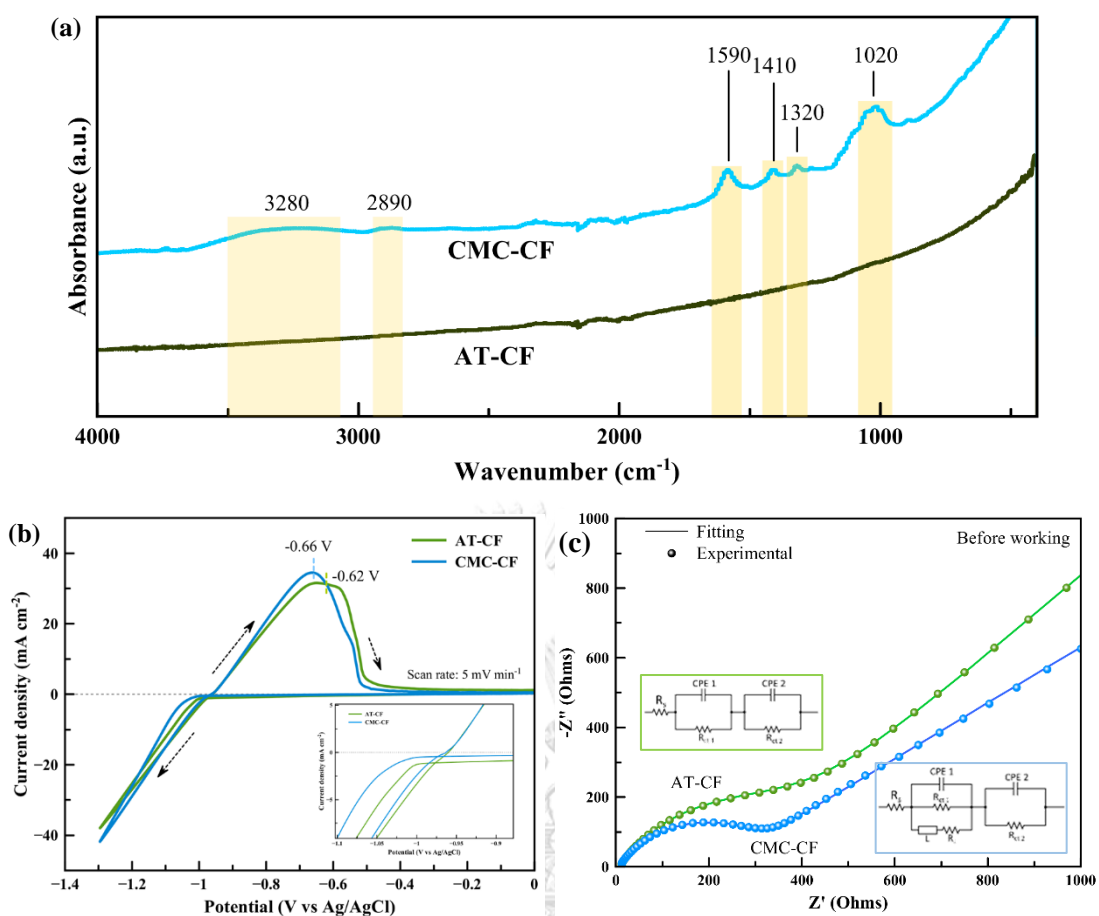
Figure 5. 17 (a) FT-TR spectra of CMC-CF and AT-CF electrode. (b) Cyclic voltammetry (CV) curve profiles of different carbon felt electrodes for 1 M ZnI₂ contain 1 M NH₄OAc. (c) The electrochemical impedance spectroscopy (EIS) curves of AT-CF and CMC-CF electrode before working in 1 M ZnI₂ + 1 M NH₄OAc. Inset: equivalent model circuit of (green) AT-CF and (blue) CMC-CF. All the measurements were carried out using a three-electrode cell as a scan rate of 5 mV/s with different carbon felts as the working electrodes, Pt plate as the counter electrode, and Ag/AgCl as the reference electrode.

Table 5. 1 EIS impedance of the AT-CF and CMC-CF electrode before working.

Electrode	R_s	CPE 1	R_{CT1}	CPE 2	R_{CT2}	L	R_L
AT-CF	6.698	9.77E-07	2.92E+02	3.45E-05	1.14E+05	-	-
CMC-CF	4.978	6.14E-07	2.48E+02	1.55E-04	3.88E+04	4.31E-01	2.78E+03

In Fig. 5.16a, we present contact angle (CA) images of the original carbon felt, AT-CF, and CMC-CF when subjected to deionized water droplets. The original carbon felt exhibited a contact angle of 125° after water was dropped onto its surface. Following cleaning and acid soaking, the AT-CF electrode showed a lower water contact angle of 121°. In contrast, the CMC-coated electrode, or CMC-CF electrode, exhibited immediate wetting, and no contact angle formation was observed on the surface. This suggests enhanced wettability of the modified carbon felt. Such results could influence the wetting properties of the electrolyte, which, in turn, can lead to improved electrochemical performance (216). Fig. 5.16b displays the results of elemental mapping through EDS analysis for carbon fibers from the original CF, AT-CF, and CMC-CF. These maps represent the distribution of elements C, O, and N, which are uniformly distributed in both AT-CF and CMC-CF. Additionally, the presence of evenly distributed Na atoms on the carbon fiber of CMC-CF confirms the uniform coating of the CMC layer on the carbon felt.

To confirm the introduction of the CMC layer on carbon felt, Fig. 5.17a represents the FT-IR spectra of different carbon felts as anode. The FT-TR spectrum of CMC-CF shows characteristic broader peaks of around 3280, and 2890 cm^{-1} and sharp peaks of 1590, 1410, and 1020 cm^{-1} for O-H, C-H, asymmetric and symmetric carboxylate, and C-O stretching mode, respectively (217). However, the absorbance of the characteristic peaks in the graphitic domain of CMC-CF on carbon felt slightly reduced, providing evidence of the existence of CMC on the carbon felt surface. The surface stability of the Zn anode depends on the initial nucleation process of Zn^{2+} ions, which affects to the satisfactory uniform formation (218). To gain deeper insights into the nucleation mechanism, cyclic voltammetry (CV) experiments were carried out using different carbon felts, with Ag/AgCl (in a saturated KCl solution) and Pt plate employed as the reference and counter electrodes, respectively. In Fig. 5.17b, the CV curves illustrate the Zn/Zn^{2+} redox reaction on both CMC-CF and AT-CF in 1 M ZnI$_2$ + 1 M NH$_4$OAc electrolytes. It can be observed that the reduction onset potential for Zn^{2+} is approximately -1.0V for both CMC-CF and AT-CF electrodes. Additionally, the Zn stripping peak notably shifts to -0.66 V in the presence of the CMC layer on the carbon felt, whereas it remains around -0.62 V for

carbon felt without the CMC layer. This shift indicates that the CMC layer enhances the reversibility of Zn plating and stripping. Furthermore, the Zn plating and stripping currents in the CMC-CF electrode are higher compared to those in the CMC-free carbon felt, underscoring the influential role of the abundant CMC-containing functional groups in enhancing reaction kinetics.
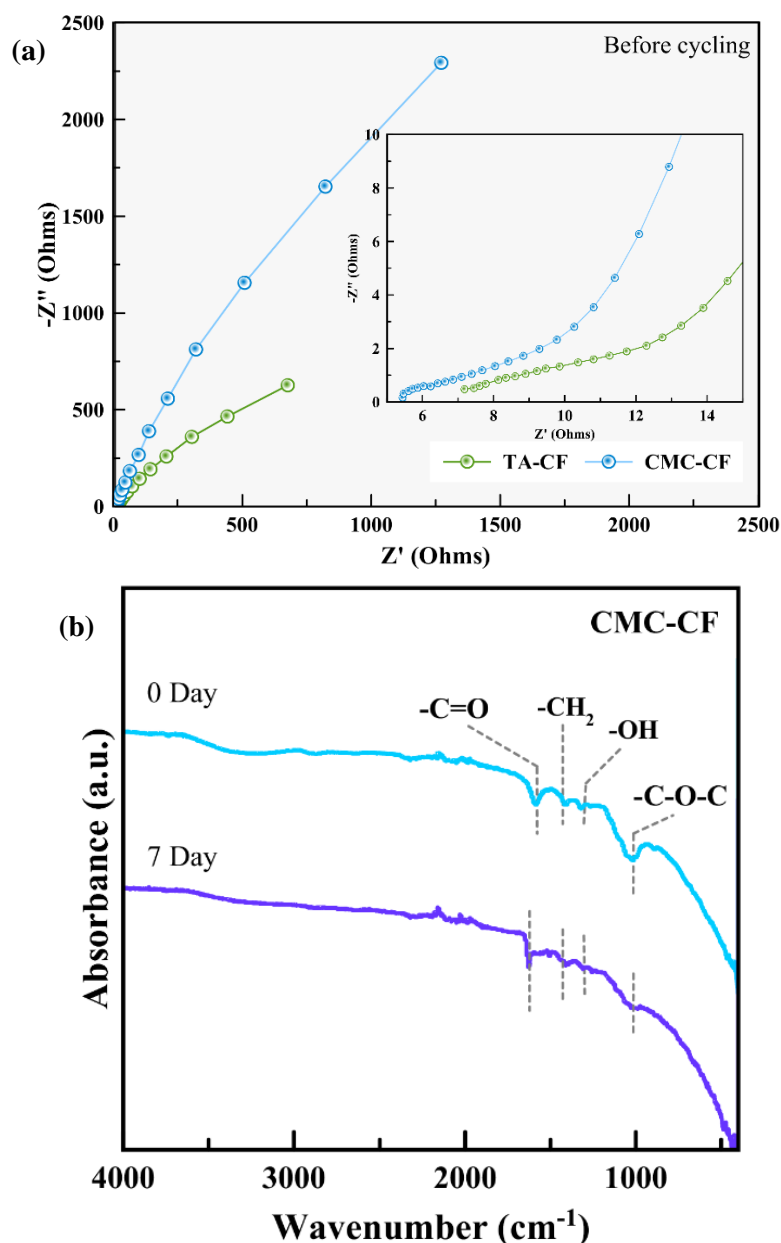
Figure 5. 18 The electrochemical impedance spectroscopy (EIS) curves (a) of AT-CF and CMC-CF electrode after working. (b) FTIR spectra of CMC-CF electrode soaked in 1 M ZnI$_2$ + 1 M NH$_4$OAc for (blue) 0 day and (purple) 7 days.
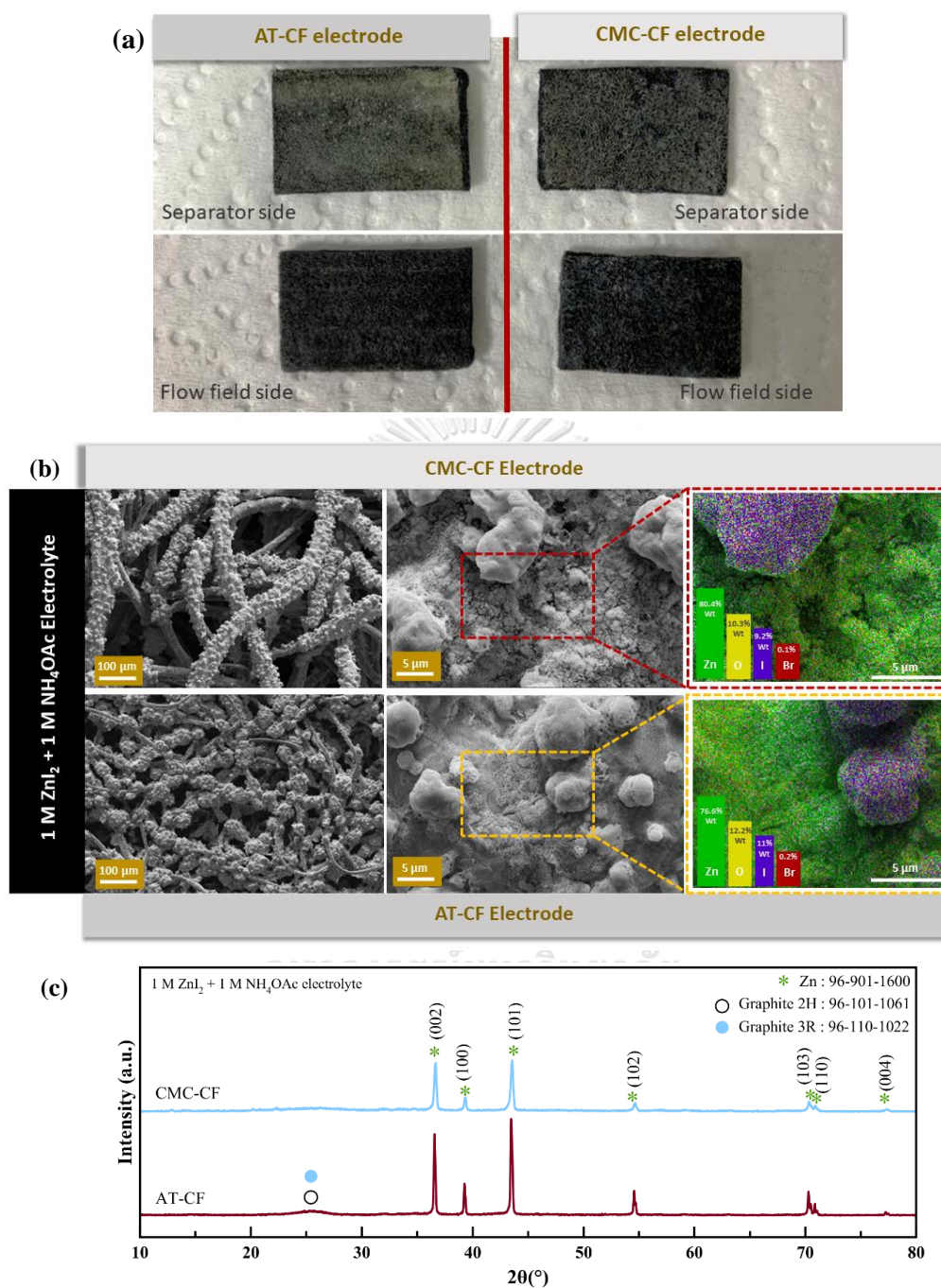
Figure 5. 19 Optical images (a) of CMC-CF and AT-CF electrode after Zn electrodeposition. FE-SEM and EDS analysis (b) of CMC-CF and AT-CF electrode on surface of carbon fiber. (c) XRD pattern of deposited Zn on different anode at current density of 20 mA cm⁻² with capacity of 10 mAh cm⁻².

Figure 5. 19 Optical images (a) of CMC-CF and AT-CF electrode after Zn electrodeposition. FE-SEM and EDS analysis (b) of CMC-CF and AT-CF electrode on surface of carbon fiber. (c) XRD pattern of deposited Zn on different anode at current density of 20 mA cm^{-2} with capacity of 10 mAh cm^{-2}.

The Nyquist plots of CMC-CF and AT-CF electrodes before cycling in the three-electrode cell are shown in Fig. 5.17c. Normally, the high-frequency semicircle in the Nyquist plots appears from the charge-transfer resistance and double-layer capacitance. The lower-frequency characteristic is the mass transfer impedance (219). The Nyquist plots of the AT-CF electrode reveal low ionic conductivity, accompanied by a substantial interface impedance when compared to the CMC-CF electrode. Furthermore, the electrode lacking a CMC layer exhibits a notably higher charge-transfer resistance. Conversely, the Nyquist plots of the CMC-CF electrode illustrate the presence of both a capacitance originating from the CMC layer and a charge transfer resistance at the high and low-frequency capacitive loops, respectively. Additionally, there is evidence of inductive (L) behavior within the high-frequency capacity loop, suggesting the absorption and desorption of Zn ions on the CMC layer. Consequently, the CMC-CF electrode displays a reduced semicircle and lower charge-transfer resistance, indicative of the formation of a polymer layer on the electrode's surface. For a more detailed overview, the impedance data for the AT-CF and CMC-CF electrodes prior to utilization are provided in Table 5.1, and the Nyquist plots of the different anodes after cyclic voltammetry (CV) cycling are presented in Fig. 5.18a.

To validate the dissolution of the CMC layer on the carbon felt in the electrolyte, the FT-IR spectra of CMC-CF soaked in the electrolyte for 7 days are presented in Fig. 5.18b. These spectra exhibit characteristic sharp peaks at ~1590, 1410, and 1020 cm^{-1}, corresponding to the O-H, C-H, asymmetric and symmetric carboxylate, and C-O stretching modes, respectively. These peaks provide clear evidence of the presence of CMC on the surface of the carbon felt even after a 7-day immersion in the electrolyte.

Surface images of Zn electrodeposition on CMC-CF and AT-CF electrodes are shown in Fig. 5.19a. It is observed that in both the AT-CF and CMC-CF, Zn plating predominantly occurs on the side facing the membrane. However, excessive Zn deposition is observed on and near the carbon felt surface facing the membrane when using the AT-CF electrode. Conversely, in the presence of the CMC layer, the carbon felt facing the membrane exhibits a more uniform distribution compared to that in the AT-CF electrode. On the flow field side, almost no zinc metal is found on the AT-CF, while a thin deposited zinc layer can be observed on the CMC-CF electrode. This observation suggests that the CMC layer on the carbon felt promotes ion transport on the carbon felt.

For a more detailed examination of the morphology of Zn deposition on the anode's surface, electrodeposition was carried out on carbon felt with and without CMC coating. An aqueous solution containing 1 M ZnI_2 and 1 M NH_4OAc was employed as the electrolyte at a charge current density of 20 mA cm^{-2} with an areal capacity of 10 mAh cm^{-2}. In Fig. 5.19b, it is evident that all the fibers, including the CMC layer, display a much more uniform and compact Zn distribution consisting of fine-grained Zn nucleation. Specifically, well-defined layered crystal structures of Zn are formed on the CMC-CF electrode compared to the coarse-grained nucleation and clusters observed among the carbon fibers in the AT-CF electrode. EDS mapping confirms the uniform distribution of Zn in both electrodes in the 1 M ZnI_2 + 1 M NH_4OAc electrolyte. However, both electrodes show microspheres of iodine compounds evenly distributed on the surface of the carbon felt.

In Figu 5.19c, the XRD patterns demonstrate that these substances on the surface of CMC-CF and AT-CF are metallic Zn. Unfortunately, although the material deposited onto the surface of the AT-CF electrode is indeed metallic Zn, the peak associated with the graphite felt is still observed due to the uneven Zn deposition on the electrode. It is apparent that the Zn morphology on the carbon felt with CMC is notably superior when compared to the electrode without a CMC layer.
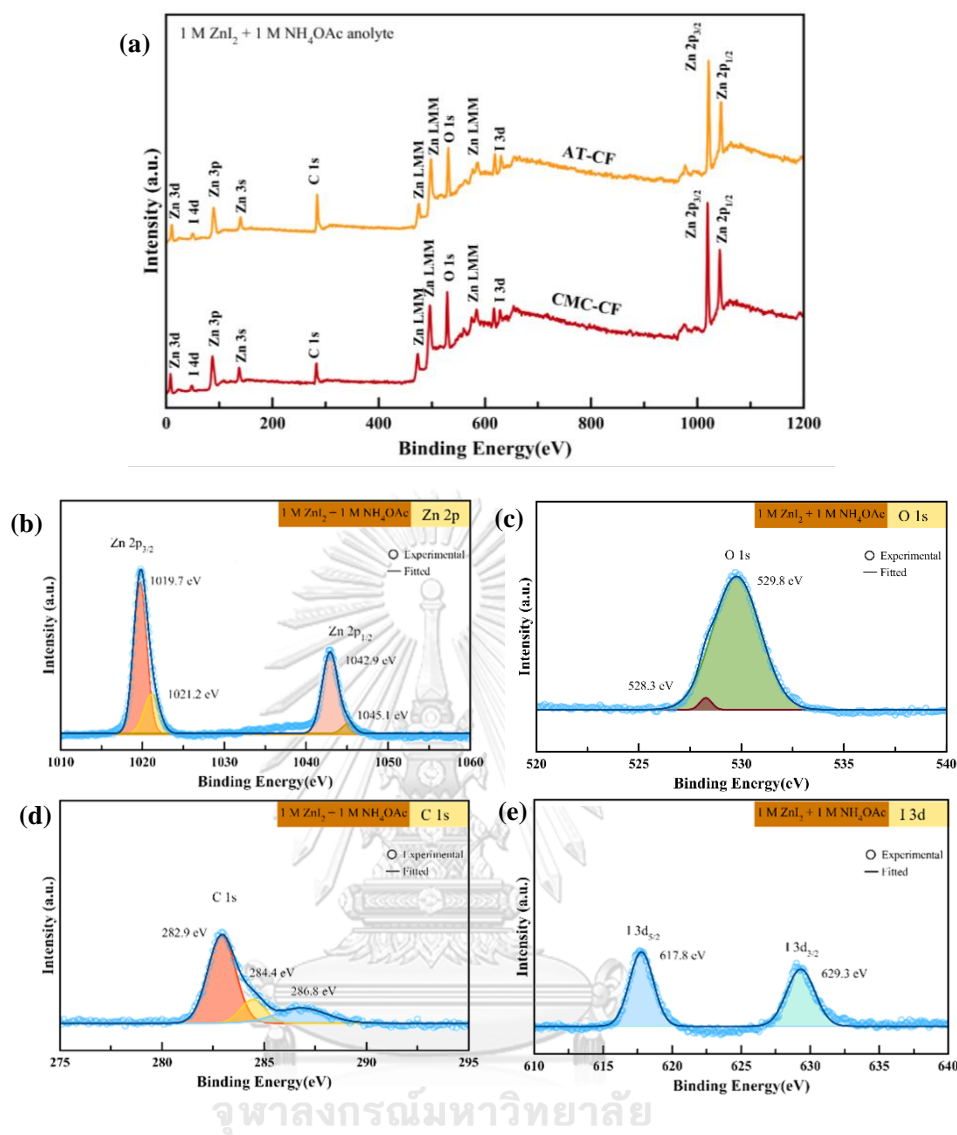
Figure 5. 20 (a) XPS survey spectra of Zn deposition using CMC-CF in 1 M ZnI₂ + 1 M NH₄OAc; high-resolution XPS spectra of (b) Zn 2p, (c) O 1s, (d) C 1s and I 3d and (e) of 1 M ZnI₂ + 1 M NH₄OAc electrolyte.

The investigation of Zn deposited structures through XPS analysis is presented in Fig. 5.20. The broad XPS spectra of both CMC-CF and AT-CF anodes confirm the composite nature, consisting of C, Zn, I, and O, as displayed in Fig. 5.20a. Fig. 5.20b depicts the XPS spectra in the Zn 2p region for the CMC-CF anode. The presence of carboxylic groups within CMC provides active sites for facilitating the transfer of Zn^{2+} ions. Furthermore, the CMC layer effectively acts as a barrier, preventing the diffusion of solvated water and anions through it. The Zn 2p spectra reveal double peaks with binding energies of 1019.9 and 1042.9 eV for Zn 2p3/2 and Zn 2p1/2,

respectively. In more detail, the peaks at around 1019.9 and 1042.9 eV are attributed to Zn metal on the carbon fiber, while the smaller peaks centered at approximately 1021.2 and 1045.1 eV correspond to the altered Zn^{2+} environment beneath the CMC layer. This observation reaffirms that Zn ions are indeed bound to the carboxyl groups within the CMC molecules present in this ASEI-coated carbon felt (220). The XPS spectrum in the O 1s region is given in Fig. 5.20c.the spectrum can be deconvoluted at 528.3 and 529.3 eV, which is attributed to O^{2-} of defects or vacancies and weak bonds of Zn-O on the surface. It seems that the O 1s spectrum is clearly dominated by the Zn-O contribution with 97.8 % of the total area (204). Fig. 5.20d shows the C1s peak, having clearly fitted into three different components. The deconvoluted peaks are centered at 282.9, 284.4, and 286.4 eV, corresponding to C=C, C-C, and O-C=O groups respectively (221). Finally, for the spectrum of the sample in NH_4OAc additive electrolyte, in Fig. 5.20e, The I 3d region can be deconvoluted at 617.8 and 629.3 eV, corresponding to doublets I $(3d_{5/2})$ and I $(3d_{3/2})$, orbitals of the iodine molecule. This observation revealed that the iodine species absorbed on the surface of the CMC-layer in 1 M ZnI_2 + 1 M NH_4OAc electrolyte (222).
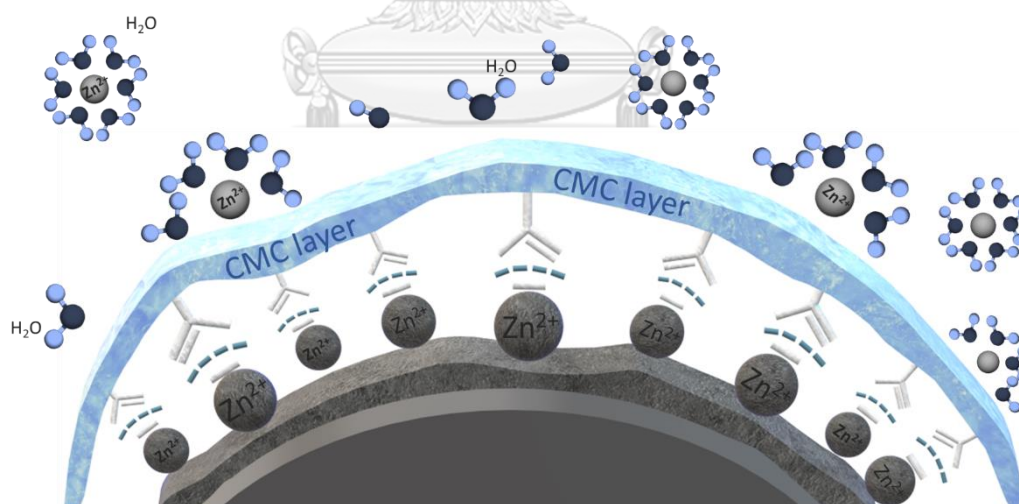
Figure 5. 21 Schematic illustration of CMC-AT electrode fabrication process.

In Fig. 5.21, the CMC layer functions as a blocking layer, creating favorable nucleation sites and preventing direct contact between the carbon fiber and the electrolyte. This results in a uniform local current density and even distribution of Zn

electrodeposition. The presence of carboxylic-containing groups in CMC generates a high potential gradient within the CMC layer, facilitating the diffusion of Zn ions through the CMC interphase. The investigation reveals that the CMC layer effectively suppresses the diffusion of solvated water and bulk anions, thereby preventing unwanted side reactions. The carboxyl groups within CMC-Na contribute to a spatially homogeneous distribution of Zn^{2+} ions, preventing dendrite formation and minimizing side reactions through coordination effects (215).
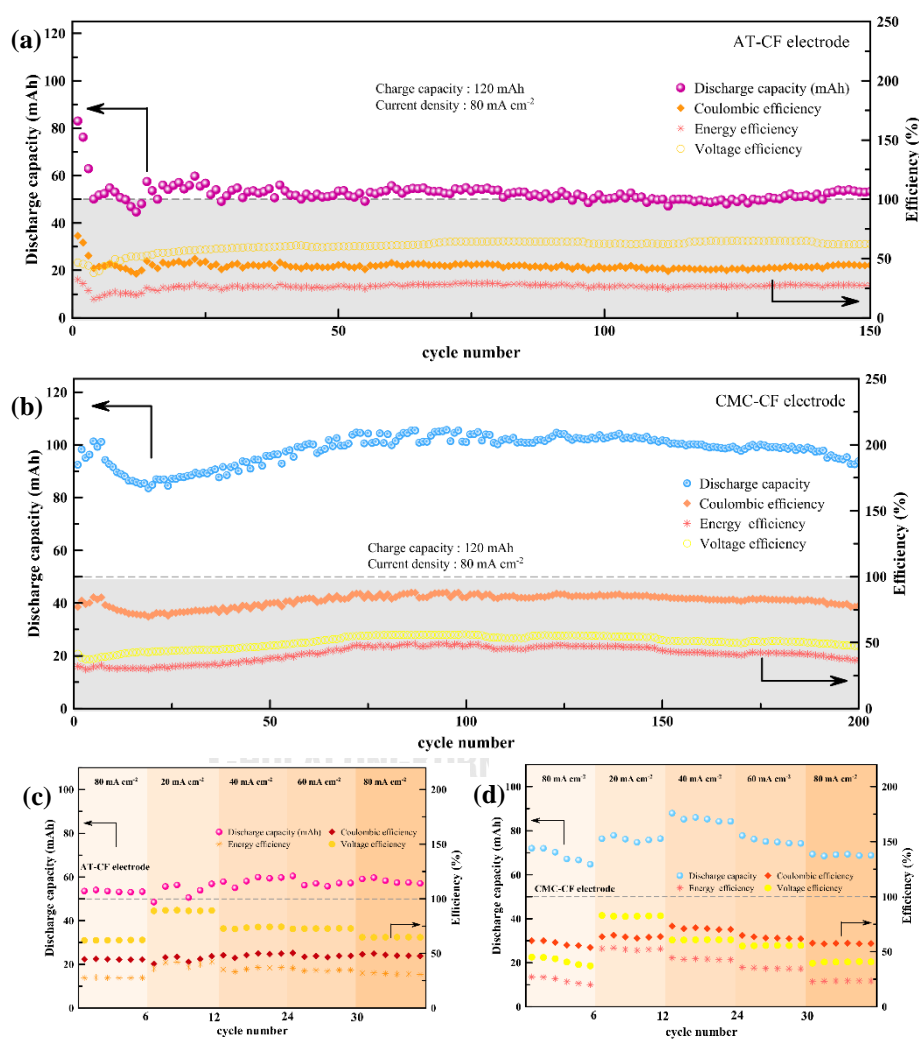
Figure 5. 22 Discharge capacity and efficiencies of the ZIFBs with NH₄OAc using (a) AT-CF and (b) CMC-CF at current density of 80 mA cm⁻² with charge capacity of 120 mAh for 150 cycles. Discharge capacity and efficiencies at different current densities for battery having (c) AT-CF and (d) CMC-CF as anode.
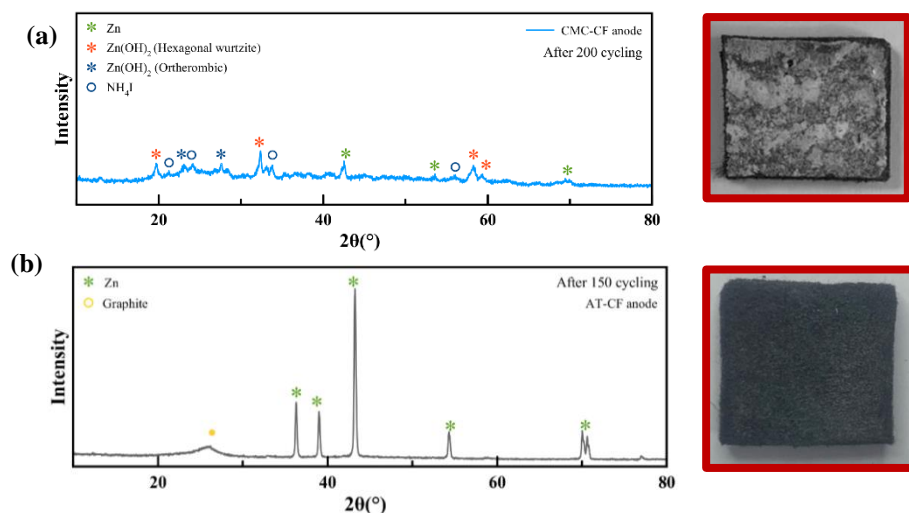
Figure 5. 23 . (a) X-ray diffraction and (inset) optical photo of CMC-CF anode after long-term cycling (b) X-ray diffraction and (inset) optical photo of AT-CF anode after long-term cycling.

To evaluate the practical application of the CMC layer on carbon felt, The cyclability of the flow batteries was evaluated at a current density of 80 mA cm^{-2} with a capacity of 10 mAh cm^{-2} (120 mAh) in 1 M ZnI$_2$ + 1 M NH$_4$OAc as anolyte. As a result, a high-capacity retention of ~90 mAh with a high CE approaching about 77 % is attained after 300 cycles for a full cell using CMC-CF anode (Fig. 5.22b). However, the capacity of the ZIFB having AT-CF anode quickly drops to ~ 4 mAh cm^{-2} (50 mAh) of the initial one due to the rapid decline of the Zn anode as shown in Fig. 5.22a. Furthermore, the discharge capacities and the corresponding efficiencies (CE, EE, VE) of the ZIFB at various current densities are shown in Fig. 5.22 (c-d). At the current densities of 20, 40, 60, and 80 mA cm^{-2}, having CMC-CF as anode as shown in Fig. 5.22d, the corresponding discharge capacities are around 76, 85, 75, and 70 mAh, respectively. The higher discharge capacity and coulombic efficiency are express when the current density to 40 mA cm^{-2}, which demonstrates the suitable rate performance and good reversibility of the ZIFB having CMC-CF as anode. In contrast, along the current density of 20-80 mA cm^{-2}, the ZIFB using AT-CF as anode shows a discharge of 60 mAh and coulombic efficiency of 50 (Fig. 5.22c). To observe the residual on the surface of the CMC-CF anode after long-term cycling, the XRD was conducted as shown in Fig. 5.23a. The small XRD reflections of Zn, Zn (OH)$_2$, and NH$_4$I were observed in the CMC-CF anode after 150 plating/stripping cycles. The

XRD spectrum of AT-CF anode after 150 cycles is shown in Fig. 5.23b. This attempt to use CMC as an ASEI layer on the carbon felt into ZIFBs demonstrates its potential to improve the morphology of Zn deposition, however, the performance condition should be further considered to improve the cycling stability and performance.

5.7 Conclusion

To effectively tackle the dual challenges of significant zinc dendrite formation and side reactions in ZIFBs, we have incorporated a cost-effective NH_4OAc additive into the anolyte. Within this system, NH_4^+ ions play a pivotal role as competing cations. They help create a dynamic electrostatic shielding layer on the zinc electrode, mitigating dendrite growth. Concurrently, OAC^- ions function as a pH buffer, maintaining the pH at an optimal level of 5.14. This dual action results in a self-regulating mechanism at the Zn/electrolyte interface, effectively curbing both zinc dendrite proliferation and the formation of unwanted side products during the battery's cycling process.

The introduction of NH_4OAc into the anolyte leads to enhanced stability in the ZIFB cells. Remarkably, these cells maintain consistent performance over 200 cycles, achieving CE of 90% at a current density of 40 mA cm^{-2} and 95% at 80 mA cm^{-2}. This performance significantly surpasses that of cells using NH_4Br additives. Additionally, we observed that CF electrodes treated with CMC as ASEI exhibit a more uniform and compact Zn distribution. This contrasts sharply with untreated CF electrodes, which show clustered Zn plating. The fine-grained Zn nucleation on CMC-coated CF electrodes results in a notably improved ZIFB performance. In tests, ZIFBs equipped with these CMC-coated CF electrodes demonstrated outstanding capacity retention, maintaining over 77% capacity even after 300 cycles.

Chapter 6
Conclusion

6.1 Conclusions

This study meticulously investigates the versatile applications of carboxymethyl cellulose (CMC) in zinc-iodide battery systems, presenting its findings across three pivotal sections: (1) the role of CMC as an artificial solid-electrolyte interphase (ASEI) for stabilizing zinc-based anodes in aqueous electrolytes, (2) the development of CMC-based polyelectrolytes as cation exchange membranes (CEMs) for zinc-iodine batteries (ZIBs), and (3) the formulation of pH-buffered electrolytes to enhance the stability of zinc-iodine flow batteries (ZIFBs), with a particular focus on the impact of CMC on zinc deposition/dissolution on carbon felt electrodes.

In the first part, CMC-ASEI is strategically utilized to fortify the stability of zinc-based anodes submerged in aqueous solutions. The research encompasses the meticulous design of Zn anodes, ranging from simple Zn sheets to more complex composite types, incorporating CMC-ASEI. The study delves into the operational dynamics of the ASEI-Zn electrode, revealing that the carboxyl groups of CMC form a unique association with Zn ions, facilitating their transfer and acting as a buffer against the bulk aqueous electrolyte. This interaction ensures a uniform Zn deposition and deters dendrite formation, enhancing the electrode's stability. The efficacy of the CMC layer is demonstrated through over 1000 cycles of consistent plating/stripping with minimal polarization and CE of approximately 99% over 100 cycles. In practical Zn-I$_2$ cell configurations, the CMC-Zn//I$_2$ setup exhibits remarkable cycling endurance, maintaining over 2000 cycles with a high-capacity retention rate, showcasing a more stable cycling trend than its counterparts.

The second part of the research explores the integration of CMC-based polyelectrolytes as CEMs in ZIBs. By combining CMC with polyvinyl alcohol (PVA), the study fabricates CEM separators that exhibit enhanced cationic exchange properties and ionic conductivity. The findings indicate that separators with higher CMC ratios significantly mitigate iodine and polyiodide crossover, thereby bolstering the stability and performance of ZIBs. This innovative approach holds promise for

broader applications in various battery systems that require cation exchange membranes.

The final part introduces pH-buffered electrolytes to improve the stability of ZIFBs and examines the effect of CMC on the zinc deposition/dissolution process on carbon felt electrodes. The research employs NH_4OAc as a dual-function additive, creating an electrostatic shielding layer on the Zn electrode while concurrently acting as a pH buffer. This novel approach effectively curtails dendrite growth and side reactions, thus enhancing the reversibility of Zn. ZIFBs with NH_4OAc-enhanced ZnI_2 electrolytes demonstrate stable cycling performance, with a CE of approximately 90% at 40 mA cm^{-2} and 95% at 80 mA cm^{-2}. XPS analysis corroborates the presence of iodide acetate on the Zn anode with the NH_4OAc additive. Moreover, CMC-coated CF electrodes exhibit a more uniform and compact Zn distribution, leading to fine-grained Zn nucleation as opposed to the clustered plating observed on untreated CF electrodes. ZIFBs featuring CMC-coated CF electrodes retain high capacity for an extended number of cycles.

Through this comprehensive research, significant advancements have been made in the development of polymer protective layers and separators, propelling the practical application of ZBBs towards a more sustainable future.

6.2 Limitation of research

The potential of zinc-iodine batteries (ZIBs) is evident, yet they are hindered by the persistent challenge of iodine and polyiodide crossover, which compromises their long-term stability. A deeper exploration into the mechanisms of iodine migration through various polyelectrolytes, coupled with kinetic studies, could lead to more robust strategies to impede this migration. Additionally, the cell performance assessments in this research were limited to a static H-cell setup, which does not fully represent the dynamic conditions of a flow battery system. To truly gauge the efficacy of polyelectrolytes in practical applications, their integration and testing within an actual flow battery system are essential for ZIBs.

Considering the nuances of recent flow cell configurations, it has been recognized that the primary constraints on the Zn-capacity within ZnI_2 electrolytes are linked to the design of the flow field and the interaction with the active area of the carbon felt within the flow channels. To ensure stable operation, it is necessary to confine the capacity to less than 300 mAh (25 mAh/cm^2). These insights highlight the critical need for innovative design enhancements in flow cell architecture to optimize Zn-capacity utilization in ZIBs, thereby advancing their performance and extending their operational life.

6.3 Recommendation and further studies

- It is imperative to delve into the de-solvation mechanisms of Zn ions within electrolytes that are augmented with NH_4OAc additives. Understanding the intricacies of this process could reveal opportunities to refine the electrolyte composition for improved battery performance.

- The behavior of Zn ions in the electrolyte matrix merits a thorough investigation through molecular dynamics simulations. Such studies could provide valuable insights into the ion transport phenomena and electrode-electrolyte interactions at the atomic level.

- A systematic examination of the effects of varying concentrations of additive electrolytes presents a promising research trajectory. Fine-tuning the additive levels could lead to significant enhancements in the electrochemical performance and stability of ZIFBs employing ZnI_2 electrolytes.

- Investigating alternative flow-through patterns within the battery's architecture offers a compelling prospect for optimizing the distribution and utilization of active materials. This could potentially lead to more efficient ion transport and improved overall battery performance in Zn-based flow batteries.

REFERENCES

1.   Smith SC, Sen PK, Kroposki B, editors. Advancement of energy storage devices and applications in electrical power system. 2008 IEEE Power and Energy Society General Meeting - Conversion and Delivery of Electrical Energy in the 21st Century; 2008 20-24 July 2008.

2.   Hamsic N, Schmelter A, Mohd A, Ortjohann E, Schultze E, Tuckey A, et al., editors. Stabilising the Grid Voltage and Frequency in Isolated Power Systems Using a Flywheel Energy Storage System2006.

3.   Abdi H, Mohammadi-ivatloo B, Javadi S, Khodaei AR, Dehnavi E. Chapter 7 - Energy Storage Systems. In: Gharehpetian GB, Mousavi Agah SM, editors. Distributed Generation Systems: Butterworth-Heinemann; 2017. p. 333-68.

4.   Ahuja R, Blomqvist A, Larsson P, Pyykkö P, Zaleski-Ejgierd P. Relativity and the Lead-Acid Battery. Physical Review Letters. 2011;106(1):018301.

5.   Lemaire-Potteau E, Perrin M, Genies S. BATTERIES | Charging Methods. In: Garche J, editor. Encyclopedia of Electrochemical Power Sources. Amsterdam: Elsevier; 2009. p. 413-23.

6.   Moseley PT, Rand DAJ. Chapter 15 - High-Temperature Sodium Batteries for Energy Storage. In: Moseley PT, Garche J, editors. Electrochemical Energy Storage for Renewable Sources and Grid Balancing. Amsterdam: Elsevier; 2015. p. 253-68.

7.   Bachman JC, Muy S, Grimaud A, Chang H-H, Pour N, Lux SF, et al. Inorganic Solid-State Electrolytes for Lithium Batteries: Mechanisms and Properties Governing Ion Conduction. Chemical Reviews. 2016;116(1):140-62.

8.   Fan X, Liu B, Liu J, Ding J, Han X, Deng Y, et al. Battery Technologies for Grid-Level Large-Scale Electrical Energy Storage. Transactions of Tianjin University. 2020;26(2):92-103.

9.   Zhu Q-N, Wang Z-Y, Wang J-W, Liu X-Y, Yang D, Cheng L-W, et al. Challenges and strategies for ultrafast aqueous zinc-ion batteries. Rare Metals. 2021;40(2):309-28.

10.   Wang N, Wan H, Duan J, Wang X, Tao L, Zhang J, et al. A review of zinc-based battery from alkaline to acid. Materials Today Advances. 2021;11:100149.

11.   Ji B, Yao W, Tang Y. High-performance rechargeable zinc-based dual-ion

batteries. Sustainable Energy & Fuels. 2020;4(1):101-7.

12.	Tang H, Peng Z, Wu L, Xiong F, Pei C, An Q, et al. Vanadium-Based Cathode Materials for Rechargeable Multivalent Batteries: Challenges and Opportunities. Electrochemical Energy Reviews. 2018;1.

13.	Shin J, Lee J, Park Y, Choi JW. Aqueous zinc ion batteries: focus on zinc metal anodes. Chemical Science. 2020;11(8):2028-44.

14.	Xie C, Li Y, Wang Q, Sun D, Tang Y, Wang H. Issues and solutions toward zinc anode in aqueous zinc-ion batteries: A mini review. Carbon Energy. 2020;2(4):540-60.

15.	Hoang TKA, Doan TNL, Sun KEK, Chen P. Corrosion chemistry and protection of zinc & zinc alloys by polymer-containing materials for potential use in rechargeable aqueous batteries. RSC Advances. 2015;5(52):41677-91.

16.	Bayaguud A, Fu Y, Zhu C. Interfacial parasitic reactions of zinc anodes in zinc ion batteries: Underestimated corrosion and hydrogen evolution reactions and their suppression strategies. Journal of Energy Chemistry. 2022;64:246-62.

17.	Tao H, Tong X, Gan L, Zhang S, Zhang X, Liu X. Effect of adding various carbon additives to porous zinc anode in rechargeable hybrid aqueous battery. Journal of Alloys and Compounds. 2016;658:119-24.

18.	Li H, Xu C, Han C, Chen Y, Wei C, Li B, et al. Enhancement on Cycle Performance of Zn Anodes by Activated Carbon Modification for Neutral Rechargeable Zinc Ion Batteries. Journal of The Electrochemical Society. 2015;162(8):A1439-A44.

19.	González MA, Trócoli R, Pavlovic I, Barriga C, La Mantia F. Layered double hydroxides as a suitable substrate to improve the efficiency of Zn anode in neutral pH Zn-ion batteries. Electrochemistry Communications. 2016;68:1-4.

20.	Bani Hashemi A, Kasiri G, Glenneberg J, Langer F, Kun R, La Mantia F. Electrochemical and Morphological Characterization of Zn–Al–Cu Layered Double Hydroxides as a Negative Electrode in Aqueous Zinc-Ion Batteries. ChemElectroChem. 2018;5(15):2073-9.

21.	Zheng J, Zhao Q, Tang T, Yin J, Quilty CD, Renderos GD, et al. Reversible epitaxial electrodeposition of metals in battery anodes. Science. 2019;366(6465):645-8.

22.	Zhao Z, Zhao J, Hu Z, Li J, Li J, Zhang Y, et al. Long-life and deeply

rechargeable aqueous Zn anodes enabled by a multifunctional brightener-inspired interphase. Energy & Environmental Science. 2019;12(6):1938-49.

23.   Hao J, Li X, Zhang S, Yang F, Zeng X, Zhang S, et al. Designing Dendrite-Free Zinc Anodes for Advanced Aqueous Zinc Batteries. Advanced Functional Materials. 2020;30(30):2001263.

24.   Hao L, Lv G, Zhou Y, Zhu K, Dong M, Yuhang L, et al. High Performance Anti-Corrosion Coatings of Poly (Vinyl Butyral) Composites with Poly N-(vinyl)pyrrole and Carbon Black Nanoparticles. Materials. 2018;11:2307.

25.   Xie X, Liang S, Gao J, Guo S, Guo J, Wang C, et al. Manipulating the ion-transfer kinetics and interface stability for high-performance zinc metal anodes. Energy & Environmental Science. 2020;13(2):503-10.

26.   Hu K, Guan X, Lv R, Li G, Hu Z, Ren L, et al. Stabilizing zinc metal anodes by artificial solid electrolyte interphase through a surface ion-exchanging strategy. Chemical Engineering Journal. 2020;396.

27.   Zhou M, Guo S, Fang G, Sun H, Cao X, Zhou J, et al. Suppressing by-product via stratified adsorption effect to assist highly reversible zinc anode in aqueous electrolyte. Journal of Energy Chemistry. 2021;55:549-56.

28.   Zhao K, Wang C, Yu Y, Yan M, Wei Q, He P, et al. Ultrathin Surface Coating Enables Stabilized Zinc Metal Anode. Advanced Materials Interfaces. 2018;5(16):1800848.

29.   He H, Tong H, Song X, Song X, Liu J. Highly stable Zn metal anodes enabled by atomic layer deposited Al2O3 coating for aqueous zinc-ion batteries. Journal of Materials Chemistry A. 2020;8(16):7836-46.

30.   Wu K, Yi J, Liu X, Sun Y, Cui J, Xie Y, et al. Regulating Zn Deposition via an Artificial Solid–Electrolyte Interface with Aligned Dipoles for Long Life Zn Anode. Nano-Micro Letters. 2021;13(1):79.

31.   Zhao R, Yang Y, Liu G, Zhu R, Huang J, Chen Z, et al. Redirected Zn Electrodeposition by an Anti-Corrosion Elastic Constraint for Highly Reversible Zn Anodes. Advanced Functional Materials. 2020;31(2).

32.   Hieu LT, So S, Kim IT, Hur J. Zn anode with flexible β-PVDF coating for aqueous

Zn-ion batteries with long cycle life. Chemical Engineering Journal. 2021;411.

33.   Kim H, Hong J, Park K-Y, Kim H, Kim S-W, Kang K. Aqueous Rechargeable Li and Na Ion Batteries. Chemical Reviews. 2014;114(23):11788-827.

34.   Zhang J, Zhou Q, Tang Y, Zhang L, Li Y. Zinc–air batteries: are they ready for prime time? Chemical Science. 2019;10(39):8924-9.

35.   Soundharrajan V, Sambandam B, Kim S, Mathew V, Jo J, Kim S, et al. Aqueous Magnesium Zinc Hybrid Battery: An Advanced High-Voltage and High-Energy MgMn2O4 Cathode. ACS Energy Letters. 2018;3(8):1998-2004.

36.   Ulaganathan M, Suresh S, Mariyappan K, Periasamy P, Pitchai R. New Zinc–Vanadium (Zn–V) Hybrid Redox Flow Battery: High-Voltage and Energy-Efficient Advanced Energy Storage System. ACS Sustainable Chemistry & Engineering. 2019;7(6):6053-60.

37.   Hao J, Li X, Zeng X, Li D, Mao J, Guo Z. Deeply understanding the Zn anode behaviour and corresponding improvement strategies in different aqueous Zn-based batteries. Energy & Environmental Science. 2020;13(11):3917-49.

38.   Jia H, Wang Z, Tawiah B, Wang Y, Chan C-Y, Fei B, et al. Recent advances in zinc anodes for high-performance aqueous Zn-ion batteries. Nano Energy. 2020;70:104523.

39.   Yang H, Chang Z, Qiao Y, Deng H, Mu X, He P, et al. Constructing a Super-Saturated Electrolyte Front Surface for Stable Rechargeable Aqueous Zinc Batteries. Angewandte Chemie International Edition. 2020;59(24):9377-81.

40.   Shivkumar R, Kalaignan GP, Vasudevan T. Studies with porous zinc electrodes with additives for secondary alkaline batteries. Journal of Power Sources. 1998;75(1):90-100.

41.   Hashimoto S, Abe M. The characterization of electrodeposited Zn-SiO2 composites before and after corrosion test. Corrosion Science. 1994;36(12):2125-37.

42.   OUE S, NAKANO H, KOBAYASHI S, AKIYAMA T, FUKUSHIMA H, OKUMURA K. Electrodeposition of Zn-Al2O3 composite from non-suspended solution containing quaternary ammonium salt. Journal of The Surface Finishing Society of Japan. 2002;53(12):920-5.

43.   Xia X, Zhitomirsky I, McDermid JR. Electrodeposition of zinc and composite zinc–yttria stabilized zirconia coatings. Journal of Materials Processing Technology.

2009;209(5):2632-40.

44.   Praveen B, Venkatesha T. Electrodeposition and properties of Zn-nanosized TiO2 composite coatings. Applied Surface Science. 2008;254(8):2418-24.

45.   Masri MN, Mohamad AA. Effect of Adding Carbon Black to a Porous Zinc Anode in a Zinc-Air Battery. Journal of The Electrochemical Society. 2013;160(4):A715-A21.

46.   Shen C, Li X, Li N, Xie K, Wang J-g, Liu X, et al. Graphene-Boosted, High-Performance Aqueous Zn-Ion Battery. ACS Applied Materials & Interfaces. 2018;10(30):25446-53.

47.   Li W, Wang K, Zhou M, Zhan H, Cheng S, Jiang K. Advanced Low-Cost, High-Voltage, Long-Life Aqueous Hybrid Sodium/Zinc Batteries Enabled by a Dendrite-Free Zinc Anode and Concentrated Electrolyte. ACS Appl Mater Interfaces. 2018;10(26):22059-66.

48.   Xia A, Pu X, Tao Y, Liu H, Wang Y. Graphene oxide spontaneous reduction and self-assembly on the zinc metal surface enabling a dendrite-free anode for long-life zinc rechargeable aqueous batteries. Applied Surface Science. 2019;481:852-9.

49.   Wang A, Zhou W, Huang A, Chen M, Chen J, Tian Q, et al. Modifying the Zn anode with carbon black coating and nanofibrillated cellulose binder: A strategy to realize dendrite-free Zn-MnO2 batteries. Journal of Colloid and Interface Science. 2020;577:256-64.

50.   Liang Y, Wang Y, Mi H, Sun L, Ma D, Li H, et al. Functionalized carbon nanofiber interlayer towards dendrite-free, Zn-ion batteries. Chemical Engineering Journal. 2021:131862.

51.   Liang P, Yi J, Liu X, Wu K, Wang Z, Cui J, et al. Highly Reversible Zn Anode Enabled by Controllable Formation of Nucleation Sites for Zn-Based Batteries. Advanced Functional Materials. 2020;30(13):1908528.

52.   Xiong W, Yang D, Hoang TKA, Ahmed M, Zhi J, Qiu X, et al. Controlling the sustainability and shape change of the zinc anode in rechargeable aqueous Zn/LiMn2O4 battery. Energy Storage Materials. 2018;15:131-8.

53.   Zhang Q, Luan J, Fu L, Wu S, Tang Y, Ji X, et al. The Three-Dimensional Dendrite-Free Zinc Anode on a Copper Mesh with a Zinc-Oriented Polyacrylamide Electrolyte Additive. Angew Chem Int Ed Engl. 2019;58(44):15841-7.

54.   Yuksel R, Buyukcakir O, Seong WK, Ruoff RS. Metal-Organic Framework Integrated Anodes for Aqueous Zinc-Ion Batteries. Advanced Energy Materials. 2020;10(16):1904215.

55.   Lu Q, Liu C, Du Y, Wang X, Ding L, Omar A, et al. Uniform Zn Deposition Achieved by Ag Coating for Improved Aqueous Zinc-Ion Batteries. ACS Applied Materials & Interfaces. 2021;13(14):16869-75.

56.   Lee BS, Cui S, Xing X, Liu H, Yue X, Petrova V, et al. Dendrite Suppression Membranes for Rechargeable Zinc Batteries. ACS Appl Mater Interfaces. 2018;10(45):38928-35.

57.   Elhalawany N, Mossad MA, Zahran MK. Novel water based coatings containing some conducting polymers nanoparticles (CPNs) as corrosion inhibitors. Progress in Organic Coatings. 2014;77(3):725-32.

58.   Rohwerder M, Michalik A. Conducting polymers for corrosion protection: What makes the difference between failure and success? Electrochimica Acta. 2007;53(3):1300-13.

59.   Deshpande PP, Jadhav NG, Gelling VJ, Sazou D. Conducting polymers for corrosion protection: a review. Journal of Coatings Technology and Research. 2014;11(4):473-94.

60.   Sathiyanarayanan S, Muthukrishnan S, Venkatachari G. Performance of polyaniline pigmented vinyl acrylic coating on steel in aqueous solutions. Progress in Organic Coatings. 2006;55(1):5-10.

61.   Nayana KO, Venkatesha TV. Bright zinc electrodeposition and study of influence of synergistic interaction of additives on coating properties. Journal of Industrial and Engineering Chemistry. 2015;26:107-15.

62.   Banik SJ, Akolkar R. Suppressing Dendrite Growth during Zinc Electrodeposition by PEG-200 Additive. Journal of The Electrochemical Society. 2013;160(11):D519-D23.

63.   Morón LE, Méndez A, Castañeda F, Flores JG, Ortiz-Frade L, Meas Y, et al. Electrodeposition and corrosion behavior of Zn coatings formed using as brighteners arene additives of different structure. Surface and Coatings Technology. 2011;205(21):4985-92.

64.   Dye JL, Faber MP, Karl DJ. Transference Numbers and Conductances of

Multivalent Salts in Aqueous Solution: Zinc Sulfate and Zinc Perchlorate1. Journal of the American Chemical Society. 1960;82(2):314-8.

65. Meng T, Yi F, Cheng H, Hao J, Shu D, Zhao S, et al. Preparation of Lithium Titanate/Reduced Graphene Oxide Composites with Three-Dimensional "Fishnet-Like" Conductive Structure via a Gas-Foaming Method for High-Rate Lithium-Ion Batteries. ACS Applied Materials & Interfaces. 2017;9(49):42883-92.

66. Chen P, Yuan X, Xia Y, Zhang Y, Fu L, Liu L, et al. An Artificial Polyacrylonitrile Coating Layer Confining Zinc Dendrite Growth for Highly Reversible Aqueous Zinc-Based Batteries. Adv Sci (Weinh). 2021;8(11):e2100309.

67. Kang L, Cui M, Jiang F, Gao Y, Luo H, Liu J, et al. Nanoporous CaCO3 Coatings Enabled Uniform Zn Stripping/Plating for Long-Life Zinc Rechargeable Aqueous Batteries. Advanced Energy Materials. 2018;8(25):1801090.

68. Zhang R, Chen X-R, Chen X, Cheng X-B, Zhang X-Q, Yan C, et al. Inside Cover: Lithiophilic Sites in Doped Graphene Guide Uniform Lithium Nucleation for Dendrite-Free Lithium Metal Anodes (Angew. Chem. Int. Ed. 27/2017). Angewandte Chemie International Edition. 2017;56(27):7682-.

69. Deng C, Xie X, Han J, Tang Y, Gao J, Liu C, et al. A Sieve-Functional and Uniform-Porous Kaolin Layer toward Stable Zinc Metal Anode. Advanced Functional Materials. 2020;30(21):2000599.

70. Karayaylali P, Tatara R, Zhang Y, Chan K-L, Yu Y, Giordano L, et al. Editors' Choice—Coating-Dependent Electrode-Electrolyte Interface for Ni-Rich Positive Electrodes in Li-Ion Batteries. Journal of The Electrochemical Society. 2019;166(6):A1022-A30.

71. Li X-P, Yang H, Tian Z-F, Liu J-L, Ren X-M. Investigation of the structure and ionic conductivity of intercalated kaolinites with potassium acetate in hydrous and anhydrous phases. Dalton Transactions. 2015;44(10):4665-70.

72. Zhang N, Huang S, Yuan Z, Zhu J, Zhao Z, Niu Z. Direct Self-Assembly of MXene on Zn Anodes for Dendrite-Free Aqueous Zinc-Ion Batteries. Angewandte Chemie International Edition. 2021;60(6):2861-5.

73. Fei B, Wach RA, Mitomo H, Yoshii F, Kume T. Hydrogel of biodegradable cellulose derivatives. I. Radiation-induced crosslinking of CMC. Journal of Applied

Polymer Science. 2000;78(2):278-83.

74. El Salmawi KM. Application of Polyvinyl Alcohol (PVA)/Carboxymethyl Cellulose (CMC) Hydrogel Produced by Conventional Crosslinking or by Freezing and Thawing. Journal of Macromolecular Science, Part A. 2007;44(6):619-24.

75. Bai C, Cai F, Wang L, Guo S, Liu X, Yuan Z. A sustainable aqueous Zn-I2 battery. Nano Research. 2018;11(7):3548-54.

76. Li Y, Liu L, Li H, Cheng F, Chen J. Rechargeable aqueous zinc–iodine batteries: pore confining mechanism and flexible device application. Chemical Communications. 2018;54(50):6792-5.

77. Mo F, Li H, Pei Z, Liang G, Ma L, Yang Q, et al. A smart safe rechargeable zinc ion battery based on sol-gel transition electrolytes. Science Bulletin. 2018;63(16):1077-86.

78. Xie C, Liu Y, Lu W, Zhang H, Li X. Highly stable zinc–iodine single flow batteries with super high energy density for stationary energy storage. Energy & Environmental Science. 2019;12(6):1834-9.

79. Lee J, Srimuk P, Fleischmann S, Ridder A, Zeiger M, Presser V. Nanoconfinement of redox reactions enables rapid zinc iodide energy storage with high efficiency. Journal of Materials Chemistry A. 2017;5(24):12520-7.

80. Yu D, Kumar A, Nguyen TA, Nazir MT, Yasin G. High-Voltage and Ultrastable Aqueous Zinc–Iodine Battery Enabled by N-Doped Carbon Materials: Revealing the Contributions of Nitrogen Configurations. ACS Sustainable Chemistry & Engineering. 2020;8(36):13769-76.

81. Zou Y, Liu T, Du Q, Li Y, Yi H, Zhou X, et al. A four-electron Zn-I2 aqueous battery enabled by reversible I–/I2/I+ conversion. Nature Communications. 2021;12(1):170.

82. Yuan Z, Yin Y, Xie C, Zhang H, Yao Y, Li X. Advanced Materials for Zinc-Based Flow Battery: Development and Challenge. Advanced Materials. 2019;31(50):1902025.

83. Lin D, Li Y. Recent Advances of Aqueous Rechargeable Zinc-Iodine Batteries: Challenges, Solutions, and Prospects. Advanced Materials. 2022;34(23):2108856.

84. Ito S, Sugimasa M, Toshimitsu Y, Orita A, Kitagawa M, Sakai M. Formation of a hydrophobic polyiodide complex during cathodic oxidation of iodide in the presence of propylene carbonate in aqueous solutions, and its application to a zinc/iodine redox

flow battery. Electrochimica Acta. 2019;319.

85. Lu K, Zhang H, Song B, Pan W, Ma H, Zhang J. Sulfur and nitrogen enriched graphene foam scaffolds for aqueous rechargeable zinc-iodine battery. Electrochimica Acta. 2019;296:755-61.

86. Yang Y, Liang S, Zhou J. Progress and prospect of the zinc–iodine battery. Current Opinion in Electrochemistry. 2021;30:100761.

87. Weng G-M, Li Z, Cong G, Zhou Y, Lu Y-C. Unlocking the capacity of iodide for high-energy-density zinc/polyiodide and lithium/polyiodide redox flow batteries. Energy & Environmental Science. 2017;10(3):735-41.

88. Jian QP, Wu MC, Jiang HR, Lin YK, Zhao TS. A trifunctional electrolyte for high-performance zinc-iodine flow batteries. Journal of Power Sources. 2021;484:229238.

89. Li H, Ma L, Han C, Wang Z, Liu Z, Tang Z, et al. Advanced rechargeable zinc-based batteries: Recent progress and future perspectives. Nano Energy. 2019;62:550-87.

90. Bard AJ, Faulkner LR, White HS. Electrochemical methods: fundamentals and applications: John Wiley & Sons; 2022.

91. Orazem M, Tribollet B. Tribollet, B.: Electrochemical Impedance Spectroscopy. Wiley-Interscience, New York2008.

92. Olaru S, Stoican F, Kheawhom S, editors. Challenges and opportunities for the control of energy storage systems. a focus on the zinc-air batteries. 2021 IEEE AFRICON; 2021 13 September 2021 - 15 September 2021; Virtual, Arusha.

93. Hannan MA, Wali SB, Ker PJ, Rahman MSA, Mansor M, Ramachandaramurthy VK, et al. Battery energy-storage system: A review of technologies, optimization objectives, constraints, approaches, and outstanding issues. Journal of Energy Storage [Internet]. 2021 2021/10/01/; 42:[103023 p.]. Available from: https://www.sciencedirect.com/science/article/pii/S2352152X21007349.

94. Abbasi A, Hosseini S, Somwangthanaroj A, Cheacharoen R, Olaru S, Kheawhom S. Discharge profile of a zinc-air flow battery at various electrolyte flow rates and discharge currents. Scientific Data [Internet]. 2020 2020/06/22; 7(1):[196 p.]. Available from: https://doi.org/10.1038/s41597-020-0539-y.

95. Kao-ian W, Mohamad AA, Liu W-R, Pornprasertsuk R, Siwamogsatham S, Kheawhom S. Stability Enhancement of Zinc-Ion Batteries Using Non-Aqueous

Electrolytes. Batteries & Supercaps [Internet]. 2022; 5(5):[e202100361 p.]. Available from: https://chemistry-europe.onlinelibrary.wiley.com/doi/abs/10.1002/batt.202100361.

96.   Khezri R, Rezaei Motlagh S, Etesami M, Mohamad AA, Mahlendorf F, Somwangthanaroj A, et al. Stabilizing zinc anodes for different configurations of rechargeable zinc-air batteries. Chem Eng J [Internet]. 2022 2022/12/01/; 449:[137796 p.]. Available from: https://www.sciencedirect.com/science/article/pii/S1385894722032831.

97.   Wang T, Li C, Xie X, Lu B, He Z, Liang S, et al. Anode Materials for Aqueous Zinc Ion Batteries: Mechanisms, Properties, and Perspectives. ACS Nano. 2020;14(12):16321-47.

98.   Mallick S, Raj CR. Aqueous Rechargeable Zn-ion Batteries: Strategies for Improving the Energy Storage Performance. ChemSusChem. 2021;14(9):1987-2022.

99.   Abbasi A, Xu Y, Abouzari-Lotf E, Etesami M, Khezri R, Risse S, et al. Phosphonated graphene oxide-modified polyacrylamide hydrogel electrolytes for solid-state zinc-ion batteries. Electrochim Acta. 2022;435:141365.

100.   Motlagh SR, Khezri R, Mohamad AA, Pornprasertsuk R, Kidkhunthod P, Nguyen MT, et al. Enhancing electrochemical performance and stabilizing zinc anode in mild acidic electrolyte using combined additive. Materials Science for Energy Technologies. 2023;6:178-91.

101.   Zhang Q, Su Y, Shi Z, Yang X, Sun J. Artificial Interphase Layer for Stabilized Zn Anodes: Progress and Prospects. Small. 2022;18(40):2203583.

102.   Gopalakrishnan M, Ganesan S, Nguyen MT, Yonezawa T, Praserthdam S, Pornprasertsuk R, et al. Critical roles of metal–organic frameworks in improving the Zn anode in aqueous zinc-ion batteries. Chemical Engineering Journal. 2023;457:141334.

103.   Zhang G, Zhang X, Liu H, Li J, Chen Y, Duan H. 3D-Printed Multi-Channel Metal Lattices Enabling Localized Electric-Field Redistribution for Dendrite-Free Aqueous Zn Ion Batteries. Advanced Energy Materials. 2021;11(19):2003927.

104.   Deng W, Zhang N, Wang X. Hybrid interlayer enables dendrite-free and deposition-modulated zinc anodes. Chem Eng J. 2022;432:134378.

105.   Qiu H, Du X, Zhao J, Wang Y, Ju J, Chen Z, et al. Zinc anode-compatible in-situ solid electrolyte interphase via cation solvation modulation. Nature Communications.

2019;10(1):5374.

106.   Di S, Nie X, Ma G, Yuan W, Wang Y, Liu Y, et al. Zinc anode stabilized by an organic-inorganic hybrid solid electrolyte interphase. Energy Storage Materials. 2021;43:375-82.

107.   Li R, Li M, Chao Y, Guo J, Xu G, Li B, et al. Hexaoxacyclooctadecane induced interfacial engineering to achieve dendrite-free Zn ion batteries. Energy Storage Materials. 2022;46:605-12.

108.   Zhang F, Wang C, Pan J, Tian F, Zeng S, Yang J, et al. Polypyrrole-controlled plating/stripping for advanced zinc metal anodes. Materials Today Energy. 2020;17:100443.

109.   Li B, Liu S, Geng Y, Mao C, Dai L, Wang L, et al. Achieving Stable Zinc Metal Anode Via Polyaniline Interface Regulation of Zn Ion Flux and Desolvation. Adv Funct Mater. 2023;n/a(n/a):2214033.

110.   Prabhu R, Jeevananda T, Reddy KR, Raghu AV. Polyaniline-fly ash nanocomposites synthesized via emulsion polymerization: Physicochemical, thermal and dielectric properties. Materials Science for Energy Technologies. 2021;4:107-12.

111.   Prabhu R, Roopashree B, Jeevananda T, Rao S, Raghava Reddy K, Raghu AV. Synthesis and corrosion resistance properties of novel conjugated polymer-Cu2Cl4L3 composites. Materials Science for Energy Technologies. 2021;4:92-9.

112.   Chen P, Zhou W, Xiao Z, Li S, Wang Z, Wang Y, et al. An integrated configuration with robust interfacial contact for durable and flexible zinc ion batteries. Nano Energy. 2020;74:104905.

113.   Shin J, Lee J, Kim Y, Park Y, Kim M, Choi JW. Highly Reversible, Grain-Directed Zinc Deposition in Aqueous Zinc Ion Batteries. Advanced Energy Materials. 2021;11(39):2100676.

114.   Ding J, Liu Y, Huang S, Wang X, Yang J, Wang L, et al. In Situ Construction of a Multifunctional Quasi-Gel Layer for Long-Life Aqueous Zinc Metal Anodes. ACS Applied Materials & Interfaces. 2021;13(25):29746-54.

115.   Tangthuam P, Pimoei J, Mohamad AA, Mahlendorf F, Somwangthanaroj A, Kheawhom S. Carboxymethyl cellulose-based polyelectrolyte as cationic exchange membrane for zinc-iodine batteries. Heliyon. 2020;6(10):e05391.

116.   Ain QT, Haq SH, Alshammari A, Al-Mutlaq MA, Anjum MN. The systemic effect of PEG-nGO-induced oxidative stress in vivo in a rodent model. Beilstein Journal of Nanotechnology. 2019;10:901-11.

117.   Si J, Ma R, Wu Y, Dong Y, Yao K. Microstructure and magnetic properties of novel powder cores composed of iron-based amorphous alloy and PTFE. Journal of Materials Science. 2022;57(17):8154-66.

118.   Mai NT, Thuy TT, Mott DM, Maenosono S. Chemical synthesis of blue-emitting metallic zinc nano-hexagons. CrystEngComm. 2013;15(33):6606-10.

119.   Saadiah MA, Zhang D, Nagao Y, Muzakir SK, Samsudin AS. Reducing crystallinity on thin film based CMC/PVA hybrid polymer for application as a host in polymer electrolytes. Journal of Non-Crystalline Solids. 2019;511:201-11.

120.   Riaz T, Zeeshan R, Zarif F, Ilyas K, Muhammad N, Safi SZ, et al. FTIR analysis of natural and synthetic collagen. Applied Spectroscopy Reviews. 2018;53(9):703-46.

121.   Ravindra C, Deepak K, Shilpa N, Saraswati M, Anand N, V RA. Design of eco-friendly PVA/TiO2-based nanocomposites and their antifungal activity study. Green Materials. 2020;8(1):40-8.

122.   Kannan K, Radhika D, Nesaraj AS, Kumar Sadasivuni K, Reddy KR, Kasai D, et al. Photocatalytic, antibacterial and electrochemical properties of novel rare earth metal oxides-based nanohybrids. Materials Science for Energy Technologies. 2020;3:853-61.

123.   López-Pérez JI, Ortiz-Quiles EO, Habiba K, Jiménez-Rodríguez M, Weiner BR, Morell G. Enhanced Structural Integrity and Electrochemical Performance of AlPO4-Coated MoO2 Anode Material for Lithium-Ion Batteries. ISRN Electrochemistry. 2014;2014:359019.

124.   Hao L, Lv G, Zhou Y, Zhu K, Dong M, Liu Y, et al. High Performance Anti-Corrosion Coatings of Poly (Vinyl Butyral) Composites with Poly N-(vinyl)pyrrole and Carbon Black Nanoparticles. Materials [Internet]. 2018; 11(11):[2307 p.]. Available from: https://www.mdpi.com/1996-1944/11/11/2307.

125.   Ning G, Haran B, Popov BN. Capacity fade study of lithium-ion batteries cycled at high discharge rates. J Power Sources. 2003;117(1):160-9.

126.   Tang A, Li Z, Wang F, Dou M, Pan Y, Guan J. One step electrodeposition of Cu2ZnSnS4 thin films in a novel bath with sulfurization free annealing. Appl Surf Sci.

2017;402:70-7.

127.   Li W, Wang K, Zhou M, Zhan H, Cheng S, Jiang K. Advanced Low-Cost, High-Voltage, Long-Life Aqueous Hybrid Sodium/Zinc Batteries Enabled by a Dendrite-Free Zinc Anode and Concentrated Electrolyte. ACS Applied Materials & Interfaces. 2018;10(26):22059-66.

128.   Zhao R, Yang Y, Liu G, Zhu R, Huang J, Chen Z, et al. Redirected Zn Electrodeposition by an Anti-Corrosion Elastic Constraint for Highly Reversible Zn Anodes. Advanced Functional Materials. 2021;31(2):2001867.

129.   Hieu LT, So S, Kim IT, Hur J. Zn anode with flexible β-PVDF coating for aqueous Zn-ion batteries with long cycle life. Chem Eng J. 2021;411:128584.

130.   Kirubasankar B, Murugadoss V, Lin J, Ding T, Dong M, Liu H, et al. In situ grown nickel selenide on graphene nanohybrid electrodes for high energy density asymmetric supercapacitors. Nanoscale. 2018;10(43):20414-25.

131.   Chu Y, Zhang S, Wu S, Hu Z, Cui G, Luo J. In situ built interphase with high interface energy and fast kinetics for high performance Zn metal anodes. Energy & Environmental Science. 2021;14(6):3609-20.

132.   Hu K, Guan X, Lv R, Li G, Hu Z, Ren L, et al. Stabilizing zinc metal anodes by artificial solid electrolyte interphase through a surface ion-exchanging strategy. Chem Eng J. 2020;396:125363.

133.   Nelson J. XANES reflects coordination change and underlying surface disorder of zinc adsorbed to silica. Journal of Synchrotron Radiation. 2021;28(4):1119-26.

134.   Li F, Bu Y, Han G-F, Noh H-J, Kim S-J, Ahmad I, et al. Identifying the structure of Zn-N2 active sites and structural activation. Nature Communications. 2019;10(1):2623.

135.   Dong H, Li J, Guo J, Lai F, Zhao F, Jiao Y, et al. Insights on Flexible Zinc-Ion Batteries from Lab Research to Commercialization. Adv Mater. 2021;33(20):2007548.

136.   Ali T, Yan C. 2 D Materials for Inhibiting the Shuttle Effect in Advanced Lithium–Sulfur Batteries. ChemSusChem. 2020;13(6):1447-79.

137.   Zhou L, Yang Y, Yang J, Ye P, Ali T, Wang H, et al. Achieving fast Zn-ion storage kinetics by confining nitrogen-enriched carbon nanofragments in a honeycomb-like matrix. Appl Surf Sci. 2022;604:154526.

138.   Choi W, Shin H-C, Kim JM, Choi J-Y, Yoon W-S. Modeling and Applications of Electrochemical Impedance Spectroscopy (EIS) for Lithium-ion Batteries. J Electrochem Sci Technol. 2020;11(1):1-13.

139.   Mei B-A, Lau J, Lin T, Tolbert SH, Dunn BS, Pilon L. Physical Interpretations of Electrochemical Impedance Spectroscopy of Redox Active Electrodes for Electrical Energy Storage. The Journal of Physical Chemistry C. 2018;122(43):24499-511.

140.   Zhang S. Status, Opportunities, and Challenges of Electrochemical Energy Storage. Frontiers in Energy Research. 2013;1(8).

141.   Abbasi A, Nasef MM, Babadi FE, Faridi-Majidi R, Takeshi M, Abouzari-Lotf E, et al. Carbon Dioxide Adsorption on Grafted Nanofibrous Adsorbents Functionalized Using Different Amines. Frontiers in Energy Research. 2019;7(145).

142.   Apergis N, Payne JE, Rayos-Velazquez M. Carbon Dioxide Emissions Intensity Convergence: Evidence From Central American Countries. Frontiers in Energy Research. 2020;7(158).

143.   Ghiani E, Pisano G. Chapter 2 - Impact of Renewable Energy Sources and Energy Storage Technologies on the Operation and Planning of Smart Distribution Networks. In: Zare K, Nojavan S, editors. Operation of Distributed Energy Resources in Smart Distribution Networks: Academic Press; 2018. p. 25-48.

144.   Guo Z, Zhang X, Feng S, Zhang H. The Impacts of Reducing Renewable Energy Subsidies on China's Energy Transition by Using a Hybrid Dynamic Computable General Equilibrium Model. Frontiers in Energy Research. 2020;8(25).

145.   Li Y, Wang C, Li G. A Mini-Review on High-Penetration Renewable Integration Into a Smarter Grid. Frontiers in Energy Research. 2020;8(84).

146.   Guney MS, Tepe Y. Classification and assessment of energy storage systems. Renewable and Sustainable Energy Reviews. 2017;75:1187-97.

147.   Frate GF, Ferrari L, Desideri U. Multi-Criteria Economic Analysis of a Pumped Thermal Electricity Storage (PTES) With Thermal Integration. Frontiers in Energy Research. 2020;8(53).

148.   Rancilio G, Lucas A, Kotsakis E, Fulli G, Merlo M, Delfanti M, et al. Modeling a Large-Scale Battery Energy Storage System for Power Grid Application Analysis. Energies. 2019;12(17):3312.

149.   Perry ML, Weber AZ. Advanced Redox-Flow Batteries: A Perspective. J Electrochem Soc. 2015;163(1):A5064-A7.

150.   García-Quismondo E, Almonacid I, Cabañero Martínez MÁ, Miroslavov V, Serrano E, Palma J, et al. Operational Experience of 5 kW/5 kWh All-Vanadium Flow Batteries in Photovoltaic Grid Applications. Batteries. 2019;5(3):52.

151.   Chen H, Cong G, Lu Y-C. Recent progress in organic redox flow batteries: Active materials, electrolytes and membranes. Journal of Energy Chemistry. 2018;27(5):1304-25.

152.   Lao-atiman W, Bumroongsil K, Arpornwichanop A, Bumroongsakulsawat P, Olaru S, Kheawhom S. Model-Based Analysis of an Integrated Zinc-Air Flow Battery/Zinc Electrolyzer System. Frontiers in Energy Research. 2019;7:15.

153.   Hosseini S, Abbasi A, Uginet L-O, Haustraete N, Praserthdam S, Yonezawa T, et al. The Influence of Dimethyl Sulfoxide as Electrolyte Additive on Anodic Dissolution of Alkaline Zinc-Air Flow Battery. Scientific Reports. 2019;9(1):14958.

154.   Hosseini S, Lao-atiman W, Han SJ, Arpornwichanop A, Yonezawa T, Kheawhom S. Discharge Performance of Zinc-Air Flow Batteries Under the Effects of Sodium Dodecyl Sulfate and Pluronic F-127. Scientific Reports. 2018;8(1):14909.

155.   Hosseini S, Han SJ, Arponwichanop A, Yonezawa T, Kheawhom S. Ethanol as an electrolyte additive for alkaline zinc-air flow batteries. Scientific Reports. 2018;8(1):11273.

156.   Gong D, Wang B, Zhu J, Podila R, Rao AM, Yu X, et al. An Iodine Quantum Dots Based Rechargeable Sodium–Iodine Battery. Advanced Energy Materials. 2017;7(3):1601885.

157.   Mousavi M, Jiang G, Zhang J, Kashkooli AG, Dou H, Silva CJ, et al. Decoupled low-cost ammonium-based electrolyte design for highly stable zinc–iodine redox flow batteries. Energy Storage Materials. 2020;32:465-76.

158.   Xie C, Li T, Deng C, Song Y, Zhang H, Li X. A highly reversible neutral zinc/manganese battery for stationary energy storage. Energy & Environmental Science. 2020;13(1):135-43.

159.   Bhunia P, Dutta K. Chapter 16 - Biochemistry and Electrochemistry at the Electrodes of Microbial Fuel Cells. In: Kundu PP, Dutta K, editors. Progress and Recent

169

Trends in Microbial Fuel Cells: Elsevier; 2018. p. 327-45.

160.	Parman AÜ. Comparison of carboxymethyl-cellulose cation-exchange chromatography and high-performance liquid chromatography in the purification of guinea-pig insulin from pancreatic extracts. Journal of Chromatography A. 1983;256:293-301.

161.	Valappil SP, Yiu HHP, Bouffier L, Hope CK, Evans G, Claridge JB, et al. Effect of novel antibacterial gallium-carboxymethyl cellulose on Pseudomonas aeruginosa. Dalton Transactions. 2013;42(5):1778-86.

162.	Isa MIN, Samsudin AS. Potential study of biopolymer-based carboxymethylcellulose electrolytes system for solid-state battery application. International Journal of Polymeric Materials and Polymeric Biomaterials. 2016;65(11):561-7.

163.	Gao Z, Yu Z, Huang C, Duan L, Gao GH. Carboxymethyl cellulose reinforced poly(vinyl alcohol) with trimethylol melamine as a chemical crosslinker. Journal of Applied Polymer Science. 2017;134(11).

164.	Shin J-Y, Lee DY, Yoon JI, Song Y-S. Effect of CMC Concentration on Cell Growth Behavior of PVA/CMC Hydrogel. Macromolecular Research. 2020;28(9):813-9.

165.	Kumar S, Prajapati GK, Saroj AL, Gupta PN. Structural, electrical and dielectric studies of nano-composite polymer blend electrolyte films based on (70–x) PVA–x PVP–NaI–SiO2. Physica B: Condensed Matter. 2019;554:158-64.

166.	Li B, Nie Z, Vijayakumar M, Li G, Liu J, Sprenkle V, et al. Ambipolar zinc-polyiodide electrolyte for a high-energy density aqueous redox flow battery. Nature Communications. 2015;6(1):6303.

167.	Yuan Z, Duan Y, Zhang H, Li X, Zhang H, Vankelecom I. Advanced porous membranes with ultra-high selectivity and stability for vanadium flow batteries. Energy & Environmental Science. 2016;9(2):441-7.

168.	El-Sawy NM, El-Arnaouty MB, Ghaffar AMA. γ-Irradiation Effect on the Non-Cross-Linked and Cross-Linked Polyvinyl Alcohol Films. Polymer-Plastics Technology and Engineering. 2010;49(2):169-77.

169.	Riaz U, Ashraf SM. Characterization of Polymer Blends with FTIR Spectroscopy.

Characterization of Polymer Blends2014. p. 625-78.

170.   Dias LLS, Mansur HS, Donnici CL, Pereira MM. Synthesis and characterization of chitosan-polyvinyl alcohol-bioactive glass hybrid membranes. Biomatter. 2011;1(1):114-9.

171.   Handaya Saputra A, Huda Apriliana N. Polyvinyl Alcohol (PVA) Partially Hydrolyzed Addition in Synthesis of Natural Hydrogel Carboxymethyl Cellulose (CMC) Based from Water Hyacinth. MATEC Web Conf. 2018;156:01007.

172.   Abbasi A, Hosseini S, Somwangthanaroj A, Mohamad AA, Kheawhom S. Poly(2,6-Dimethyl-1,4-Phenylene Oxide)-Based Hydroxide Exchange Separator Membranes for Zinc–Air Battery. International Journal of Molecular Sciences. 2019;20(15):3678.

173.   Alipoori S, Mazinani S, Aboutalebi SH, Sharif F. Review of PVA-based gel polymer electrolytes in flexible solid-state supercapacitors: Opportunities and challenges. Journal of Energy Storage. 2020;27:101072.

174.   Svensson PH, Kloo L. Synthesis, Structure, and Bonding in Polyiodide and Metal Iodide–Iodine Systems. Chemical Reviews. 2003;103(5):1649-84.

175.   Vidya K, Nikhil G. FOURIER TRANSFORM INFRARED SPECTROSCOPY SPECTROSCOPIC STUDIES IN EMBELIA RIBES BURM. F.: A VULNERABLE MEDICINAL PLANT. Asian Journal of Pharmaceutical and Clinical Research. 2016;9(9).

176.   Coates J. Interpretation of Infrared Spectra, A Practical Approach. Encyclopedia of Analytical Chemistry2006.

177.   Zhang J, Jiang G, Xu P, Ghorbani Kashkooli A, Mousavi M, Yu A, et al. An all-aqueous redox flow battery with unprecedented energy density. Energy & Environmental Science. 2018;11(8):2010-5.

178.   Winsberg J, Janoschka T, Morgenstern S, Hagemann T, Muench S, Hauffman G, et al. Poly(TEMPO)/Zinc Hybrid-Flow Battery: A Novel, "Green," High Voltage, and Safe Energy Storage System. Advanced Materials. 2016;28(11):2238-43.

179.   Rajarathnam GP, Schneider M, Sun X, Vassallo AM. The Influence of Supporting Electrolytes on Zinc Half-Cell Performance in Zinc/Bromine Flow Batteries. Journal of The Electrochemical Society. 2016;163(1):A5112.

180.   Schneider M, Rajarathnam GP, Easton ME, Masters AF, Maschmeyer T, Vassallo Anthony M. The influence of novel bromine sequestration agents on zinc/bromine flow

battery performance. RSC Advances. 2016;6(112):110548-56.

181.   Bae S, Lee J, Kim DS. The effect of Cr3+-Functionalized additive in zinc-bromine flow battery. Journal of Power Sources. 2019;413:167-73.

182.   Zhao Y, Li Y, Mao J, Yi Z, Mubarak N, Zheng Y, et al. Accelerating the dissolution kinetics of iodine with a cosolvent for a high-current zinc–iodine flow battery. Journal of Materials Chemistry A. 2022;10(26):14090-7.

183.   Ito S, Sugimasa M, Toshimitsu Y, Orita A, Kitagawa M, Sakai M. Formation of a hydrophobic polyiodide complex during cathodic oxidation of iodide in the presence of propylene carbonate in aqueous solutions, and its application to a zinc/iodine redox flow battery. Electrochimica Acta. 2019;319:164-74.

184.   Chen H, Lu Y-C. A High-Energy-Density Multiple Redox Semi-Solid-Liquid Flow Battery. Advanced Energy Materials. 2016;6(8):1502183.

185.   Li Z, Weng G, Zou Q, Cong G, Lu Y-C. A high-energy and low-cost polysulfide/iodide redox flow battery. Nano Energy. 2016;30:283-92.

186.   Boschloo G, Hagfeldt A. Characteristics of the Iodide/Triiodide Redox Mediator in Dye-Sensitized Solar Cells. Accounts of Chemical Research. 2009;42(11):1819-26.

187.   Zhao Y, Hong M, Bonnet Mercier N, Yu G, Choi HC, Byon HR. A 3.5 V Lithium–Iodine Hybrid Redox Battery with Vertically Aligned Carbon Nanotube Current Collector. Nano Letters. 2014;14(2):1085-92.

188.   Rodby KE, Carney TJ, Ashraf Gandomi Y, Barton JL, Darling RM, Brushett FR. Assessing the levelized cost of vanadium redox flow batteries with capacity fade and rebalancing. Journal of Power Sources. 2020;460:227958.

189.   Chao D, Zhou W, Xie F, Ye C, Li H, Jaroniec M, et al. Roadmap for advanced aqueous batteries: From design of materials to applications. Sci Adv. 2020;6(21):eaba4098.

190.   Goh FT, Liu Z, Hor TA, Zhang J, Ge X, Zong Y, et al. A near-neutral chloride electrolyte for electrically rechargeable zinc-air batteries. Journal of The Electrochemical Society. 2014;161(14):A2080.

191.   Qaiser Fatmi M, Hofer TS, Rode BM. The stability of [Zn(NH3)4]2+ in water: A quantum mechanical/molecular mechanical molecular dynamics study. Physical Chemistry Chemical Physics. 2010;12(33):9713-8.

192.   Lee B, Seo HR, Lee HR, Yoon CS, Kim JH, Chung KY, et al. Critical Role of pH Evolution of Electrolyte in the Reaction Mechanism for Rechargeable Zinc Batteries. ChemSusChem. 2016;9(20):2948-56.

193.   Han D, Wang Z, Lu H, Li H, Cui C, Zhang Z, et al. A Self-Regulated Interface toward Highly Reversible Aqueous Zinc Batteries. Advanced Energy Materials. 2022;12(9):2102982.

194.   Wakita H, Johansson G, Sandström M, Goggin PL, Ohtaki H. Structure determination of zinc iodide complexes formed in aqueous solution. Journal of Solution Chemistry. 1991;20(7):643-68.

195.   Ghazvini MS, Pulletikurthi G, Lahiri A, Endres F. Electrochemical and Spectroscopic Studies of Zinc Acetate in 1-Ethyl-3-methylimidazolium Acetate for Zinc Electrodeposition. ChemElectroChem. 2016;3(4):598-604.

196.   Lucazeau G, Guemas L, Novak A. Vibrational spectra and structure of K2Zn(NH2)4 and Rb2(NH2)4 amides. Inorganica Chimica Acta. 1976;20:11-8.

197.   Foley S, Enescu M. A Raman Spectroscopy and Theoretical Study of Zinc-Cysteine complexation. Vibrational Spectroscopy. 2007;44:256-65.

198.   Soloveichik GL. Flow Batteries: Current Status and Trends. Chemical Reviews. 2015;115(20):11533-58.

199.   Jiang HR, Wu MC, Ren YX, Shyy W, Zhao TS. Towards a uniform distribution of zinc in the negative electrode for zinc bromine flow batteries. Applied Energy. 2018;213:366-74.

200.   Liu H, Zhai H, Hu C, Yang J, Liu Z. Hydrothermal synthesis of In2O3 nanoparticles hybrid twins hexagonal disk ZnO heterostructures for enhanced photocatalytic activities and stability. Nanoscale Research Letters. 2017;12(1):466.

201.   Zhao Z, Wu J, Zheng Y-Z, Li N, Li X, Tao X. Ni3C-Decorated MAPbI3 as Visible-Light Photocatalyst for H2 Evolution from HI Splitting. ACS Catalysis. 2019;9(9):8144-52.

202.   Dilasari B, Jung Y, Kwon K. Effect of water on the stability of zinc in 1-butyl-1-methylpyrrolidinium bis(trifluoromethylsulfonyl)imide ionic liquid. Journal of Industrial and Engineering Chemistry. 2017;45:375-9.

203.   Al-Gaashani R, Radiman S, Daud AR, Tabet N, Al-Douri Y. XPS and optical studies of different morphologies of ZnO nanostructures prepared by microwave methods.

Ceramics International. 2013;39(3):2283-92.

204.   Claros M, Setka M, Jimenez YP, Vallejos S. AACVD Synthesis and Characterization of Iron and Copper Oxides Modified ZnO Structured Films. Nanomaterials [Internet]. 2020; 10(3).

205.   Diler E, Lescop B, Rioual S, Nguyen Vien G, Thierry D, Rouvellou B. Initial formation of corrosion products on pure zinc and MgZn2 examinated by XPS. Corrosion Science. 2014;79:83-8.

206.   Karamat S, Rawat RS, Lee P, Tan TL, Ramanujan RV. Structural, elemental, optical and magnetic study of Fe doped ZnO and impurity phase formation. Progress in Natural Science: Materials International. 2014;24(2):142-9.

207.   Rocks C, Svrcek V, Maguire P, Mariotti D. Understanding surface chemistry during MAPbI3 spray deposition and its effect on photovoltaic performance. Journal of Materials Chemistry C. 2017;5(4):902-16.

208.   Rajendra Kumar G, Dennyson Savariraj A, Karthick SN, Selvam S, Balamuralitharan B, Kim H-J, et al. Phase transition kinetics and surface binding states of methylammonium lead iodide perovskite. Physical Chemistry Chemical Physics. 2016;18(10):7284-92.

209.   Zhou M, Wang S, Yang P, Luo Z, Yuan R, Asiri AM, et al. Layered Heterostructures of Ultrathin Polymeric Carbon Nitride and ZnIn2S4 Nanosheets for Photocatalytic CO2 Reduction. Chemistry – A European Journal. 2018;24(69):18529-34.

210.   Yuan K, Xu Y, Uihlein J, Brunklaus G, Shi L, Heiderhoff R, et al. Straightforward Generation of Pillared, Microporous Graphene Frameworks for Use in Supercapacitors. Advanced Materials. 2015;27(42):6714-21.

211.   Chiang CL, Yang JM. 11 - Flame retardance and thermal stability of polymer/graphene nanosheet oxide composites. In: Wang D-Y, editor. Novel Fire Retardant Polymers and Composite Materials: Woodhead Publishing; 2017. p. 295-312.

212.   Chen J, Yang P, Yu H, Hu Z, Wang J, Wu Y, et al. Designing a Strong Second-Harmonic Generation Polar Iodate by the Structure-Directing Properties of the "Tumbler-like" [Zn(IO3)(I2O5(OH))] Polyanions. ACS Materials Letters. 2023;5(6):1665-71.

213.   Liu H, Wu Q, Liu L, Lin Z, Halasyamani PS, Chen X, et al. AgBi(SO4)(IO3)2: aliovalent substitution induces structure dimensional upgrade and second harmonic

generation enhancement. Chemical Communications. 2021;57(30):3712-5.

214. Yin Y, Wang S, Zhang Q, Song Y, Chang N, Pan Y, et al. Dendrite-Free Zinc Deposition Induced by Tin-Modified Multifunctional 3D Host for Stable Zinc-Based Flow Battery. Advanced Materials. 2020;32(6):1906803.

215. Tangthuam P, Kao-ian W, Sangsawang J, Rojviriya C, Chirawatkul P, Kasemchainan J, et al. Carboxymethyl cellulose as an artificial solid electrolyte interphase for stable zinc-based anodes in aqueous electrolytes. Materials Science for Energy Technologies. 2023;6:417-28.

216. Saupsor J, Sangsawang J, Kao-ian W, Mahlendorf F, Mohamad AA, Cheacharoen R, et al. Compressed composite carbon felt as a negative electrode for a zinc–iron flow battery. Scientific Reports. 2022;12(1):21156.

217. Ko SY, Sand A, Shin NJ, Kwark Y-J. Synthesis and Characterization of Superabsorbent Polymer Based on Carboxymethyl Cellulose-graft-Itaconic Acid. Fibers and Polymers. 2018;19(2):255-62.

218. Pei A, Zheng G, Shi F, Li Y, Cui Y. Nanoscale Nucleation and Growth of Electrodeposited Lithium Metal. Nano Letters. 2017;17(2):1132-9.

219. Landon-Lane L, Marshall AT, Harrington DA. EIS at carbon fiber cylindrical microelectrodes. Electrochemistry Communications. 2019;109:106566.

220. Zhang D, Du C, Chen J, Shi Q, Wang Q, Li S, et al. Improvement of structural and optical properties of ZnAl2O4:Cr3+ ceramics with surface modification by using various concentrations of zinc acetate. Journal of Sol-Gel Science and Technology. 2018;88(2):422-9.

221. Chen D, Gan C, Fan X, Zhang L, Li W, Zhu M, et al. Improving the Dynamic Mechanical Properties of XNBR Using ILs/KH550-Functionalized Multilayer Graphene. Materials [Internet]. 2019; 12(17).

222. Pourebrahimi S, Pirooz M. Reversible iodine vapor capture using bipyridine-based covalent triazine framework: Experimental and computational investigations. Chemical Engineering Journal Advances. 2021;8:100150.

Appendix A
Supplementary information
Carboxymethyl cellulose as an artificial Solid electrolyte interphase for zinc based anode in aqueous electrolyte
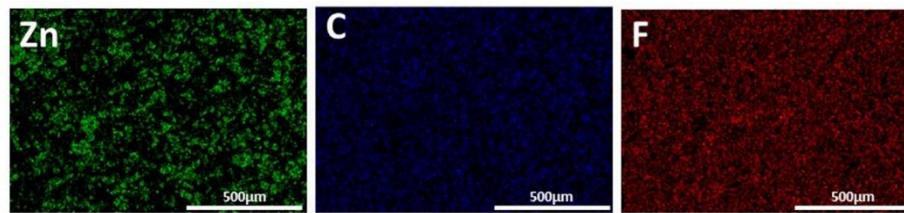
Elements	%wt.
Zn	38.5
C	31.5
F	30

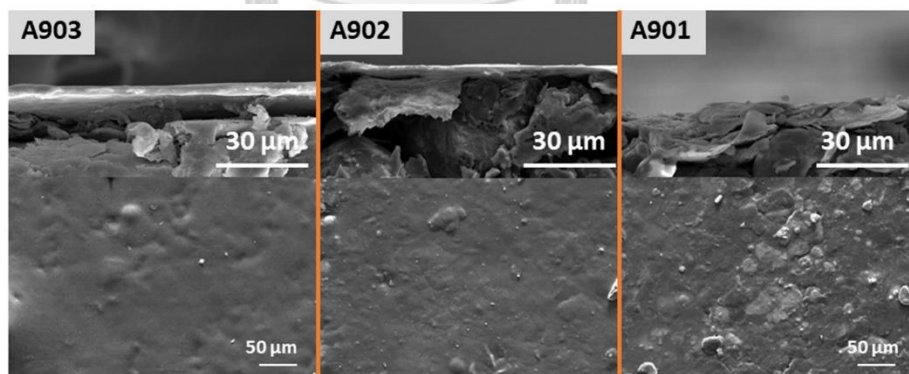**Figure A1.** EDS element on the bare Zn composite anode.

Α

Figure A2. SEM images of zinc anode: coating 3.5 wt.% of CMC (left), 2.5 wt.% of CMC (middle), 1.5 wt.% of CMC (right); CMC Mw.90,000: CMC-ASEI samples are in the order A903, A902, and A901, respectively.

Table A1. FTIR spectra: assignments of the CMC- Zn composite anode surface, before and after 100 cycles, at 1mA cm^{-2} with 0.1 mA h cm^{-2}.

Wave number (cm^{-1})	Assignments
CMC-Zn composite anode	
3356	-OH stretching
2881	-CH$_3$ stretching
1589	-C=O region
1409	-CH$_2$ scissoring
1316	-OH bending
1019	-C-O-C asymmetry stretching
After 100 cycles	
3333	-OH stretching
1624	-C=O region
1397	-CH$_2$ bonding
1023	-C-O-C asymmetry stretching
608	-OH bending
446	Zn-O bond
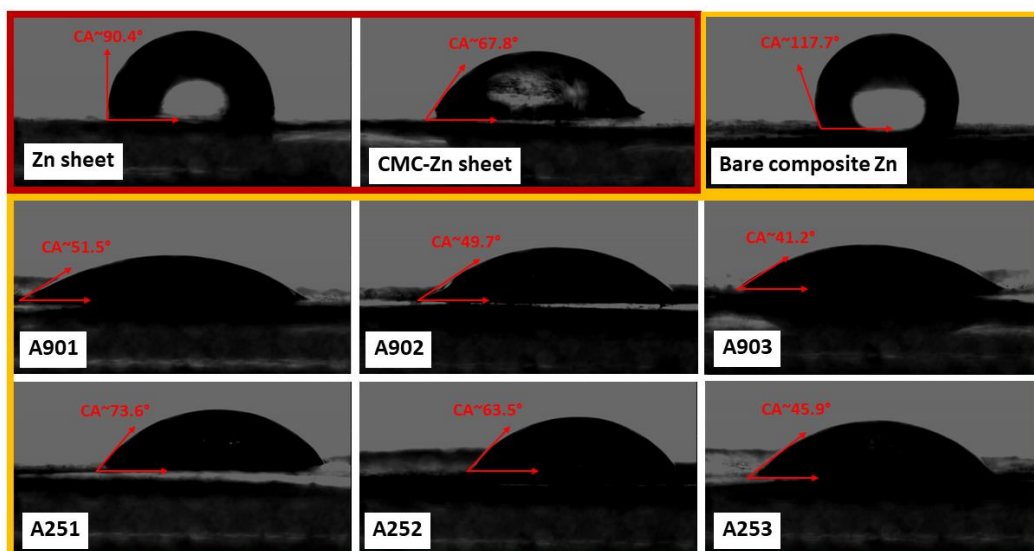
Figure A3. Contact angle measurement of the different anode.
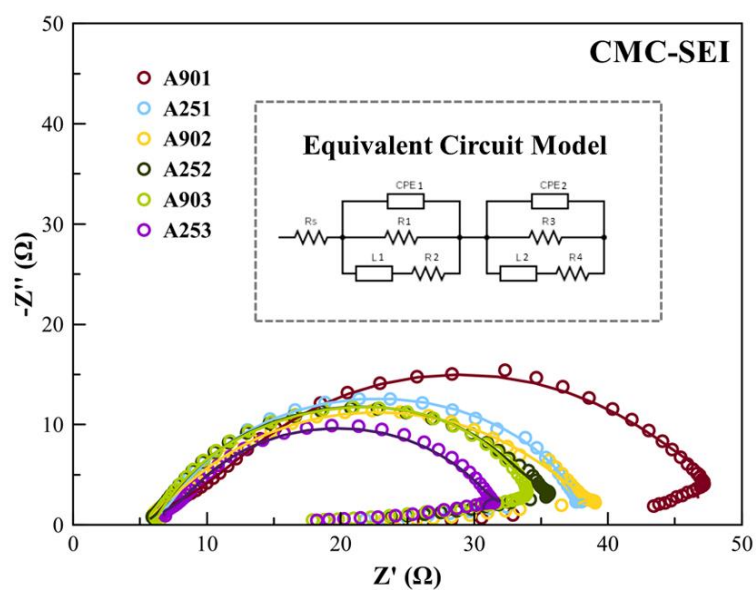
Figure A4. Electrochemical impedance spectra of the CMC-SEI Zn composite anode. Inset: equivalent model circuit.
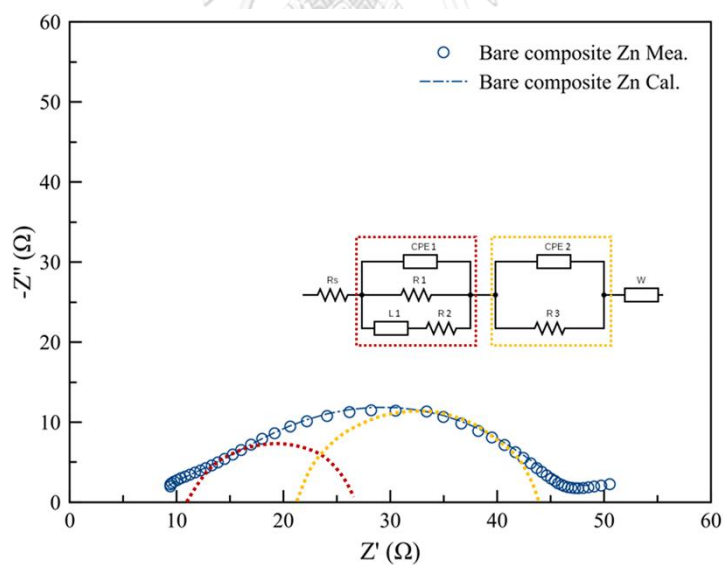

Figure A5. Electrochemical impedance spectra of the bare Zn composite anode in the three-electrode system. Inset: circuit model. (red) high and (yellow) middle frequency capacitive loop.

Table A2. EIS impedances of the symmetrical cells.

Sample	Rs	R_{SEI}	R_{ct}	CPE_{SEI}	CPE_{ct}	W
Bare Zn composite anode	0.144	130.4	37.0	7.20 e-3	1.226 e-5	0.022
A901	2.733	36.4	19.5	1.02 e-4	1.83 e-2	0.120
A902	6.371	40.2	12.45	1.76 e-4	1.97 e-2	0.077
A903	1.485	48.0	24.83	1.753 e-2	6.146 e-5	0.16
A251	2.852	37.1	16.57	6.679 e-5	5.945 e-3	0.051
A252	9.052	28.73	33.40	1.335 e-2	9.161 e-5	0.150
A253	1.454	14.36	14.99	1.188 e-4	2.397 e-2	0.222
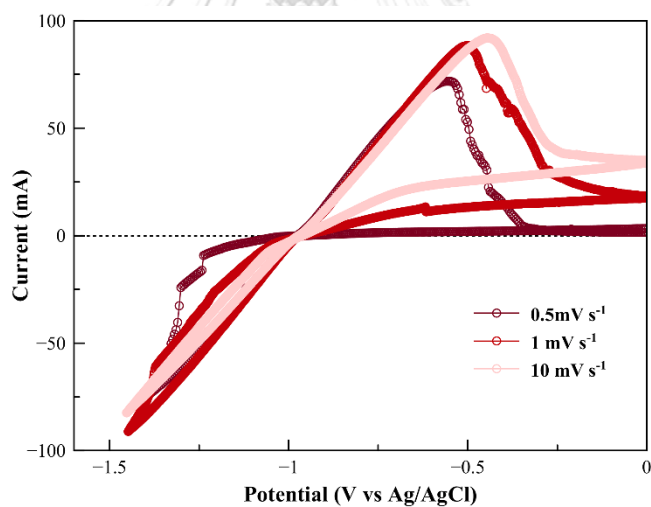
Figure A6. Electrochemical characterization of the three-electrode cell: CV curves of zinc plating/stripping of A253 on Pt plate using Ag/AgCl as reference electrode (the third cycle) in 1.5 M $ZnSO_4$ solution.
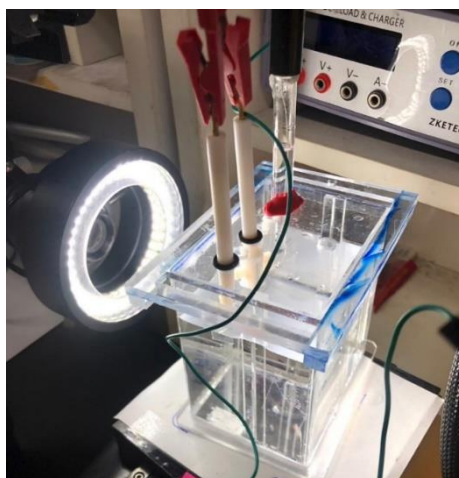
Figure A7. Home-made cell.

Table A3. Values of corrosion potential and anode slope.

Sample	Corrosion potential (mV)	Anodic slope (mV/decade)
Pure Anode	-980.71	279
A901	-980.35	148
A251	-979.21	178
A902	-980.06	150
A252	-979.13	188
A903	-979.08	166
A253	-967.583	130

Table A4. Peak positions of sample and reference.

Sample name	The peak positions of Zn K-edge (Energy (eV))
Zn foil (Ref.)	9666.1
Bare composite Zn	9668.1
A901	9667.5
A902	9667.7
A903	9667.7
A251	9667.3
A252	9667.1
A253	9667.3
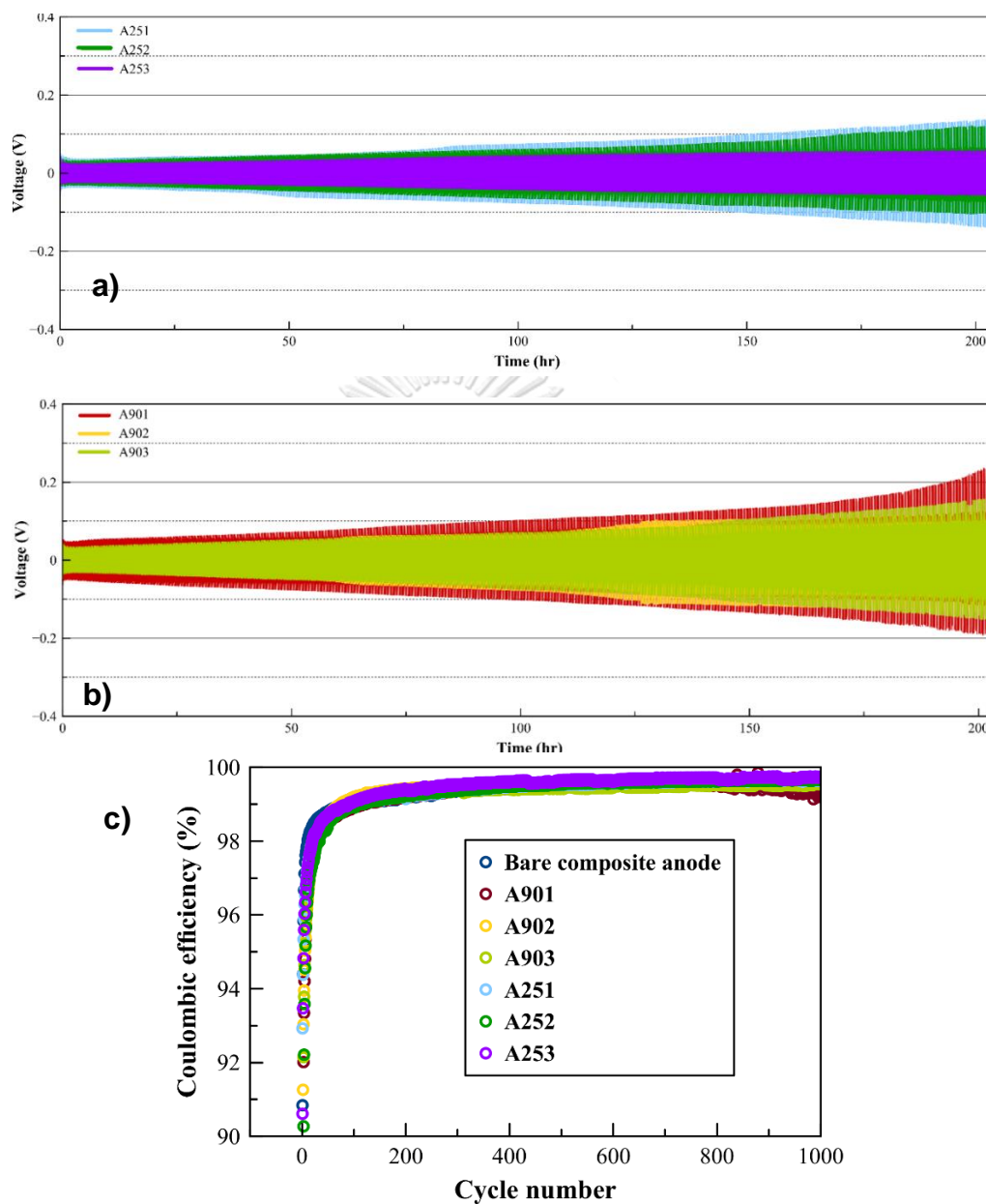
Figure A8. Cycling performance of the symmetrical cells with varying CMC concentration at 1 mA cm^{-2} of current density with 0.1 mA h cm^{-2} of capacity: (a) A251-253, (b) A901-A903, and (c) Coulombic efficiency.
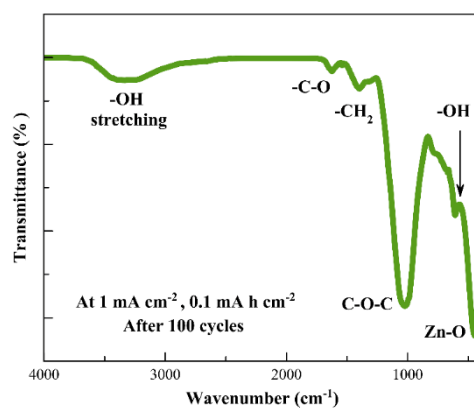
Figure A9. FTIR spectrum of the CMC-coated Zn composite anode after 100 cycles.
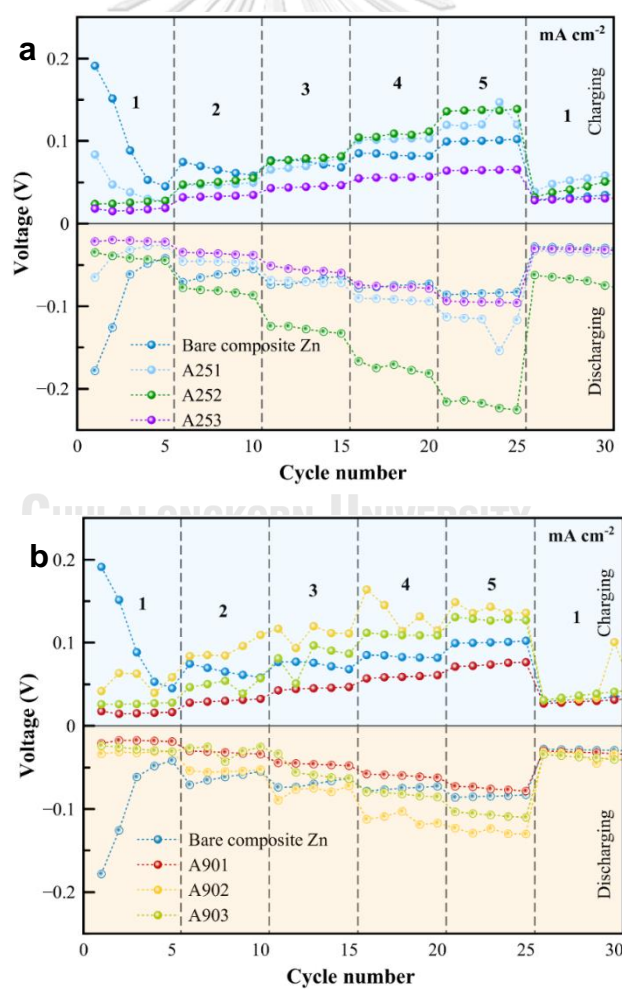

Figure A10. Rate performance of symmetrical cells: 1 to 5 mA cm^{-2} with 1 mA h cm^{-2} (a) Bare Zn composite anode: A251, A252, A253, and (b) A901, A902, A903.
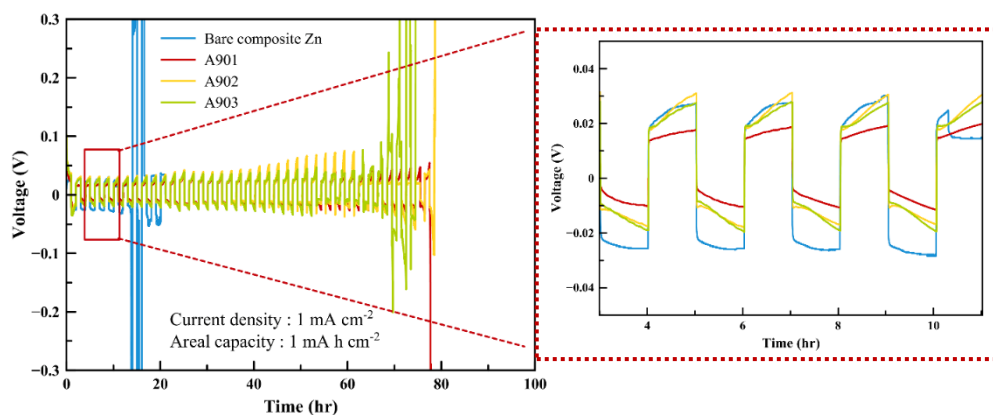
Figure A11. Galvanostatic cycling of the bare Zn composite anode: A901, A902 and A903, at 1 mA cm^{-2} with capacity of 1 mA h cm^{-2}.
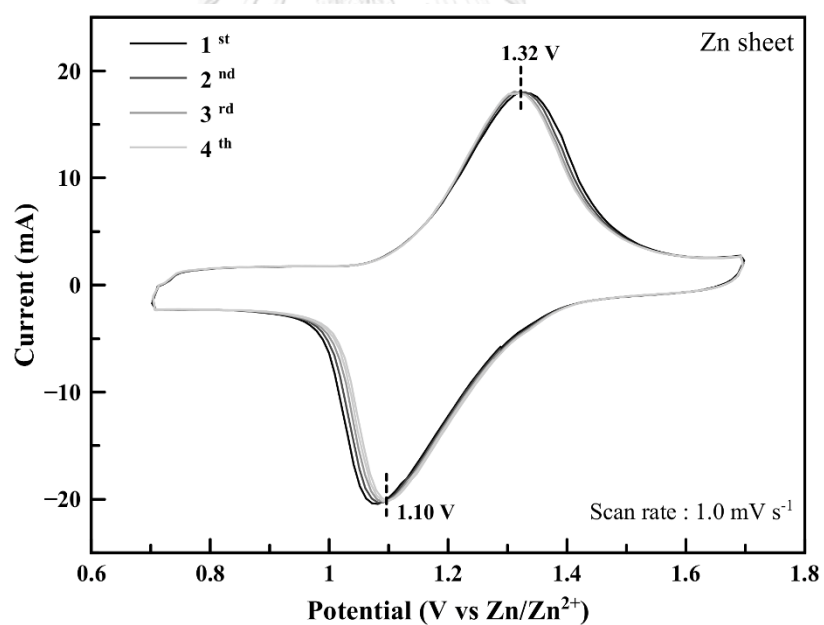

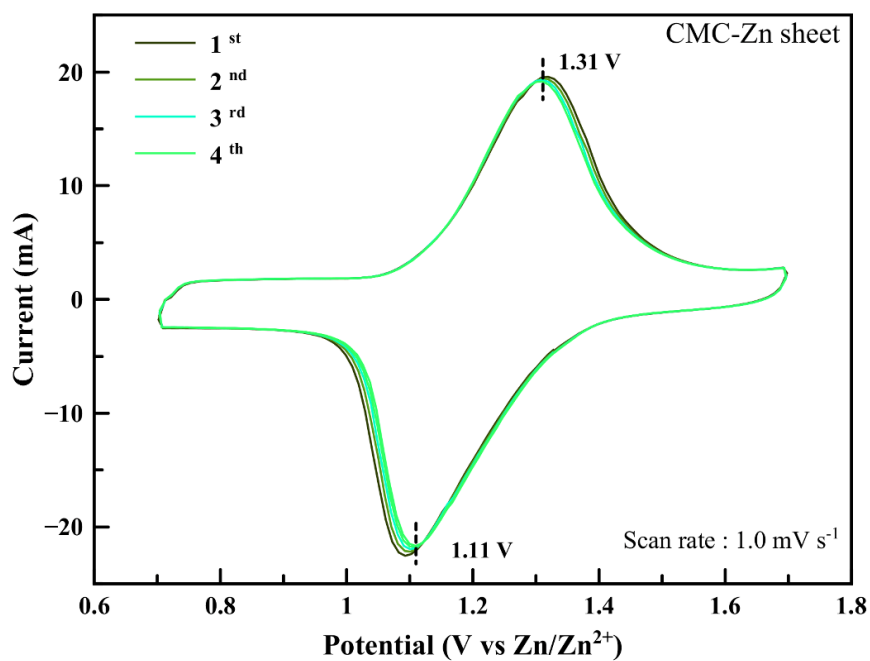**Figure A12.** CV curves: bare Zn sheet anode in full cell at 1.0 mV s^{-1} of scan rate.

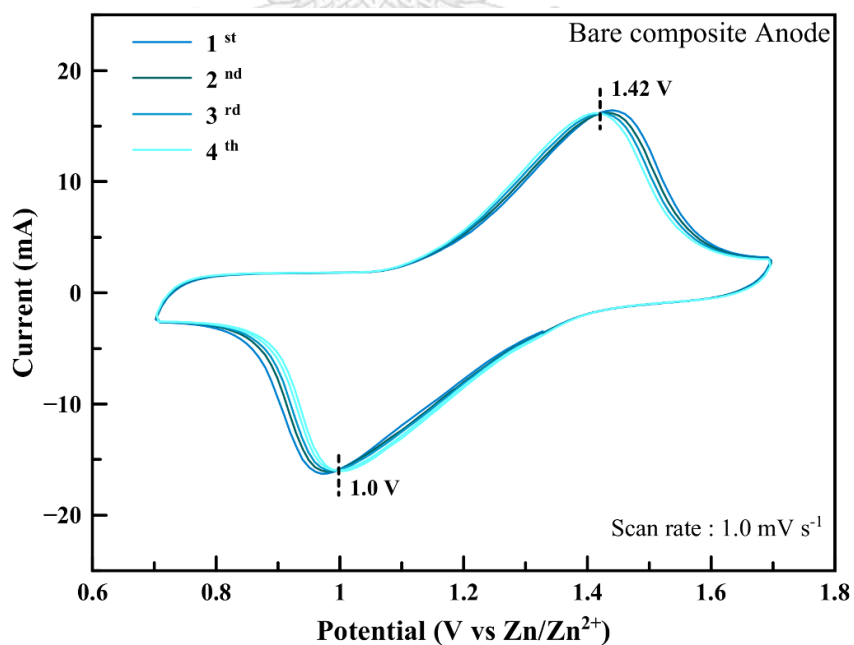**Figure A13.** CV curves: Zn sheet with CMC layer in full cell at 1.0 mV s^{-1} of scan rate.

Figure A14. CV curves: bare composite Zn anode in full cell at 1.0 mV s^{-1} of scan rate.
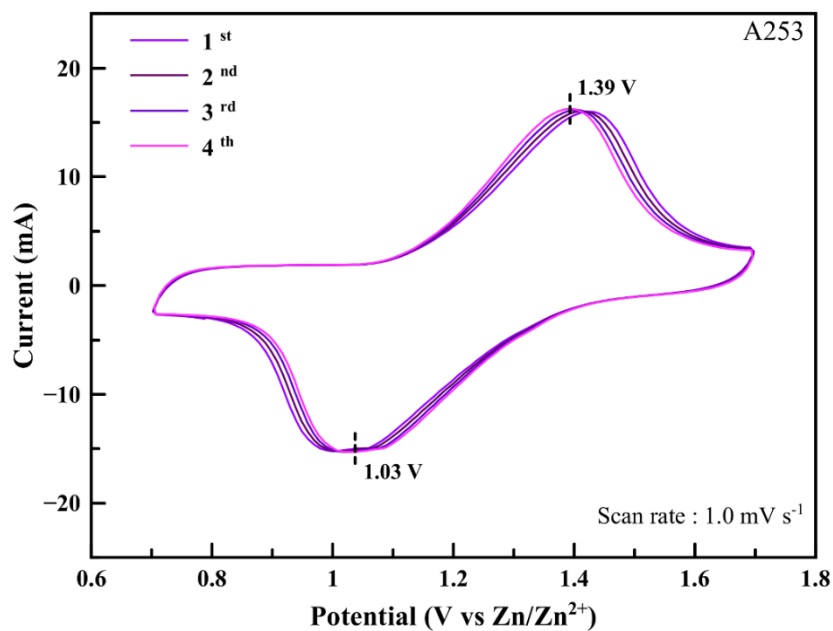
Figure A15. CV curves: CMC-coating on the Zn composite anode in full cell at 1.0 mV s^{-1} of scan rate.
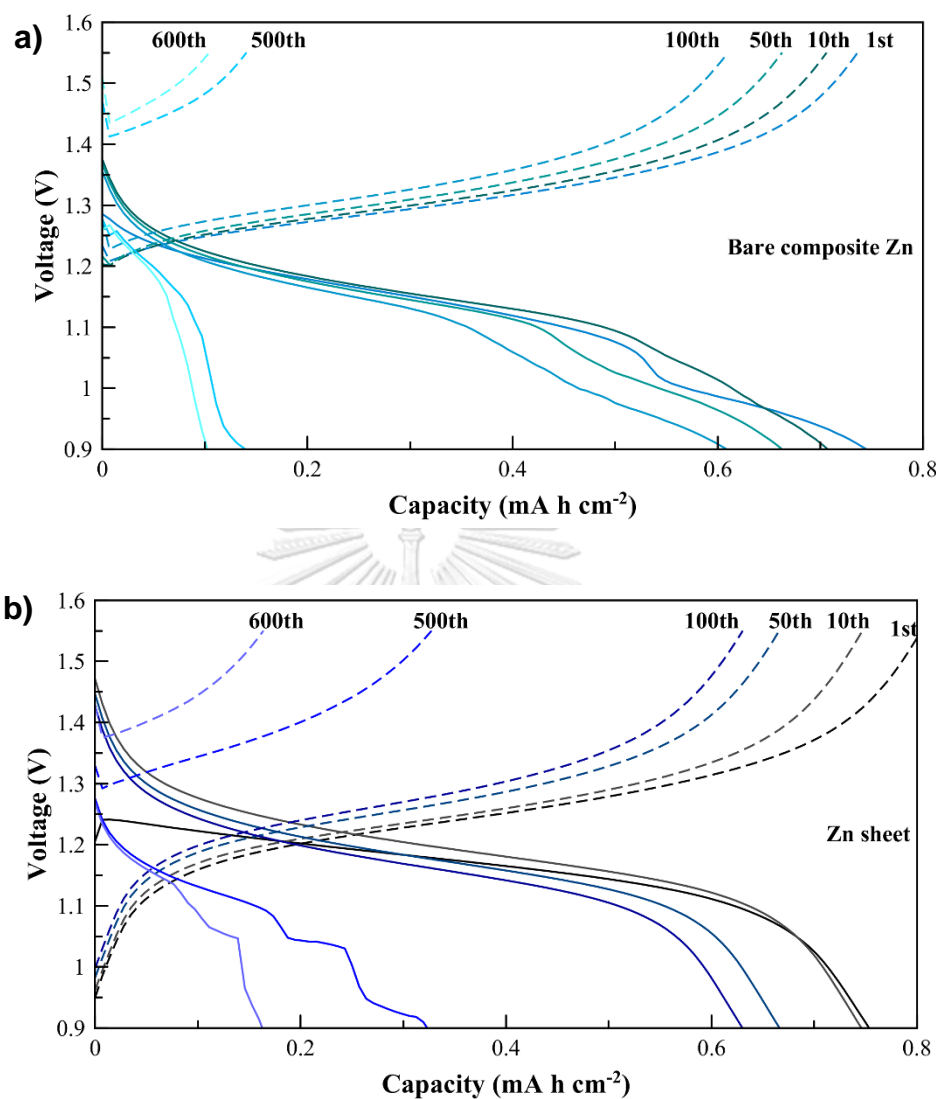
Figure A16. Galvanostatic charge-discharge profiles: (a) Bare composite Zn anode, and (b) Bare Zn sheet anode full cell at 5 mA cm^{-2} with cut-off voltage 1.55-0.9V.

Appendix B
Supplementary information
Carboxymethyl cellulose-based polyelectrolyte as cationic exchange membrane for zinc-iodine batteries

B1. Material

Analytical grade PVA (Mw 117, Chem-Supply Pty Ltd, Gillman, SA, Australia) and CMC (Mw 250,000, Sigma-Aldrich, St. Louis, MO, USA) were used to prepare the polyelectrolyte membranes. Iodine (I_2) and potassium iodide (KI, 99.0%) used for the catholyte were purchased from Univar (Shanghai, China). Graphite felt (AvCarb G200, AvCarb Material Solutions, Lowell, MA, USA.) was employed for both negative and positive electrodes. Zinc sheet (99.9% purity, Shandong AME Energy Co., Ltd., Shenzhen, China) and zinc sulfate ($ZnSO_4 \cdot 7H_2O$, Kemaus, New South Wales, WA, Australia) were used for the electroplating process to prepare the negative electrode. Nylon membrane filter (0.1 µm) was purchased from Sterlitech Corporation (Kent, WA, USA). 100 mesh of woven wire 304 stainless steel, purchased from Alikafeii Trading Co., Ltd. (China), was used as the current collector.

B2. Battery fabrication

To fabricate the negative electrode, graphite felt was cut into pieces 1×1 cm^2 in dimension. Zn was electroplated on graphite felt using a Zn sheet (counter electrode) and a Zn sulfate solution (2 M) under a current density of 50 mA/cm^2, for a duration of 1 h. As for the positive electrode, the graphite felt was cut into pieces 1×1 cm^2 in dimension and used, as is, without any treatment.

Polyelectrolyte membranes were synthesized by a casting process using solutions of CMC and PVA having different ratios. The weight ratios of CMC:PVA in the polymer electrolyte membrane used in this study were as follows: 25:75, 50:50 and 75:25 and were denoted as C25, C50 and C75. First, the solution having different ratios was prepared by dissolving CMC (1.25, 2.5 and 3.75 g) in 95 ml distilled water. Then, PVA (3.75, 2.5 and 1.25 g) was added to the solution. The solution was further stirred for 1 h at 60 °C. After that, 1 M Zn sulfate (100 ml) was gradually dripped into the solution while the solution was continuously stirred, using a homogenizer (10,000 rpm). After that, the mixture was de-gassed using an ultrasonic sonicator for 2 min. The mixture (10 ml) was cast into a glass Petri dish where nylon membrane was used as a supportive structure. The sample was dried naturally at 27 °C for 36 h. A schematic diagram of the polymer electrolyte membrane is shown, as in Fig. B1a. The thickness of the membrane was

controlled by the volume of polymer solution in the Petri dish. The average thickness of the polyelectrolytes was 1 mm.

Fig. B1b shows a schematic diagram of the testing cell. The cell consists of an anode, a polymer electrolyte membrane, and a cathode. The anode and cathode are attached to both sides of the electrolyte membrane. Strips of stainless-steel mesh (1×10 cm^2) were used as current collectors for both the anode and cathode. The anolyte contained 15 ml of 1 M Zn sulfate. A mild acidic aqueous electrolyte based on Zn sulfate supports highly reversible Zn deposition/dissolution behavior on the negative electrode anode. The catholyte contained 15 ml of 0.5 N iodine solution (1:1 molar ratio between I_2 and KI). In an aqueous solution, the increase in solubility of iodine is due to the formation of triiodide ions.
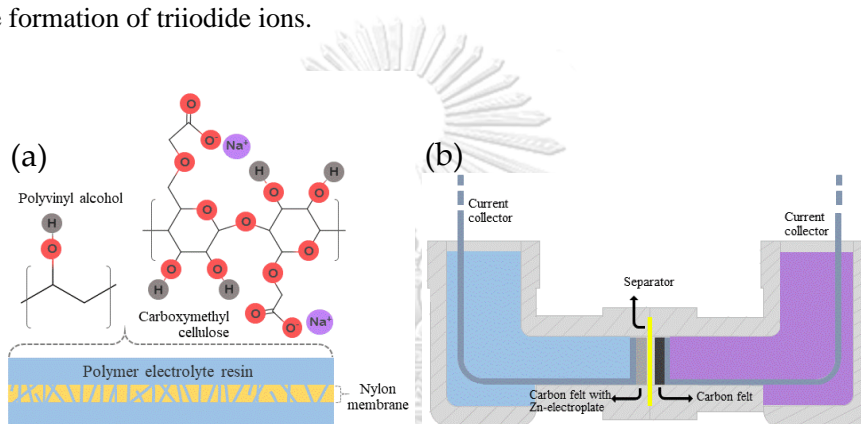

Figure B1. (a) Schematic diagram of polyelectrolyte membrane and (b) Schematic diagram of ZIFB cells

B3. Characterization

Both, the CMC/PVA interaction and the stability of the polyelectrolyte membranes were investigated via FTIR, PerkinElmer Spectrum One (PerkinElmer Inc., Waltham, MA, USA.), in transmission mode in the range of wave numbers: 400-4000 cm^{-1}. Surface morphological analysis of the membrane was studied using scanning electron microscope (SEM), JEOL (Peabody, MA, USA) JSM-6480LV, 15 kV. Iodine and polyiodide crossover were investigated via titration using thiosulfate solution and starch indicator (1 g starch in 100 ml of water).

Electrochemical performance was studied via Versa STATE 3A (Ametek Inc., Berwyn, PA, USA) in the frequency range: 0.1 - 200,000 Hz at ambient temperature for conductivity measurement. Galvanostatic charge-discharge cycling tests were carried out using Battery Tester CT-4008-5V20mA, Neware Technology Ltd. (Shenzhen, China). The discharge voltage-current polarization characteristics of the batteries were investigated in the range of current density: 5 - 50

mA/cm^2. Cycling capability was examined at a constant current density of 10 mA/cm^2 and charge-discharge capacity of 0.1 mAh.

Appendix C
Supplementary information
Unveiling the synergy of pH-buffered electrolytes and CMC in zinc deposition and dissolution for zinc-iodine flow batteries

C1. Theoretical capacity calculation

As per Faraday´s law,

$$\text{Capacity} = F * c * n * V$$

Where F is Faraday´s constant 96,485 C/mol, c is the concentration of ions in the salt, n is the number of electrons participating in the reaction per mole of reactant, V is the volume of electrolyte.

Negative half-cell: (Zn^{2+} as reactant)

For 30 mL of a solution of 1.0 M ZnI_2 , n = 2 ;

$$\text{Theoretical capacity } = \ 1.608 \text{Ah}$$

Positive half-cell: (I^- as reactant)

For 30 mL of a solution of:

1.0 M ZnI_2, n = 4/3 ;   Theoretical capacity = 1.072 Ah

1.0 M Br^- salt, n = 2/3;   Theoretical capacity = 0.536Ah

In total: Theoretical capacity = (1.072 Ah + 0.536Ah) = 1.608 Ah

Specific capacity (Ah/L) has been calculated based on the volume of the catholyte (30 mL).

C2. Efficiency calculation

Coulombic (CE) efficiency;

$$CE = \left({Q_{discharge}} \middle/ {Q_{charge}} \right) * 100$$

Energy (EE) efficiency;

$$EE = \left({E_{discharge}} \middle/ {E_{charge}} \right) * 100$$

Voltage (VE) efficiency;

$$VE = \left({EE} \middle/ {CE} \right) * 100$$

Where Q is the battery capacity and E is the battery energy during the charge/discharge.

Table C1. Comparison of R_{ohm} from the output voltage versus current plot at current densities of 10-100 mA cm^{-2} in different electrolyte.

Anolyte	Catholyte		Ohmic resistance (Ω cm^2)
1 M ZnI$_2$	1 M ZnI$_2$	Charge	7.454
		Discharge	7.665
1 M ZnI$_2$:0.5 M NH$_4$Br	1 M ZnI$_2$:0.5 M NH$_4$Br	Charge	7.581
		Discharge	6.097
1 M ZnI$_2$: 0.5 M LiBr	1 M ZnI$_2$: 0.5 M LiBr	Charge	8.904
		Discharge	8.838
1 M ZnI$_2$: 0.5 M KBr	1 M ZnI$_2$: 0.5 M KBr	Charge	7.469
		Discharge	7.314
1 M ZnI$_2$:0.5 M NH$_4$OAc	1 M ZnI$_2$:0.5 M NH$_4$Br	Charge	6.915
		Discharge	3.678
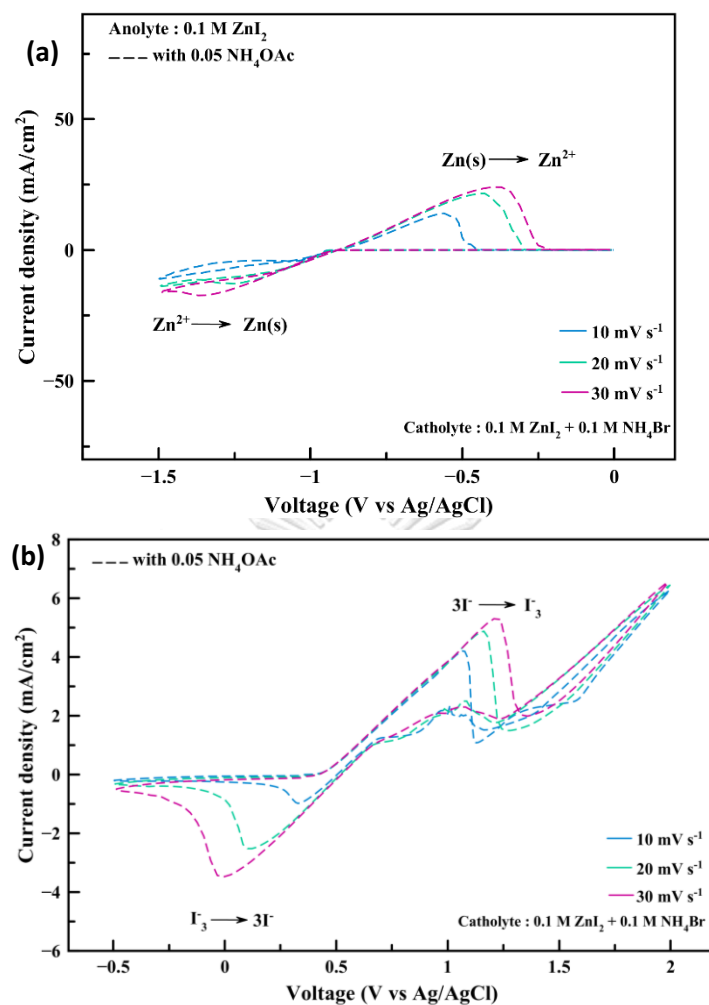
Figure C1. Cyclic voltammetry (CV) curve of (a) Zn/Zn^{2+} redox reaction and (b) I_3^-/I^- redox reaction in 0.1 M ZnI_2 + 0.05 M NH_4OAc at a scan rate of 10-30 mV s^{-1}.

VITA

NAME   Phonnapha Tangthuam

DATE OF BIRTH   19 November 1995

PLACE OF BIRTH Ratchaburi, Thailand

**INSTITUTIONS
ATTENDED**   Bachelor's Degree in Science from Chulalongkorn University

HOME ADDRESS 33 Village No.1 Dan Thap Tako, Chom Bueng, Ratchaburi, Thailand, 70150

PUBLICATION   Tangthuam, P.; Pimoei, J.; Mohamad, A.A.; Mahlendorf, F.; Somwangthanaroj, A.; Kheawhom, S. Carboxymethyl cellulose-based polyelectrolyte as cationic exchange membrane for zinc-iodine batteries. Heliyon 2020, 6, e05391, doi:10.1016/j.heliyon.2020.e05391.

Tangthuam, P.; Kao-ian, W.; Sangsawang, J.; Rojviriya, C.; Chirawatkul, P.; Kasemchainan, J.; Mahlendorf, F.; Nguyen, M.T.; Yonezawa, T.; Kheawhom, S. Carboxymethyl cellulose as an artificial solid electrolyte interphase for stable zinc-based anodes in aqueous electrolytes. Materials Science for Energy Technologies 2023, 6, 417-428, doi:10.1016/j.mset.2023.04.003.